Imperial College London
Department of Mechanical Engineering

Data-Driven Modelling of Compressor Stall Flutter

Marco Rauseo

March 2023

A thesis submitted to Imperial College London
in part fulfilment of the requirements for the degree of Doctor of Philosophy

Abstract

Modern aircraft engines need to meet ever more stringent requirements that greatly increase the complexity of design, which strives for enhanced performance, reduced operating costs, emissions and noise simultaneously. The drive for performance leads to the development of thin, lightweight, highly loaded fan and compressor blades which are increasingly more prone to incur high, sustained vibratory stresses and aeroelastic problems such as flutter.

The current practice employs preliminary design tools for flutter that are often based on empiricism or simplified analytical models, requiring extensive use of computational fluid dynamics to verify aeroelastic stability. As the industry moves to new designs, fast and accurate prediction tools are needed. In this thesis, data-driven techniques are employed to model the aeroelastic response of compressor blades.

Machine learning has been applied to a plethora of engineering problems, with particular success in the field of turbulence modelling. However, conventional, black-box data-driven methods based on simple input parameters require large databases and are unable to generalise. In this work a combination of machine learning techniques and reduced order models is proposed to address both limitations at the same time. Previous knowledge of flutter is introduced in the physics guided framework by formulating relevant, steady state input features, and by injecting results from low-fidelity analytical models.

The models are tested on several unseen cascades and it is found that training on even a single geometry yields accurate results. The models developed here allow flutter prediction of fan and compressor flutter stability based on the steady state flow only without a need for any CPU intensive unsteady simulations. Hence, one can predict flutter stability of a given blade for different mechanical properties (mode shape, frequency) at near zero additional cost once the mean flow is known. Moreover, for fan flutter, the model developed here can be integrated with available analytical models of intake to analyse the consequences of intake properties, such as length and acoustic liners location, on the stability of fan blades. The EU goal of climate-neutrality by 2050 requires novel design concepts in aviation which is unachievable without complimentary novel prediction and design tools. The research presented in this thesis will allow one to explore the design space for flutter stability based on steady flow only, and hence offers such an alternative. To the best of the author's knowledge, no previous research is available on modelling of compressor stall flutter with data-driven techniques.

Statement of Originality

I hereby declare that except where specific reference is made to the work of others, the contents of this thesis are original and have not been submitted in whole or in part for consideration for any other degree or qualification in this, or any other University or Institution. This thesis is my own work and contains nothing which is the outcome of work done in collaboration with others, except as specified in the text and Acknowledgements.

I will make use of nosism throughout this work.

Marco Rauseo
March 2023

Copyright Declaration

Acknowledgements

I would like to express my gratitude to my supervisor Prof. Mehdi Vahdati, for giving me the opportunity to carry out this project and for his support throughout my PhD. He encouraged me to explore different ideas on my own, and was always available to clear any doubts I might have. I always liked his honesty, he taught me a lot and if I can call myself a researcher now is largely thanks to him. I am also grateful to my de facto second supervisor Dr. Fanzhou Zhao, an outstanding researcher and one of the smartest people I know. His help has been instrumental, from reviewing my writing to setting up computers and everything in between. I am not quite sure what this thesis would have looked like without him. They've both become good friends and I am glad I got to work with them.

I would also like to thank my colleagues Dr. Xiao He, for introducing me to the fundamentals of turbulence modelling and machine learning, and Dr. Quentin Rendu for sharing lots of useful papers and his vast knowledge of CFD. Being able to work with these people filled me with pride.

I would also like to acknowledge Dr. Paul Petrie-Repar, who provided me with LUFT, the CFD code I used throughout this PhD, and Chuanxiang Yan and Baotong Wang from Tsinghua University who provided data for the comparisons with ANSYS.

I have met a bunch of people in the years I spent doing this PhD and have been lucky enough to become friends with some of them. Thanks to the several housemates I had, Alessandra and Andrea in particular, the people in the VUTC (Sam, Tom, Jonah, Harry and that lot) where I worked for more than a year, the French crowd and the north London crew. Special mention to my old mates Alessandro, for the nights out and the long talks, and Luca, whose visits during the past year made me feel like we were back at uni.

Thanks to Chris, Juliet, Jen and Pete for treating me like family while I was away from my own.

Thanks to my family, for their love and support during my studies, no matter how far I ended up living. I especially thank my parents, who don't speak English so: grazie mamma e papà per aver appoggiato le mie decisioni e avermi permesso di vivere ben al di sopra delle mie possibilità. Alla fine della fiera, non sarei arrivato qua senza di voi. Ho fatto il possibile per rendervi fieri.

Thanks to Alessia and Francesco for talking to me pretty much everyday and being there when I needed it most. I can't tell you how important your friendship has been.

Finally, thank you my darling Bex. You have meant so much to me in these years, the support you have given me I cannot quite put into words and, to be fair, even if I did, I'm not sure I would like to have it in an open-access document on the Internet. Suffice to say, I couldn't have made it without you. This PhD is as much mine as it is yours.

I skimmed through, read and studied a number of theses during the past few years, or at least I made it as far as the acknowledgements of each one. Unmistakably, after thanking their loved ones same way as I just did, the authors go on to tell what an amazing journey their PhD experience has been. At the time, their statements confused me as I wasn't exactly enjoying myself, but I thought that, if I waited a little longer, I would get it. I too would be shown the light on my very own way to Damascus and start looking at this whole thing as "amazing". Well, turns out the time has passed, I have done the work, learnt a lot of things, written this thesis and still I have no clue what these people were on about. Thank Christ I'm done.

Table of contents

List of figures **xv**

List of tables **xxv**

1 Introduction **1**

1.1 The Compressor Map 1

1.2 Aeroelasticity 3

  1.2.1 Static Aeroelasticity 3

  1.2.2 Dynamic Aeroelasticity 4

  1.2.3 Properties of interest in turbomachinery 6

1.3 Flutter 10

  1.3.1 Choke Flutter 10

  1.3.2 Stall Flutter 10

1.4 Prediction Methods for Flutter 12

1.5 Machine Learning in Fluid Mechanics 15

1.6 Motivation and Research Objectives 17

1.7 Thesis Outline 18

2 Methodology **21**

2.1 Introduction 21

2.2 CFD Solver 21

  2.2.1 Navier-Stokes Equations 21

  2.2.2 Time-Linearised Navier-Stokes Equations 23

  2.2.3 Boundary Conditions 25

  2.2.4 Aeroelastic Equations 26

2.3 Aeroelastic Stability 30

2.4 Cut-off conditions in a two-dimensional cascade 32

2.5 Standard Configuration 10 36

  2.5.1 Comparison with time-accurate solver 37

2.6 Machine Learning Techniques 46

  2.6.1 Fully Connected Neural Network 46

  2.6.2 Random Forest 48

  2.6.3 Model Explainability 48

2.7 Summary 50

3 Neural Network Model 51
3.1 Introduction 51
3.2 Training Geometry 51
3.3 Input Features 51
3.4 Databases of Aerodynamic Damping 53
3.5 Surrogate Model 54
  3.5.1 Forward Propagation 54
  3.5.2 Backpropagation 55
  3.5.3 Hyperparameters Tuning 55
3.6 Comparison with CFD 59
3.7 Application to Blade Redesign 60
3.8 Summary 65

4 Analytical Methods for the Aeroelastic Response of Cascades 67
4.1 Introduction 67
4.2 Linearised Subsonic Unsteady Flow in Cascades 68
4.3 Verification of Implementation 73
4.4 Comparison against CFD 74
  4.4.1 Unloaded Cascade 74
  4.4.2 Loaded Cascade 75
4.5 Summary 76

5 Physics Guided Neural Network Model 77
5.1 Introduction 77
5.2 Machine Learning Algorithm 78
5.3 Reduced Order Model 79
5.4 Output Formulation 80
5.5 Input Formulation 81
  5.5.1 Steady State Features 82
  5.5.2 Unsteady Features 85
5.6 Effect of change in geometry on steady and unsteady aerodynamics . . 86
  5.6.1 Definition of zero incidence 86
  5.6.2 Change in solidity 88
  5.6.3 Change in stagger 91
  5.6.4 Change in camber 94
  5.6.5 Change in thickness 96
5.7 Model Selection 97
  5.7.1 Comparison against CFD and explanation of results 101
5.8 Increasing training database size 110
5.9 Fan Blade test case 111
  5.9.1 Steady State 111

5.9.2 Unsteady results and comparison with PGML 113
5.10 Summary 126

6 Uncertainty of Aerodynamic Damping Predictions 127
6.1 Introduction 127
6.2 Test Case 129
6.3 Sensitivity of Aerodynamic Damping in Transonic Flow 130
6.4 Uncertainty Quantification Method 133
6.4.1 Training Data 136
6.4.2 Hyperparameter tuning and feature selection 136
6.5 Comparison of QRF with CFD 140
6.6 Validation of Prediction Intervals 142
6.7 Conservative Flutter Margin 145
6.8 Summary 147

7 Conclusions and Future Work 149
7.1 Conclusions 149
7.2 Comments on the role of the reduced order model 150
7.3 Future Work 151

References 153

Appendix A PGML hyperparameters 167

Appendix B Further PGML results 169

Appendix C Computational Cost 175

List of figures

1.1 Illustration of an axial compressor map. Adapted from Bontemps (2020) 2
1.2 Transonic flow topologies as mass flow rate decreases along a speedline. Shock wave (—) and sonic line (- - -) delimit the pocket of supersonic flow in the passage. Illustration adapted from Rendu (2016). 3
1.3 Collar (1946) Triangle of forces 4
1.4 Illustration of a Campbell diagram 5
1.5 Variation of mode frequency due to aerodynamic loads for: **(a)** a wing; **(b)** a turbomachinery blade. The crossing of two lines denotes coalescence flutter. Adapted from Rendu (2016). 6
1.6 Blade-disk assembly vibration pattern with different nodal diameters. 7
1.7 Pressure fields in annular duct for different circumferential-radial order 9
1.8 Typical flutter regions on a compressor map. Adapted from Bontemps (2020) 10
1.9 Illustration of accuracy as a function of computational cost of methods employed to assess compressor aeroleastic stability during design stages. 18

2.1 Schematic displacement history depending on the sign of aerodynamic damping ratio 31
2.2 Cut-off reduced frequency against interblade phase angle 36
2.3 Standard Configuration 10 mesh 38
2.4 Steady steady pressure coefficient in subsonic flow 40
2.5 Aerodynamic damping coefficient against interblade phase angle for plunging motion in subsonic flow: **(a)** $k = 0.5$, **(b)** $k = 1.0$ 41
2.6 Imaginary part of the unsteady pressure coefficient for plunging motion at subsonic flow conditions, with reduced frequency $k = 0.5$: **(a)** $\sigma = 0^\circ$, **(b)** $\sigma = 90^\circ$ 42
2.7 Aerodynamic damping coefficient against interblade phase angle for pitching motion in subsonic flow: **(a)** $k = 0.5$, **(b)** $k = 1.0$ 42
2.8 Imaginary part of the unsteady pressure coefficient for pitching motion at subsonic flow conditions, with reduced frequency $k = 0.5$: **(a)** $\sigma = 0^\circ$, **(b)** $\sigma = 90^\circ$ 42

2.9 Aerodynamic damping coefficient against interblade phase angle for pitching motion in subsonic flow. Comparison of time-accurate computations with increasing number of blade N_b 43
2.10 Steady steady pressure coefficient in transonic flow 43
2.11 Aerodynamic damping coefficient against interblade phase angle for plunging motion in transonic flow: **(a)** $k = 0.5$, **(b)** $k = 1.0$ 44
2.12 Imaginary part of the unsteady pressure coefficient for plunging motion at transonic flow conditions, with reduced frequency $k = 0.5$: **(a)** $\sigma = 0°$, **(b)** $\sigma = 90°$ 44
2.13 Aerodynamic damping coefficient against interblade phase angle for pitching motion in transonic flow. Comparison of time-accurate computations with increasing number of blade N_b 45
2.14 Illustration of a neuron. Adapted from Chen (2022) 46
2.15 Common activation units: **(a)** sigmoid, **(b)** hyperbolic tangent (tanh), **(c)** rectified linear unit (ReLU) and **(d)** swish. Adapted from Chen (2022) 46
2.16 Illustration of a fully connected neural network. Adapted from He et al. (2020). 47

3.1 Schematic illustration of modeshape at different X_t. 52
3.2 Illustration of the difference between parameters that control the plunge-pitch ratio of a flap mode as a function of the chordwise location of pitching axis: **(a)** α as defined by Vahdati and Cumpsty (2015); **(b)** X_t defined in this work 53
3.3 Training database independence study: **(a)** Difference between test and training error; **(b)** Test and training errors 56
3.4 Test percentage error as a function of: **(a)** regularisation parameter λ, **(b)** number of hidden layers L 57
3.5 Test percentage error as a function of W, number of connections in the FCNN 57
3.6 Evaluation of FCNN predictive capabilities 58
3.7 Comparison of FCNN (**- - -**) and CFD (**—**) aerodamping predictions for the conditions listed in Table (3.4). **(a)** Case 1: Incidence sweep; **(b)** Case 2: Reduced Frequency sweep; **(c)** Case 3: Plunge-pitch ratio sweep; **(d)** Case 4: Interblade Phase Angle sweep 60
3.8 Mean flow field of application test case: **(a)** Mach Number contour; **(b)** Isentropic Mach Number on the blade 61
3.9 Normalised gradients for Case 4 at $\sigma = 20°$ and $\sigma = 120°$. 62
3.10 Change in aerodynamic damping at $\sigma = 20°$ and $\sigma = 120°$. 63
3.11 CFD prediction of damping for original (**- - -**) and restaggered (**—**) blade 63
3.12 Normalised gradients after restaggering, at $\sigma = 0°$ and $\sigma = 10°$. 64
3.13 Change in aerodynamic damping for restaggered blade at $\sigma = 0°$ and $\sigma = 10°$. 64
3.14 CFD prediction of damping for original (**- - -**) and final (**—**) blade . . . 65

4.1 Illustration of the infinite cascade of flat plates modelled in LINSUB . . 69
4.2 Comparison of LINSUB predictions for test cases shown in Table (4.1). Black solid line (—) shows results of the current implementation, the circle marker (◯) are results from the implementation in Donini (2012). 73
4.3 Comparison of LINSUB predictions (—) and CFD (- - -) for NACA0006 test case shown in Table (4.2): **(a)** Plunging mode; **(b)** Pitching about mid-chord. 74
4.4 Comparison of LINSUB predictions (—) and CFD (- - -) for SC10 test case shown in Table (4.3). First and second row are subsonic and transonic flow. First and second column are plunge and pitch modes. Pitching axis is at midchord. 75

5.1 A schematic representation of a PGML network with two hidden layers and one-dimensional output. 79
5.2 Diagram representing the proposed PGML framework 82
5.3 Example of blockage region definition using velocity gradient with a close-up around the trailing edge. 84
5.4 Location of stagnation points around leading edge **(a)** and associated pressure distribution **(b)**, **(c)** on an airfoil for different solidity and inflow angles, with a fixed inlet Mach number $M_1 = 0.7$.. The dashed line (- - -) is the chord line, starting at the leading edge of the blade. . . 87
5.5 Change in steady performance with solidity: **(a)** Pressure ratio against solidity at different inlet Mach number at constant incidence $\beta_1 = 5°$; **(b)** Total pressure loss coefficient against inlet Mach number at different solidity, constant incidence $\beta_1 = 5°$; **(c)** Lift against drag coefficients at different solidity and fixed $M_1 = 0.85$. 88
5.6 Imaginary component of unsteady force coefficients against interblade phase angle, with fixed inlet Mach number $M_1 = 0.85$, incidence $\beta_1 = 3°$ and reduced frequency $k = 0.5$, at different solidity: **(a)** $s = 0.833$; **(b)** $s = 1.25$ 89
5.7 Imaginary component of unsteady force coefficients against solidity, with fixed inlet Mach number $M_1 = 0.85$, incidence $\beta_1 = 3°$ and reduced frequency $k = 0.5$, at different interblade phase angle: **(a)** $\sigma = 20°$; **(b)** $\sigma = 150°$ 90
5.8 Aerodynamic damping contributions for a flap mode at $x = 2$ as a function of incidence, with fixed inlet Mach number $M_1 = 0.85$, interblade phase angle $\sigma = 20°$, and reduced frequency $k = 0.5$, at different solidity: **(a)** $s = 0.833$; **(b)** $s = 1.25$ 90
5.9 Aerodynamic damping contributions for a flap mode at $x = 2$, with fixed inlet Mach number $M_1 = 0.85$, incidence $\beta_1 = 5°$, interblade phase angle $\sigma = 20°$, and reduced frequency $k = 0.5$, against solidity 91

5.10 Change in steady performance with stagger angle at constant incidence $\beta_1 = 5°$: **(a)** Pressure ratio against stagger angle at different inlet Mach number; **(b)** Total pressure loss coefficient against inlet Mach number at different stagger angles; **(c)** Lift against drag coefficients at different stagger angles and fixed $M_1 = 0.85$. 91

5.11 Change in throat area with stagger angle 92

5.12 Imaginary component of unsteady force coefficients against interblade phase angle, with fixed inlet Mach number $M_1 = 0.85$, incidence $\beta_1 = 3°$ and reduced frequency $k = 0.5$, at different stagger angles: **(a)** $\xi = 30°$; **(b)** $\xi = 50°$ 92

5.13 Imaginary component of unsteady force coefficients against stagger angle, with fixed inlet Mach number $M_1 = 0.85$, incidence $\beta_1 = 3°$ and reduced frequency $k = 0.5$, at different interblade phase angle: **(a)** $\sigma = 20°$; **(b)** $\sigma = 120°$ 93

5.14 Aerodynamic damping contributions for a flap mode at $x = 2$ as a function of incidence, with fixed inlet Mach number $M_1 = 0.85$, interblade phase angle $\sigma = 20°$, and reduced frequency $k = 0.5$, at different stagger angles: **(a)** $\xi = 30°$; **(b)** $\xi = 50°$ 93

5.15 Aerodynamic damping contributions for a flap mode at $x = 2$, with fixed inlet Mach number $M_1 = 0.85$, incidence $\beta_1 = 5°$, interblade phase angle $\sigma = 20°$, and reduced frequency $k = 0.5$, against stagger angle . . 94

5.16 Change in steady performance with camber at constant incidence $\beta_1 = 5°$: **(a)** Pressure ratio against camber at different inlet Mach number; **(b)** Total pressure loss coefficient against inlet Mach number at different camber; **(c)** Lift against drag coefficients at different camber and fixed $M_1 = 0.85$. 94

5.17 Aerodynamic damping contributions for a flap mode at $x = 2$ as a function of incidence, with fixed inlet Mach number $M_1 = 0.85$, interblade phase angle $\sigma = 20°$, and reduced frequency $k = 0.5$, at different camber : **(a)** $Z/Z_{SC10} = 0.8$; **(b)** $Z/Z_{SC10} = 1.2$ 95

5.18 Aerodynamic damping contributions for a flap mode at $x = 2$, with fixed inlet Mach number $M_1 = 0.85$, incidence $\beta_1 = 5°$, interblade phase angle $\sigma = 20°$, and reduced frequency $k = 0.5$, against camber 95

5.19 Change in steady performance with thickness at constant incidence $\beta_1 = 5°$: **(a)** Pressure ratio against thickness at different inlet Mach number; **(b)** Total pressure loss coefficient against inlet Mach number at different thickness; **(c)** Lift against drag coefficients at different thickness and fixed $M_1 = 0.85$. 96

5.20 Aerodynamic damping contributions for a flap mode at $x = 2$, with fixed inlet Mach number $M_1 = 0.85$, incidence $\beta_1 = 5°$, interblade phase angle $\sigma = 20°$, and reduced frequency $k = 0.5$, against thickness 96

5.21 Illustration of the PGML model selection and evaluation. **(a)** Flowchart of the full process. **(b)** Illustration of the 5-fold cross validation approach for finding the model hyperparameters, with training (▬) and test (🟥) data. . . . 98

5.22 Training history of PGML for: **(a)** Plunge induced lift coefficient C_L^h ; **(b)** Pitch induced moment coefficient C_M^α . . . 99

5.23 Performance of PGML, FCNN and LINSUB: **(a)** R^2 values on training (—) and validation (—) sets; **(b)** normalised distribution of PGML relative error on validation set . . . 99

5.24 Scatter plot of normalised QoI form validation set. The CFD and PGML predictions are on horizontal and vertical axis respectively. QoIs reported on each panel. . . . 100

5.25 Predictions of plunge lift and pitch moment coefficients from CFD, PGML, FCNN and LINSUB against solidity. The steady state conditions are constant at $M_1 = 0.85$ and $\beta_1 = 3°$. The panels, from left to right, are run with reduced frequency $k = 0.5$, $k = 0.7$, $k = 1.0$, respectively, while the interblade phase angle is constant at $\sigma = 20°$. . . . 101

5.26 Blade profiles due to pitching motion calculated from LINSUB: **(a)** Unsteady pressure jump, real (—) and imaginary (—) components; **(b)** Local aerodynamic work. . . . 102

5.27 Blade profiles due to pitching motion calculated from CFD: **(a)** Steady isentropic Mach number; **(b)** Unsteady pressure coefficient, real (—) and imaginary (—) components; **(c)** Local aerodynamic work. . . . 103

5.28 Normalised feature importance for a dataset with changing solidity, $\sigma = 20°$: **(a)** FCNN; **(b)** PGML. . . . 104

5.29 Predictions of plunge lift and pitch moment coefficients from CFD, PGML, FCNN and LINSUB against solidity. The steady state conditions are constant at $M_1 = 0.85$ and $\beta_1 = 3°$. The panels, from left to right, are run with reduced frequency $k = 0.5$, $k = 0.7$, $k = 1.0$, respectively, while the interblade phase angle is constant at $\sigma = 150°$. . . . 105

5.30 Blade profiles due to pitching motion calculated from LINSUB: **(a)** Unsteady pressure jump, real (—) and imaginary (—) components; **(b)** Local aerodynamic work. . . . 106

5.31 Blade profiles due to pitching motion calculated from CFD: **(a)** Unsteady pressure coefficient, real (—) and imaginary (—) components; **(b)** Local aerodynamic work. . . . 107

5.32 Normalised feature importance for a dataset with changing solidity, $\sigma = 150°$: **(a)** FCNN; **(b)** PGML. . . . 107

5.33 Predictions of plunge lift and pitch moment coefficients from CFD, PGML, FCNN and LINSUB against camber. The steady state conditions are constant at $M_1 = 0.85$ and $\beta_1 = 3°$. The panels, from left to right, are run with reduced frequency $k = 0.5$, $k = 0.7$, $k = 1.0$, respectively, while the interblade phase angle is constant at $\sigma = 20°$. 108
5.34 Normalised feature importance for a dataset with changing camber: **(a)** FCNN; **(b)** PGML. 109
5.35 R^2 values for PGML (—) and FCNN (······) as a function of the increment in the training database size. 110
5.36 Blade profile of a fictitious fan blade section 111
5.37 Steady state solution at design point, $M_1 = 0.7$, $\alpha_1 = 43°$ 112
5.38 Steady state solution near stall, $M_1 = 0.9$, $\alpha_1 = 51°$. 112
5.39 Steady state solution near choke, $M_1 = 0.9$, $\alpha_1 = 41°$. 113
5.40 Illustration of the torsion and flap modes used in this study. 113
5.41 Isentropic Mach Number profile with $M_1 = 0.7$, $\beta_1 = 0°$ of training (—) and current test (—) geometry 114
5.42 Isentropic Mach Number profile with $M_1 = 0.9$, $\beta_1 = 8°$ of training (—) and current test (—) geometry 115
5.43 Aerodynamic damping predictions from CFD (—) and PGML (······) at design point, $M_1 = 0.7$, $\alpha_1 = 43°$. First and second column show plunge and pitch contributions, third column plots the total damping. The shaded area is one standard deviation obtained from the different PGML predictions. First and second row are torsion mode results with $k = 0.5$ and $k = 1.0$. Third and fourth row are flap mode results. 117
5.44 Aerodynamic damping predictions from CFD (—) and PGML (······) with $M_1 = 0.9$, $\alpha_1 = 51°$. First and second column show plunge and pitch contributions, third column plots the total damping. The shaded area is one standard deviation obtained from the different PGML predictions. First and second row are torsion mode results with $k = 0.5$ and $k = 1.0$. Third and fourth row are flap mode results. 118
5.45 Aerodynamic damping predictions from CFD (—) and PGML (······) with $M_1 = 0.9$, $\alpha_1 = 41°$. First and second column show plunge and pitch contributions, third column plots the total damping. The shaded area is one standard deviation obtained from the different PGML predictions. First and second row are torsion mode results with $k = 0.5$ and $k = 1.0$. Third and fourth row are flap mode results. 119
5.46 Aerodynamic damping predictions from CFD (—) and PGML (······) with $\sigma = 20°$, $k = 0.5$. First and second column show plunge and pitch contributions, third column plots the total damping. The shaded area is one standard deviation obtained from the different PGML predictions. First and second row are torsion and flap mode results with $M_1 = 0.9$. Third and fourth row are torsion and flap mode results with $\alpha_1 = 51°$. . 120

5.47 Aerodynamic damping maps with modeshape and reduced frequency. Rows one to four show results for inlet Mach numbers $M_1 = 0.6, 0.7, 0.8, 0.9$, respectively. The three colums are results from CFD, PGML and FCNN. The inlet flow angle and interblade phase angle are fixed at $\alpha = 51^\circ$ and $\sigma = 0^\circ$. The solid line (—) shows the zero damping line, while the dashed line (- - -) marks the zero damping line obtained with ±1 standard deviation from the mean PGML predictions. 123

5.48 Aerodynamic damping predictions from CFD (—) and PGML (······) with $\sigma = 0^\circ$, $M_1 = 0.9$, $\alpha_1 = 51^\circ$. First and second column show plunge and pitch contributions, third column plots the total damping. The shaded area is one standard deviation obtained from the different PGML predictions. First and second row are torsion and flap mode results as a function of reduced frequency k. Third and fourth row are results as a function of pitching axis x for $k = 0.5$ and $k = 1.0$, respectively. 124

5.49 Compressor map with flutter boundary calculated from CFD and PGML. The shaded area corresponds to the flutter boundary within 1 standard deviation from the mean PGML prediction. 125

6.1 Standard Configuration 10 compressor map with stall and flutter boundaries 129

6.2 **(a)** Lift and **(b)** aerodynamic damping coefficients computed with constant $\dot{m}/\dot{m}_{\mathrm{ref}} = 0.9$, $\sigma = 20^\circ$. The solid line (—) is a spline fit of the CFD points (black dots) 131

6.3 Blade profiles at selected points: **(a)** Steady isentropic Mach number; **(b)** Imaginary component of unsteady pressure coefficient; **(c)** Real component of unsteady pressure coefficient; **(d)** Local aerodynamic work 132

6.4 Steady Mach Number contours computed at points **B,C,D**, from left to right 132

6.5 **(a)** blockage size near trailing edge on suction side as a function of pressure ratio with constant $\dot{m}/\dot{m}_{\mathrm{ref}} = 0.9$; **(b)** blockage size on suction side as a function of streamwise coordinate. 133

6.6 An illustrative empirical distribution function with quantiles $q = 0.975$ and $q = 0.025$ 136

6.7 Cross validation R^2 as a function of number of features. 138

6.8 Kernel density estimation plots of aerodynamic damping coefficient databases as a function of: **(a)** C_L and C_D; **(b)** $\dot{m}$ and Π 139

6.9 **(a)** Coverage fraction convergence with number of trees; **(b)** QRF calibration curve showing the coverage fraction as a function of confidence level 139

6.10 Aerodynamic damping coefficient from CFD (markers with spline fit —) and QRF (red dots with error bars) as a function of pressure ratio with constant $\dot{m}/\dot{m}_{\mathrm{ref}} = 0.9$, $\sigma = 20^\circ$ 140

6.11 Aerodynamic damping coefficient from CFD (—) and QRF (— with error bars) as a function of mass flow rate with constant $M_1 = 0.825$, $\sigma = 20°$ . . . 141

6.12 Aerodynamic damping coefficient from CFD (—) and QRF (— with error bars) as a function of interblade phase angle with constant $M_1 = 0.6$, $\beta_1 = 6°$. The vertical lines represent downstream (- - -) and upstream (-·-·) cut-off values, respectively. . . . 141

6.13 Scatter plot and kernel density estimation of the training data subsets formed by QRF around the three test points of interest. **(a)** Percentage difference in mass flow rate against percentage difference in pressure ratio; **(b)** Difference in aerodynamic damping against percentage difference in pressure ratio. . . . 143

6.14 Empirical cumulative distribution function of the difference between subset of observations ζ_i and the resulting aerodynamic damping prediction ζ_j at test point j. The quantiles $q = 0.975$ and $q = 0.025$ form the 95% prediction intervals. . . . 143

6.15 Kernel density estimation of Monte Carlo analysis samples. **(a)** Distribution of samples against percentage difference in pressure ratio; **(b)** Distribution of samples against percentage difference in mass flow rate. 144

6.16 Aerodynamic damping predictions from CFD, QRF and Monte Carlo analysis against delivered pressure ratio, with confidence intervals. **(a)** The prediction intervals from QRF (—) and MC (—) are obtained as quantiles of the distribution around a point; **(b)** The confidence intervals from MC (—) refer to the mean of the distribution and are obtained by bootstrapping. . . . 145

6.17 Standard Configuration 10 compressor map with flutter boundaries computed from CFD and QRF . . . 146

B.1 Predictions of plunge lift and pitch moment coefficients from CFD, PGML, FCNN and LINSUB against stagger angle. The steady state conditions are constant at $M_1 = 0.85$ and $\beta_1 = 3°$. The panels, from left to right, are run with reduced frequency $k = 0.5$, $k = 0.7$, $k = 1.0$, respectively, while the interblade phase angle is constant at $\sigma = 20°$. . . 169

B.2 Normalised feature importance for a dataset with varying stagger angle, $\sigma = 20°$: **(a)** FCNN; **(b)** PGML. . . . 170

B.3 Predictions of plunge lift and pitch moment coefficients from CFD, PGML, FCNN and LINSUB against stagger angle. The steady state conditions are constant at $M_1 = 0.85$ and $\beta_1 = 3°$. The panels, from left to right, are run with reduced frequency $k = 0.5$, $k = 0.7$, $k = 1.0$, respectively, while the interblade phase angle is constant at $\sigma = 150°$. . 170

B.4 Normalised feature importance for a dataset with varying stagger angle, $\sigma = 150°$: **(a)** FCNN; **(b)** PGML. . . . 171

B.5 Predictions of plunge lift and pitch moment coefficients from CFD, PGML, FCNN and LINSUB against airfoil thickness. The steady state conditions are constant at $M_1 = 0.85$ and $\beta_1 = 3°$. The panels, from left to right, are run with reduced frequency $k = 0.5$, $k = 0.7$, $k = 1.0$, respectively, while the interblade phase angle is constant at $\sigma = 20°$. . . 171
B.6 Predictions of plunge lift and pitch moment coefficients from CFD, PGML, FCNN and LINSUB against airfoil thickness. The steady state conditions are constant at $M_1 = 0.85$ and $\beta_1 = 3°$. The panels, from left to right, are run with reduced frequency $k = 0.5$, $k = 0.7$, $k = 1.0$, respectively, while the interblade phase angle is constant at $\sigma = 150°$. . 172
B.7 Predictions of plunge lift and pitch moment coefficients from CFD, PGML, FCNN and LINSUB against inlet Mach number. The incidence is constant at $\beta_1 = 3°$ and reduced frequency $k = 0.5$. The panels, from left to right, are run with stagger angle $\xi = 30°$, $\xi = 40°$, $\xi = 50°$, respectively, while the interblade phase angle is constant at $\sigma = 20°$. . . 173
B.8 Predictions of plunge lift and pitch moment coefficients from CFD, PGML, FCNN and LINSUB against incidence. The inlet Mach number is constant at $\beta_1 = 0.85$ and reduced frequency $k = 0.5$. The panels, from left to right, are run with stagger angle $\xi = 30°$, $\xi = 40°$, $\xi = 50°$, respectively, while the interblade phase angle is constant at $\sigma = 20°$. . . 174

List of tables

1.1 Conditions of stall flutter appearance in literature (in part from Bontemps (2020)) . . . 12

2.1 Freestream flow quantities for a compressor test case . . . 36
2.2 SC10 Aeroelastic parameters . . . 39

3.1 Intervals of design parameters. . . . 54
3.2 Data for training database independence study . . . 56
3.3 Hyperparameters range . . . 56
3.4 Input parameters for FCNN sweep test. Relative percentage error of FCNN predictions is computed against CFD data. . . . 59

4.1 Aeroelastic parameters for LINSUB validation. Results shown in Fig. (4.2). . . . 73
4.2 Aeroelastic parameters for CFD comparison. Results shown in Fig. (4.3). 74
4.3 Aeroelastic parameters for CFD comparison. Results shown in Fig. (4.4). 75

5.1 Input features to PGML model . . . 85
5.2 Cross validation R^2 values . . . 98

6.1 Set of input features . . . 137
6.2 Flutter margin loss accounting for uncertainty . . . 147

A.1 Hyperparameters optimisation range for PGML networks . . . 168
A.2 Hyperparameters of PGML networks . . . 168

Chapter 1

Introduction

This chapter provides the fundamental concepts to understand turbomachinery flutter, along with building the vocabulary required for the literature, methods and results presented in this thesis. The basics of aeroelasticity are discussed, with a focus on the important characteristics in a turbomachinery context and a classification of compressor specific aeroelastic instabilities. An overview of the methods to predict flutter is offered, with the intent of both reviewing the state-of-the-art and providing clear reasoning as to why a data-driven approach to modelling has been proposed. Finally, the work's objective and outline are given.

1.1 The Compressor Map

Axial flow compressors and fans are crucial components of aircraft engines. Modern compressors must reliably operate over a wide range of conditions, in order to accommodate every stage of the aircraft flight envelope. At takeoff, the aircraft requires maximum thrust which is achieved by pushing the shaft to its maximum rotation speed, allowing a greater mass of air through the engine and ultimately increasing the loading on the blades. At cruise, the compressor operates at design, or nominal, conditions and maximum efficiency. During the landing phase, the wheel speed is reduced to decrease the speed of the aircraft and allow descent.

The operating condition of the machine is conventionally represented on a compressor map, such as the one in Fig. (1.1), which shows the delivered pressure ratio as a function of mass flow rate. A speedline is a line of constant wheel speed, expressed as percentage of nominal speed. The working line is the line along which the compressor operates in steady conditions. This is not always the case as, during transient manoeuvres such as acceleration or deceleration of the compressor, the operating conditions deviate from this line (Rolls-Royce, 2015, Chapter 1.5). The safe and reliable operation of the engine is limited by the surge and choke lines.

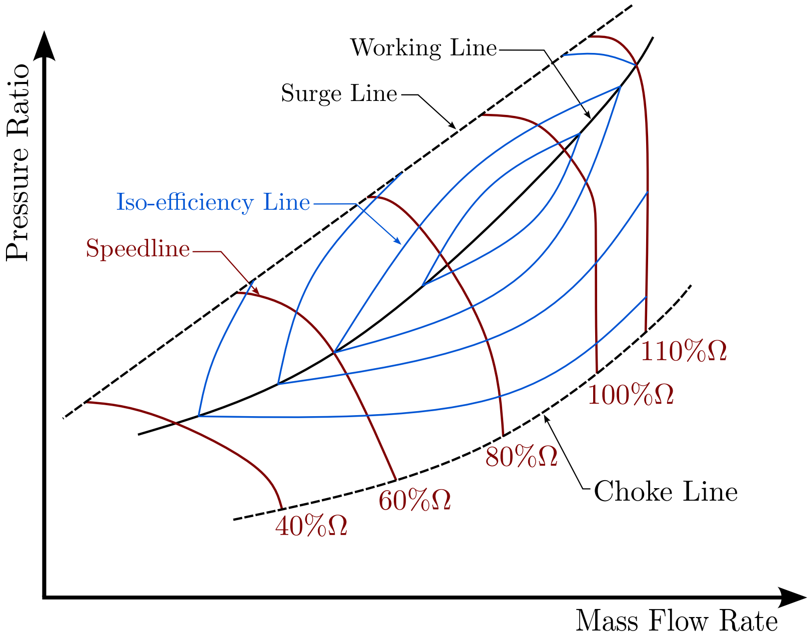

Figure 1.1 *Illustration of an axial compressor map. Adapted from Bontemps (2020)*

When reducing mass flow rate at constant speed, the angle of attack on the blades increases, increasing the work input which in turn delivers higher pressure ratio, but, at the same time, higher incidence could lead to flow separation, reducing efficiency and pressure ratio. The balance between these effects make it so that a peak pressure ratio exists for every speedline. If the mass flow is reduced further the blades can oscillate between being stalled and unstalled, and longitudinal oscillations of the flow occur; this process is known as surge. In severe cases, when the flow can no longer be compressed to the required outlet pressure, surge can cause a complete flow reversal which causes violent axial vibrations which damage the shaft and compromise the whole engine.

On the other hand, increasing the mass flow rate at constant speed reduces the angle of attack onto the blades, increasing the axial velocity of the flow through the compressor. The bladed passage acts as a convergent-divergent nozzle, thus the mass flow can increase until, eventually, when the Mach number at the throat reaches unity, a shock wave spanning the whole passage appears, the mass flow rate can no longer be increased by reducing the outlet pressure and the flow is said to be choked.

Assuming a subsonic relative inlet Mach number, with transonic flow conditions over the blade, the flow topology encountered as the compressor throttles along a speedline, from choke up to near stall, is schematically illustated in Fig. (1.2). At high mass flow rate, the incidence is negative and from the throat section onwards the Mach number is greater than one until a shock wave covering the whole passage appears. As the mass flow is reduced, the incidence is close to zero, the shock wave moves upstream and the supersonic region is limited to a small pocket near the leading edge. Finally, nearing the stall condition, the incidence is high and the shock wave moves very close to the leading edge. All three configurations, depending on incidence and shock strength, can display a degree of flow separation on the aft section of the airfoil. These flow features play an important role in the interaction between fluid and vibrating blade.

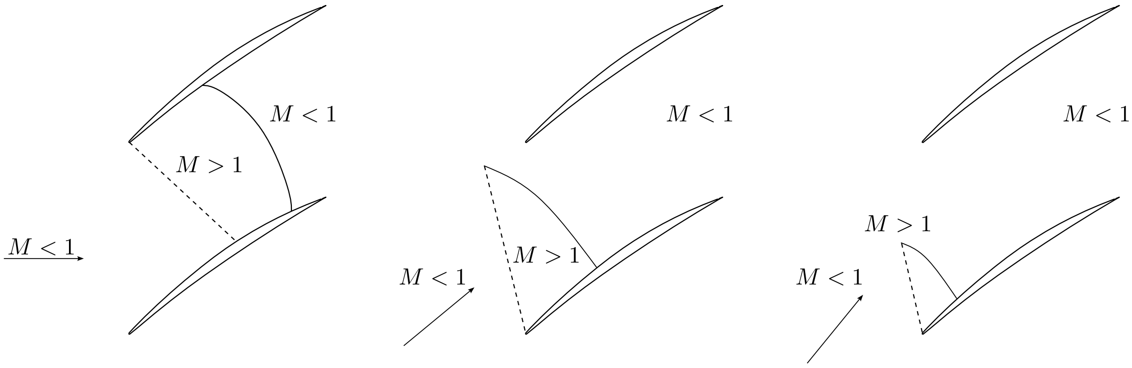

(a) *Choked condition* **(b)** *Nominal condition* **(c)** *Near stall condition*

Figure 1.2 *Transonic flow topologies as mass flow rate decreases along a speedline. Shock wave (**—**) and sonic line (**- - -**) delimit the pocket of supersonic flow in the passage. Illustration adapted from Rendu (2016).*

1.2 Aeroelasticity

The study of interactions between the inertial, elastic, and aerodynamic forces acting on a body in a fluid stream is the subject matter of aeroelasticity. The combinations of these forces give rise to different sub-fields of study that are conventionally positioned on the Collar (1946) triangle shown in Fig. (1.3). Mechanical vibration is the discipline concerned with studying the interaction between inertial and the restoring forces arising from the elasticity of materials; stability and control are affected by the interaction of aerodynamic forces with a rigid body, and static aeroelasticity describes the interaction of aerodynamic and elastic forces. The interplay between all three forces is the subject of dynamic aeroelasticity. Static and dynamic aeroelasticity are the disciplines of particular interest in turbomachinery.

1.2.1 Static Aeroelasticity

Static aeroelasticity in turbomachinery is concerned with studying the effect of aerodynamic and centrifugal loads on the elastic deformation of the blade, when both can be assumed to be invariant in time. In fact, if the flow through the machine is completely steady, the blade will deform under these loads until a new equilibrium is established, which means that during operation, the blades will have a different shape compared

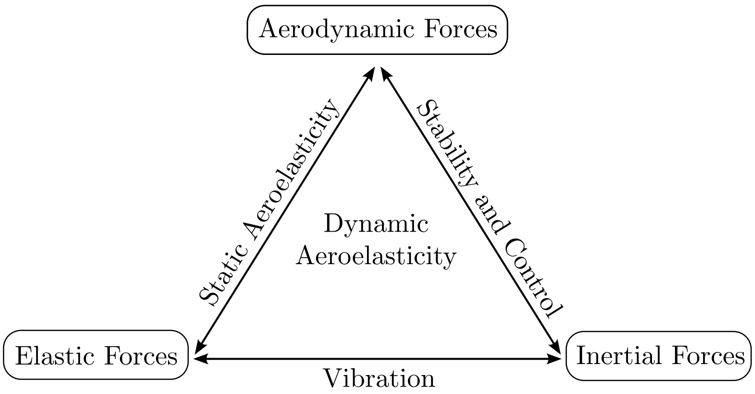

Figure 1.3 *Collar (1946) Triangle of forces*

to the original design. Although static deformation does not usually pose a stability problem in the context of turbomachinery, the resulting untwist and change in passage shape can change the steady performance of the machine and ultimately alter the surge and flutter margin. This is, of course, assuming that the blades do not incur into static divergence, i.e. the blades break under these static loads.

1.2.2 Dynamic Aeroelasticity

Dynamic aeroelasticity studies the unsteady interaction between the vibrating blade and the time varying aerodynamic forces acting on it. The concern of the aeroelastician is to ultimately evaluate the energy exchange that takes place between blade and fluid flow, in order to assess the aeroleastic stability of the system. If the fluid extracts energy from the structure, the vibration amplitude will decay with time and the blade is said to be stable. On the other hand, a blade is unstable if the fluid imparts work to the structure, since the vibration amplitude will increase until the blade breaks. The blade can also reach a dynamic equilibrium and exhibit a limit cycle oscillation with constant amplitude. Although this last scenario is not characterised by an abrupt failure, it is equally undesirable as fatigue can and will eventually cause the blade to break. As a matter of fact, this is how the vast majority of blades fail, they reach high cycle fatigue and crack. It is customary to separate dynamic aeroelastic phenomena into two categories: vibrations induced by an external forcing, further differentiated in forced response and non synchronous vibrations, and self-excited vibrations, i.e. flutter.

Forced response vibrations are characterised by an external forcing whose periodicity is a multiple of some base frequency, normally the engine angular frequency, and whose source is found at a different spatial location from the vibrating blade. The wakes coming from an upstream blade row are a source of forced response vibration, as they induce velocity and pressure fluctuations that ultimately result into a periodic forcing due to the relative motion of the blade rows. Intake distortions and downstream potential effects are also sources of forced response.

Non synchronous vibrations (NSV) are also driven by a forcing coming from the flow, but unlike forced response, the frequency of unsteadiness is characteristic of an aerodynamic instability that takes place at the same spatial location of the blade row, e.g. vortex shedding due to stalling of the blade themselves can be a source of NSV. This means that NSV is not characterised by forcing that is a multiple of the blade row angular frequency. NSV are an important topic in turbomachinery aeroelasticity, but are rather difficult to predict accurately even with CFD. Efforts have been made recently to rigorously model their behaviour (Stapelfeldt and Brandstetter, 2020).

Flutter is a self-excited, self-sustained aeroelastic instability and as such it requires no external forcing. The unsteady aerodynamic loading is neither convected from upstream nor generated by downstream potential disturbances, but it is produced in the immediate vicinity of the blade by its own vibration.

The discussed aeroelastic instabilities can be represented on a Campbell (1924) diagram shown in Fig. (1.4). The diagram shows the rotor shaft speed on the horizontal axis and frequency on the vertical axis. The horizontal lines represent the blade natural vibration frequency, while the family of lines starting from the origin represent engine orders (EO), i.e. excitations whose frequency is a harmonic of the shaft speed. One can see that forced response takes place where EO and mode frequency coincide, while flutter and NSV are not associated to any specific EO.

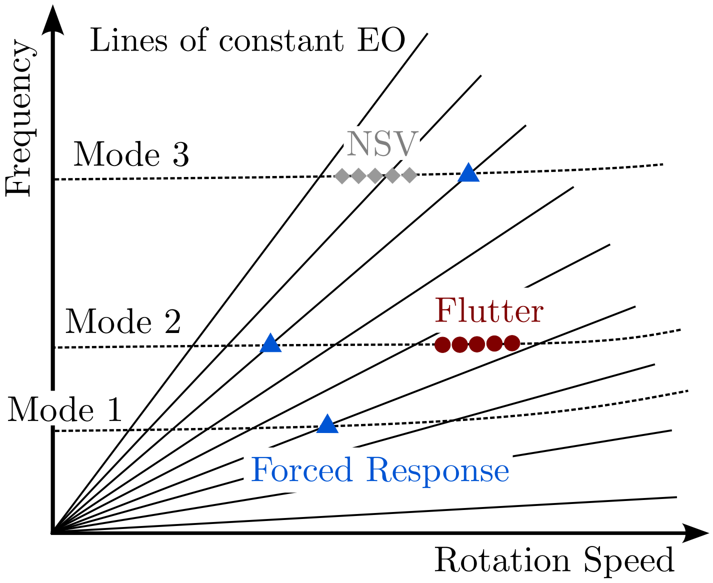

Figure 1.4 *Illustration of a Campbell diagram*

In the following section, we examine a number of properties of importance in the study of turbomachinery flutter and that will start hinting at the multidisciplinary nature of the problem.

1.2.3 Properties of interest in turbomachinery

Blade mode shape

As any mechanical system, turbomachinery blades are characterised by natural frequencies and mode shapes of vibration. These are referred to as in-vacuo vibration characteristics as they are obtained in absence of a surrounding medium, such as air. In operation, the unsteady aerodynamic forces resulting from the blade oscillation can be significant enough to alter the vibration characteristics of the structure. The aeroelastic system, i.e. the coupled unsteady flow and vibrating blade, can therefore vibrate with modes and frequencies that are different from the ones obtained in-vacuo. The separation in modeshape and frequency between the coupled aeroelastic system and the structure in-vacuo depends on the magnitude of aerodynamic forces, the amplitude of vibration and the ratio of blade's mass to the mass of surrounding fluid, simply referred to as mass ratio. For example, wings are hollow, lightweight and highly flexible structures that typically exhibit *coalescence* bending-torsion flutter, because the two modes are close in frequency and the stiffness added by the aerodynamic forces is enough to make them coalesce into a unique coupled mode. On the other hand, turbomachinery flutter predominantly occurs in a single mode and frequency, quite close to the in-vacuo vibration characteristics of the blade (Srinivasan, 1997).

Fig. (1.5) shows the variation of mode frequency due to aerodynamic loads for a wing and a turbomachinery blade, with coalescnce flutter taking place at the crossing of two mode lines.

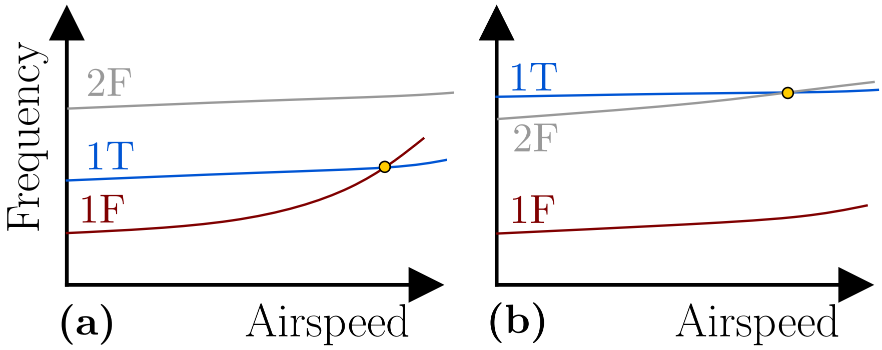

Figure 1.5 *Variation of mode frequency due to aerodynamic loads for:* ***(a)*** *a wing;* ***(b)*** *a turbomachinery blade. The crossing of two lines denotes coalescence flutter. Adapted from Rendu (2016).*

Nevertheless, coalescence flutter has also been observed in unducted fans (Ducharme, 1987), low mass ratio, low solidity fans (Clark et al., 2012), and turbines (Corral et al., 2009).

Vibration of bladed disk assemblies

The blades in a turbomachinery row are in close proximity to one another, allowing them to interact with each other. The blades' behaviour is said to be coupled and the nature of this interaction can be mechanical in nature, with the extent of the mechanical coupling depending on the disk and on the presence of support structures such as shrouds. For example, highly rigid disks with removable locking mechanism do not affect the blades which vibrate in their own mode, whereas flexible disks, or disks with blades cast directly inside (blisk), exhibit strong interaction and have well defined assembly modes (Srinivasan, 1997). The rest of this discussion is focused on rigid disks only, as these are most common in the vast majority of compressor and fan flutter studies. The aerodynamic coupling occurs because the unsteadiness caused by the blade's vibration affects the flow field around its neighbours.

If mechanical and aerodynamic nonuniformities are negligible, the vibration of the assembly can be easily described as a summation of orthogonal modes defined by the number of nodal diameters, ND. This parameter formally refers to the number of diameters where the vibration amplitude is null, separating lobes with positive and negative displacement at a given instant in time. An illustration with different nodal diameters is shown in Fig. (1.6). During operation, the vibratory pattern can be a standing wave, always the case of ND = 0, or a travelling wave, forward if it travels in the direction of the rotor speed, backward in the opposite case.

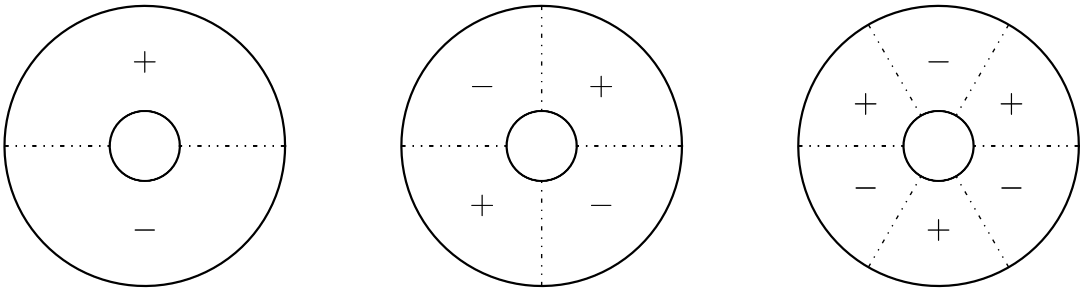

(a) ND = 1 **(b)** ND = 2 **(c)** ND = 3

Figure 1.6 *Blade-disk assembly vibration pattern with different nodal diameters.*

In a travelling wave mode, the blades oscillate identically except for a constant phase shift between neighbours. This phase shift is defined as the interblade phase angle, IBPA or σ, and it represents one of the most important aeroleastic parameters in turbomachinery. The interblade phase angle can only take a finite number of values due to the cyclic symmetry of the problem and it is defined as

$$\sigma = \frac{2\pi m}{N_b} \tag{1.1}$$

where N_b is the number of blades and $m = \mathrm{ND}$ is the equivalent circumferential order.

Reduced frequency

An important parameter for the study of fluid-structure interaction is the ratio between the characteristic time of the flow and the characteristic time of the vibration. The definition of reduced frequency for a turbomachinery blade is

$$k = \frac{\omega c}{U} \tag{1.2}$$

where ω is the vibration angular frequency, c is the blade chord and U the relative inlet flow velocity. Eq. (1.2) expresses the reduced frequency as ratio of time taken for a fluid particle to flow past one chord length to the time taken for the blade to complete one vibration cycle. The value of k is highly influential in aeroelasticity and three main category of problems can be identified:

- quasi-steady aerodynamics $(k \ll 1)$: the flow responds immediately to disturbances caused by the vibration
- unsteady aerodynamics $(k \approx 1)$: the flow and vibration are strongly coupled
- highly unsteady aerodynamics $(k \gg 1)$: the flow can be considered constant during a vibration cycle

Aeroacoustics in annular ducts

Aeroacoustics concerns the study of sound generation and propagation within a compressible flow, most often with the intent of understanding and reducing the noise signature of lifting devices.

In turbomachinery, wave propagation takes place within an annular duct rather than a free field. The presence of solid walls gives boundary conditions that constrain the characteristics of pressure fluctuations in the flow field. Therefore only certain modes are allowed. These are identified by the pair (m, n), representing the circumferential and radial order, respectively. Fig. (1.7) shows examples of such pressure fluctuation modes at given axial location and time instant. Moreover, for a given frequency, only certain modes can travel undisturbed. Modes that propagate without attenuation are said to be cut-on, while modes whose amplitude decays exponentially with distance are said to be cut-off. The frequency at which waves change from cut-on to cut-off and viceversa is aptly named cut-off frequency (Tyler and Sofrin, 1962). The cut-off frequency depends on the Mach number and flow angles of the base flow, thus, as the blades in a turbomachinery row change the flow field, we will have different cut-off frequencies and propagation angles upstream and downstream of the blades.

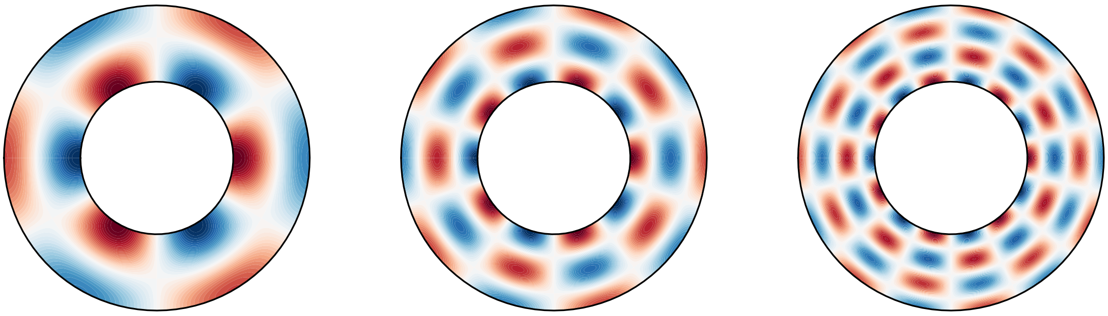

(a) $(m,n) = (3,1)$ **(b)** $(m,n) = (5,2)$ **(c)** $(m,n) = (7,3)$

Figure 1.7 *Pressure fields in annular duct for different circumferential-radial order*

In a flutter context, several researchers have shown the importance of characterising acoustic propagation conditions. Atassi et al. (1995) have shown that the amplitude of upstream running waves increases greatly in the vicinity of shocks, in a phenomenon named acoustic blockage. Vahdati and Cumpsty (2015) performed a three-dimensional CFD analysis of a state-of-the-art fan blade, and observed that flutter occurs in the frequency and nodal diameter range where the generated acoustic waves are cut-on upstream and cut-off downstream. Zhao et al. (2017) developed a model to calculate the change in aerodynamic damping due to pressure waves reflected at the intake of a fan, which may contribute positively or negatively to aeroelastic stability. There is therefore a strong link between aeroacoustics and aeroelasticity.

Operating point sensitivity

Flutter can occur in different locations of the compressor operating map. This allows to categorise flutter into several classes, pictured in Fig. (1.8):

- choke flutter occurs when the incidence of the incoming flow is reduced and a shock wave spanning the entire passage is formed
- stall flutter, the most common type and the object of this thesis, occurs when flow separates from the blade, or when viscous effects are important, and can be further categorised into subsonic, transonic and supersonic, depending on flow velocity

Classical flutter has not been listed since it is not associated with any particular operating point. It occurs when the flow is subsonic and remains attached to the blade, thus it is dominated by inviscid effects, which drive the phase lag between aerodynamic forces and airfoil velocity. The phase lag can be caused by acoustic and vortical waves, and by the interaction with neighbouring blades.

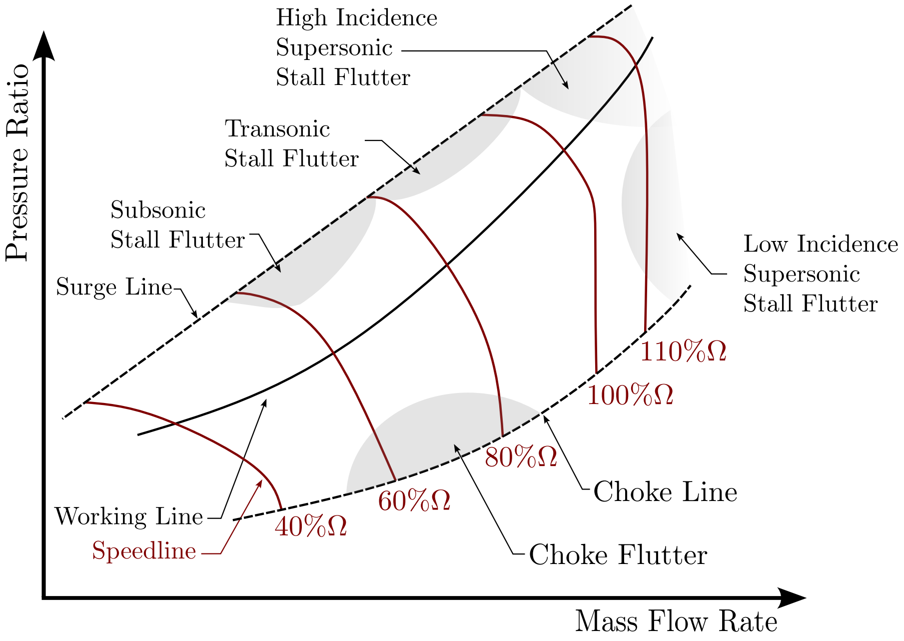

Figure 1.8 *Typical flutter regions on a compressor map. Adapted from Bontemps (2020)*

1.3 Flutter

The types of compressor flutter listed previously will now be discussed further to identify the main flow features driving each one.

1.3.1 Choke Flutter

Choke flutter occurs when the flow in the passage is transonic and the oscillation of a shock wave extending from suction to pressure side interacts with the blade movement. The accurate numerical prediction of this phenomenon is difficult as it involves large shock oscillations that can induce non-linear effects. Nevertheless, the triggering mechanism was studied by Rendu et al. (2020) using linearised CFD methods. They found that choke flutter is triggered by a combination of viscous effects, namely flow separation after the shock, and inviscid effects, that is the amplification of upstream running acoustic waves generated at the trailing edge and amplified at the shock front. This mechanism is analogous to the acoustic blockage described by Atassi et al. (1995). It is a less common type of flutter in civil fans and compressors, which receives less attention as compared to other types.

1.3.2 Stall Flutter

Stall flutter occurs at part-speed regime, when airfoils operate at an incidence higher than nominal (Dowell, 2015); it is normally associated with high steady loading and low reduced frequency, for blades vibration in the first flap (1F), sometimes referred to as flapwise bending (also simply bending), or torsion (1T) mode (Srinivasan, 1997), in forward travelling assembly modes, with positive low nodal diameters from 1 to 6 (Vahdati et al., 2001). Vahdati et al. (2011) state there are two types of mechanisms that drive stall flutter: flow driven and acoustic driven.

For the flow driven mechanism, the inception of stall itself is not a necessary condition, though the flow separation, and its interaction with the suction side shock wave, is a key component for this type of instability. On the other hand, the acoustic driven mechanism is driven by the interaction of blade vibration with an upstream running wave caused by the blade vibration itself and the reflected wave from the intake. These conclusions are confirmed by a number of previous and subsequent studies.

Isomura and Giles (1998) carried out a numerical study of a transonic fan and concluded that the source of the instability is the shock wave/boundary layer interaction (SBLI) which primes the shock to oscillate, destabilising the blade. Vahdati et al. (2001) also performed a numerical study on a different fan blade, finding that actually the shock wave has a stabilising effect, while the opposite is true of the flow separation. It is therefore clear that these flow features can both exacerbate and eradicate flutter, depending on geometry, flow field, modeshape and frequency. Vahdati et al. (2011) carried out a numerical campaign to investigate the mechanism of wide-chord fan flutter. They found that SBLI only is not sufficient to explain the loss of stability near stall, and that this event is driven by acoustic waves propagating upstream being reflected at the intake highlight. They name this loss of stability “flutter bite”. Vahdati and Cumpsty (2015) performed a numerical analysis of a state-of-the-art fan blade, and concluded that flow separation, followed by radial migration of flow along the span towards the casing, decreases aerodynamic damping. They found that aerodynamic damping reduces as the twist component in the first flap mode increases, similar to what Panovsky and Kielb (1999) concluded for turbines. Finally, they state that flutter occurs in the frequency and nodal diameter range where the generated acoustic waves are cut-on upstream and cut-off downstream.

Building on this knowledge, Stapelfeldt and Vahdati (2019) presented two strategies to improve the flutter margin of an unstable fan blade. The first addresses the flow driven mechanism by restaggering sections of the blade, so that the radial pressure distribution is altered and the flow separation, with consequent radial flow migration, is mitigated. The second strategy involves bleeding a small amount of fluid at different chord locations, in order to attenuate the upstream running pressure wave from trailing edge to leading edge, thus addressing the acoustic driven mechanism. Finally, Rendu et al. (2019) presented a radial decomposition method of the blade vibration to identify the flutter source of a fan blade. They show that the fan blade is rendered unstable due to the highly destabilising contribution of the tip section of the blade, where the separation is most severe. By dividing the blade into radial panels and vibrating them individually, they found that the instability though is not caused by the tip itself, but rather is the vibration of lower panels that induces a destabilising unsteady pressure on the tip.

Bontemps (2020) compiled a list of references studying stall flutter events, reported here in Table (1.1), from which transpires that stall flutter events are most common when:

- the wheel speed is in the range for which the flow is transonic and away from the design point
- the reduced frequency is between 0.5 and 1.0
- the critical modeshape is the first flap (1F)
- the nodal diameter is small and positive

The work of this thesis is based on these observations.

Table 1.1 *Conditions of stall flutter appearance in literature (in part from Bontemps (2020))*

Reference	Speed	k	N_b	Mode	ND
Isomura and Giles (1998)	79%Ω	0.88	22	1F	2
Srivastava et al. (2003)	90%Ω	-	22	1F	2
Sanders et al. (2004) (1)	70%Ω	0.72	22	1F	2
Sanders et al. (2004) (2)	85%Ω	0.68	22	1F	2
Vahdati et al. (2011)	78%Ω	-	20	1F	2
Aotsuka and Murooka (2014)	80%Ω	-	18	1F	2
Vahdati and Cumpsty (2015)	89%Ω	0.54	20	1F	$1-2-3$
Stapelfeldt and Vahdati (2018) (1)	$M_{\text{tip}} = 0.86 - 0.98$	0.54	20	1F	$2-3$
Stapelfeldt and Vahdati (2018) (2)	$M_{\text{tip}} = 0.80 - 0.94$	0.66	18	1F	2
Rendu et al. (2019)	$M_{\text{tip}} = 0.86 - 0.98$	0.7	20	1F	2
Jia et al. (2021)	80%Ω	-	18	1F	$2-3$

1.4 Prediction Methods for Flutter

This section aims at presenting a brief overview of the prediction methods employed to characterise the unsteady flow field in turbomachinery, and the consequent fluid-structure interaction that might lead to flutter instability. The methods are organised in increasing order of complexity, from semi-analytical to the numerical solution of the full 3D Navier-Stokes equations, and can be roughly divided into classical and integrated methods. The summary presented here is based on the exhaustive reviews by Marshall and Imregun (1996) and Casoni and Benini (2021).

Uncoupled methods approach the aeroelastic problem without taking into account the impact of flow on structural vibration. These methods typically involve first determining the free vibration of blades to obtain their modeshape, followed by calculating unsteady aerodynamic loading caused by the imposed modeshape (with any amplitude), and subsequently determining blade flutter stability. This way, the complex non-linear interaction between fluid and structure is broken down into two simpler, independent linear systems that can be analyzed separately with reduced complexity. These normally assume small perturbations about a steady state, subsonic or supersonic, inviscid, irrotational flow. Whitehead (1960) developed a model to calculate the unsteady forces induced on an infinite, two-dimensional cascade of vibrating flat plates. The flow was assumed to be inviscid and incompressible, and never predicted flutter for plunge (bending) mode, due to the lack of steady loading. This argument was later proved by Whitehead (1962), who extended his previous method to include deflection and thus loading. The strong correlation between steady loading and blade stability is also shown by Akai and Atassi (1980), using results obtained from an incompressible flow model for cascades of thick and cambered airfoils developed by Atassi and Akai (1980). Compressibility effects were considered by Whitehead (1972) and Smith (1972) to develop a model for, again, a cascade of flat plates in subsonic flow; while Adamczyk (1978) developed an unsteady, compressible actuator disk theory for supersonic flow where the effects of shocks and steady loading were included by means of empirical correlations. An extension to the model proposed by Whitehead (1972) has been formulated by Barbarossa et al. (2016), who were able to account for flow deflection by modelling the curvature of airfoils with zero thickness. The latest analytical model to be developed is that of Corral and Vega (2017), which is able to quantify the effect of modeshape and aerodynamic loading on flutter stability, in the low reduced frequency limit, although it does require the mean flow field to be computed with CFD.

Integrated methods for computation typically involve coupling the motion of blades with the flow, using either a fully integrated or a partially integrated approach. The partially integrated method involves separate computations of fluid and structural equations, with information exchanged at every time step at the interface between the solid and fluid domains. The treatment of the structural problem has great impact on the accuracy and computational cost of partially integrated methods. Taking into account the non-linearity of the structure, e.g. including friction (Corral and Gallardo, 2014), allows the investigation of limit cycle oscillations. The structural motion at time step t is obtained by projecting the aerodynamic loads calculated at $t-1$ onto the solid surface. Consequently the motion of the structure is used to update the flow field, thus advancing the solution. The staggered nature of such algorithms makes it so that fluid and structure can be computed by separate solvers and only an interface is needed to pass the solutions from one to the other (Srivastava et al., 1991; Yamamoto and August, 1992). As the computational expense of such an approach can become high, a simplified approach usually relies on the assumption of a linear structure, resorting to a modal representation of the aeroelastic equations. This approach casts the system of equations into a set of modal coordinates, represented by the natural modes (eigenmodes) of the structure, which are obtained by solving the undamped free vibration problem. Therefore, this approach assumes that the fluid perturbation has negligible effect on the natural vibration of the blade. This method has been successfully applied to a number of turbomachinery cases (Debrabandere et al., 2012; Sayma et al., 2000), and it is among the most popular approaches in aeroelasticity (see references in Table 1.1).

The fully integrated approach solves fluid and structural equations simultaneously at the same time step, by treating the fluid-structure system as one continuum dynamics problem (Bendiksen, 1991). These methods can achieve high accuracy, but they are not commonly employed in turbomachinery applications due to high computational cost.

The advance in computing power led to methods based on the numerical discretisation of flow governing equations using different techniques such as finite-differences, finite-elements or finite-volumes. The governing equations' complexity grew with the computing capabilities, starting from potential flow (Whitehead, 1990), through Euler equations which neglect viscosity (Hall and Lorence, 1993), to three-dimensional, unsteady, Reynolds-averaged Navier-Stokes (URANS) equations (Corral et al., 2004; Sayma et al., 2000). (scale resolving methods are still rare in turbomachinery flutter and are therefore ignored in this summary). Currently, fluid-structure interaction problems are usually tackled by solving the structural equations with a finite-elements method, while the flow equations are approached with either time or frequency domain methods, depending on whether the two solvers are uncoupled or coupled with one of the approaches discussed previously. Time domain methods involve marching the solution in time with suitable temporal resolution, depending on the frequency of interest. Such methods can accurately model non-linear phenomena, such as limit cycle oscillations, and complex interactions between blade rows; however the large computational demands of such analyses led to the development of frequency domain, or time-linearised, solvers. Similarly to classical methods, time-linearised models operate under the assumption that the flow field can be decomposed in a mean steady state flow and an unsteady perturbation which is small in amplitude and harmonic (Clark and Hall, 1999; Giles, 1992; Petrie-Repar, 2006). This assumption does not allow time-linearised solvers to predict limit cycle oscillations, though the ability to predict asymptotic stability is often sufficient for design.

The inability of time-linearised methods to capture flow phenomena that occur at frequencies other than the specified base, led to the development of non-linear harmonic methods (Hall et al., 2002; Ning and He, 1998; Yao and Marques, 2017). The flow equations are, again, time-linearised and cast into the frequency domain, though multiple frequencies can be specified. The equations pertaining to each harmonic are solved iteratively and simultaneously due to coupling terms, so that phenomena occurring at different frequencies can interact. Both the computational cost and the solution accuracy increase greatly with the number of included harmonics.

1.5 Machine Learning in Fluid Mechanics

The unprecedented quantity of fluid flow data available today, alongside the quick development and democratisation of machine learning (ML) algorithms thanks to projects such as TENSORFLOW (Abadi et al., 2015), has allowed researchers to seek data-driven solutions to a plethora of fluid mechanics problems. The field has moved forward with a staggering pace and with enough successes to grant the compilation of several review articles in just a few years, by Xiao and Cinnella (2019), Duraisamy et al. (2019), Brunton et al. (2020), Michelassi and Ling (2021), Willard et al. (2022) and Hammond et al. (2022). In this section, we discuss only a small number of these studies, with particular focus on how previous physical knowledge has been introduced in each.

Turbulence modelling has proven to be a particularly fertile ground for ML. RANS simulations exhibit deficiencies in predicting complicated flow features, such as the ones that may be found in state-of-the-art compressors, e.g. tip leakage vortex, when compared to higher fidelity, scale resolving methods. Researchers have been trying to bridge this gap by leveraging various ML techniques. Dow and Wang (2012) and Wu et al. (2016) used Bayesian calibration to reduce model-form uncertainties in RANS simulations, by leveraging high fidelity data. However, these methods lack the ability to predict flows with different geometries from the calibration flow, as the input features were based in physical space.

Tracey et al. (2013) started introducing physical knowledge by training their model on mean flow features to develop a multiplier of the production term for existing turbulence models. They used high fidelity data to train their model and it showed good generalisation capabilities for different flows around airfoils (Singh et al., 2017). The importance of meaningful input features for generalisation was also shown by Ling and Templeton (2015), who employed a number of rotationally invariant inputs to developed classifiers of high uncertainty regions in RANS computations. Ling et al. (2016) corroborated the importance of introducing previous knowledge in their models. They employed a deep neural network architecture to model the Reynolds stress tensor, with the introduction of a layer that preserves Galilean invariance of the predicted tensor, thus embedding physical knowledge into the architecture itself.

A particularly successful example of physically consistent machine learning is the physics informed neural network (PINN) concept, developed by Raissi et al. (2019). PINNs are used as a surrogate model of the Navier-Stokes equations, with the conservation laws and boundary conditions being introduced directly as loss terms inside the cost function. Since their introduction, PINNs have been used widely on several problems. Another example of combining neural networks with physics is the physics guided machine learning (PGML) of Pawar et al. (2021). The PGML framework in this case refers to a fully connected neural network where, at some hidden layer, results from a reduced order model (ROM) of the process are injected, thus augmenting the knowledge of the algorithm and “guiding” it to a physically consistent formulation. The researchers successfully applied it to the prediction of lift coefficient on 4 and 5 digits NACA airfoils. Effectively, the PGML applies a complex correction to the results of a simplified model. This idea is not, in itself, new: Motta et al. (2015) developed polynomial corrections to the Theodorsen function, based on observations of numerical experiments, to introduce the effect of thickness when computing unsteady lift and moment of pitching airfoils.

Regarding aeroelasticity, early efforts in reduced order modelling were based on some form of decomposition of the unsteady flow into a series of orthogonal modes. Willcox (1999) employed a proper orthogonal decomposition technique to develop a reduced aerodynamic model for a transonic rotor in plunging motion, while Florea et al. (1998) performed an eigenmode decomposition of the linearised equations of unsteady flow through a cascade of vibrating airfoils. More recently, the interest of data-driven aeroelasticity modelling seems to have moved towards isolated airfoils, in particular towards the computation of limit cycle oscillations (LCO). Zhang et al. (2012) computed the LCO of NACA6410 airfoil in pitching employing a radial basis function neural network with good degree of success; Zhang et al. (2016) later improved their results by having the machine learnt model trained on a few proper orthogonal modes rather than the full flow field. Zahn and Breitsamter (2022) employed a long short-term memory (LSTM) recurrent neural network (RNN) to predict excitation amplitudes on a buffeting NACA0012 airfoil vibrating in both pitch and plunge modes. Opgenoord et al. (2018) developed a model for transonic flow around a two-dimensional airfoil, and used a dynamic mode decomposition technique (DMD) to calibrate the coefficients of their model from CFD data. The drawback of their approach though is the need for calibration every time a new airfoil is to be analysed. All the previous studies have developed computationally efficient reduced order models that are useful for aeroelastic control, but all share a major fallacy: they are valid only for the training geometry.

To the best of the author’s knowledge, no research is available on modelling of compressor stall flutter with data-driven techniques (with the exception of Gambitta et al. (2022), who use an autoencoder to model the geometrical variability of a compressor rotor due to manufacturing, though still employ unsteady CFD to calculate aerodynamic damping).

1.6 Motivation and Research Objectives

The development of fan and compressor blades can be approximately categorised in three stages:

- an early design phase in which preliminary aeroelastic considerations are made via analytical, semi-analytical methods and empirical models based on knowledge obtained from previous designs
- a core design phase aimed at maximising efficiency and aerodynamic stability. Flutter behaviour is assessed with semi-analytical models and correlations, starting from the data obtained with steady RANS, which are necessary to evaluate performance. Simplified computational models, such as time-linearised RANS (LRANS), can be employed to analyse operating conditions and vibration characteristic of interest
- a detailed analysis is conducted with expensive computational methods in order to understand flow phenomena, assess interactions between blade rows and obtain more accurate flutter predictions for selected critical operating conditions, such as near the stall boundary

Fig. (1.9) is an illustration of prediction accuracy as a function of computational cost of aeroelasticity models, showing the subdivision of methods used for each design phase. Although purely schematic, we can see that as the accuracy is increased, the computational cost grows by orders of magnitude. Therefore, a gap in available methodologies and a need for fast and accurate design tools can be identified.

Analytical and computational methods for the prediction of compressor stall flutter have reached maturity, and development of new efficient techniques seems to have come to a halt. Machine learning offers a large set of tools to explore and model complicated phenomena with a large number of parameters involved, and it has proved successful in turbulence modelling, bridging the gap between closure models and high fidelity methods in a number of applications.

This research aims to introduce a predictive, reusable data-driven model for the computation of aerodynamic damping of compressors, with similar accuracy to a RANS based model, at the cost of only steady state computations, in order to obtain more accurate predictions in earlier stages of the design cycle.

The main contribution of this work is the development of a physics guided machine learning model for the prediction of aerodynamic damping of compressors. It is reiterated that, to the best of the author's knowledge, no previous research is available on modelling of compressor stall flutter with data-driven techniques.

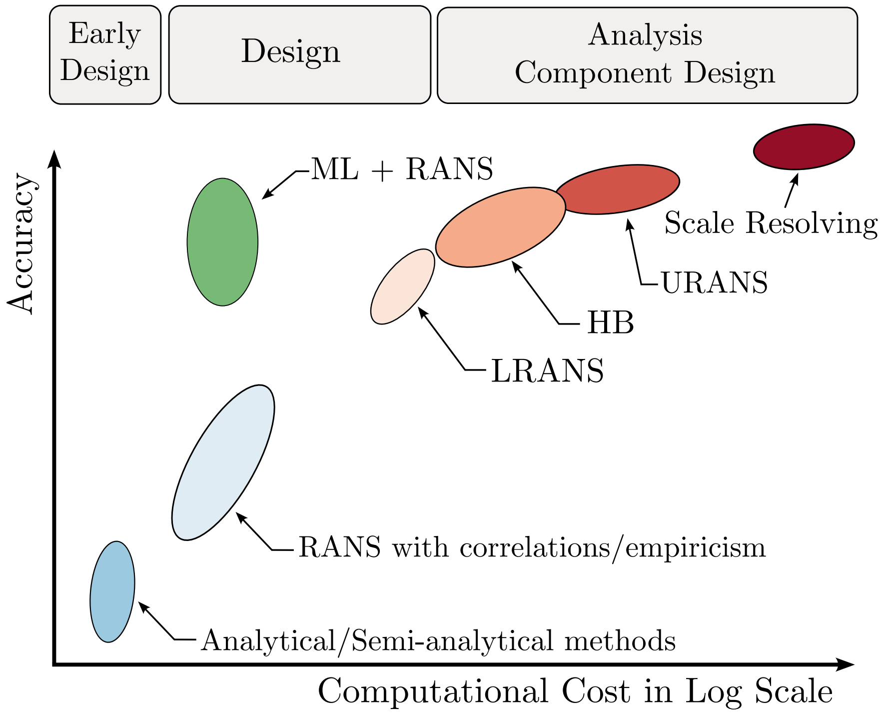

Figure 1.9 *Illustration of accuracy as a function of computational cost of methods employed to assess compressor aeroleastic stability during design stages.*

1.7 Thesis Outline

Training a physics guided machine learning model requires the following ingredients:

1. Appropriate input parameters fed into the input layer
2. High-fidelity data fed into the output layer
3. Low-fidelity physical data fed into the input and/or intermediate layers

Hence to address these needs and achieve the objectives, the thesis is structured as follows:

- Chapter (2) provides a detailed account of the RANS flow solver algorithms, the assumptions and methods employed to evaluate aeroelastic stability. The main test case of this work is introduced, and a comparison of solutions obtained from different solvers, at canonical operating conditions, is offered. The machine learning methods used are also introduced.
- As a first attempt at modelling aeroelastic stability in compressors with machine learning, Chapter (3) presents the development of a purely data-driven neural network model trained to predict aeroelastic stability of the compressor cascade introduced in the previous Chapter. The generation of computational databases

is discussed, along with a possible blade redesign application based on simple input parameters.

- Chapter (4) reviews, on the other hand, a purely theory based model for predicting the response of unloaded blades in a cascade. The assumptions of the theory are reported, along with the main equations. The current implementation is compared against previous ones and the shortcomings of this model in predicting the response of loaded cascades are discussed and shown via comparison with CFD data.

- Chapter (5) builds on the work and knowledge acquired from Chapters (3) and (4), introducing a physics guided neural network model that is able to generalise and predict aeroelastic stability of unseen geometries with good degree of accuracy. The inputs, outputs and training of the method are discussed and the model is thoroughly tested on a large number of cascades. An explanation of the predictions is offered with model agnostic techniques aimed at opening the proverbial “black-box” of data-driven methods. This chapter constitutes the main contribution of this thesis.

- Chapter (6) focuses on describing the uncertainty of aeroelastic predictions due to the sensitivity of unsteady flow to complex features such as shock waves and flow separation. A method to predict the uncertainty in the computational database obtained in Chapter (3) is devised. The results are consequently verified via Monte Carlo analysis and, finally, a possible application is offered.

- Chapter (7) gathers the major findings of the thesis, proposes ideas for future work and presents a discussion regarding data availability and feasibility of such an approach in an industrial setting.

Chapter 2

Methodology

2.1 Introduction

This chapter provides a brief introduction to the computational fluid dynamics and machine learning methods the thesis relies upon. The flow and structural models are discussed alongside the employed strategy to assess aeroelastic stability. In addition, the basic notions of the employed machine learning techniques are presented.

2.2 CFD Solver

The CFD solver utilised throughout this work is `LUFT` (Petrie-Repar, 2006), and it is specifically designed for turbomachinery applications. The code comprises of a steady aerodynamic solver, an unsteady linearised solver and the aeroelastic equations are approached using the modal form representation. The components of the solver will now be discussed in detail.

2.2.1 Navier-Stokes Equations

The three-dimensional, unsteady, compressible, Favre-averaged Navier-Stokes are the governing equations of the RANS turbomachinery solver. The equations are cast in terms of absolute velocity, but solved in a relative reference frame rotating with the blades about an axis with angular velocity $\boldsymbol{\omega}$. The arising system of equations can be written in integral conservative form, for a control volume $\mathcal{V}$ with boundary Γ, in Cartesian coordinates $\boldsymbol{x} = (x, y, z)$, as

$$\frac{d}{dt}\int_{\mathcal{V}} \boldsymbol{U}\, d\mathcal{V} + \oint_{\partial\mathcal{V}} \left(\boldsymbol{F} - \frac{1}{Re}\boldsymbol{G}\right) \cdot \boldsymbol{n}\, d\Gamma = \int_{\mathcal{V}} \boldsymbol{S}\, d\mathcal{V} \tag{2.1}$$

where $\boldsymbol{n}$ is the outward unit vector of the control volume boundary Γ; $\boldsymbol{U}$, $\boldsymbol{F}$, $\boldsymbol{G}$ and $\boldsymbol{S}$ denote the solution vector of conservative variables, inviscid and viscous flux vectors and source terms vector, respectively, and can be written as:

$$\boldsymbol{U} = \begin{bmatrix} \rho \\ \rho \boldsymbol{u} \\ \rho e \end{bmatrix}, \quad \boldsymbol{F} = \boldsymbol{U} \otimes \boldsymbol{v} + \begin{bmatrix} 0 \\ p\delta_{ij} \\ u_j p \end{bmatrix}, \quad \boldsymbol{G} = \begin{bmatrix} 0 \\ \tau_{ij} \\ u_k \tau_{ik} + k_{th} \frac{\partial T}{\partial x_i} \end{bmatrix}, \quad \boldsymbol{S} = \begin{bmatrix} 0 \\ \rho \boldsymbol{\omega} \times \boldsymbol{u} \\ 0 \end{bmatrix} \tag{2.2}$$

In Eq. (2.2), δ_{ij} represents the Kronecker delta function; $\boldsymbol{u}$, $\boldsymbol{\omega}$ are the vectors of absolute and angular velocity. The vector $\boldsymbol{v}$ represents the velocity in the relative frame

$$\boldsymbol{v} = \boldsymbol{u} - \boldsymbol{\omega} \times \boldsymbol{x} - \frac{d\boldsymbol{x}}{dt} \tag{2.3}$$

where the last term of Eq. (2.3) is the velocity of the boundary Γ. ρ, p, T and e denote density, pressure, temperature and internal energy, respectively; τ_{ij} and k_{th} are the viscous stress tensor and the effective thermal conductivity.

The working fluid is assumed to be a perfect gas, thus providing an equation of state $f(\rho, p, T) = 0$ for the thermodynamic variables

$$p = \rho R T = \rho(\gamma - 1)\left(e - \frac{|\boldsymbol{u}|^2}{2}\right) \tag{2.4}$$

and specific gas constant

$$R = c_p - c_v = c_v(\gamma - 1) \tag{2.5}$$

where c_p and c_v represent the specific heat capacities and $\gamma = \frac{c_p}{c_v}$ is the specific heat ratio.

The viscous stress tensor τ_{ij} follows the eddy viscosity concept and the Boussinesq assumption, which considers the turbulent stresses to be linearly correlated to the strain rate tensor. The laminar viscosity μ_l follows Sutherland's law and the thermal conductivity k_{th} is assumed to be linearly correlated with viscosity. The above assumptions result in the following set of equations

$$\begin{aligned} \tau_{ij} &= \mu\left(\frac{\partial u_i}{\partial x_j} + \frac{\partial u_j}{\partial x_i}\right) + \lambda \delta_{ij} \left(\nabla \cdot \boldsymbol{u}\right) \\ \mu &= \mu_l + \mu_t \\ k_{th} &= \frac{\gamma}{\gamma - 1}\left(\frac{\mu_l}{Pr_l} + \frac{\mu_t}{Pr_t}\right) \end{aligned} \tag{2.6}$$

where the value of $\lambda = -\frac{2}{3}\mu$ is given by Stokes' relation, the laminar and turbulent Prandtl number, Pr_l and Pr_t, are equal to 0.7 and 0.9 respectively. Finally, the turbulent eddy viscosity μ_t is determined by the one-equation Spalart and Allmaras (1994) turbulence model, with no wall functions.

The flow solver uses a cell-centered finite volume scheme to solve the compressible RANS equations, on an unstructured computational grid, composed exclusively of hexahedral elements. The fluxes are calculated by means of an upwind AUSMDV scheme (Wada and Liou, 1997). The flow state at the interfaces is reconstructed using a MUSCL interpolation coupled with the van Albada limiter (van Albada et al., 1982). The spatial accuracy is, therefore, second-order throughout the domain, except near sharp gradient regions such as shock waves, where the accuracy reverts back to first-order. A least squared multidimensional interpolation method is used to calculate the flow gradients required for the viscous fluxes. For steady flows, a predictor-corrector scheme is used to march the solution to convergence; local time stepping with residual smoothing is also applied, and a preconditioned GMRES method is used to solve the linear system arising at every iteration.

The discretised flow equations for the i-th cell, on a time-varying computational grid, read

$$\frac{d}{dt}\left(\mathcal{V}_i \boldsymbol{U}_i\right) + \sum_j \boldsymbol{H}_j \Gamma_j = \boldsymbol{S}_i \mathcal{V}_i \tag{2.7}$$

where j runs over the cell faces Γ_j, $\boldsymbol{H}_j$ denotes the numerical flux, viscous and inviscid, for the j-th face, estimated from *left* and *right* states by means of MUSCL approach and AUSMDV scheme, $\mathcal{V}_i$ is the volume of the i-th cell, and $\boldsymbol{S}_i$ is the mean source term. By declaring a residual function

$$\boldsymbol{R}_i = \boldsymbol{S}_i - \mathcal{V}_i^{-1} \sum_j \boldsymbol{H}_j \Gamma_j \tag{2.8}$$

Eq. (2.7) can be written in the general form

$$\frac{d}{dt}\left(\mathcal{V}_i \boldsymbol{U}_i\right) = \mathcal{V}_i \boldsymbol{R}_i \tag{2.9}$$

Finally, one must note that $\boldsymbol{R}_i$ depends on the flow variables $\boldsymbol{U}$, grid coordinates $\boldsymbol{x}$ and, given Eq. (2.3), on the grid velocity $\dot{\boldsymbol{x}}$

$$\boldsymbol{R} = \boldsymbol{R}\left(\boldsymbol{U}, \boldsymbol{x}, \dot{\boldsymbol{x}}\right) \tag{2.10}$$

2.2.2 Time-Linearised Navier-Stokes Equations

The linearisation of the governing equations leverages the assumption that both the displacements and solution can be decomposed in a time independent, steady contribution and a time dependent, small perturbation

$$\begin{aligned}
\boldsymbol{x}(t) &= \bar{\boldsymbol{x}} + \delta\boldsymbol{x}(\bar{\boldsymbol{x}}, t) \\
\mathcal{V}(\boldsymbol{x}, t) &= \bar{\mathcal{V}}(\bar{\boldsymbol{x}}) + \delta\mathcal{V}(\bar{\boldsymbol{x}}, t) \\
\boldsymbol{U}(\boldsymbol{x}, t) &= \bar{\boldsymbol{U}}(\bar{\boldsymbol{x}}) + \delta\boldsymbol{U}(\bar{\boldsymbol{x}}, t)
\end{aligned} \tag{2.11}$$

with $\bar{\boldsymbol{U}}$ being the steady state solution, which yields

$$\boldsymbol{R}\left(\bar{\boldsymbol{U}},\bar{\boldsymbol{x}},\boldsymbol{0}\right)=0 \tag{2.12}$$

The residual $\boldsymbol{R}$ can now be approximated by its first-order Taylor expansion about the steady state solution

$$\boldsymbol{R}\left(\boldsymbol{U},\boldsymbol{x},\dot{\boldsymbol{x}}\right)\approx\boldsymbol{R}\left(\bar{\boldsymbol{U}},\bar{\boldsymbol{x}},\boldsymbol{0}\right)+\left.\frac{\partial\boldsymbol{R}}{\partial\boldsymbol{U}}\right|_{\left(\bar{\boldsymbol{U}},\bar{\boldsymbol{x}},\boldsymbol{0}\right)}\delta\boldsymbol{U}+\left.\frac{\partial\boldsymbol{R}}{\partial\boldsymbol{x}}\right|_{\left(\bar{\boldsymbol{U}},\bar{\boldsymbol{x}},\boldsymbol{0}\right)}\delta\boldsymbol{x}+\left.\frac{\partial\boldsymbol{R}}{\partial\dot{\boldsymbol{x}}}\right|_{\left(\bar{\boldsymbol{U}},\bar{\boldsymbol{x}},\boldsymbol{0}\right)}\delta\dot{\boldsymbol{x}} \tag{2.13}$$

Plugging Eq. (2.13) into Eq. (2.9), neglecting second-order terms such as $\delta\mathcal{V}\delta\boldsymbol{U}$, the linearised unsteady equations read

$$\frac{d}{dt}\delta\boldsymbol{U}+\frac{\bar{\boldsymbol{U}}}{\bar{\mathcal{V}}}\frac{d}{dt}\delta\mathcal{V}=\left.\frac{\partial\boldsymbol{R}}{\partial\boldsymbol{U}}\right|_{\left(\bar{\boldsymbol{U}},\bar{\boldsymbol{x}},\boldsymbol{0}\right)}\delta\boldsymbol{U}+\left.\frac{\partial\boldsymbol{R}}{\partial\boldsymbol{x}}\right|_{\left(\bar{\boldsymbol{U}},\bar{\boldsymbol{x}},\boldsymbol{0}\right)}\delta\boldsymbol{x}+\left.\frac{\partial\boldsymbol{R}}{\partial\dot{\boldsymbol{x}}}\right|_{\left(\bar{\boldsymbol{U}},\bar{\boldsymbol{x}},\boldsymbol{0}\right)}\delta\dot{\boldsymbol{x}} \tag{2.14}$$

Finally, the blade motion is imposed as a single harmonic, thus the computational grid deformation and the unsteady perturbation are also harmonic with fixed angular frequency ω

$$\begin{aligned}\delta\boldsymbol{x}(\bar{\boldsymbol{x}},t)&=\Re\left\{\widehat{\boldsymbol{x}}e^{j\omega t}\right\}\\\delta\mathcal{V}(\bar{\boldsymbol{x}},t)&=\Re\left\{\widehat{\mathcal{V}}e^{j\omega t}\right\}\\\delta\boldsymbol{U}(\bar{\boldsymbol{x}},t)&=\Re\left\{\widehat{\boldsymbol{U}}e^{j\omega t}\right\}\end{aligned} \tag{2.15}$$

Plugging Eq. (2.15) into Eq. (2.14), one obtains

$$\left(j\omega\boldsymbol{I}-\frac{\partial\boldsymbol{R}}{\partial\boldsymbol{U}}\right)\widehat{\boldsymbol{U}}=\frac{\partial\boldsymbol{R}}{\partial\boldsymbol{x}}\widehat{\boldsymbol{x}}+\frac{\partial\boldsymbol{R}}{\partial\dot{\boldsymbol{x}}}j\omega\widehat{\boldsymbol{x}}-j\omega\frac{\bar{\boldsymbol{U}}}{\bar{\mathcal{V}}}\widehat{\mathcal{V}} \tag{2.16}$$

The right hand side of the linearised equation is now independent of the unkonwn $\widehat{\boldsymbol{U}}$ and can be seen as a source term. It can be evaluated by calculating the change in residual from the steady state due to the grid perturbation with amplitude $\widehat{\boldsymbol{x}}$ and velocity $j\omega\widehat{\boldsymbol{x}}$. The Jacobian $\partial\boldsymbol{R}/\partial\boldsymbol{U}$ is calculated by numerically differentiating fluxes at the cell interfaces, by means of finite difference, and summing over a small number of neighbouring cells

$$\frac{\partial\boldsymbol{R}_i}{\partial\boldsymbol{U}_k}=\delta_{ik}\frac{\partial\boldsymbol{S}_i}{\partial\boldsymbol{U}_k}-\mathcal{V}_i^{-1}\sum_j\frac{\partial\boldsymbol{H}_j}{\partial\boldsymbol{U}_k}\Gamma_j \tag{2.17}$$

Eq. (2.16) is a complex linear system of the form $\boldsymbol{A}\widehat{\boldsymbol{U}}=\boldsymbol{b}$ which is solved, with appropriate boundary conditions, by means of a preconditioned GMRES method.

2.2.3 Boundary Conditions

Boundary conditions need to be correctly formulated in order to solve the system of partial differential equations arising for the Navier-Stokes equations. Four main sets of conditions can be identified: solid walls, inviscid and viscous, periodicity and far-field boundaries treatment. Moreover, a concise discussion regarding the calculation of grid displacements is presented.

Inviscid Wall

This boundary condition imposes flow tangency at the wall, requiring that there is no flow through the surface. This is attained by vanishing the velocity component normal to the moving wall

$$\{\boldsymbol{u} - \boldsymbol{\omega} \times \boldsymbol{x} - \dot{\boldsymbol{x}}\} \cdot \boldsymbol{n} = 0 \tag{2.18}$$

The linearisation of the above results in tangency conditions for the mean flow and the perturbation

$$\begin{aligned} \{\bar{\boldsymbol{u}} - \boldsymbol{\omega} \times \bar{\boldsymbol{x}}\} \cdot \bar{\boldsymbol{n}} &= 0 \\ \{\widehat{\boldsymbol{u}} - \boldsymbol{\omega} \times \widehat{\boldsymbol{x}} - j\omega\widehat{\boldsymbol{x}}\} \cdot \bar{\boldsymbol{n}} + \{\bar{\boldsymbol{u}} - \boldsymbol{\omega} \times \bar{\boldsymbol{x}}\} \cdot \widehat{\boldsymbol{n}} &= 0 \end{aligned} \tag{2.19}$$

Note that $\boldsymbol{\omega}$ and ω are, respectively, the shaft's angular velocity vector and the angular frequency of the harmonic perturbation.

Viscous Wall

Referred to also as *no-slip*, this boundary condition states that, on the wall, the fluid velocity relative to the moving wall itself is zero

$$\boldsymbol{u} - \boldsymbol{\omega} \times \boldsymbol{x} - \dot{\boldsymbol{x}} = 0 \tag{2.20}$$

The linearisation yields

$$\begin{aligned} \bar{\boldsymbol{u}} - \boldsymbol{\omega} \times \bar{\boldsymbol{x}} &= 0 \\ \widehat{\boldsymbol{u}} - \boldsymbol{\omega} \times \widehat{\boldsymbol{x}} - j\omega\widehat{\boldsymbol{x}} &= 0 \end{aligned} \tag{2.21}$$

Periodicity

In absence of aperiodic upstream disturbances, e.g. inlet flow distortion, the mean flow in a turbomachinery row can be modelled as a single blade-to-blade passage with periodic boundaries. The boundary condition can be written in cylindrical and Cartesian coordinates, respectively, as

$$\begin{aligned} \bar{\boldsymbol{U}}\left(x, r, \theta + \frac{2\pi}{B}\right) &= \bar{\boldsymbol{U}}\left(x, r, \theta\right) \\ \bar{\boldsymbol{U}}\left(x, y + P, z\right) &= \bar{\boldsymbol{U}}\left(x, y, z\right) \end{aligned} \tag{2.22}$$

where B is the number of blades in a full annulus row and P is the linear pitch for a 2D cascade. For the time-linearised equations, the periodic boundary condition needs to be modified. Particularly in the context of flutter, blades may oscillate with a constant phase shift with respect to their neighbours, that is with an interblade phase angle σ. The boundary condition for a 2D cascade now reads

$$\widehat{\boldsymbol{U}}\left(x, y+P, z\right)=\widehat{\boldsymbol{U}}\left(x, y, z\right) e^{j\sigma} \tag{2.23}$$

An analogous expression can be written in cylindrical coordinates.

Far-field boundaries

Unlike isolated airfoils, the far-field boundaries in turbomachinery applications are usually less than one chord away from the blade. The close proximity of the boundaries may lead to non-physical, spurious inward reflections of the outward propagating waves, which can significantly affect the solution. To mitigate this effect, appropriate non-reflecting boundary conditions need to be applied at inlet and outlet boundaries. In this work, the 2D non-reflecting boundary conditions presented by Giles (1990) are applied. The boundary conditions are based on the characteristics of the Euler equations and are exact for unsteady computations with a single frequency, which is the case for the time-linearised solver. As for the steady-state boundary treatment, the following averaged physical quantities are specified:

- Inlet: stagnation temperature and pressure, flow angles
- Outlet: static pressure

and subsequently, the same unsteady boundary conditions are applied, in the limiting case of zero frequency.

Grid Displacement

The grid motion vector $\widehat{\boldsymbol{x}}$ is an input to the linearised solver. Conventionally, a mass-normalised modeshape of the blade is obtained from a finite-element solver and interpolated from the FE to the CFD mesh to obtain the displacement of nodes on the blade. Periodic and far-field boundaries are set to be static, therefore with zero displacement. Now, with the previous constraints in place, the grid motion is determined by solving the Laplace equation. In this thesis, the modeshapes are not calculated but imposed as a rigid body motion.

2.2.4 Aeroelastic Equations

This section introduces the main concepts and formulations necessary to perform aeroelastic analyses of a turbomachinery blade row. The description of the aeroelastic problem requires a structural dynamic model, a kinematic description of blade motion and a useful aerodynamic model for the fluid forces, that is, a model that can be accomodated by the current CFD capabilities. The following equations have been treated and manipulated by several authors according to the problem at hand, and detailed accounts, among many, are provided by Crawley (1987) and Försching (1994).

The most general linear equation of motion that describes a flexible structure, such as a bladed disk, under aerodynamic loads reads

$$\boldsymbol{M}\ddot{\boldsymbol{x}}(t) + \boldsymbol{D}\dot{\boldsymbol{x}}(t) + \boldsymbol{K}\boldsymbol{x}(t) = \boldsymbol{F}^{A}(\boldsymbol{x}, t) \tag{2.24}$$

where $\boldsymbol{M}$, $\boldsymbol{D}$, $\boldsymbol{K}$ are mass, damping and stiffness matrices, while $\boldsymbol{F}^{A}$ is a generic vector of forces resulting from aerodynamic loads. In turbomachinery applications, a number of simplifications can be made. Under the assumption of small vibration amplitude, the forces on the right-hand side of Eq. (2.24) can be expressed as the linear combination of two separate contributions, one $\boldsymbol{F}^{m}$ that is motion dependent, the other $\boldsymbol{F}^{d}$ coming from external sources. As this thesis focuses on self-induced vibration, the term $\boldsymbol{F}^{d}$ is set to zero for the rest of this discussion. It is further assumed that the disk is infinitely stiff, resulting in mechanically uncoupled blades. Finally, the mechanical damping of the blades is assumed to be null, so that the equation of motion for the i-th blade of a turbomachinery row reads

$$\boldsymbol{M}_i\ddot{\boldsymbol{x}}_i(t) + \boldsymbol{K}_i\boldsymbol{x}_i(t) = \boldsymbol{F}_i^{m}(\boldsymbol{x}, t) \tag{2.25}$$

The equation of motion can be cast into modal or generalised coordinates q, by representing the structural response of the blade as a linear combination of modes $\boldsymbol{\Phi}$

$$\boldsymbol{x}_i(t) = \sum_{p=1}^{n} \boldsymbol{\Phi}_{i,p} \cdot q_{i,p}(t) \tag{2.26}$$

The modes are obtained from the free vibration problem, assuming a harmonic solution $\boldsymbol{x}(t) = \boldsymbol{\Phi}e^{j\omega t}$, where $(\omega_p, \boldsymbol{\Phi}_p)$ are the p-th eigenfrequency and eigenvector satisfying

$$\left(\boldsymbol{K}_i - \omega_{i,p}^2 \boldsymbol{M}_i\right)\boldsymbol{\Phi}_{i,p} = \boldsymbol{0} \tag{2.27}$$

In the case of a blade section, simple modes such as pitching and plunging can be simply imposed as rigid body modes. Regardless, the modes are assumed to be mass normalised so that, after applying the change of coordinates, the system of aeroelastic equations of motion reads

$$\underbrace{\boldsymbol{V}_{i,n}^{T}\boldsymbol{M}_i\boldsymbol{V}_{i,n}}_{\boldsymbol{I}}\ddot{\boldsymbol{q}}_{i,n} + \underbrace{\boldsymbol{V}_{i,n}^{T}\boldsymbol{K}_i\boldsymbol{V}_{i,n}}_{\boldsymbol{\Omega}_{i,n}^{2}}\boldsymbol{q}_{i,n} = \underbrace{\boldsymbol{V}_{i,n}^{T}\boldsymbol{F}_i}_{\boldsymbol{f}_{i,n}} \tag{2.28}$$

with $\boldsymbol{V}$ being the matrix of eigenvectors for each blade, $\boldsymbol{V}_i = [\boldsymbol{\Phi}_{i,1}, ..., \boldsymbol{\Phi}_{i,n}]$, $\boldsymbol{I}$ is the identity matrix, $\boldsymbol{\Omega}^2_{i,n} = \mathrm{diag}(\omega^2_{i,n})$ is a diagonal matrix containing the squares of natural frequencies for each blade and mode, and $\boldsymbol{f}_{i,n}$ the vector of modal forces. The orthogonality of eigenmodes diagonalises the system of Eq. (2.28), so that each equation is decoupled and the modal response for an assembly of N blades vibrating with a given mode can be written as

$$\begin{Bmatrix} \ddot{q}_0(t) \\ \vdots \\ \ddot{q}_i(t) \\ \vdots \\ \ddot{q}_{N-1}(t) \end{Bmatrix} + \begin{bmatrix} \omega_0^2 & 0 & \dots & \dots & 0 \\ 0 & \ddots & & & \vdots \\ \vdots & & \omega_i^2 & & \vdots \\ \vdots & & & \ddots & 0 \\ 0 & \dots & \dots & 0 & \omega_{N-1}^2 \end{bmatrix} \begin{Bmatrix} q_0(t) \\ \vdots \\ q_i(t) \\ \vdots \\ q_{N-1}(t) \end{Bmatrix} = \begin{Bmatrix} f_0(t) \\ \vdots \\ f_i(t) \\ \vdots \\ f_{N-1}(t) \end{Bmatrix} \tag{2.29}$$

Note that, although the modes of each blade are orthogonal and decoupled, Eq. (2.29) states that the blades in the assembly are coupled due to the aerodynamic forcing. As a matter of fact, as shown by Crawley (1987), the force on any given blade i does not only depend on the motion of the blade itself, but also on the effect due to the vibration of the neighbouring airfoils; such an effect is very generally described by Eq. (2.30), where f depends on flow conditions, frequency and geometry. The effect of time history of blades' motion is condensed in the variable Λ.

$$\begin{aligned} f_i = {} & f_0(q_i, \dot{q}_i, \ddot{q}_i, \Lambda_i) \\ & + f_{+1}(q_{i+1}, \dot{q}_{i+1}, \ddot{q}_{i+1}, \Lambda_{i+1}) \\ & + f_{-1}(q_{i-1}, \dot{q}_{i-1}, \ddot{q}_{i-1}, \Lambda_{i-1}) \\ & + \dots \end{aligned} \tag{2.30}$$

In general, the form of aerodynamic forces above is difficult to find. Instead, it is sufficient to find operators for simple harmonic motion, since such an analysis is still able to retrieve the stability boundary of the modes. Moreover, the derivation of unsteady aerodynamic forces is particularly convenient in travelling wave coordinates, when the cascade vibrates with a fixed interblade phase angle between airfoils. The kinematic relationship between travelling wave coordinates and individual blade coordinates is

$$q_i(t) = \Re \left\{ \sum_{k=0}^{N-1} \bar{q}_{\sigma_n} e^{j(\omega t + k\sigma_n)} \right\} \tag{2.31}$$

where $\bar{q}_{\sigma_n}$ is the amplitude of the travelling wave of interblade phase angle $\sigma_n = \frac{2\pi n}{N}$. Eq. (2.31) can be conveniently rewritten in matrix form as

$$\boldsymbol{q}_i(t) = \widehat{\boldsymbol{E}} \bar{\boldsymbol{q}}_{\sigma_n} e^{j\omega t} = \bar{\boldsymbol{q}}_i e^{j\omega t} \tag{2.32}$$

where $\bar{q}_i$ is the amplitude of the individual blade harmonic motion and $\widehat{\boldsymbol{E}}$ represents the coefficients of a discrete Fourier transform in complex matricial form

$$\widehat{\boldsymbol{E}} = \begin{bmatrix} E_{0,0} & \dots & E_{0,i} & \dots & E_{0,N-1} \\ \vdots & & & & \vdots \\ E_{i,0} & \dots & E_{i,i} & \dots & E_{i,N-1} \\ \vdots & & & & \vdots \\ E_{N-1,0} & \dots & E_{N-1,i} & \dots & E_{N-1,N-1} \end{bmatrix} \tag{2.33}$$

$$E_{k,l} \equiv e^{j\frac{2\pi kl}{N}} \;\; ; \;\; E_{k,l}^{-1} \equiv \frac{1}{N} e^{-j\frac{2\pi kl}{N}}$$

Similarly to the kinematic relationship of Eq. (2.32), the aerodynamic force on the i-th blade can be written as the force induced by the superposition of all travelling waves

$$\begin{aligned} \boldsymbol{f}_i(t) &= \widehat{\boldsymbol{E}} \left[\mathrm{diag} \left(\widehat{\ell}_{\sigma_n} \right) \right] \bar{\boldsymbol{q}}_{\sigma_n} e^{j\omega t} \\ &= \underbrace{\widehat{\boldsymbol{E}} \left[\mathrm{diag} \left(\widehat{\ell}_{\sigma_n} \right) \right] \widehat{\boldsymbol{E}}^{-1}}_{\widehat{\boldsymbol{L}}} \boldsymbol{q}_i \end{aligned} \tag{2.34}$$

where $\widehat{\ell}_{\sigma_n}(\omega)$ is the complex force coefficient due to σ_n and $\widehat{\boldsymbol{L}}(\omega)$ is the aerodynamic influence coefficient (AIC) matrix. Due to the cyclic symmetry of the cascade, the matrix $\widehat{\boldsymbol{L}}$ is circulant, thus it contains only N independent terms

$$\widehat{\boldsymbol{L}} = \begin{bmatrix} L_0 & L_{N-1} & \dots & L_1 \\ L_1 & L_0 & L_{N-1} & \dots \\ \dots & L_1 & L_0 & L_{N-1} \\ L_{N-1} & \dots & L_1 & L_0 \end{bmatrix} \tag{2.35}$$

The matrix $\widehat{\boldsymbol{L}}$ gives insight into the unsteady aerodynamic interactions in the cascade because it allows to quantify the effect induced by the vibration of one airfoil on another. The term on row a and column b denotes the force induced on blade a by the vibration of airfoil b, so that, for example, the diagonal term quantifies the force induced on the blade by its own motion. As for the transformation of coordinates, from individual blade to travelling wave, the force coefficients are also related by a complex Fourier transform as shown in Eq. (2.34). This allows to devise experimental or computational methods where only one blade in the cascade oscillates with a prescribed motion, while the others are at rest. The unsteady aerodynamic loads can be measured and the solution can be translated into travelling wave.

Finally, the equations of motion in individual blade and travelling wave coordinates become, respectively

$$\ddot{\boldsymbol{q}}_i(t) + \left[\operatorname{diag}\left(\omega_i^2\right) - \widehat{\boldsymbol{L}}\right] \boldsymbol{q}_i(t) = \boldsymbol{0} \tag{2.36}$$

$$\ddot{\boldsymbol{q}}_{\sigma_n}(t) + \left[\operatorname{diag}\left(\omega_{\sigma_n}^2\right) - \operatorname{diag}\left(\widehat{\ell}_{\sigma_n}\right)\right] \boldsymbol{q}_{\sigma_n}(t) = \boldsymbol{0} \tag{2.37}$$

Both formulations have their merit. The individual blade formulation is a powerful tool to investigate the physics of the aeroelastic problem, by probing the AIC matrix, and it also represents the correct model for more complex configurations where mistuning is present in the system. Travelling waves are the natural modes of the cascade, as the system of equations is diagonal, which allows to calculate each aeroelastic eigenvalue separately. This is the formulation implemented in the time-linearised solver to calculate unsteady aerodynamic loads for a tuned system and it will be our preferred formulation.

2.3 Aeroelastic Stability

Let

$$\boldsymbol{q}_{\sigma_n}(t) = \bar{\boldsymbol{q}}_{\sigma_n} e^{j s_{\sigma_n} t} \tag{2.38}$$

be the solution to Eq. (2.37). By plugging in and assuming a tuned rotor with a single structural vibration frequency ω_σ, the equation of motion now reads

$$\left[\omega_\sigma^2 \boldsymbol{I} - \operatorname{diag}\left(s_{\sigma_n}^2 + \widehat{\ell}_{\sigma_n}\right)\right] \bar{\boldsymbol{q}}_{\sigma_n} = \boldsymbol{0} \tag{2.39}$$

The system is diagonal and every travelling wave can be treated separately so that the n-th aeroelastic eigenvalue is

$$s_{\sigma_n} = \pm\sqrt{\omega_\sigma^2 - \widehat{\ell}_{\sigma_n}} \tag{2.40}$$

which is a complex number that can be rewritten as

$$s_{\sigma_n} = \Re\left\{s_{\sigma_n}\right\} + j\Im\left\{s_{\sigma_n}\right\} = \omega_n + j\delta_n \tag{2.41}$$

Considering the wave-like solution of Eq. (2.38), ω_n represents the aeroelastic angular frequency of the travelling wave with interblade phase angle σ_n, while δ_n denotes the corresponding decay rate of the damped vibration. As only positive frequencies are physically significant, the solution s_{σ_n} with positive real component is retained. The relation between natural frequency ω_0, damping δ and damped angular frequency ω of a vibrating system is known from the general solution of the damped single degree of freedom oscillator (Meirovitch, 2001)

$$\omega_0^2 = \delta^2 + \omega^2 \tag{2.42}$$

So that the aerodynamic damping ratio can be found as

$$\xi_n = \frac{\delta_n}{\omega_\sigma} = \frac{\Im\left\{s_{\sigma_n}\right\}}{\sqrt{\Re\left\{s_{\sigma_n}\right\}^2 + \Im\left\{s_{\sigma_n}\right\}^2}} \tag{2.43}$$

The above can be simplified by considering that usually $\omega_n \gg \delta_n$, yielding

$$\xi_n \approx \frac{\Im\left\{s_{\sigma_n}\right\}}{\Re\left\{s_{\sigma_n}\right\}} \tag{2.44}$$

with $\Re\left\{s_{\sigma_n}\right\} > 0$ as it corresponds to a vibration frequency. The motion is finally determined by

$$\boldsymbol{q}_{\sigma_n}(t) = \Re\left\{\bar{\boldsymbol{q}}_{\sigma_n} e^{-\xi_n \omega_\sigma t} e^{j\sqrt{1-\xi_n^2}\omega_\sigma t}\right\} \tag{2.45}$$

Assuming $|\xi_n| < 1$, Fig. (2.1) illustrates the time history of displacement: the blade is stable and the amplitude decays when the aerodynamic damping ratio is positive, while the blade is unstable and therefore flutters when the aerodynamic damping ratio is negative. From Eq. (2.45) one can see that the aeroelastic angular frequency is

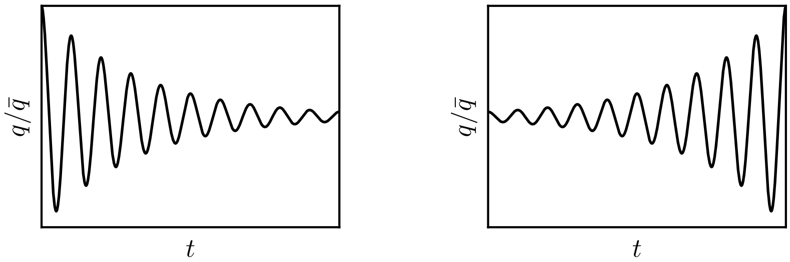

(a) *Stable behaviour with* $\xi > 0$ **(b)** *Unstable behaviour with* $\xi < 0$

Figure 2.1 *Schematic displacement history depending on the sign of aerodynamic damping ratio*

$$\omega = \omega_\sigma \sqrt{1-\xi^2} \tag{2.46}$$

which means that when the aerodynamic damping ratio is $\xi \ll 1$ (corresponding to high mass ratio, see Vega (2016)), the aeroelastic frequency is nearly equal to the natural frequency of the blade, $\omega \approx \omega_\sigma$. This allows to simplify the problem further, because now modeshape, amplitude, frequency and interblade phase angle are all constant, therefore the stability of the system can be evaluated by calculating the work exerted by the fluid on the structure over one vibration cycle. The aerodynamic work per cycle is expressed as

$$\begin{aligned}\mathcal{W} &= \int_T \int_S p(x,t) \cdot \dot{\boldsymbol{x}}(t) \cdot \boldsymbol{n} dS dt \\ &= \int_T \int_S \dot{q}(t) \boldsymbol{\Phi}^T p(x,t) \cdot \boldsymbol{n} dS dt \\ &= \int_0^{\frac{2\pi}{\omega}} \Re \left\{ j\omega \bar{q} e^{j\omega t} \right\} \Re \left\{ \widehat{f} e^{j\omega t} \right\} dt \\ &= \pi \bar{q} \, \Im \left\{ \widehat{f} \right\}\end{aligned} \tag{2.47}$$

where p denotes the unsteady pressure, $\dot{\boldsymbol{x}}$ the airfoil velocity and S its surface. The result means that the aerodynamic work is proportional to the imaginary part of the modal force, therefore to the component which is out-of-phase with the motion. It is convenient to normalise the aerodynamic work to obtain the aerodynamic damping coefficient that will be used throughout this thesis

$$\zeta = -\frac{\mathcal{W}}{\pi \, b \, \bar{q}^2 \, (p_0 - p_1)} \tag{2.48}$$

where b is a length, blade span in this case, and $(p_0 - p_1)$ is the difference between inlet total and static pressure. The aerodynamic damping coefficient is thus positive for stable motion. The implications of this scaling choice are important for the rest of the work and are discussed in Section (7.2).

2.4 Cut-off conditions in a two-dimensional cascade

As mentioned in Chapter (1), acoustic perturbations inside a duct can either propagate without attenuation or decay exponentially as they travel. These waves are said to be cut-on and cut-off, respectively. The frequency at which this change in regime takes place is named cut-off frequency. Throughout this thesis, we will encounter this concept often enough that a discussion regarding the system of waves in a duct is in order. This section reports the main necessary steps to compute wavenumbers in a two-dimensional duct, following the detailed analysis of Giles (1990).

Upstream and downstream refer to the location with respect to the blade row, e.g. upstream cut-off frequency refers to waves which originate upstream of the blade. The direction of travel of the waves is denoted by positive and negative x direction, which in our case correspond to waves that run towards downstream and upstream, irrespective of where they are originated.

The two-dimensional Euler equations which describe an unsteady, inviscid, compressible flow in Cartesian coordinates can be expressed as

$$\frac{\partial}{\partial t}\begin{pmatrix}\rho\\ \rho u\\ \rho v\\ \rho E\end{pmatrix}+\frac{\partial}{\partial x}\begin{pmatrix}\rho u\\ \rho u^2+p\\ \rho uv\\ \rho Eu+pu\end{pmatrix}+\frac{\partial}{\partial y}\begin{pmatrix}\rho v\\ \rho uv\\ \rho v^2+p\\ \rho Ev+pv\end{pmatrix}=0 \tag{2.49}$$

where ρ is the density, u and v are velocity components and E is the total internal energy per unit mass. The system of equations is closed with the equation of state for the pressure p (Eq. 2.4). Plugging Eq. (2.4) into Eq. (2.49) and rearranging for the primitive variables one obtains

$$\frac{\partial}{\partial t}\begin{pmatrix}\rho\\ u\\ v\\ p\end{pmatrix}+\begin{pmatrix}u&\rho&0&0\\ 0&u&0&\frac{1}{\rho}\\ 0&0&u&0\\ 0&\gamma p&0&u\end{pmatrix}\frac{\partial}{\partial x}\begin{pmatrix}\rho\\ u\\ v\\ p\end{pmatrix}+\begin{pmatrix}v&0&\rho&0\\ 0&v&0&0\\ 0&0&v&\frac{1}{\rho}\\ 0&0&\gamma p&v\end{pmatrix}\frac{\partial}{\partial y}\begin{pmatrix}\rho\\ u\\ v\\ p\end{pmatrix}=0 \tag{2.50}$$

The equations can be linearised as in Section (2.2.2), by considering small perturbations from a uniform, steady flow, and neglect all but the first order linear terms. The resulting linear equation reads

$$\frac{\partial \boldsymbol{U}}{\partial t}+\boldsymbol{A}\frac{\partial \boldsymbol{U}}{\partial x}+\boldsymbol{B}\frac{\partial \boldsymbol{U}}{\partial y}=0 \tag{2.51}$$

with $\boldsymbol{U}$ being the vector of perturbation variables

$$\boldsymbol{U}=\begin{pmatrix}\widehat{\rho}\\ \widehat{u}\\ \widehat{v}\\ \widehat{p}\end{pmatrix} \tag{2.52}$$

while $\boldsymbol{A}$ and $\boldsymbol{B}$ are constant matrices of uniform, steady variables

$$\boldsymbol{A}=\begin{pmatrix}u&\rho&0&0\\ 0&u&0&\frac{1}{\rho}\\ 0&0&u&0\\ 0&\gamma p&0&u\end{pmatrix},\quad \boldsymbol{B}=\begin{pmatrix}v&0&\rho&0\\ 0&v&0&0\\ 0&0&v&\frac{1}{\rho}\\ 0&0&\gamma p&v\end{pmatrix} \tag{2.53}$$

Considering a wave-like solution of the form

$$\boldsymbol{U}(x,y,t)=\boldsymbol{u}e^{j(k_x x+k_y y-\omega t)} \tag{2.54}$$

and plugging into Eq. (2.51), one obtains a generalised eigenvalue problem

$$\left(-\omega \boldsymbol{I} + k_x \boldsymbol{A} + k_y \boldsymbol{B}\right) \boldsymbol{u} = 0 \tag{2.55}$$

For the above generalised eigenvalue problem, the possible eigenvalues must satisfy

$$\det\left(-\omega \boldsymbol{I} + k_x \boldsymbol{A} + k_y \boldsymbol{B}\right) = 0 \tag{2.56}$$

After deriving and rearranging, one obtains a dispersion relation which relates the angular frequency ω with the axial and transverse wavenumbers k_x and k_y

$$\left(k_x u + k_y v - \omega\right)^2 \left(\left(k_x u + k_y v - \omega\right)^2 - a^2(k_x^2 + k_y^2)\right) = 0 \tag{2.57}$$

where $a = \sqrt{\gamma p/\rho}$ is the mean flow speed of sound. The polynomial equation has 4 roots.

The first two roots are identical and satisfy

$$k_x u + k_y v - \omega = 0 \tag{2.58}$$

In applications the eigenvalue of most interest is often the axial wavenumber k_x, since this is the main direction of acoustic energy transfer, thus the above equation can be expressed as

$$k_{x,1,2} = \frac{\omega - k_y v}{u} \tag{2.59}$$

Giles (1990) shows that the above roots correspond to vorticity and entropy waves that, assuming ω is real, are fully convected by the mean flow, thus run in the positive x direction, i.e. downstream, with group velocity

$$v_g = \frac{\partial \omega}{\partial k_x} = u > 0 \tag{2.60}$$

The other two eigenvalues satisfy

$$\left(k_x u + k_y v - \omega\right)^2 - a^2(k_x^2 + k_y^2) = 0 \tag{2.61}$$

thus obtaining

$$\begin{aligned} k_{x,3} &= \frac{(\omega - k_y v)(-u + aS)}{c^2 - u^2} \\ k_{x,4} &= \frac{(\omega - k_y v)(-u - aS)}{c^2 - u^2} \end{aligned} \tag{2.62}$$

where

$$S = \sqrt{1 - \frac{k_y^2(a^2 - u^2)}{(\omega - k_y v)^2}} \tag{2.63}$$

If ω is real and S^2 is real and positive, we can obtain the group velocity as

$$\begin{aligned} \frac{\partial k_{x,3}}{\partial \omega} = \frac{-u + a/S}{c^2 - u^2} \Rightarrow \frac{\partial \omega}{\partial k_{x,3}} = \frac{c^2 - u^2}{-u + a/S} = v_{g,3} \\ \frac{\partial k_{x,4}}{\partial \omega} = \frac{-u - a/S}{c^2 - u^2} \Rightarrow \frac{\partial \omega}{\partial k_{x,4}} = \frac{c^2 - u^2}{-u - a/S} = v_{g,4} \end{aligned} \qquad (2.64)$$

For subsonic flow $0 < u < c$, then $0 < S < 1$, we can show that

$$\begin{aligned} \frac{\partial \omega}{\partial k_{x,3}} > 0 \\ \frac{\partial \omega}{\partial k_{x,4}} < 0 \end{aligned} \qquad (2.65)$$

therefore the axial wavenumbers $k_{x,3}$ and $k_{x,4}$ represent acoustic waves running in the positive and negative x direction respectively.

If the square root function S is complex, then one of the two roots for k_x has positive imaginary part and the other has negative imaginary part. To be consistent with the results when S^2 is real and positive, $k_{x,3}$ is defined to be the root with positive imaginary component $\Im\{k_{x,3}\} > 0$, and $k_{x,4}$ with negative imaginary component $\Im\{k_{x,4}\} < 0$. Assuming real angular frequency, with complex axial wavenumber, $k_x = \Re\{k_x\} + j\Im\{k_x\}$, the solution to Eq. (2.51) becomes

$$\boldsymbol{U}(x, y, t) = \boldsymbol{u} e^{-\Im\{k_x\}x} e^{j(\Re\{k_x\}x + k_y y - \omega t)} \qquad (2.66)$$

corresponding to a wave decaying in the positive x direction for $k_{x,3}$, i.e. downstream decaying acoustic wave. Similarly, $k_{x,4}$ corresponds to a wave decaying in the negative x direction, i.e. upstream decaying acoustic wave. Thus Eq. (2.66) represents an *evanescent* or cut-off wave that travels with decaying amplitude in the positive ($\Im\{k_x\} > 0$) or negative ($\Im\{k_x\} < 0$) x direction. If $\Im\{k_x\} = 0$ we obtain a cut-on wave, that propagates with constant amplitude. The cut-off condition is given by

$$S = 0 \Rightarrow (\omega - k_y v)^2 - k_y^2(a^2 - u^2) = 0 \qquad (2.67)$$

The frequency satisfying the above equation is called the cut-off frequency ω_c

$$\omega_c = k_y \left(v \pm \sqrt{a^2 - u^2}\right) = k_y a \left(M_y \pm \sqrt{1 - M_x^2}\right) \qquad (2.68)$$

where M_x and M_y are the free-stream axial and transverse Mach numbers.

In the context of a vibrating turbomachinery cascade, the transverse wavenumber k_y is fixed by the interblade phase angle σ due to periodicity

$$k_y = \frac{\sigma + 2\pi m}{P} \tag{2.69}$$

with P being the pitch of the cascade. As the blades impart flow deflection, we will have different flow angles and Mach numbers upstream and downstream of the blade, thus two different cut-off frequencies on either side of the blades. Fig. (2.2) shows the upstream and downstream cut-off frequencies, in terms of reduced frequency k, against interblade phase angle σ, for a compressor with flow conditions given in Table (2.1).

Table 2.1 *Freestream flow quantities for a compressor test case*

	M_x	M_y	a [m/s]
Upstream	0.4	0.575	331
Downstream	0.35	0.3	340

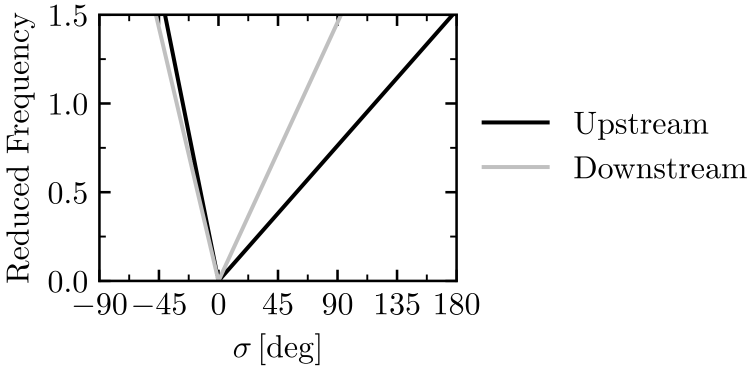

Figure 2.2 *Cut-off reduced frequency against interblade phase angle*

If the cascade operates exactly at the cut-off frequency, the generated acoustic waves have no axial component and travel solely in the transverse direction. This phenomenon is called acoustic resonance and it is usually associated with a spike in aerodynamic damping value.

2.5 Standard Configuration 10

The main test case used in this work is the Standard Configuration 10 (SC10), a two-dimensional compressor cascade. The airfoil profile is obtained by applying the thickness distribution of a modified NACA5506 airfoil on a circular-arc camber line

(Frannson and Verdon, 1991). The thickness, T, and camber, Z, distributions are given by Eq. (2.70)

$$
\begin{aligned}
T(p) &= 0.06 \cdot (2.969\sqrt{p} - 1.26p - 3.516p^2 + 2.843p^3 - 1.036p^4) \\
Z(p) &= -2.475 + \sqrt{r^2 - (p - 0.5)^2}
\end{aligned}
\tag{2.70}
$$

where $0 \leq p \leq 1$ and the camber radius is $r = 2.525$. The upper and lower surface of the airfoil are given by Eq. (2.71)

$$
\begin{aligned}
x(p) &= p \mp \frac{1}{2}T(p)\sin(\phi) \\
y(p) &= Z(p) \pm \frac{1}{2}T(p)\cos(\phi)
\end{aligned}
\tag{2.71}
$$

where

$$\phi = \tan^{-1}\left(\frac{dZ}{dp}\right) \tag{2.72}$$

The stagger angle of the cascade $\xi = 45°$, the chord is fixed at $c = 0.1$ m, while the solidity, or chord to pitch ratio, is $s = 1.0$. In this study, the total inlet pressure and temperature are fixed at 101.3 kPa and 300 K respectively and, at design point, the cascade operates with inlet Mach number $M_1 = 0.7$ and inflow angle $\alpha_1 = 55°$. Throughout the rest of the thesis, we will refer to incidence of flow onto the blade as β_1: positive values indicate incidence higher than nominal, therefore moving the cascade closer to stall. In the case of SC10, the incidence is defined as $\beta_1 = \alpha_1 - 55°$.

The grid used for both steady and unsteady computations has been obtained through a convergence study and it consists of $42,268$ nodes with a $y^+ < 1$ at the blade surface. The grid is quasi-2D, with only a single layer along the third dimension. The boundaries are located 1.5 chord lengths away from leading and trailing edge. The computational grid, with a close-up around the leading edge of the airfoil, is shown in Fig. (2.3).

2.5.1 Comparison with time-accurate solver

The Standard Configuration 10 is, originally, an inviscid test case with no experimental data available. Hall and Crawley (1989) and Montgomery and Verdon (1997) thoroughly characterised this test case employing linearised Euler solvers. Ayer and Verdon (1996) and Höhn (2000) performed viscous, time-accurate computations and compared to inviscid solutions. They observed discrepancies in the computed unsteady pressures solely near shock waves.

The aforementioned studies, although still valid, have been performed over two decades to date, in a time where CFD and turbulence modelling techniques have evolved quickly. For this reason, before tackling the generation of the databases needed

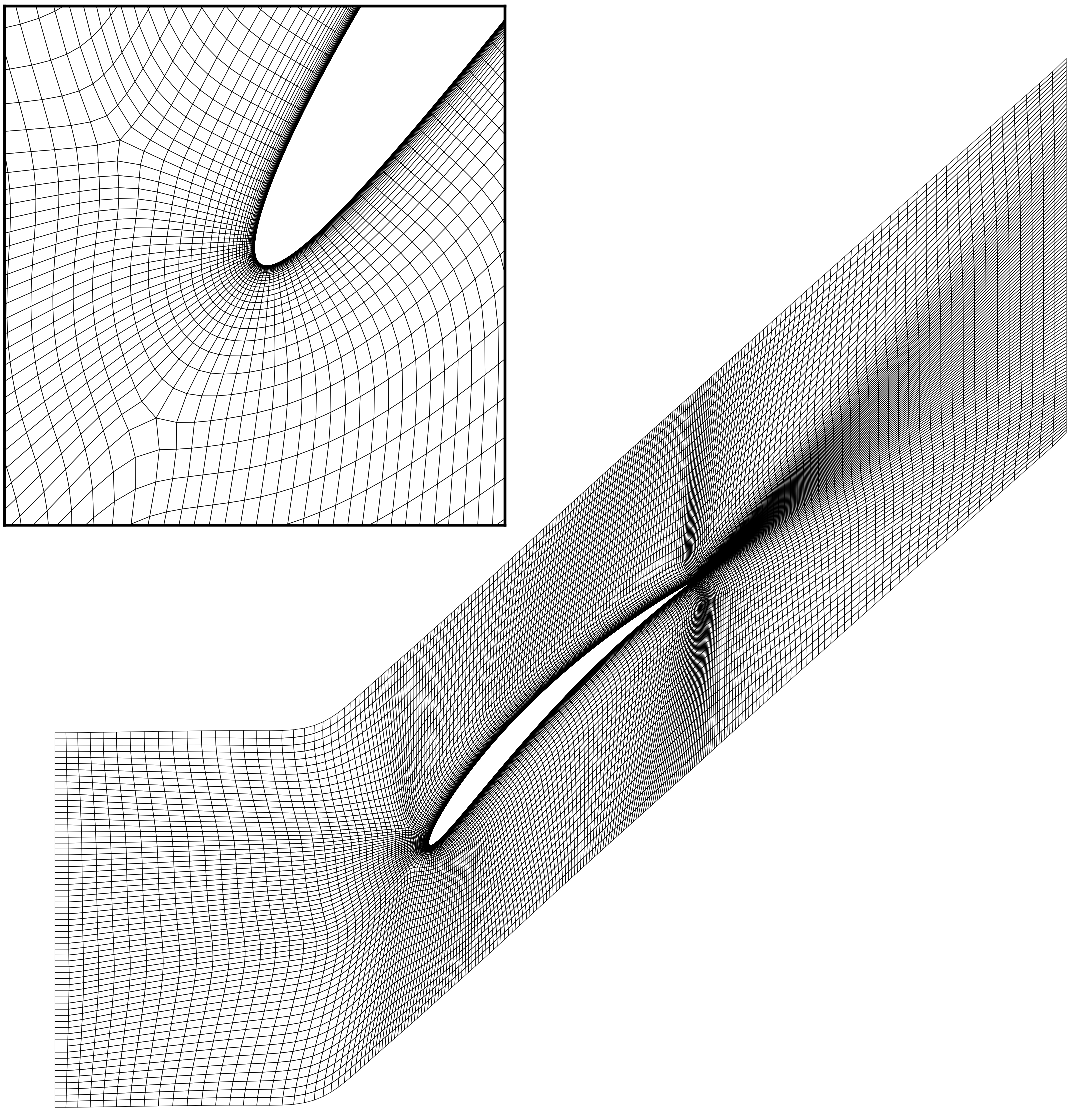

Figure 2.3 *Standard Configuration 10 mesh*

to develop ML models, we assess the discrepancies between the current time-linearised solver, LUFT, and the commercial time-accurate code, ANSYS CFX 20.1, in predicting the unsteady aerodynamic response for the SC10 test case.

The computations in ANSYS CFX have been performed at Tsinghua University. The author would like to acknowledge Chuanxiang Yan and Baotong Wang for providing the data used in this section.

Flow conditions

Two steady-state flow conditions have been defined for this test case: a nominal, subsonic condition and a transonic, off-design one. For each flow condition, two modeshapes are specified: a plunging motion orthogonal to the chord line, and a pitching motion about a point at mid-chord. Furthermore, each mode is computed at two different reduced frequencies. The aeroelastic parameters for the computations are given in Table (2.2).

Table 2.2 *SC10 Aeroelastic parameters*

Steady parameters		Subsonic	Transonic
Inlet Mach Number	M_1	0.7	0.8
Inlet Inflow Angle	α_1	55°	58°
Incidence	β_1	0°	3°

Unsteady parameters		Plunge	Pitch
Reduced Frequency	k	$0.5, 1.0$	$0.5, 1.0$
Amplitude	$\bar{q}$	$0.01c$	1°
Pitching axis chordwise coordinates	(x_c, y_c)	–	$(0.5c, 0.0)$

Numerical Setup

The numerical simulations in `LUFT` have been setup following the methodology outlined in Section (2.2). The aerolastic stability is assessed by calculating the aerodynamic damping coefficient as in Eq. (2.48).

`ANSYS CFX` employs an element-based finite volume approach with unstructured mesh elements to model the RANS equations. A second-order accurate central scheme is employed to discretise the diffusion term, while the advection term is discretised with a high resolution upwind scheme coupled with the limiter of Barth and Jespersen (1989). A second-order accurate backward Euler method is employed for time integration and the arising linear system is solved through an Incomplete Lower Upper (ILU) factorization method, which is accelerated by an algebraic multigrid preconditioner. The steady-state solution is marched to convergence with a pseudo-time stepping technique. The governing equation are solved in combination with the k-ω shear stress transport (SST) turbulence model (Menter et al., 2003). Further details about the solver may be found in the user guide (ANSYS, Inc., 2021). The inlet boundary conditions are stagnation temperature and pressure, flow angles. The outlet boundary condition is static pressure. The aerodynamic damping is obtained with an aerodynamic influence coefficients approach. The time resolution is set to 200 time steps per vibration cycle and one-dimensional non-reflecting boundary conditions are applied. To avoid spurious reflections from the farfield boundaries, the mesh in CFX is extended and coarsened at both inlet and outlet.

The cascade in CFX is composed of 5 blades. The central blade vibrates and the unsteady pressure is recorded on all blades. It is then Fourier transformed to obtain the AIC matrix ($\widehat{\boldsymbol{L}}$) which can be converted into the travelling wave mode force coefficient matrix (diag $\left(\widehat{\ell}_\sigma\right)$) (see Eq. (2.34)), allowing to calculate the aeroelastic eigenvalues starting from Eq. (2.39).

The steady and unsteady blade loading are shown in terms of pressure coefficients

$$\begin{aligned} C_p &= \frac{p - p_1}{p_0 - p_1} \\ \widetilde{C_p} &= \frac{\widehat{p}}{(p_0 - p_1)\bar{q}} \end{aligned} \tag{2.73}$$

where p_0 and p_1 are total and static pressure at the inlet, $\bar{q}$ is the modal amplitude and $\widehat{p}$ the unsteady pressure. As only the imaginary component of unsteady pressure exerts work for simple modes (see Eq. (2.47)), we will only show $\Im\{\widetilde{C_p}\}$.

Subsonic Flow

The steady pressure coefficient is shown in Fig. (2.4). There is excellent agreement between the two codes. The aerodynamic damping coefficient for plunging motion

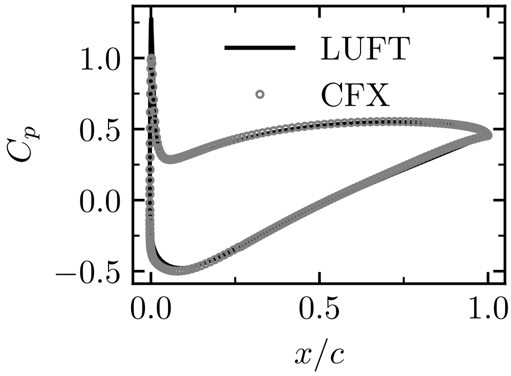

Figure 2.4 *Steady steady pressure coefficient in subsonic flow*

at two reduced frequencies is shown in Fig. (2.5). The overall agreement is good for both cases, and the discrepancies are due to the fundamental difference in modelling linear cascades between the two codes. The time-linearised code models an infinite cascade and apply exact non reflecting boundary conditions, because it assumes the fundamental frequency of the flow is known a priori. This allows the code to model any interblade phase angle with a single blade passage and avoid spurious reflections from the farfield boundaries. On the other hand, the time-accurate code can only model a finite number of airfoils in the cascade and thus calculate a finite number of influence coefficients. Obviously a large number of blade passages can be modelled, though these need to be included in the computational grid, thus increasing computational cost, which is the reason why we use only 5. As the travelling wave mode force coefficient matrix is obtained as a Fourier transform of the AIC matrix, by having more blades we will have more Fourier coefficients and thus will be able to model the discontinuity caused by the acoustic resonance more accurately (see Nipkau (2011, Chapter 5)). The unsteady pressure coefficient for plunging motion, with $k = 0.5$ and interblade phase angles $\sigma = 0°$ and $\sigma = 90°$, is reported in Fig. (2.6). There is good agreement between the computations, with CFX underpredicting the unsteady loading ever so slightly at zero IBPA.

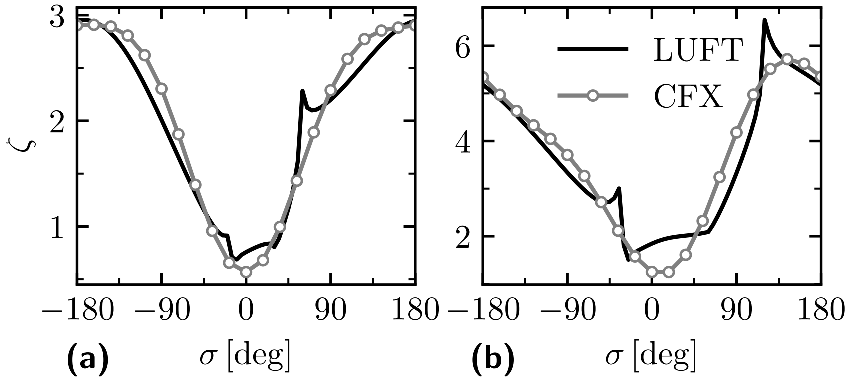

Figure 2.5 *Aerodynamic damping coefficient against interblade phase angle for plunging motion in subsonic flow:* ***(a)*** $k = 0.5$, ***(b)*** $k = 1.0$

Analogous results are shown for a pitching motion about mid-chord in Fig. (2.7) and Fig. (2.8). The vaguely sinusoidal trend of aerodynamic damping predicted by CFX is also predicted by LUFT, if not for the discontinuities caused by acoustic resonance.

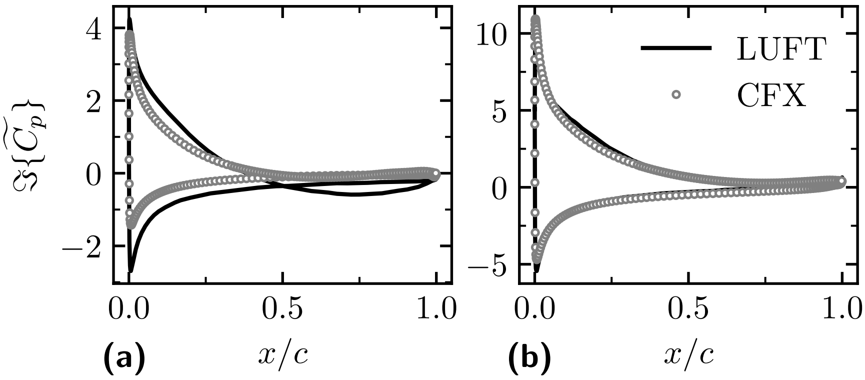

Figure 2.6 *Imaginary part of the unsteady pressure coefficient for plunging motion at subsonic flow conditions, with reduced frequency $k = 0.5$: **(a)** $\sigma = 0°$, **(b)** $\sigma = 90°$*

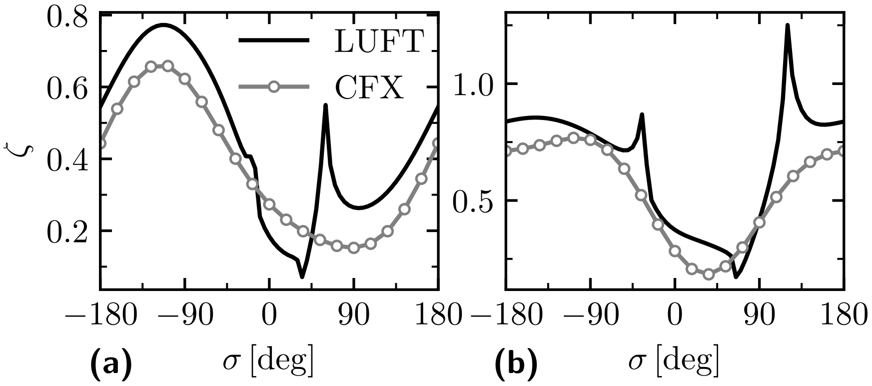

Figure 2.7 *Aerodynamic damping coefficient against interblade phase angle for pitching motion in subsonic flow: **(a)** $k = 0.5$, **(b)** $k = 1.0$*

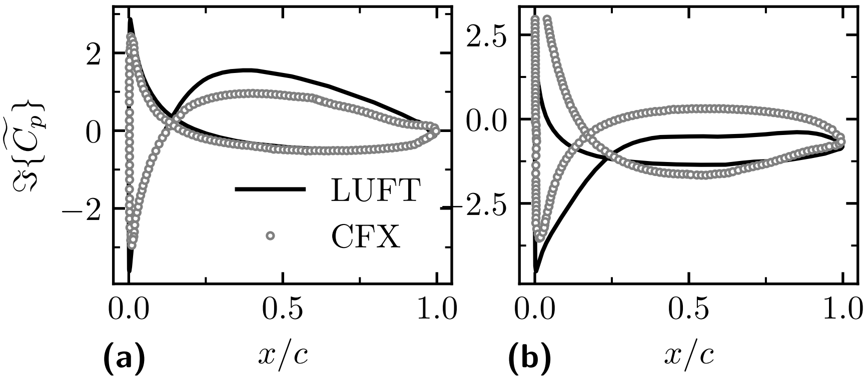

Figure 2.8 *Imaginary part of the unsteady pressure coefficient for pitching motion at subsonic flow conditions, with reduced frequency $k = 0.5$: **(a)** $\sigma = 0°$, **(b)** $\sigma = 90°$*

One would expect that by adding more blades, the time-accurate results move closer to the time-linearised ones. This statement is confirmed by the results in Fig. (2.9), which show aerodynamic damping as a function of interblade phase angle for the pitching mode with $k = 0.5$, as computed by `LUFT`, and by `CFX` with an increasing number of blades, N_b. In particular, one can see that both solvers now predict the same minimum damping value, at $\sigma \approx 40°$.

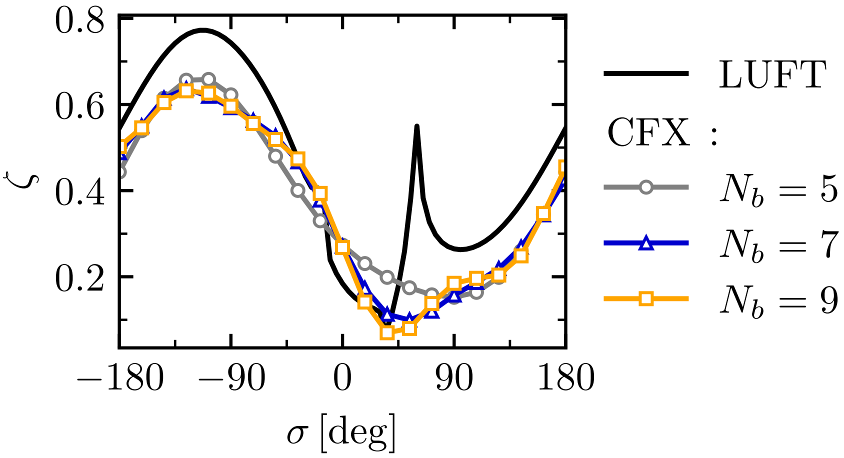

Figure 2.9 *Aerodynamic damping coefficient against interblade phase angle for pitching motion in subsonic flow. Comparison of time-accurate computations with increasing number of blade N_b*

Transonic Flow

The steady pressure coefficient is shown in Fig. (2.10). There is satisfactory agreement between the two codes, with only a very slight difference near the shock wave.

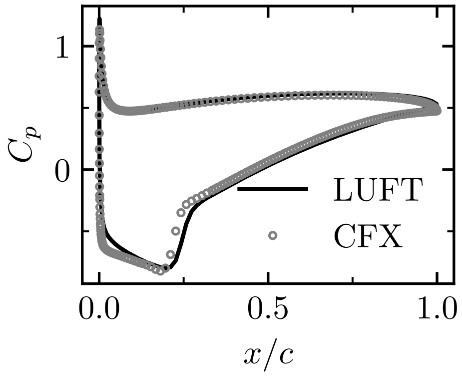

Figure 2.10 *Steady steady pressure coefficient in transonic flow*

The aerodynamic damping coefficient for plunging motion at two reduced frequencies is shown in Fig. (2.11). The overall agreement is good for both cases. Once again, the effect of the non-reflecting boundary conditions is influential, especially at low interblade phase angles, with $k = 1.0$, where the waves are cut-on.

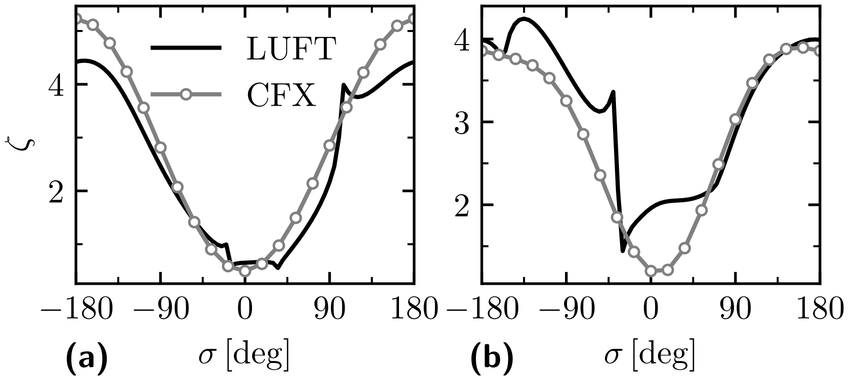

Figure 2.11 *Aerodynamic damping coefficient against interblade phase angle for plunging motion in transonic flow:* ***(a)*** $k = 0.5$, ***(b)*** $k = 1.0$

The unsteady pressure coefficient for plunging motion, with $k = 0.5$ and interblade phase angles $\sigma = 0°$ and $\sigma = 90°$, is shown in Fig. (2.12). At zero interblade phase angle, CFX predicts a lower unsteady loading (less area contained in the curve). There is good agreement at the shock wave, though LUFT predicts a larger unsteady pressure drop right after the shock. On the other hand, for $\sigma = 90°$, the solvers agree very well for most of the blade surface, showing some discrepancies before the shock wave.

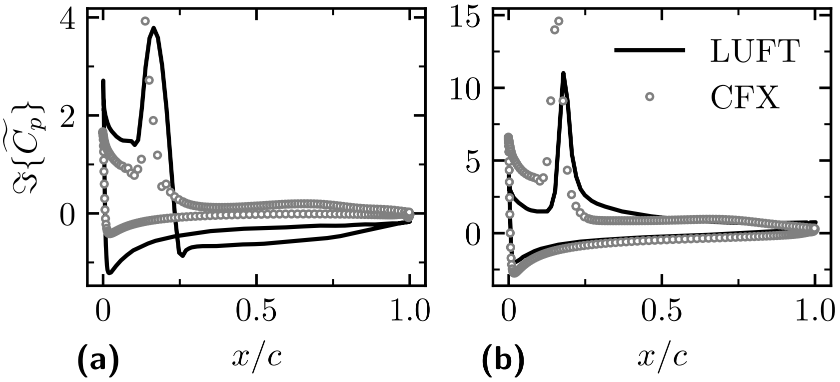

Figure 2.12 *Imaginary part of the unsteady pressure coefficient for plunging motion at transonic flow conditions, with reduced frequency* $k = 0.5$*:* ***(a)*** $\sigma = 0°$, ***(b)*** $\sigma = 90°$

Fig. (2.13) illustrates aerodynamic damping as a function of interblade phase angle for the pitching mode with $k = 0.5$ in transonic flow. Similarly to the subsonic flow case, the agreement between the solvers improves by increasing the number of blades modelled in the time-accurate code.

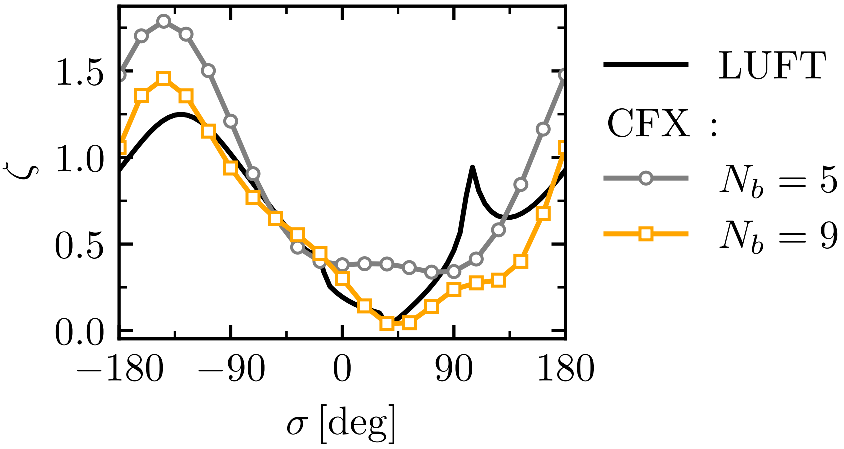

Figure 2.13 *Aerodynamic damping coefficient against interblade phase angle for pitching motion in transonic flow. Comparison of time-accurate computations with increasing number of blade* N_b

Summary

The previous results have shown good agreement between time-accurate and time-linearised code for the two-dimensional SC10 test case. The main discrepancies come from the inability of the time-accurate code to model acoustic resonance with a limited number of blades in the domain, and from the inaccuracies in non-reflecting boundary conditions.

By modelling more blade passages in the domain, the agreement between solvers is improved though the computational cost associated to the time-accurate simulations grows large. In particular, we notice that the minimum aerodynamic damping is captured by both solver and that, as the number of blades increases, the time-accurate solver approaches the results from the time-linearised solver, confirming its ability model the response the aeroelastic response of the 2D cascade, in both subsonic and transonic flow. The overall behaviour of aerodynamic damping is compliant between the two codes. For this particular problem, i.e. modelling of a 2D infinite cascade, the time-linearised approach is superior to the time-accurate one.

Nevertheless, our goal is to obtain a ML model that mimics the results of the CFD code. In a pure machine learning sense, whether the code is time-accurate or not is irrelevant, as long as its predictions are consistent. Having shown that `LUFT` can predict the unsteady flow to a good degree of accuracy for our test case, we can move onto generating aerodynamic damping databases with it.

2.6 Machine Learning Techniques

2.6.1 Fully Connected Neural Network

The fully connected neural network (FCNN), or multi-layer perceptron (MLP), is a fundamental algorithm in machine learning and it is possibly the most widely used regression model in the field. The building block of the FCNN is the "artificial neuron", shown in Fig. (2.14), an operator that applies a nonlinear function to the linear combination of its inputs. Assuming we have an input vector $\boldsymbol{x} \in \mathbb{R}^n$, the output of the neuron reads

$$y = g\left(\boldsymbol{w} \cdot \boldsymbol{x} + b\right) \tag{2.74}$$

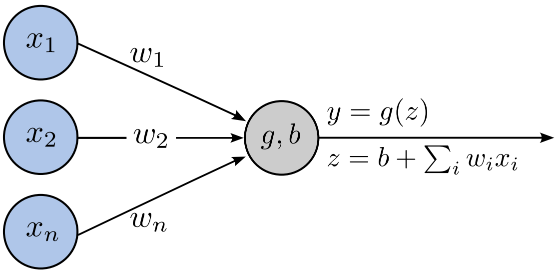

Figure 2.14 *Illustration of a neuron. Adapted from Chen (2022)*

where $g(\cdot)$ is the nonlinear function, $\boldsymbol{w}$ is a vector of weights with the same dimensions of $\boldsymbol{x}$ and b is called the bias and it is usually equals to unity. The nonlinear function is often called activation. Fig. (2.15) shows four of the most commonly employed activations: **(a)** the sigmoid, **(b)** the hyperbolic tangent (tanh), **(c)** the rectified linear unit (ReLU), **(d)** the swish function. An FCNN is composed of multiple layers of such neurons, each one connected to all the other neurons in the previous and in the following layer, as shown in Fig. (2.16). The input, hidden and output layers store input variables, intermediate outputs and quantity of interest, respectively.

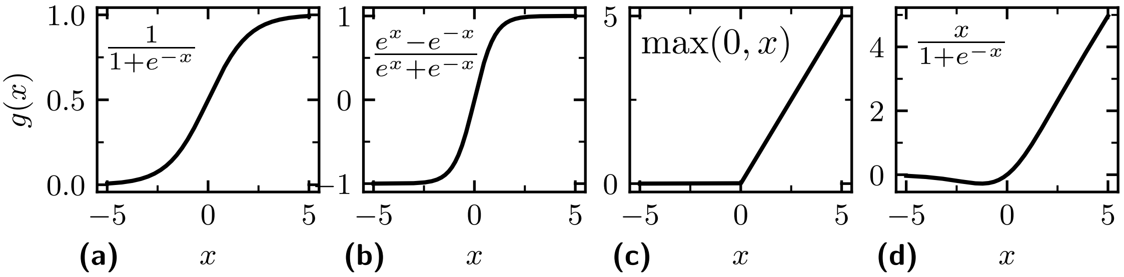

Figure 2.15 *Common activation units:* ***(a)*** *sigmoid,* ***(b)*** *hyperbolic tangent* (tanh)*,* ***(c)*** *rectified linear unit (ReLU) and* ***(d)*** *swish. Adapted from Chen (2022)*

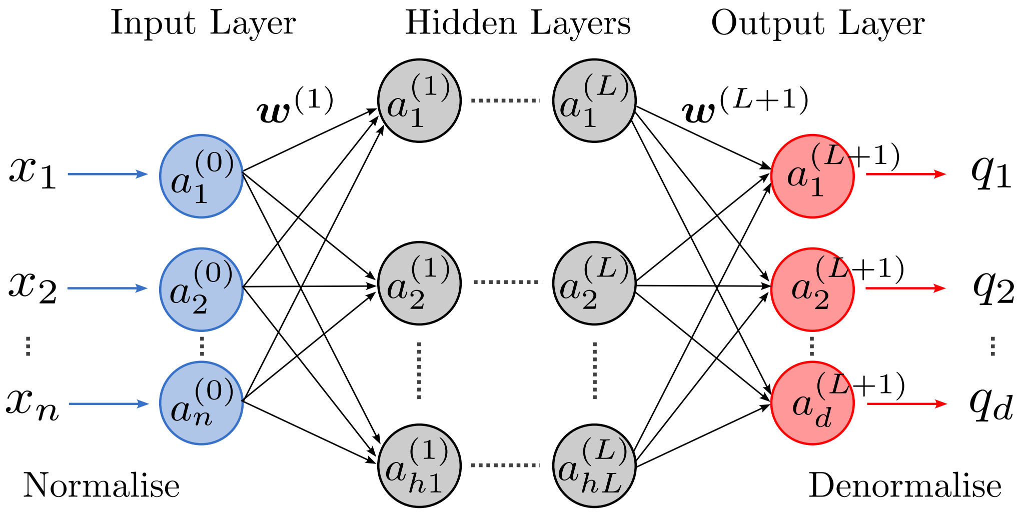

Figure 2.16 *Illustration of a fully connected neural network. Adapted from He et al. (2020).*

The inputs are usually normalised in a number of ways (min-max, standard scaling) depending on the activation function and are subsequently propagated forward through the network. The values at layer $(l+1)$ are therefore obtained from the previous layer as

$$\boldsymbol{a}^{(l+1)} = g(\boldsymbol{z}^{(l+1)}) = g(\boldsymbol{w}^{(l+1)} \cdot \boldsymbol{a}^{(l)} + \boldsymbol{b}^{(l+1)}) \tag{2.75}$$

where the symbols are the same as in Eq. (2.74), expect for $\boldsymbol{w}$ and $\boldsymbol{b}$ which are now a matrix and a vector of dimension $(h_{(l+1)} \times h_{(l)})$ and $(h_{(l+1)} \times 1)$ respectively, with h being the number of neurons at a given layer. Once the ouput layer is reached, the values are denormalised back to their original range, which is dependent on the training dataset.

The training of the FCNN relies on the concept of backpropagation. The FCNN solves an optimisation problem by iteratively updating the weights $\boldsymbol{w}$ that connect the neurons. These are initialised randomly and are updated by minimising the cost function J:

$$J(\boldsymbol{w}, \boldsymbol{b}) = \frac{1}{2m} \sum_{i=1}^{m} \|\boldsymbol{q}_i - \widehat{\boldsymbol{q}}_i\|^2 + \frac{\lambda}{2m} \sum_{l=1}^{L+1} (\boldsymbol{w}^{(l)})^2 \tag{2.76}$$

where $\|\cdot\|$ indicates the L2-norm, m is the number of training samples, $\boldsymbol{q}$, $\widehat{\boldsymbol{q}}$ are the quantity of interest and the prediction from the FCNN respectively, and λ is a regularisation factor that penalises large weights norm, thus avoiding overfitting. The gradient of the cost function is calculated as:

$$\begin{aligned}\frac{\partial J}{\partial \boldsymbol{w}^{(l)}} &= \frac{1}{m}\sum_{i=1}^{m}\Delta^{(l)}\cdot(\boldsymbol{a}^{(l-1)})^T + \frac{\lambda}{m}\boldsymbol{w}^{(l)} \\ \frac{\partial J}{\partial \boldsymbol{b}^{(l)}} &= \frac{1}{m}\sum_{i=1}^{m}\Delta^{(l)}\end{aligned} \tag{2.77}$$

where:

$$\Delta^{(l)} = \begin{cases}(\boldsymbol{a}^{(l)} - \widehat{\boldsymbol{a}}^{(l)})\cdot g'(\boldsymbol{z}^{(l)}), & l = L+1 \\ (\boldsymbol{w}^{(l+1)})^T\Delta^{(l+1)}\cdot g'(\boldsymbol{z}^{(l)}), & 1 \leq l \leq L\end{cases} \tag{2.78}$$

The choice of normalisation of input and outputs, activation function and optimiser used will be explained in the relevant Chapters (3, 5)

2.6.2 Random Forest

Random Forest (RF) (Breiman, 2001) is a supervised, ensemble learning algorithm employed in both classification and regression problems. RF is an ensemble of decision trees, which recursively split the data at each node of the tree until either a stop criterion is met, e.g. maximum tree depth, or all data points are sorted into leaf nodes. The splitting algorithm optimises a measure of accuracy depending on the task. In regression problems, decision trees minimise the mean squared error and make predictions by traversing the tree to find the corresponding leaf and taking the weighted mean of its values. RF works by randomly selecting a subset of features for each tree, thus preventing overfitting. A more detailed description is given in the relevant Chapter (6).

2.6.3 Model Explainability

Machine learning models, especially those based on complex algorithms and deep learning techniques, constitute a proverbial "black-box" and are usually difficult to understand. The interpretability of a model can be improved by either intrinsic or post-hoc methods (Molnar, 2022).

Intrinsic methods aim at improving interpretability by limiting the complexity of a machine learning model, under the assumption that simplicity of the model and ability to understand its output go hand in hand. By design, this assumption does not necessarily hold for a neural network, as even simple architectures provide results that can be hard to interpret.

On the other hand, reducing the number of input features is usually beneficial to model interpretation. A feature selection study would require a considerable computational cost when using a neural network, therefore the number of features in this work has been restricted based on physical considerations. Nevertheless, a small input feature space does not directly equate with interpretability, thus other methods are needed.

The post-hoc methodology refers to explanation techniques that are applied to existing models, rather than being incorporated into the development process. These methods can be model agnostic, such as a perturbation analysis, or model specific, such as the extraction of gradients from a neural network.

The model-agnostic explanation method named Shapley additive explanations (SHAP) (Lundberg and Lee, 2017) is used to explain the trained neural network model in this work. SHAP is based on Shapley values (Shapley, 1953), a method from coalition game theory, which states that a model prediction can be explained by framing the problem as the fair distribution of payouts to players of a game. In this work, the *game* is the prediction of the machine learnt model; the *players* are the input features; the *payouts* are the contributions of each input feature to the predicted y. SHAP aims at explaining the prediction of a data point, a so called instance $\boldsymbol{x}$, by calculating each feature's contribution to the overall prediction as a linear model, as shown below in Eq. (2.79)

$$y = g\left(\boldsymbol{x}\right) = \phi_0 + \sum_{j=0}^{M-1} \phi_j\left(\boldsymbol{x}\right) \tag{2.79}$$

where g is the model, M is the number of features or *maximum coalition size*, ϕ_j is the attribution for feature j and is referred to as the SHAP value, and $\phi_0 = \mathbb{E}(g(\boldsymbol{x}))$ is the expected value of the model prediction over a specified range of input features.

The calculation of the SHAP value ϕ_j for feature j considers the attribution from x_j itself plus the combinations between x_j and the remaining features

$$\begin{aligned} \phi_j(g, \boldsymbol{x}) &= \sum_{S \subseteq \mathcal{M} \setminus \{x_j\}} \frac{|S|!(|\mathcal{M}| - |S| - 1)!}{|\mathcal{M}|!} \left[g_x(S \cup \{x_j\}) - g_x(S)\right] \\ g_x(S) &= \mathbb{E}(g(x_k)|S) \end{aligned} \tag{2.80}$$

Eq. (2.80) shows the sum over all possible subsets S of input features, excluding feature value j; $|\cdot|$ denotes the number of elements in a set, e.g., $|\mathcal{M}| = M$; $|S|!$ and $(|\mathcal{M}| - |S| - 1)!$ are the permutations number of feature values appearing before and after j, respectively; $[g_x(S \cup \{x_j\}) - g_x(S)]$ is the marginal contribution of $\{x_j\}$ when added to the subset S and $\mathbb{E}(g(x_k)|S)$ is the conditional expectation of the model prediction, given the subset S. For neural network architectures, the method is implemented in the SHAP[1] library in PYTHON.

The SHAP value ϕ_j provides global and local sensitivities for the model. The global significance of each input feature is ranked by the mean SHAP value $|\phi_j|$.

---

[1] https://github.com/slundberg/shap

2.7 Summary

In this Chapter, the computational methods and machine learning algorithms necessary to build a data-driven model have been discussed.

The training data will be obtained from a time-linearised flow solver, and the figures of merit, aerodynamic damping and/or unsteady forces, are computed under the assumption that the blades vibrate in a prescribed modeshape, which is not influenced by the aerodynamic loads, and with a constant phase shift between them. This is commonly known as energy method (Carta, 1967). This choice of computational methods is advantageous because: 1) it can produce results much quicker than time-accurate methods and 2) it is able to capture asymptotic stability, which is sufficient for the design stage this work is targeting.

The main test case of this work has been introduced. The choice of a two-dimensional geometry preserves most of the driving physics of flutter apart from two effects: three-dimensional flow profiles, and consequent radial migration, and presence of radial acoustic modes in the duct. Although relevant, these are not considered essential at this stage, allowing us to develop the data-driven modelling framework incrementally, starting from a simplified problem.

The machine learning algorithms employed in this thesis have been presented. These have been chosen for their ease of use and the relatively low computational cost associated with their training (only small neural networks will be considered).

Chapter 3

Neural Network Model

The contents of this chapter have been published in Rauseo et al. (2021).

3.1 Introduction

This chapter presents the first effort in predicting aerodynamic damping for a vibrating compressor cascade using machine learning techniques. As such, no attempt at generalisation will be made yet, and this study will simply serve as an experiment to evaluate the feasibility of the data-driven approach we are seeking. Tackling the interpolation problem first will give us an estimate of the database sizes needed to have a model that can compute aerodynamic damping to an acceptable degree of accuracy, providing the necessary stepping stone needed to build more complicated models.

3.2 Training Geometry

The test case is the Standard Configuration 10, illustrated in Section (2.5).

3.3 Input Features

The input features chosen for this purely data-driven model are quite simple, as their only purpose is to clearly define a point in the sample space. Thus, five independent quantities are selected: inlet Mach number, M_1 and incidence angle, β_1, define the steady operating conditions, while reduced frequency k, interblade phase angle, σ and modeshape define the unsteady boundary conditions.

β_1 is imposed as boundary condition, M_1 is varied by changing the pressure ratio across the cascade, k is imposed in the unsteady solver which, in turn, calculates the correct structural frequency using the steady state inlet flow velocity as reference. σ is specified in degrees and imposed as phase lag at the passage interfaces in the unsteady solver. The modeshape requires a concise discussion.

When it comes to stall flutter, we are mainly interested in the first flap-wise bending mode 1F (see Table 1.1). A flap mode is a combination of a pure plunging motion, orthogonal to the chord line, and a pure pitching motion about an axis. In the case of a fan blade it is convenient to define the pitching axis at mid-chord, and the corresponding pitching mode is referred to as torsion (1T). Vahdati and Cumpsty (2015) showed that the amount of pitching in a flap mode is highly influential for stability and define a parameter named α to control the pitch-to-plunge ratio:

$$\alpha = 2\frac{\|\boldsymbol{X}_{LE}\| - \|\boldsymbol{X}_{TE}\|}{\|\boldsymbol{X}_{LE}\| + \|\boldsymbol{X}_{TE}\|} \tag{3.1}$$

where $\boldsymbol{X}_{LE}$, $\boldsymbol{X}_{TE}$ are signed leading and trailing edge displacements, respectively and $\| \cdot \|$ indicates the L2-norm. In this work, the pitch-to-plunge ratio is controlled by keeping a fixed leading edge displacement, while changing the parameter X_t, defined as a slight modification of α :

$$X_t = \frac{\|\boldsymbol{X}_{LE} + \boldsymbol{X}_{TE}\|}{\|\boldsymbol{X}_{LE} - \boldsymbol{X}_{TE}\|} \tag{3.2}$$

The limiting cases are pure torsion with $X_t = 0$ and pure plunge with $X_t \to \infty$ ($\boldsymbol{X}_{LE} \to \boldsymbol{X}_{TE}$); all other cases, i.e., $X_t \in (0, \infty)$, are referred to as flap mode. The case of $X_t < 0$ is ignored as it is not relevant for fan and compressor flutter. The effect of increasing X_t is, essentially, to move the pitching axis further downstream from the blade, e.g. $X_t = 2$ locates the pitching axis half a chord away from the trailing edge; therefore, decreasing the pitching component of the modeshape. Fig. (3.1) shows a schematic illustration of the effect of increasing X_t.

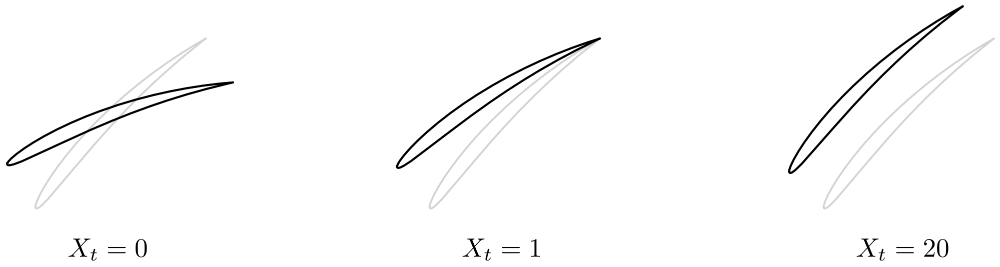

Figure 3.1 *Schematic illustration of modeshape at different X_t.*

The choice of defining a new parameter to control the modeshape, as opposed to Vahdati and Cumpsty (2015), is due to the fact that the parameter α does not behave monotonically with the location of the pitching axis, presenting a cusp when the axis is located at the trailing edge, i.e. $x/c = 1$. Although this is perfectly fine for analysis, such a behaviour is ill-suited for an input parameter to an ML model, as two different modeshapes can exhibit same values of α. On the other hand, X_t simply scales linearly with the picthing axis location. Fig. (3.2) shows the behaviour of the two parameters as a function of the chordwise pitching axis location.

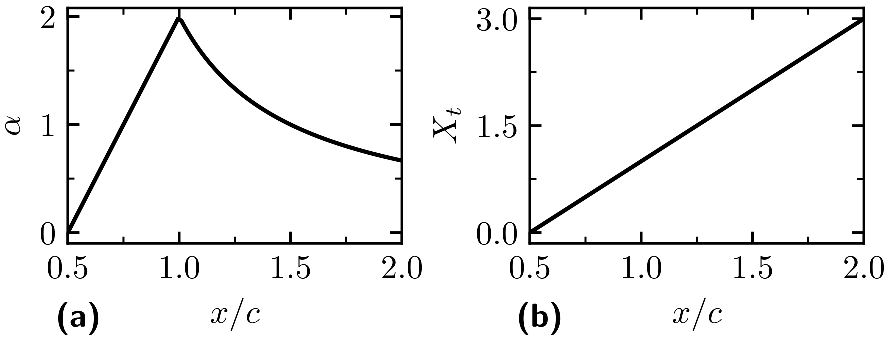

Figure 3.2 *Illustration of the difference between parameters that control the plunge-pitch ratio of a flap mode as a function of the chordwise location of pitching axis:* ***(a)*** *α as defined by Vahdati and Cumpsty (2015);* ***(b)*** *X_t defined in this work*

3.4 Databases of Aerodynamic Damping

Having selected the input parameters, the next step is to decide the intervals in which these parameters will vary. The range for inlet Mach number is chosen to be symmetric about the nominal value of 0.7, to study both subsonic flow, where no shock appears, and transonic flow conditions, where a shock is present on the suction side. M_1, thus, changes between 0.5, anything lower is discarded as excessively low speed, and 0.9, so that the shock stays on the suction side and does not move too far upstream. The incidence of incoming flow onto the blade is varied between $0°$ and $6°$, which is the largest value before inception of stall for all the Mach numbers studied in this work. This choice of intervals for the steady state variables is, once again, based on the literature shown in Table (1.1).

The interblade phase angle σ ranges from $-180°$ to $180°$; the extremes are the same point, although no special treatment has been specified for them in the training phase of the surrogate model. In practice, the combination of reduced frequency and modeshape is not arbitrary: the same blade will be characterised by very different reduced frequencies whether it is vibrating in a pure torsion or in a flap mode. Moreover, this combination also depends on the machine being considered: the flap mode of a fan blade will have a lower reduced frequency (Rendu, 2016; Stapelfeldt and Vahdati, 2018) compared to an embedded compressor blade (Zhao et al., 2016). Nevertheless, to cover the whole spectrum of combinations, modeshape and frequency in this study are assumed to be independent from each other during training of the surrogate model and, therefore, take large intervals. Table (3.1) summarises the space of input variables.

Table 3.1 *Intervals of design parameters.*

Parameter		**Min**	**Max**
Inlet Mach Number	M_1	0.5	0.9
Incidence	β_1	0°	$+6^\circ$
Reduced Frequency	k	0.4	1.5
Plunge-pitch ratio	X_t	0.0	4.0
Interblade Phase Angle	σ	-180°	180°

The Latin Hypercube sampling method (McKay et al., 1979) is applied to generate five independent databases of input parameters within the range in Table (3.1): this approach ensures a uniform distribution of samples in the space of interest and that arbitrary samples from different databases are mutually independent. The databases have size 128, 256, 512, 1024, 2048, and are referred to as db1 to db5. Each input sample corresponds to a set of computations, steady and unsteady, of the time-linearised solver outlined in Chapter (2). The quantity of interest (QoI) of the computations will be the aerodynamic damping paramter ζ.

3.5 Surrogate Model

The fully connected neural network (FCNN) is used as a surrogate model of the CFD solver. The FCNN is composed of multiple layers of nonlinear activation units called neurons. The input, hidden and output layers store input variables, intermediate outputs and quantity of interest, respectively. The vector of input variables $\boldsymbol{x}$ and quantity of interest $\boldsymbol{q}$ are defined below

$$\begin{aligned} \boldsymbol{x} &= [M_1, \beta_1, k, X_t, \sigma] \\ \boldsymbol{q} &= \zeta \end{aligned} \tag{3.3}$$

The rest of this section introduces the training strategy employed.

3.5.1 Forward Propagation

The input variables are normalised by their maximum and minimum and then rescaled in the range $\{-1, 1\}$:

$$\boldsymbol{a}_i^{(0)} = 2\frac{\boldsymbol{x}_i - \min(\boldsymbol{x}_i)}{\max(\boldsymbol{x}_i) - \min(\boldsymbol{x}_i)} - 1 \tag{3.4}$$

where $\boldsymbol{x}_i$ is the vector of input variable i, with dimension m, where m is the number of samples. The outputs at intermediate layers are propagated as below:

$$\boldsymbol{a}^{(l+1)} = g(\boldsymbol{z}^{(l+1)}) = g(\boldsymbol{w}^{(l+1)}\boldsymbol{a}^{(l)} + \boldsymbol{b}^{(l+1)}) \tag{3.5}$$

where $\boldsymbol{w}$ is the weights matrix, $\boldsymbol{b}$ is the bias vector and $g(\cdot)$ is the activation function, all already discussed in Chapter (2). The function $g(x) = A \cdot \tanh(Hx)$ with $A = 1.7159$ and $H = \frac{2}{3}$ is a scaled hyperbolic tangent as proposed by Lecun (1989). The results at the output layer $(L + 1)$ are then denormalised to yield the quantity of interest:

$$\widehat{\boldsymbol{q}} = (\max(\boldsymbol{q}) - \min(\boldsymbol{q})) \cdot \frac{\boldsymbol{a}^{(L+1)} + A}{2A} + \min(\boldsymbol{q}) \tag{3.6}$$

The min-max normalisation of the aerodynamic damping is symmetric with respect to zero so that $\widehat{q}/|\widehat{q}| = \zeta/|\zeta|$, i.e., negative $\widehat{q}$ (output of FCNN) corresponds to negative aerodynamic damping. Lastly, the accuracy of FCNN predictions is measured by the relative error on the test database:

$$\epsilon = \frac{1}{m} \sum_{j=1}^{m} \frac{|q_j - \widehat{q}_j|}{\max(\boldsymbol{q}) - \min(\boldsymbol{q})} \tag{3.7}$$

3.5.2 Backpropagation

The mean squared error cost function J (see Eq. (2.76)) is used at the core of the optimisation problem. The weights are updated through iterations, by minimising $J(\boldsymbol{w}, \boldsymbol{b})$. The optimiser employed to perform this task is BFGS (Fletcher, 1987). The gradient of the cost function is shown in Eq. (2.77).

3.5.3 Hyperparameters Tuning

The weights determined in the optimisation process are influenced by multiple parameters, the hyperparameters, namely number of layers L and number of neurons per layer N_L, training database size and regularisation factor λ.

First, a training database independence study is carried out, using 5 different combinations of databases summarised in Table (3.2). The training/test split is kept constant at 80/20 for all the combinations. The gradient-based optimisation can lead to local minima of the cost function, therefore, 16 networks with different initial conditions and randomly reshuffled datasets are trained in parallel. A baseline FCNN with $L = 2$, $N_L = 12$ and $\lambda = 10^{-4}$ will be used for this study.

The mean difference between test and training error $(\epsilon_{\text{te}}, \epsilon_{\text{tr}})$ is shown in Fig. (3.3a). The error bars show ±1 standard deviation from the mean value. As the training database size increases, the difference between the test and training errors reduces to nearly zero, and thus, the accuracy of the FCNN becomes independent of the training database size. Moreover, the error bar size also converges to zero when all the datasets are used, indicating independence from initial conditions. The rest of the hyperparameters study is carried out using all data, with the training/test split discussed above. For completeness, the value of test and training errors separately is

Table 3.2 *Data for training database independence study*

Data	Total Size	Training Data	Test Data	Trained FCNNs
db1 ∪ db2	384	80%	20%	16
db2 ∪ db3	768	80%	20%	16
db3 ∪ db4	1536	80%	20%	16
db4 ∪ db5	3072	80%	20%	16
All dbs	3968	80%	20%	16

shown in Fig. (3.3b). Both errors converge, albeit to a value of $\epsilon \approx 2\%$, which will be improved upon by tuning the hyperparameters.

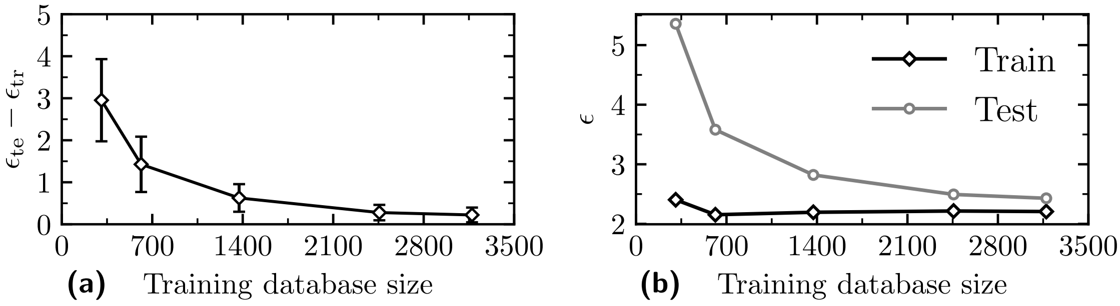

Figure 3.3 *Training database independence study: **(a)** Difference between test and training error; **(b)** Test and training errors*

As for finding the hyperparameters, a full factorial or grid search approach is followed. The grid search exhaustively considers all parameter combinations, from the variability specified in Table (3.3). In total, 1485 combinations are tested.

Table 3.3 *Hyperparameters range*

	Min	Max	Samples
L	1	15	15
N_L	2	12	11
$\log_{10}(\lambda)$	-6	2	9
Total			1485

Fig. (3.4a) shows the test percentage error against the logarithm of the regularisation parameter λ, for different numbers of hidden layers L, each containing $N_L = 12$ neurons. We can see that, a large value of λ applies too much regularisation and causes the FCNN to learn poorly. The error quickly diminishes with a decrease in λ and stays nearly constant with $\lambda \leq 10^{-2}$. Fig. (3.4b) shows the test percentage error against the number of layers, for different N_L, with $\lambda \leq 10^{-4}$. The plot shows that increasing the number of layers is beneficial until an asymptote is reached, e.g. with $N_L = 12$, the error stops decreasing at $L \approx 9$. It is also shown that, increasing the number of neurons is beneficial in the investigate range, apart for $N_L = 4$.

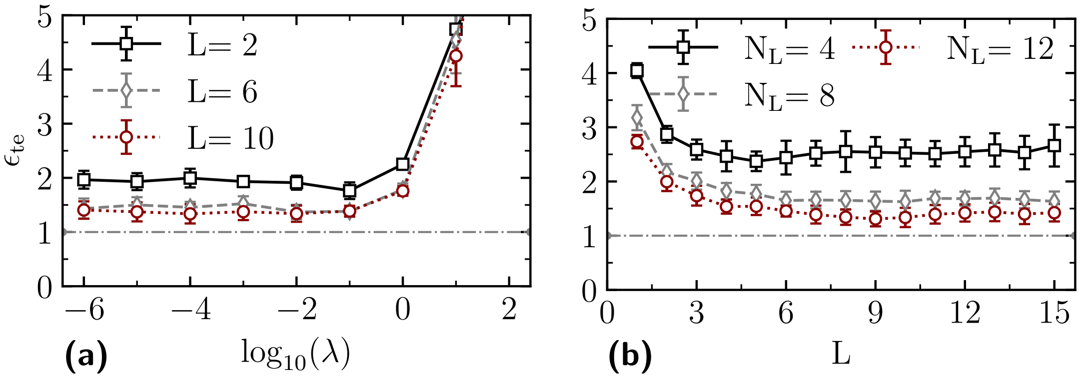

Figure 3.4 *Test percentage error as a function of:* ***(a)*** *regularisation parameter λ,* ***(b)*** *number of hidden layers L*

The effect of increasing number of neurons and hidden layers can be represented by a single variable, that is the number of connections or weights W

$$W = (I + 1) \times N_L + (N_L + 1) \times N_L \times (L - 1) + (N_L + 1) \times O \tag{3.8}$$

where I and O are input and output dimensions, respectively. Fig. (3.5) depicts the error as a function of W. Each scatter point represents the results from a grid search sample, while the solid line is a polynomial least square fit of the data. The plot shows that, irrespective of how the number of connections is changed, the prediction error plateaus at $\epsilon \approx 1\%$ for $W \geq 10^3$.

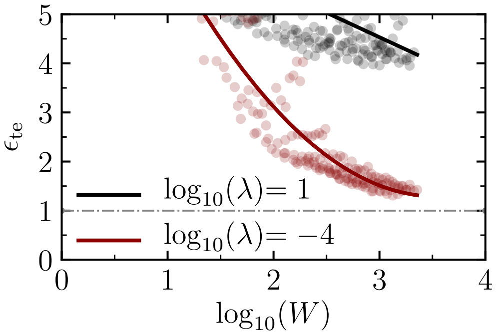

Figure 3.5 *Test percentage error as a function of W, number of connections in the FCNN*

This is true for the current case because, once the network becomes deep enough, there is little change in performance with an increasing number of layers or neurons.

Normally, the variable W is employed by keeping one of the parameters fixed (see for example Belkin et al. (2019)). The FCNN employed in the rest of this work is, therefore, characterised by the following hyperparameters: $N_L = 12$, $L = 10$, $\lambda = 10^{-4}$.

Fig. (3.6a) shows normalised aerodynamic damping from CFD and FCNN: good agreement is achieved between the two methods, with only minor differences especially for values far from zero damping.

It is also interesting to setup an equivalent classification problem, i.e. rather than evaluating the capability of the FCNN to predict damping directly, we investigate whether the machine learnt model is able to predict instability, irrespective of the precise value. In order to do so, a confusion matrix is built in Fig. (3.6b). The four quadrants show, starting from top right and going anti-clockwise: true positive samples (stable in CFD and FCNN), false positives (unstable in CFD and stable in FCNN), true negatives (unstable in CFD and FCNN) and false negatives (stable in CFD and unstable in FCNN). The quadrants are coloured according to the number of samples in that group, and the classification accuracy for each group is also reported.

By examining the bottom row of the matrix, we see that the FCNN classifies the samples correctly for the large part, with circa 92% of the samples the FCNN predicts to be unstable being actually unstable, while the remaining 8% are misclassified. The top row shows a similar results, with circa 98% of the samples the FCNN predicts to be stable being actually stable, while the remaining 2% are misclassified. This number of false positives, although small, is of most interest and should be reduced as much as possible.

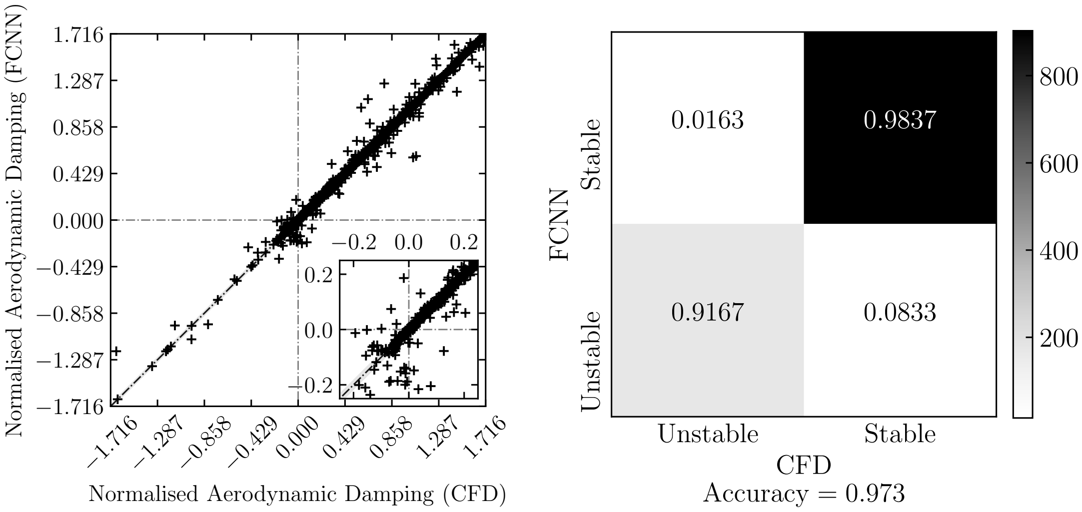

(a) *Scatter plot of CFD data points and FCNN predictions*

(b) *Confusion matrix for equivalent classification problem*

Figure 3.6 *Evaluation of FCNN predictive capabilities*

3.6 Comparison with CFD

The following results show a comparison between FCNN and CFD predictions. Four cases are setup to demonstrate the capability of the FCNN: 4 out of 5 input variables are fixed while the remaining one is swept. The CFD computations employed in this comparison do not explicitly coincide with any training sample, they will therefore represent a further, and final, test to evaluate the machine learnt surrogate model. The combination of parameters for the four comparisons are reported in Table (3.4). These conditions still constitute an interpolation within the training range. The results in Fig. (3.7) show good agreement between FCNN and CFD, quantified by the relative percentage error in Table (3.4).

Table 3.4 *Input parameters for FCNN sweep test. Relative percentage error of FCNN predictions is computed against CFD data.*

	$\mathbf{M_1}$	β_1	**k**	$\mathbf{X_t}$	σ	ϵ %
Case 1	0.8	Sweep	0.5	3.0	20°	4.5
Case 2	0.55	+5°	Sweep	1.5	20°	4.1
Case 3	0.7	+6°	0.7	Sweep	0°	2.3
Case 4	0.55	+5°	0.5	1.0	Sweep	1.8

Fig. (3.7a) shows that for a blade vibrating in flap mode, in transonic flow, aerodynamic damping decreases with increasing flow incidence. The flow conditions for this case are very similar to what a fan blade section would experience as it moves up a constant speed characteristic. This behaviour has been already reported in the literature (Vahdati and Cumpsty, 2015). The FCNN is able to follow the trend of the CFD closely, and to predict the flutter boundary within 0.2°, confirming that its predictions can be trusted for engineering-relevant cases.

Fig. (3.7b) shows a reduced frequency sweep; at these flow conditions and with the given interblade phase angle, the upstream and downstream cut-off frequencies are 0.230 and 0.408, respectively. As the frequency of vibration is increased, the unsteady pressure fields upstream and downstream of the blade change from cut-on to cut-off. The frequencies at which this change takes place are the cut-off frequencies and their crossing is associated with a strong change in aerodynamic damping. The crossing in Fig. (3.7b) takes place at $k = 0.408$ and is visible by the drop in aerodynamic damping. The behaviour of aerodamping with frequency is not monotonic. If we consider aerodynamic damping as a function of σ, it is known from Corral and Vega (2016) that an increase in frequency results in an increase in mean damping value and in a shift of the damping curves; therefore, since we are plotting damping against frequency at fixed IBPA, the combination of both effects results into the behaviour shown in Fig. (3.7b). The surrogate model captures the overall trend as well as the crossing of the zero damping line.

Fig. (3.7c) shows a sweep of X_t; as the modeshape approaches a pure plunge (increasing X_t), the aerodynamic damping increases, in agreement with the literature. The minimum damping, which is negative in this case, is attained at $X_t = 1$, which corresponds to a mode with pitching axis at the trailing edge. The FCNN is, again, able to follow the CFD closely (see Table 3.4).

The peak in aerodynamic damping due to acoustic resonance in Fig. (3.7d) is well predicted, both in location ($\sigma \approx 40^\circ$) and magnitude, and so is the overall shape of the curve. The negative damping, thus flutter, is predicted correctly as well.

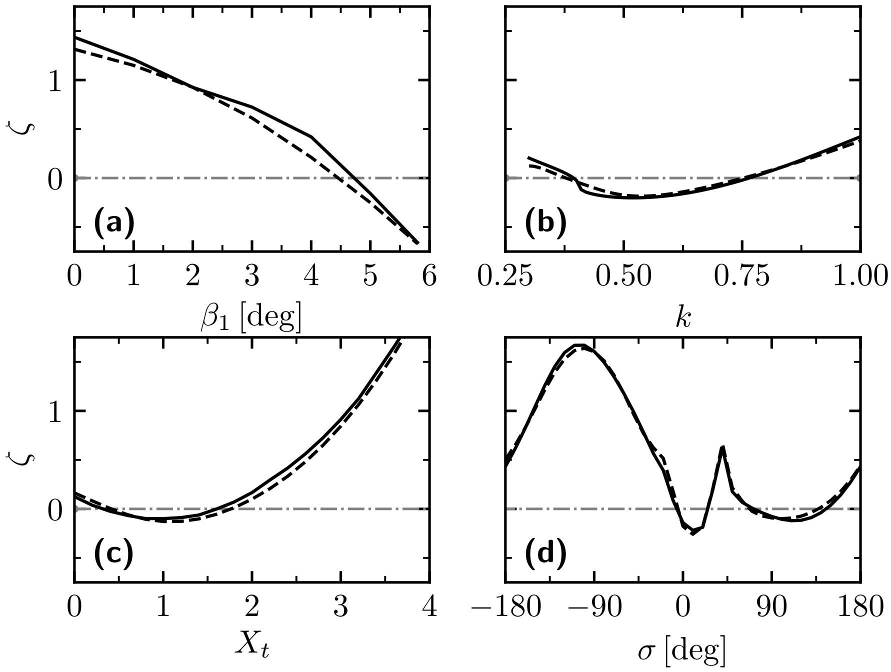

Figure 3.7 *Comparison of FCNN (- - -) and CFD (—) aerodamping predictions for the conditions listed in Table (3.4). **(a)** Case 1: Incidence sweep; **(b)** Case 2: Reduced Frequency sweep; **(c)** Case 3: Plunge-pitch ratio sweep; **(d)** Case 4: Interblade Phase Angle sweep*

The results discussed above show that the FCNN is able to correctly predict aerodynamic damping across a range of flow conditions and structural parameters. Moreover, the surrogate model captures the zero damping crossing point (flutter boundary). In the next section, an example of how the method can be used in a design environment is given.

3.7 Application to Blade Redesign

In this section, the application of the surrogate model to a hypothetical engineering problem is addressed. During the early design stage of a turbomachinery blade, the surrogate model can be used to produce aerodynamic damping predictions of numerous design samples at low cost. Ideally, expensive numerical simulations should only be needed at certain critical operating points (such as design point) and regions where negative aerodynamic damping is predicted by the surrogate model. In the case where flutter is predicted for an aerodynamically optimised blade, even at the cost of reducing aerodynamic performance, the design parameters need to be adjusted to increase damping and regain stability. Under the assumption that a mechanical solution (e.g., introduction of under-platform dampers) is either not convenient or not possible at all (e.g., the blade is part of a blisk), the most viable solution is to increase aerodynamic damping. Traditional wisdom suggests that, for example, increasing reduced frequency is beneficial for aeroelastic stability. However, this generalisation has been shown to achieve mixed results in real applications (see Fig. (3.7b)). Therefore, there is a need for tools which can provide guidelines for blade re-design or optimisation to improve aerodynamic damping.

The surrogate model $\boldsymbol{S}$ is a nonlinear function which given an input $x \in \mathbb{R}^d$ outputs $\widehat{q} \in \mathbb{R}^m$; the Jacobian of the outputs with respect to input is:

$$J_{ij}(x) = \frac{\partial S_i(x)}{\partial x_j} = \nabla S_i(x) \tag{3.9}$$

The value of $\nabla S_i(x)$ will give a measure of how sensitive the output i is to the input j in the vicinity of x. In order to have a comparison between the inputs and across different locations of the sample space, the gradient is normalised by its magnitude $|\nabla S_i(x)|$, yielding the normalised gradient. By extracting this quantity, we can investigate the local sensitivity of aerodynamic damping to the input design parameters, thus having a clear guide as to what actions can be taken to affect stability.

Take a blade behaving like Fig. (3.7d) as test case. The flow field of such a case, in terms of Mach number contour and isentropic Mach number on the blade, is shown in Fig. (3.8).

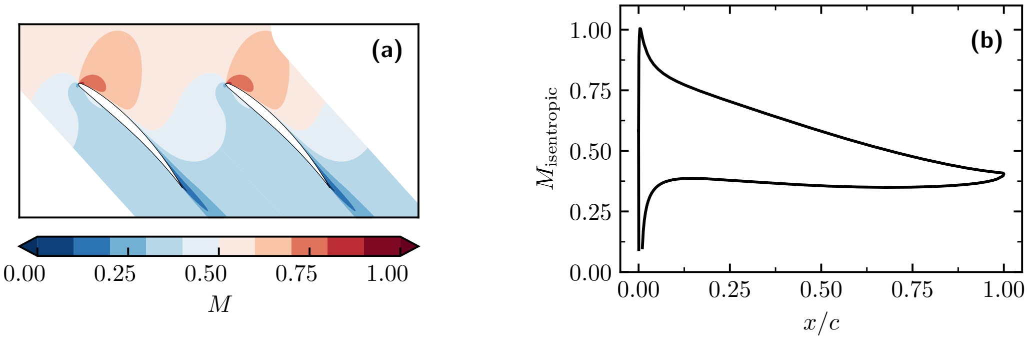

Figure 3.8 *Mean flow field of application test case: **(a)** Mach Number contour; **(b)** Isentropic Mach Number on the blade*

Two intervals of σ are predicted to flutter: 0° to 30° and 60° to 140°. The objective is to adjust the design parameters so that instability can be avoided. In order to achieve this goal, one can compute the normalised gradients (Eq. (3.9)), and use them as a guide for deciding the best action to take in order to increase damping in an unstable configuration.

The normalised gradients at $\sigma = 20°$ and $\sigma = 120°$ are shown in Fig. (3.9). The bar height, value of normalised gradient, is a measure of aerodynamic damping sensitivity, while the sign on top gives the type of correlation between input and output, i.e., a $(+)$ sign indicates that an increase in input variable results in greater aerodynamic damping. The most important parameter in both cases of Fig. (3.9) is β_1 which is negatively correlated with damping. M_1 is important for $\sigma = 20°$ but exerts negligible influence at $\sigma = 120°$. The influence of k diminishes from $\sigma = 120°$ to $\sigma = 20°$, and, most importantly, the nature of its correlation with aerodynamic damping is opposite between the two cases; i.e., an increment in k is beneficial at $\sigma = 120°$ but detrimental at $\sigma = 20°$. Finally, X_t shows the same behaviour as k.

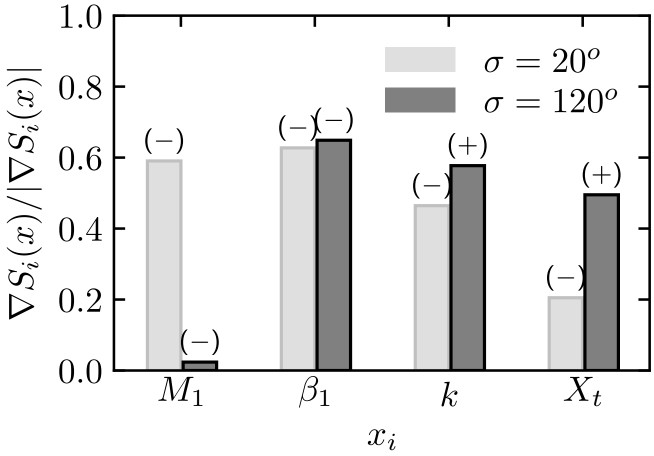

Figure 3.9 *Normalised gradients for Case 4 at* $\sigma = 20°$ *and* $\sigma = 120°$*.*

The previous considerations lead to the conclusion that, varying only one parameter, the most effective action one can take (for both IBPAs) is to reduce the incidence of incoming flow onto the blade (e.g., restaggering the blade). The change in aerodynamic damping due to variation in incidence angle and reduced frequency is shown in Fig. (3.10). The predictions are results from the surrogate model. As expected, a reduction in incidence angle is beneficial for both IBPAs (see Fig. (3.10a)).

In particular, a decrease of 0.3° is sufficient to stabilise $\sigma = 120°$, whereas a reduction of 1.8° is necessary to stabilise $\sigma = 20°$. Fig. (3.10b) confirms the contradicting behaviour of aerodynamic damping with respect to reduced frequency for the two cases:

an increase in k leads to a more stable blade at $\sigma = 120°$, but aggravates the instability at $\sigma = 20°$ in the vicinity of the design point. The method also provides an "exchange rate" between different parameters so that the designer can make the best choice for improving flutter margin. For example, in Fig. (3.10) for $\sigma = 120°$, a decrease of 0.3° in incidence is equivalent to an increase of, roughly, 0.06 in reduced frequency for eradicating flutter.

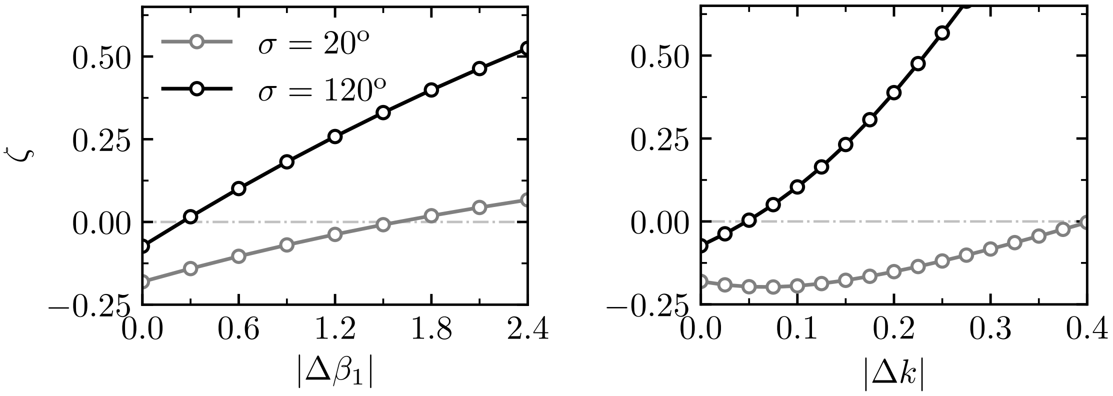

(a) *Decreasing incidence* **(b)** *Increasing reduced frequency*

Figure 3.10 *Change in aerodynamic damping at $\sigma = 20°$ and $\sigma = 120°$.*

In summary, the surrogate model predicts that a decrease of 1.8° in flow incidence should stabilise the blade at both $\sigma = 20°$ and $\sigma = 120°$. To verify this claim, a "restaggered" case is setup, where the inflow angle is kept constant and the incidence is reduced by restaggering the blade by 1.8°. The other parameters are kept constant. The aerodynamic damping predicted by the CFD is shown in Fig. (3.11). As anticipated by the surrogate model, $\sigma = 120°$ becomes highly stable while the point at $\sigma = 20°$ sits just above the zero damping line.

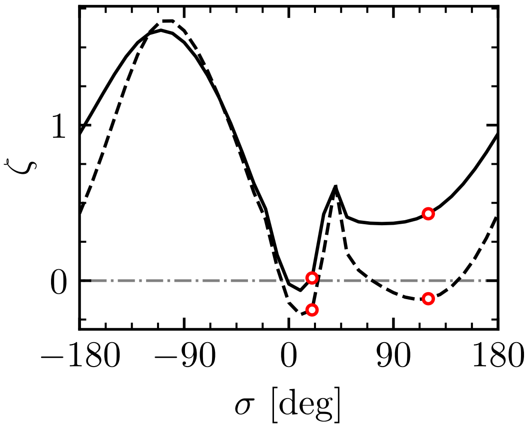

Figure 3.11 *CFD prediction of damping for original (- - -) and restaggered (—) blade*

At this point, one can see that flutter is still predicted for two interblade phase angles $\sigma = 0°$ and $\sigma = 10°$. Therefore the process is repeated to stabilise these conditions. The gradients are shown in Fig. (3.12). We see that inlet Mach number is negatively correlated with damping at $\sigma = 10°$, but exerts no effect at $\sigma = 0°$; the change in modeshape is irrelevant for this condition and a reduction in torsion component, i.e. increase in X_t produces essentially no effect at both interblade phase angles. Again, there is strong correlation with both the incidence of incoming flow and reduced frequency.

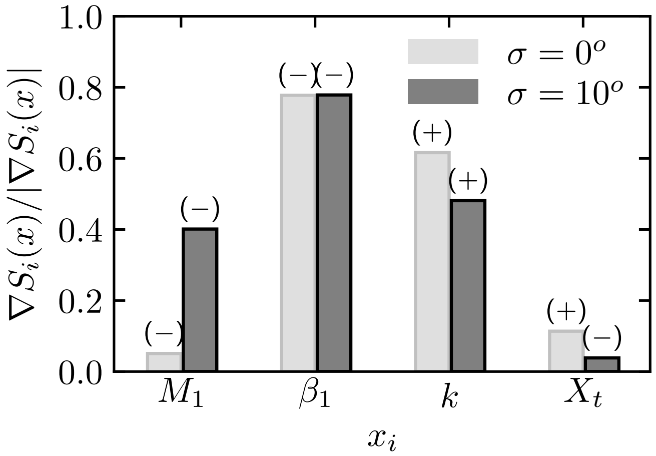

Figure 3.12 *Normalised gradients after restaggering, at $\sigma = 0°$ and $\sigma = 10°$.*

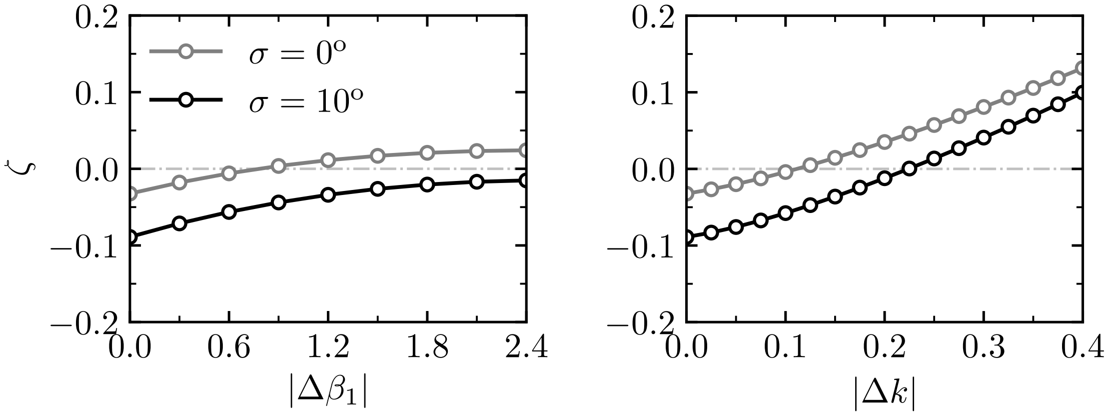

(a) *Decreasing incidence* **(b)** *Increasing reduced frequency*

Figure 3.13 *Change in aerodynamic damping for restaggered blade at $\sigma = 0°$ and $\sigma = 10°$.*

It can be seen from Fig. (3.13), that a large change in flow incidence, $|\Delta\beta_1| = 2.4°$ is still not sufficient to stabilise the point at $\sigma = 10°$ and even if it did, it is important to remember that for small amount of restaggering, no great effect is exerted on the behaviour of the cascade, but with large changes, not only the aerodynamics of the passage would be altered significantly, but also the duct acoustics, as the metal and flow angles are now different. The resulting cascade would depart significantly from the original geometry, thus breaking the assumptions for the validity of the model. Fig. (3.13b) thus shows that the only viable route to stabilise both IBPAs is an increase in reduced frequency.

The resulting cascade is modelled in CFD, and the aerodynamic damping coefficient in shown in Fig. (3.14). Again, the CFD confirms with the predictions from the FCNN and the whole IBPA range is now stable.

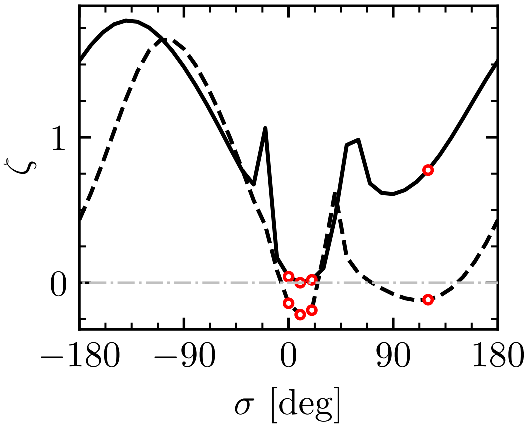

Figure 3.14 *CFD prediction of damping for original (- - -) and final (—) blade*

3.8 Summary

A first attempt at modelling aerodynamic damping in a compressor cascade with an FCNN has been made.

The surrogate model has been trained on results from a linearised aeroelastic solver and its validity has been tested through evaluation of relative errors. The training data concern flap modes, with different interblade phase angles, across a range of reduced frequencies, and flow conditions. The trained FCNN shows good prediction accuracy for aerodynamic damping when compared with CFD. To explore additional potential engineering applications of the surrogate model, it is shown that the sensitivity analysis, i.e. extraction of FCNN gradients, can be used as a guide to take appropriate measures to stabilise unstable operating points, thus provinding an application for this simple model. Although promising, the results in this Chapter are obtained with a simple artificial neural network that has no knowledge of the flow physics in turbomachinery.

This characteristic limits the validity of the model to the geometry used in the training phase.

In the next Chapter, we will examine the landscape of analytical reduced order models for the aeroelastic response of turbomachinery, in order to start building a data-driven model with integrated physical knowledge that can generalise to unseen geometries.

Chapter 4

Analytical Methods for the Aeroelastic Response of Cascades

4.1 Introduction

The model introduced in the previous chapter has no knowledge of the physical phenomenon it makes predictions for. The chosen input features were not particularly meaningful and merely served to define a point in the design space. For example, we could have employed mass flow rate and pressure ratio, rather than incidence and inlet Mach number, to define a steady operating condition without harming the performance of the FCNN. This kind of agnostic learning is a necessary stepping stone to build more complicated models, but the resulting machine learnt models are not useful when it comes to generalisation. These models are capable of very accurate predictions for a very limited amount of test cases.

On the other end of the spectrum, we find analytical and semi-analytical models. They are solely based on theory and physical understanding, and while they are applicable to a wide variety of test cases, they often involve stringent assumptions that limit the accuracy of their predictions. Having previously shown a solely data-driven approach, we now examine a number of theories in decreasing order of complexity (compared to solving the linearised Navier-Stokes equations), and investigate the capabilities of the most widely used reduced order model for the aeroelastic response of turbomachinery cascades.

The Euler equations model most of the important features for compressor flutter and give quite accurate results for well behaved flows. However, the computational methods required to solve the set of equations set them apart from analytical and semi-analytical methods.

Atassi and Akai (1980) developed a model to calculate unsteady forces and moments on the blade, that accounts fully for the geometry of the airfoil and cascade. The model is, though, only valid for incompressible flow, and the results in the original paper contain mistakes according to Whitehead (1987, p. 3.18). Moreover, there are no validation studies and the model just seems to have been shelved by the wider community.

The only truly widespread reduced order model for the aeroelastic response of turbomachinery cascades is the linearised subsonic, inviscid theory developed by Whitehead (1972), later implemented in the code LINSUB. The derivation of the theory is quite lengthy, therefore only a brief summary of the main assumptions and equations of the model is given here, though a full account can be found in Whitehead (1987, Chapter 3).

It will be shown in Chapter (5) that reduced order models can be employed to enhance the prediction capabilities of data-driven models. Considering our target accuracy and application, LINSUB constitutes an appropriate candidate due to its computational efficiency and capability of taking into account important factors for flutter, such as the cascade geometry and compressibility.

4.2 Linearised Subsonic Unsteady Flow in Cascades

The method implemented in LINSUB is based on a theory for linearised, subsonic, unsteady flow through an infinite cascade of two-dimensional flat plates. The cascade, pictured in Fig. (4.1), is defined by a chord length c, stagger angle χ, blade spacing s, inlet Mach number M, inlet flow velocity U_∞, and operates at zero incidence. The general assumptions are listed below:

- The flow is subsonic, irrotational and isentropic.
- The fluid is inviscid and the Kutta-Joukowski condition at the trailing edges of the blades is satisfied.
- The cascade is two-dimensional, therefore bending modes are represented by a translation orthogonal to the chord, while torsional or pitching modes by a rigid body rotation about a known axis. The axis is assumed to be located at the leading edge. Motion parallel to the chord line is neglected.
- The blades are not stalled, thus the flow always follows the airfoil surface.
- The blades are flat plates, so that camber and thickness effects are neglected.
- The mean incidence is zero, so that there is no steady blade loading and the flow passes through the cascade undeflected.
- The amplitude of perturbations from the uniform mean flow are assumed to be small, therefore the governing equations are linearised and the principle of

superposition can be applied to the solutions obtained. It also follows that the wakes of the blades, which are vortex sheets whose strength varies sinusoidally with distance from the trailing edge, can be taken to be straight.

- All events occurring on the blades are identical, except for a constant phase shift σ between each blade and its neighbours.
- All time varying events are harmonic with angular frequency ω

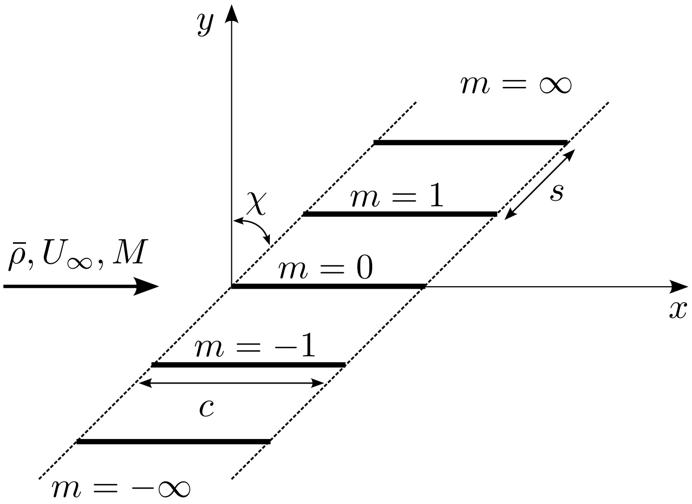

Figure 4.1 *Illustration of the infinite cascade of flat plates modelled in* LINSUB

The assumptions allow to model the blades and their wakes as vortex sheets that induce an axial velocity jump across the airfoil surface. The total vorticity, γ_t, on the blade is expressed as

$$\gamma_t = [\![u]\!] = \gamma + \epsilon \tag{4.1}$$

where $[\![u]\!]$ indicates the jump in axial flow velocity and γ, ϵ are bound and free vorticity. A relationship between bound and free vorticity is found

$$\frac{d\epsilon}{dx} + \frac{j\omega}{U_\infty}(\gamma + \epsilon) = 0 \tag{4.2}$$

The linearised axial momentum equation for points just below and above the blades can be subtracted to obtain an expression for the pressure jump and manipulated by using Eq. (4.1) and Eq. (4.2)

$$\begin{aligned} -\frac{1}{\bar{\rho}}\frac{\partial}{\partial x}[\![p]\!]e^{j\omega t} &= \left(\frac{\partial}{\partial t} + U_\infty \frac{\partial}{\partial x}\right)[\![u]\!]e^{j\omega t} \\ &= \left(j\omega(\gamma+\epsilon) + U_\infty\frac{d\gamma}{dx} + U_\infty\frac{d\epsilon}{dx}\right)e^{j\omega t} \\ &= U_\infty \frac{d\gamma}{dx}e^{j\omega t} \end{aligned} \tag{4.3}$$

Integrating and noting that both the pressure jump and bound vorticity are zero off the blade, the expression for the pressure jump is

$$[\![p(x)]\!] = -\bar{\rho}U_\infty \gamma(x) \tag{4.4}$$

The blades will experience a lift force F and moment m_z, acting anti-clockwise at the leading edge

$$\begin{aligned} F &= -\bar{\rho}U_\infty \int_0^c \gamma(x)dx \\ m_z &= -\bar{\rho}U_\infty \int_0^c \gamma(x)\, x\, dx \end{aligned} \tag{4.5}$$

From Eq. (4.5), we see that in order to find the unsteady loads, an expression for γ is needed. The vorticity induces an upwash velocity on the blade. The induced velocity at any point on the airfoil is a function of both the bound and shed vorticity, whose contribution can be condensed through a kernel function. The expression for the upwash reads

$$v_y(x') = \frac{1}{c}\int_0^c K\left(\frac{x'-x}{c}\right)\gamma(x)\, dx \tag{4.6}$$

In order to find $\gamma(x)$, we need expressions for the kernel and the upwash.

Whitehead (1960) found an analytical expression for the kernel function in incompressible flow, replacing the cascade by a row of bound vortices with strength

$$\Gamma_m = \Gamma_0 e^{jm\sigma} \tag{4.7}$$

The corresponding solution in subsonic compressible flow involves an infinite series that cannot be summed analytically and that shows bad convergence when evaluated numerically. The approach used is therefore to build the solution for the row of vortices as a superposition of waves that satisfy the linearised momentum and continuity equations. Three waves are superimposed to obtain a solution: two acousic waves, upstream and downstream travelling, and one vorticity wave convected downstream by the mean flow. The method is described in Smith (1972) and it ultimately leads to a kernel function that can be used in Eq. (4.6).

The blades are assumed to vibrate in plunge h and pitch θ, thus inducing an upwash

$$v_y(x') = \dot{h} + \theta\,(U_\infty + j\omega x') \tag{4.8}$$

The expression in Eq. (4.8) ignores the contribution of incoming acoustic and vortical disturbances, which are also implemented in LINSUB, but that are not relevant for flutter of the isolated blade row we are trying to model.

The solution is now sought numerically, by placing N_p discrete vortices and control points along the airfoil length, respectively placed at x and x' according to a cosine spacing law

$$\begin{aligned} x &= \frac{1}{2}c\,(1-\cos(\psi))\ ; \quad \psi = \frac{\pi l}{N_p}\ ; \qquad\qquad l = 0,1,\ldots N_p - 1 \\ x' &= \frac{1}{2}c\,(1-\cos(\phi))\ ; \quad \phi = \frac{\pi(2r+1)}{2N_p}\ ; \quad r = 0,1,\ldots N_p - 1 \end{aligned} \tag{4.9}$$

Note that the trailing edge is omitted as it requires zero vorticity to satisfy the Kutta condition. Plugging Eq. (4.9) into Eq. (4.6) and Eq. (4.5) we obtain

$$v_y(\phi) = \frac{1}{2}\int_0^\pi K\left(\frac{1}{2}(\cos\psi - \cos\phi)\right)\gamma(\psi)\sin\psi d\psi \tag{4.10}$$

and

$$\begin{aligned} F &= -\frac{1}{2}\bar{\rho}U_\infty c\int_0^\pi \gamma(\psi)\sin\psi d\psi \\ m_z &= -\frac{1}{4}\bar{\rho}U_\infty c^2\int_0^\pi \gamma(\psi)\sin\psi(1-\cos\psi)d\psi \end{aligned} \tag{4.11}$$

The integral in Eq. (4.10) may be evaluated by trapezoidal rule. The result expressed in matrix form reads

$$\boldsymbol{U} = \boldsymbol{K\Gamma} \tag{4.12}$$

where $\boldsymbol{U}$ is the upwash matrix of dimension $(N_p \times 2)$, due to plunge and pitch motion, whose entries are

$$\boldsymbol{U} = \begin{bmatrix} 1 & (1 + jkx'/c) \end{bmatrix} \tag{4.13}$$

$\boldsymbol{K}$ is the kernel matrix $(N_p \times N_p)$ whose elements are given by $K\left(1/2(\cos\psi - \cos\phi)\right)$. $\boldsymbol{\Gamma}$ is the bound vorticity matrix of dimension $(N_p \times 2)$. For each motion, there is a vorticity solution and hence a column of discrete vortices given by

$$\boldsymbol{\Gamma} = \begin{bmatrix} (\pi/2N_p)(\gamma/U_\infty) & \sin\psi \end{bmatrix} \tag{4.14}$$

with the exception of the first row which is multiplied by 1/2. Similarly, the integrals in Eq. (4.11) can be written as

$$\boldsymbol{C} = \boldsymbol{X\Gamma} \tag{4.15}$$

with

$$\begin{aligned} \boldsymbol{C} &= \begin{bmatrix} \dfrac{F}{\bar{\rho}U_\infty c\dot{h}} & \dfrac{F}{\bar{\rho}U_\infty^2 c\theta} \\[2ex] \dfrac{m_z}{\bar{\rho}U_\infty c^2\dot{h}} & \dfrac{m_z}{\bar{\rho}U_\infty^2 c^2\theta} \end{bmatrix} \\ \boldsymbol{X} &= \begin{bmatrix} -1 & -\dfrac{1}{2}(1-\cos\psi) \end{bmatrix} \end{aligned} \tag{4.16}$$

Finally, plugging Eq. (4.12) into Eq. (4.15), we obtain an expression for the unsteady aerodynamic load coefficients

$$\begin{aligned}\boldsymbol{C} &= \boldsymbol{X}\boldsymbol{K}^{-1}\boldsymbol{U}\\ &= \begin{bmatrix} C_L^{\dot{h}} & C_L^{\theta} \\ C_M^{\dot{h}} & C_M^{\theta} \end{bmatrix}\end{aligned} \tag{4.17}$$

Plunge and pitch displacements, and the resulting lift and moment, are calculated with reference to the leading edge of the blade. The moment is assumed to be positive when *pitch down*, i.e. anti-clockwise, and the lift coefficient is normalised by the blade plunge velocity, whereas modal aeroelastic models normalise by displacement. The output from LINSUB can be converted into a more convenient form for a generic pitch axis x, with pitch-up positive rotation, and lift normalised by displacement using the relation in Eq. (4.18) found in Donini (2012). Note that the multiplication by jk of the plunge induced terms normalises the lift by displacement, rather than velocity, while multiplying by -1 renders the moments positive pitch-up.

$$\begin{aligned}\boldsymbol{H} &= 2\begin{bmatrix} 1 & 0 \\ x & -1 \end{bmatrix} \begin{bmatrix} C_L^{\dot{h}} & C_L^{\theta} \\ C_M^{\dot{h}} & C_M^{\theta} \end{bmatrix} \begin{bmatrix} jk & 0 \\ 0 & 1 \end{bmatrix} \begin{bmatrix} 1 & x \\ 0 & -1 \end{bmatrix}\\ &= 2\begin{bmatrix} 1 & 0 \\ x & 1 \end{bmatrix} \begin{bmatrix} jkC_L^{\dot{h}} & -C_L^{\theta} \\ -jkC_M^{\dot{h}} & C_M^{\theta} \end{bmatrix} \begin{bmatrix} 1 & x \\ 0 & 1 \end{bmatrix}\end{aligned} \tag{4.18}$$

The original definition of the matrix $\boldsymbol{C}$ can now be modified into a more convenient form, used throughout the rest of the thesis

$$\boldsymbol{C} = \begin{bmatrix} C_L^{h} & C_L^{\alpha} \\ C_M^{h} & C_M^{\alpha} \end{bmatrix} = \begin{bmatrix} jkC_L^{\dot{h}} & -C_L^{\theta} \\ -jkC_M^{\dot{h}} & C_M^{\theta} \end{bmatrix} \tag{4.19}$$

The modal forces can be converted into aerodynamic work by multiplying with modal velocity and integrating over one vibration cycle. The expressions for aerodynamic work coefficients are given by Frannson and Verdon (1991) and for pure plunge and pitch modes they read

$$\begin{aligned} C_w^h &= \pi\bar{h}^2\Im\left\{C_L^h\right\}\\ C_w^\alpha &= \pi\bar{\alpha}^2\Im\left\{C_M^\alpha\right\} \end{aligned} \tag{4.20}$$

The aerodynamic work can be expressed in normalised form as aerodynamic damping parameter ζ

$$\begin{aligned} \zeta_h &= -\frac{C_w^h}{\pi\bar{h}^2} &= -\Im\left\{C_L^h\right\}\\ \zeta_\alpha &= -\frac{C_w^\alpha}{\pi\bar{\alpha}^2} &= -\Im\left\{C_M^\alpha\right\} \end{aligned} \tag{4.21}$$

The stability of simple modes can be thus assessed by inspecting only the imaginary part of the unsteady force coefficients.

4.3 Verification of Implementation

Although the code for `LINSUB` can be found, in full, in Whitehead (1987, Chapter 3), the original implementation in `FORTRAN` has been translated into `PYTHON` to ease the interface between machine learning and reduced order model, thus granting a verification of the code implemented. The results from the current implementation are compared against the one in Donini (2012). The test cases are two Standard Configuration compressor cascades (Frannson and Verdon, 1991), namely SC1 and SC5. The aeroelastic parameters are compiled in Table (4.1), while the results are shown in Fig. (4.2).

Table 4.1 *Aeroelastic parameters for LINSUB validation. Results shown in Fig. (4.2).*

		(a)	**(b)**
Test Case		SC1	SC5
Mach Number	M	0.18	0.5
Stagger	χ	55°	59.3°
Pitch to chord ratio	s/c	0.75	0.95
Pitching axis	x	0.5	0.5
Reduced Frequency	k	0.244	Sweep
Interblade Phase Angle	σ	Sweep	180°

The results overlap perfectly, thus the implementation of the code is correct. Moreover, we can see that torsional flutter is predicted by `LINSUB`, even when disregarding steady blade loading. This is not true for pure plunging motion, as Whitehead (1962) showed that finite flow deflection needs to be taken into account to predict flutter.

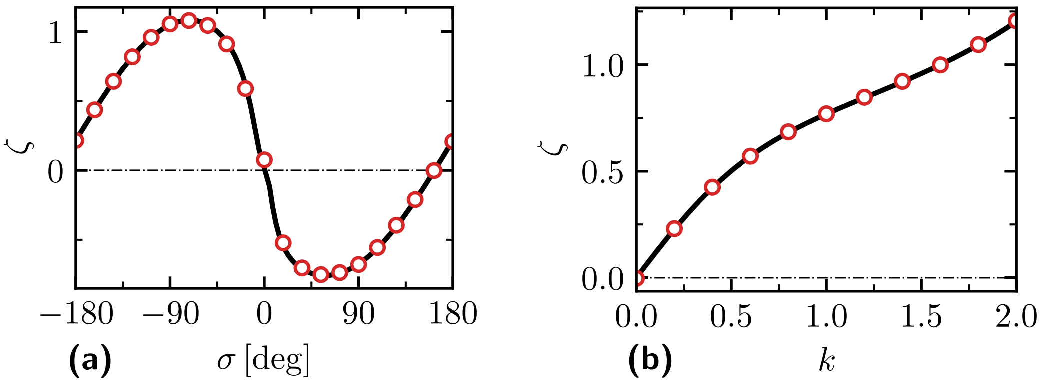

Figure 4.2 *Comparison of LINSUB predictions for test cases shown in Table (4.1). Black solid line (—) shows results of the current implementation, the circle marker (○) are results from the implementation in Donini (2012).*

4.4 Comparison against CFD

The results from LINSUB are now compared to aerodynamic damping values obtained with CFD. The numerical setup of the solver and methodology employed to compute aerodynamic damping have been discussed in Chapter (2).

4.4.1 Unloaded Cascade

The test case employed in this comparison is a fictitious cascade made up of unloaded blades, that is NACA0006 profiles. The computational grid is obtained by morphing the original SC10 mesh (Section 2.5) with a radial basis function technique (Kedward et al., 2017). The aeroelastic parameters are shown in Table (4.2), while the results are shown in Fig. (4.3).

Table 4.2 *Aeroelastic parameters for CFD comparison. Results shown in Fig. (4.3).*

		(a)	**(b)**
Test Case		NACA0006	NACA0006
Mach Number	M	0.423	0.423
Stagger	χ	45°	45°
Pitch to chord ratio	s/c	1.0	1.0
Modeshape		Plunging	Pitching about midchord
Reduced Frequency	k	0.87	0.87
Interblade Phase Angle	σ	Sweep	Sweep

The predictions from LINSUB agree well with the CFD. The discrepancies are attributable to the fact that, first, the blade modelled in CFD has, albeit small, non-zero thickness that differentiates it from a flat plate and, second, the loading on the blade modelled in CFD is not exactly zero.

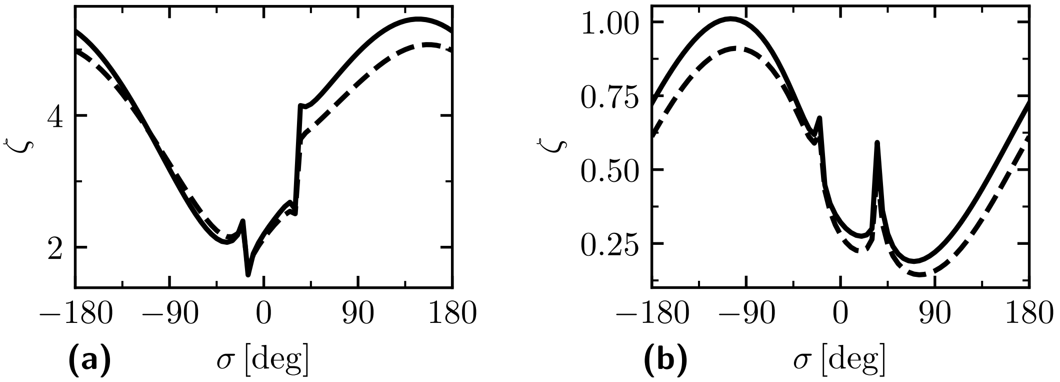

Figure 4.3 *Comparison of LINSUB predictions (—) and CFD (- - -) for NACA0006 test case shown in Table (4.2):* ***(a)*** *Plunging mode;* ***(b)*** *Pitching about mid-chord.*

4.4.2 Loaded Cascade

The test case employed in this comparison is the Standard Configuration 10. The aeroelastic parameters are shown in Table (4.3); the results are shown in Fig. (4.4).

Table 4.3 *Aeroelastic parameters for CFD comparison. Results shown in Fig. (4.4).*

		(a)	(b)	(c)	(d)
Test Case		SC10	SC10	SC10	SC10
Mach Number	M	0.7	0.7	0.8	0.8
Inflow Angle	α_1	55°	55°	58°	58°
Incidence	β_1	0°	0°	3°	3°
Stagger	χ	45°	45°	45°	45°
Pitch to chord ratio	s/c	1.0	1.0	1.0	1.0
Modeshape		Plunging	Pitching†	Plunging	Pitching†
Reduced Frequency	k	0.5	0.5	0.5	0.5
Interblade Phase Angle	σ	Sweep	Sweep	Sweep	Sweep

†Pitching axis is located at midchord

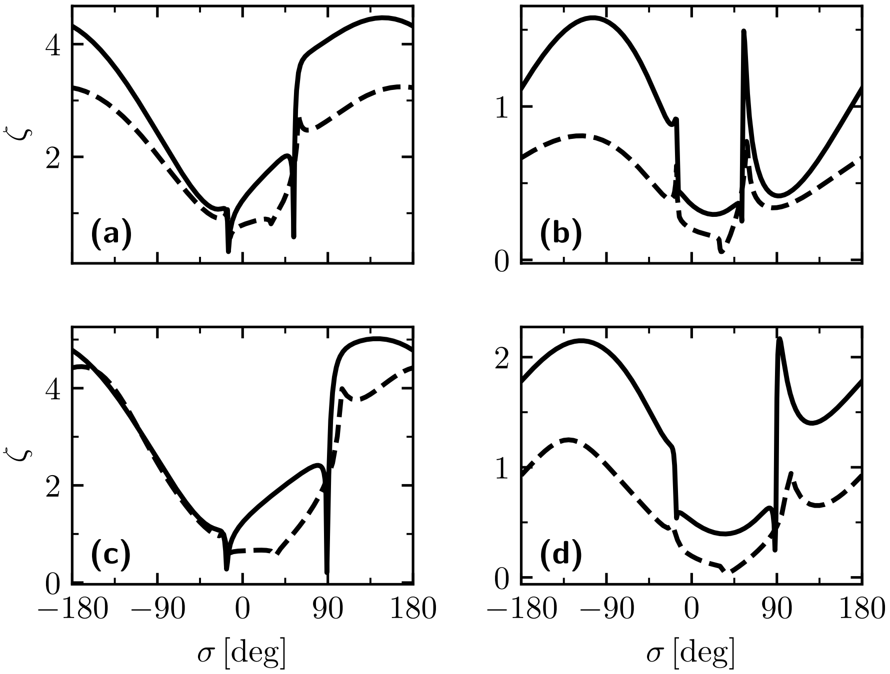

Figure 4.4 *Comparison of LINSUB predictions (—) and CFD (---) for SC10 test case shown in Table (4.3). First and second row are subsonic and transonic flow. First and second column are plunge and pitch modes. Pitching axis is at midchord.*

The blades in this case are loaded (see Fig. (2.4) for subsonic flow and Fig. (2.10) for transonic flow), therefore, as expected, the predictions from `LINSUB` do not agree well with the results from CFD, though the overall shape with IBPA is well approximated. The upstream cut-off frequencies, denoted by the peaks in aerodynamic damping, are also well captured.

4.5 Summary

The predictive capabilities of the analytical model discussed in this Chapter are limited to unloaded blades, which is rarely the case in reality. The prediction accuracy degrades dramatically for loaded blades especially at transonic conditions. Therefore, we cannot rely solely on these models in practice. However, `LINSUB` captures relevant trends and it is able to model important features such as cascade geometry, compressibility effects and modeshape. Therefore, in the following Chapter, an attempt at combining the merits of `LINSUB` with a machine learning technique is made, in order to build a prediction model that is able to generalise to unseen conditions and geometries.

Chapter 5

Physics Guided Neural Network Model

5.1 Introduction

The model presented in Chapter (3) proved to be useful in a redesign context and provides a good stepping stone for a data-driven solution for compressor flutter. The fallacy of the simple FCNN though is clear: the model is not reusable, as it can predict aerodynamic damping for the training geometry only. The difficulties with extrapolation from the training space are well known in machine learning and efforts have been made to address these limitations with varying degrees of success. All the paradigms are based on introducing physical or domain knowledge into the process, and a brief summary of such approaches is in order to justify the choices made in this work. A more exhaustive review of machine learning studies in fluid mechanics is given in Chapter (1).

Raissi et al. (2019) introduced the physics informed neural network (PINN) concept and applied it to solve a number of problems, including two dimensional shedding around a cylinder. The PINN framework includes the differential form of the governing equations, and relative boundary conditions, as loss terms inside the cost function so that predictions are consistent with the underlying physical problem, allowing the model to extrapolate to unseen conditions. However, even in their state-of-the-art form, PINNs have only been applied to relatively simple fluid flow problems (Jin et al., 2021; Oldenburg et al., 2022) and, more importantly, are still geometry dependent, i.e. a model trained on one geometry cannot be used on another.

Physical understanding can be incorporated through domain knowledge as well. Manepalli et al. (2019) built a model to predict snow accumulation on mountains and have incorporated certain domain knowledge via additional penalty terms into the cost function, which penalise the model for predicting snow accumulation on water surfaces. Daw et al. (2020) used an LSTM to predict lake water density and, as density can only increase with depth, they constrained their model to only predict monotonic, increasing trends. Frey Marioni et al. (2021) seeked to improve the modelling of the eddy viscosity term in the Boussinesq assumption, using neural networks trained on DNS data, with the ultimate goal of improving flow field predictions in a turbomachinery cooling flow. Rather than directly training on the complicated flow, they approximated it with a serpentine passage and employed hierarchical agglomerative clustering to classify and divide flow regions. They showed improved results by training only on regions without flow separation. Frey Marioni et al. (2022) built on their work to model wakes in an LPT cascade. Once again they showed that dividing the domain into simpler subdomains and employing clustering improves the predictive capabilities of their ML models.

Particularly in turbulence modelling, physical knowledge is incorporated in the formulation of meaningful input features. Ling and Templeton (2015) developed a number of classifiers to identify regions of high uncertainty in RANS computations, and ensured that the models had good generalisation properties by providing several features that are rotationally invariant and based on physical intuition. Their set of features has since been adopted by other researchers (He et al., 2022; Wang et al., 2017).

Finally, Pawar et al. (2021) introduced the concept of physics guided machine learning (PGML) and applied it to the prediction of lift coefficient on 4 and 5 digits NACA airfoils. The PGML framework in this case refers to a fully connected neural network where, at some hidden layer, results from a reduced order model (ROM) of the process are injected, thus augmenting the knowledge of the algorithm and "guiding" it to a physically consistent formulation. The same framework has been applied to modelling of dynamical systems with good degree of success (Robinson et al., 2022), and both studies show good generalisation properties. This framework is appealing as it is computationally inexpensive, easily implemented, builds incrementally on previous, physically sound knowledge and acts as a regulariser, avoiding excessive overfitting even in a *small-data* regime.

Considering the discussion above, we seek to build a machine learnt model using the PGML framework with meaningful input and output features, based on physical understanding of stall flutter. Each component of the PGML model developed in this work will now be discussed.

5.2 Machine Learning Algorithm

The algorithm chosen as backbone of the PGML model is, again, a fully connected neural network. The choice of an FCNN is motivated by the encouraging results of Chapter (3) and, mainly, because its layered structure allows full control over the location at which the low-fidelity results are injected. A schematic representation of the FCNN is given in Fig. (5.1).

A number of hyperparameters need to be specified now to build the model, such as number of hidden layers, number of neurons per hidden layer, regularisation coefficient, bias value, number of iterations, minibatch and step size, activation function and location of low-fidelity results injection. In this case, a full factorial exploration is unfeasible to say the least, therefore the standard practice of random search is employed. A set number of FCNNs will be trained with hyperparameters chosen randomly within pre-established ranges; the loss metrics are evaluated and the best models are then selected for a posteriori assessment.

In this work, we aim for small, simple FCNN architectures in order to reduce the computational cost associated to training, thus allowing a large number of hyperparameters to be tested in parallel, even on conventional CPUs. The optimisation algorithm is Adam (Kingma and Ba, 2014), and the cost function is the standard mean squared error (MSE). The model is implemented in `PYTHON` with the `TENSORFLOW` (Abadi et al., 2015) library.

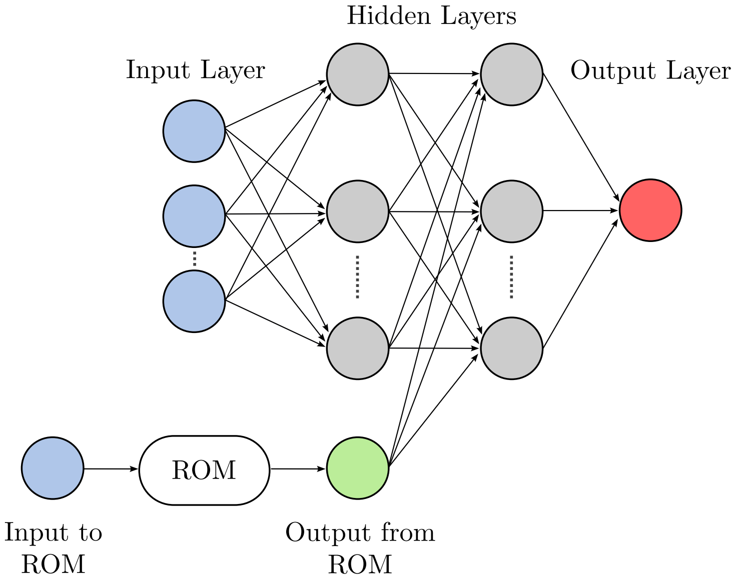

Figure 5.1 *A schematic representation of a PGML network with two hidden layers and one-dimensional output.*

5.3 Reduced Order Model

The reduced order model we are seeking must:

- be efficient, thus adding minimum computational effort
- take into account some, if not all, geometrical features of the cascade

- model compressibility effects, due to the Mach number range of interest for stall flutter
- be validated

Unlike the machine learning algorithm, there are not many reduced order models for the aeroelastic response of turbomachinery cascade. The most viable option, fitting our requirements, is the semi-analytical model `LINSUB`, discussed in Chapter (4).

5.4 Output Formulation

`LINSUB` calculates a matrix of unsteady load coefficients induced by simple rigid body modes, plunging normal to the chord and pitching about the leading edge. The same coefficients can be calculated using CFD. Two computations are necessary to calculate the unsteady pressures induced by each mode, which are consequently integrated along the blade to find forces and moments. Eq. (5.1) shows the definition of the coefficients. The superscript refers to the mode causing the unsteady loads, while the subscript refers to the modal force, thus, L for lift when projecting the loads onto the plunge mode and M for moment, which is the modal force for a pure pitch.

$$
\begin{aligned}
C_L^h &= \frac{1}{S(p_0 - p_1)\bar{h}} \int_S \widehat{p}^h \boldsymbol{n} \cdot \boldsymbol{\Phi}^h dS \\
C_L^\alpha &= -\frac{1}{S(p_0 - p_1)\bar{h}} \int_S \widehat{p}^\alpha \boldsymbol{n} \cdot \boldsymbol{\Phi}^h dS \\
C_M^h &= -\frac{1}{cS(p_0 - p_1)\bar{\alpha}} \int_S \left(\boldsymbol{r} \times \widehat{p}^h \boldsymbol{n}\right) \cdot \boldsymbol{\Phi}^\alpha dS \\
C_M^\alpha &= \frac{1}{cS(p_0 - p_1)\bar{\alpha}} \int_S \left(\boldsymbol{r} \times \widehat{p}^\alpha \boldsymbol{n}\right) \cdot \boldsymbol{\Phi}^\alpha dS \\
\boldsymbol{C} &= \begin{bmatrix} C_L^h & C_L^\alpha \\ C_M^h & C_M^\alpha \end{bmatrix}
\end{aligned}
\tag{5.1}
$$

S is the blade surface area, c its chord, $(p_0 - p_1)$ is the difference between inlet total and static pressure equals to the dynamic head, $\boldsymbol{\Phi}$ is the modeshape and $\bar{h}$, $\bar{\alpha}$ the modal amplitudes, $\boldsymbol{n}$ is the blade surface unit vector, $\widehat{p}$ the complex unsteady pressure and, finally, $\boldsymbol{r}$ is the position vector from the pitching axis to the blade.

The interest of this work lies in stall flutter which, mostly, affects blades vibrating in first flap mode. A flap mode is a rotation about a generic axis x, therefore, we can use Eq. (4.18)[1] to convert the matrix $\boldsymbol{C}$ into the new reference frame centered at x. Finally, the obtained unsteady moment coefficient can be translated into an

---

[1] As the lift coefficient calculated from CFD is already normalised by displacement, the term jk in the equation is dropped

aerodynamic damping coefficient ζ using Eq. (4.21), resulting in

$$\zeta = -\Im\left\{C_M^\alpha\right\} + \left(\Im\left\{C_M^h\right\} + \Im\left\{C_L^\alpha\right\}\right)x - \Im\left\{C_L^h\right\}x^2 = \zeta_M^\alpha + \zeta_M^h + \zeta_L^\alpha + \zeta_L^h \tag{5.2}$$

where, again, the superscript refers to the mode causing the unsteady loads, while the subscript refers to the induced force.

The quantity of interest (QoI) of the PGML model will therefore be the matrix $\boldsymbol{C}$, from which plunge, pitch and any flap mode stability can be evaluated.

5.5 Input Formulation

The purpose of the proposed model is to predict unsteady force coefficients for different geometries.

The most basic avenue to achieve this goal requires an expansion of the training database through the inclusion of several different geometries, so that the surrogate model can then interpolate to produce predictions on cases that fall within the training space. This approach is appealing as, once the surrogate model is trained, it bypasses the CFD solver completely and only boundary conditions and geometry are needed to obtain the set of unsteady forces. Unfortunately, this approach is also unfeasible as the number of training samples needed would be extremely large, moreover, even if one were to simulate a large number of cases, the definition of these geometries would most likely need to be parametrised through an autoencoder, which is a task with pitfalls in itself (Gambitta et al., 2022; Yonekura et al., 2022). Therefore, the approach followed in this work relies on a different strategy.

In order to predict unsteady forces on the blade, the surrogate model needs information about the geometry and flow variables. If the geometry is to be explicitly passed as an input, clearly several cascades need to be used to build a training set. On the other hand, the flow features, and their relationship, form a set of dependent variables which is defined by the boundary conditions and geometry themselves. It is thus argued that, rather than passing the geometry explicitly, the PGML model can build a functional mapping for the QoI from a set of unsteady boundary conditions and steady state features, which already encode the geometry in their mutual dependence. Effectively, the steady CFD solver acts as an encoder to translate the geometry into an input the PGML can work with, thus the input to the model will be steady state flow quantities, rather than the blade geometry directly. This approach is somewhat similar to that of Ling and Templeton (2015). The drawback of this solution is that a run of steady state solver is needed to calculate the input features at prediction time. This is deemed an acceptable price to pay, as the aerodynamic damping for different modeshapes, frequencies and interblade phase angles, can be calculated at no extra cost. A diagram of the PGML framework is depicted in Fig (5.2).

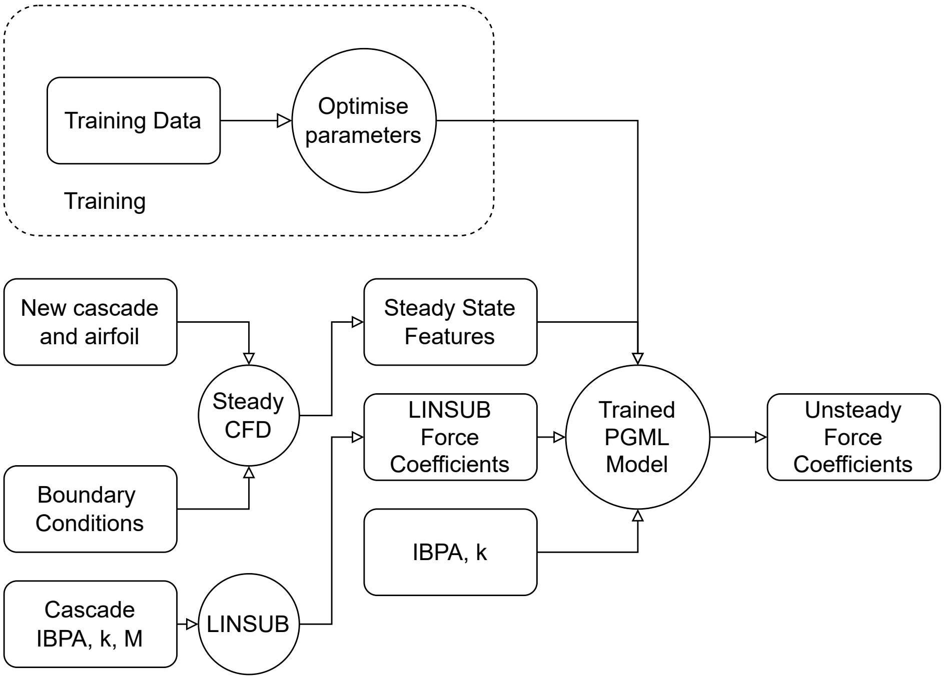

Figure 5.2 *Diagram representing the proposed PGML framework*

The careful choice of input features is crucial to develop a model that can generalise. The features must not only be relevant for stall flutter, but must also carry information about the domain, without harming the learning process: too many input features will introduce information that might be irrelevant and add dimensions to the data; on the other hand, if the number of inputs is too low, the model will not be able to capture a change in geometry or flow conditions and will thus be unable to generalise.

5.5.1 Steady State Features

A number of constraints are established to reduce the space of possible features, which would otherwise grow too large. The features must be continuous and relevant for both subsonic and transonic flow, thus no binary variables, e.g. shock/no shock or pressure jump at shock front. They must also be relevant for both attached and separated flow, which denies the inclusion of quantities such as size of separation. Finally, these features must be either non-dimensional or rescaled by a relevant quantity. The last point will be explained more carefully as we list them.

It is stressed that the absence of quantities relating “directly” to the presence of shocks and separation does not imply that these flow features are unimportant, but simply that their effect can be represented by other flow features. The following features have been chosen based on physical intuition.

Inlet Mach number

The inlet Mach number is one of the most important non-dimensional groups in turbomachinery and it is also an input to `LINSUB`.

Chordwise center of pressure

The steady pressure distribution on the blade is important to determine stability, thus a parameter to capture loading is needed. Force and moment coefficients give a good indication of loading, but vary widely between geometries and cannot be used for generalisation unless normalised by some reference value which is hard to define. The same applies to pressure ratio, pressure rise and flow coefficients, and similar parameters. Wong (1997) and Kiss (2021) both showed strong correlation between aerodynamic damping and location of chordwise center of pressure x_{cp}. The center of pressure carries a lot of information regarding the state of the pressure field around the blade and for a typical compressor section, unless the flow is severely stalled or choked, it is bounded between 0 and 1, corresponding to leading and trailing edge respectively.

Blockage near trailing edge

Blockage is the reduction in flow area caused by local velocity deficit which is a result of the displacement thickness associated with boundary layers. It is a crucial variable for compressor design and a great indicator of either increasing incidence onto the blades or flow separation due to a strong shock wave. The blockage definition used in this work is adapted from Khalid et al. (1999) and is briefly discussed here. First, the authors define a main flow direction to select a velocity component, u_m, to use in blockage definition. As we are interested in the blockage due to the boundary layers in the bladed passage, the main flow direction is the one aligned with the stagger angle ξ. Second, they identify the edge of the velocity deficit region by recognising that near solid walls, the gradients are stronger than in the core flow. The edge is defined as the region where the magnitude of the gradient $\vec{\nabla}\rho u_m$, normalised by inlet density, inlet axial velocity and blade chord, is equals to a target value. The target is set to 3 as in the original paper, since *“ the defect area over which the blockage integration is performed is relatively insensitive to the precise value selected (e.g., 2, 3, or 4) as the edge criterion.”*. (Khalid et al. (1999), also see Fig. 5.3). As our test case is two-dimensional, the expression for blockage area becomes a blockage width δ defined as

$$\delta = \int \left(1 - \frac{\rho u_m}{\rho_e U_e}\right) \cdot dl \tag{5.3}$$

where dl refers to integration along a line normal to the blade surface, while ρ_e and U_e are the values of density and velocity at the blockage edge. The blockage can only grow on the blade, therefore it is calculated near the trailing edge where it reaches its maximum, both for suction and pressure side, because the relationship between the two changes depending on the operating conditions. In subsonic flow, the blockage

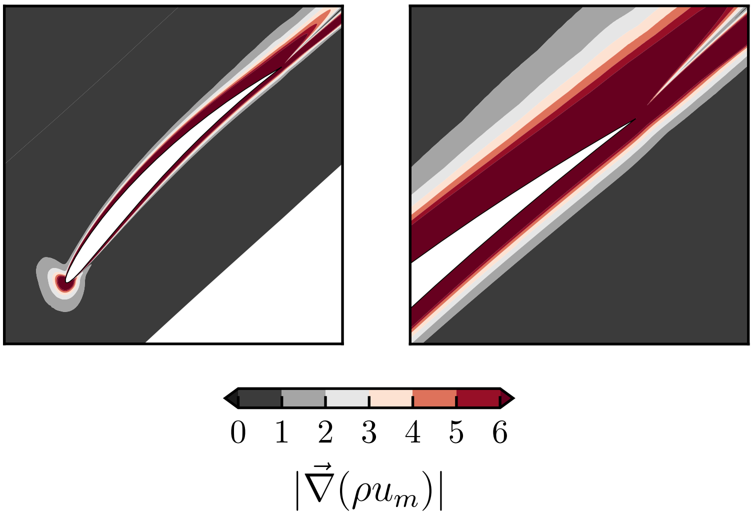

Figure 5.3 *Example of blockage region definition using velocity gradient with a close-up around the trailing edge.*

on suction and pressure side are, respectively, directly and inversely proportional to incidence; in transonic flow this is not necessarily the case as, even with low incidence, the shock wave forming on the suction side will grow the blockage while the pressure side is effectively unchanged (assuming the flow is not choked). This feature is bounded by the passage width but, at the same time, the boundary layer growth is also a function of the chord length. Moreover, in the limiting case of null mass flow rate, there should not be any blockage at all. It is found that the best approach to account for these observations is to rescale the blockage size by the solidity s, i.e. chord to pitch ratio.

Wake Momentum Thickness

A further indicator of the state of boundary layers and losses of the cascade is the wake momentum thickness. This quantity, similar to blockage, is proportional to incidence and inlet Mach number. Moreover, it correlates to the diffusion factor u_{max}/u (Lieblein and Roudebush, 1956), which gives an indication of fluid velocities on the suction side, but unlike the diffusion factor, the same considerations put forth regarding blockage size can be applied here, therefore this feature can also be rescaled by the solidity. The definition of momentum thickness used here is found in Dixon and Hall (2013)

$$\Theta = \int \frac{u}{U}\left(1 - \frac{u}{U}\right) dy \tag{5.4}$$

where U and u are velocity outside and inside the wake region respectively, and dy indicates integration in the pitchwise direction.

Stagnation Pressure Loss Coefficient

Losses in cascades are commonly expressed in terms of stagnation loss coefficient.

$$\bar{\omega} = \frac{p_{01} - p_{02}}{p_{01} - p_1} \tag{5.5}$$

where 1 and 2 indicate inlet and outlet. This quantity is easy to calculate and correlates well with other loss parameters.

5.5.2 Unsteady Features

The unsteady features are the interblade phase angle σ and the blade reduced frequency k. Arguably, these quantities could be better represented by their ratio with cut-off frequencies (see Section (2.4)), but for any given combination of frequency and interblade phase angle, there are multiple cut-off conditions. It is thus unclear which one would be the most appropriate to choose for normalisation and for this reason, the values of σ and k are used directly. The periodicity with interblade phase angle is enforced by simply duplicating training samples on either side of the ±180° range.

Finally, one would argue that a feature able to capture the change in passage shape is missing. Although this is true, we can make two considerations. First, the change in passage shape is partially modelled in LINSUB. Second, and more importantly, this effect becomes highly relevant for torsional modes at high interblade phase angle, which is a condition that very rarely exhibits stall flutter. Table (5.1) summarises the input features used in this work.

Table 5.1 *Input features to PGML model*

Feature	Description	Normalised by
M_1	Inlet Mach Number	
x_{cp}	Chordwise center of pressure	c
δ_{SS}	Blockage at trailing edge on suction surface	s
δ_{PS}	Blockage at trailing edge on pressure surface	s
Θ	Wake Momentum Thickness	s
$\bar{\omega}$	Stagnation Pressure Loss Coefficient	
σ	Interblade Phase Angle	
k	Reduced Frequency	

5.6 Effect of change in geometry on steady and unsteady aerodynamics

In this section we investigate the behaviour of the unsteady aerodynamic coefficients due variations in airfoil and cascade geometry.

The different cascades presented here are a departure from the nominal geometry introduced in Chapter (2), and are obtained by varying one parameter at a time. The solidity $s = c/P$ is changed by varying the pitch of the cascade, the stagger angle ξ is varied at 5° intervals, while thickness, T, and camber, Z, of the airfoil are varied by multiplying their definitions (see Eq. 2.70) by a constant. The necessary computational grids are obtained by morphing the original SC10 mesh (Section 2.5) with a radial basis function technique (Kedward et al., 2017), to ensure they all share the same characteristics, such as preserving orthogonality of the grid edges.

The steady state effects, as a results of geometry change, can be easily explained from first principles and such analyses can be readily found in textbooks (Cumpsty, 2004; Dixon and Hall, 2013). These will be discussed briefly before moving on to the more relevant unsteady behaviour. The results are presented in terms of coefficients of the matrix $\boldsymbol{C}$, and in terms of each coefficient's contribution to aerodynamic damping for a specific mode of interest, each shown in Eq. (5.2). This representation is at times more insightful as it allows to identify which components are beneficial or detrimental to the overall stability of a mode. Eq. (5.2) shows that for flap modes, i.e. $x \geq 1$, the contribution of plunge induced lift to stability quickly becomes dominant, so it is extremely important that this component is well predicted by the PGML model.

Finally, for the sake of brevity, the unsteady results shown concern only one transonic condition, $M_1 = 0.85$, at a representative reduced frequency, $k = 0.5$. A more exhaustive set of results is presented in Section (5.7.1) and Appendix (B).

5.6.1 Definition of zero incidence

The location of the stagnation point on the airfoil is of great importance and its precise position depends on several factors, but the main ones are mean inlet flow angle, thickness in the leading edge region, solidity and camber (Cumpsty, 2004, Chapter 4). The topology of the flow in the passage changes drastically, especially at high Mach number, depending on whether the stagnation point moves onto the pressure or suction surface. Thus, to have a comparison between different geometries, a consistent definition of the operating conditions is needed.

In this work, the results are grouped by inlet Mach number and incidence, therefore a nominal or "zero" incidence condition must be specified for each speed. Among the several definitions available (see Cumpsty (2004, Chapter 4, p. 162)), the one chosen here was given by Emery et al. (1958), who chose the zero incidence condition to be the inlet flow angle which renders a smooth distribution of pressure around the leading edge, i.e. there is no suction peak present on the pressure surface.

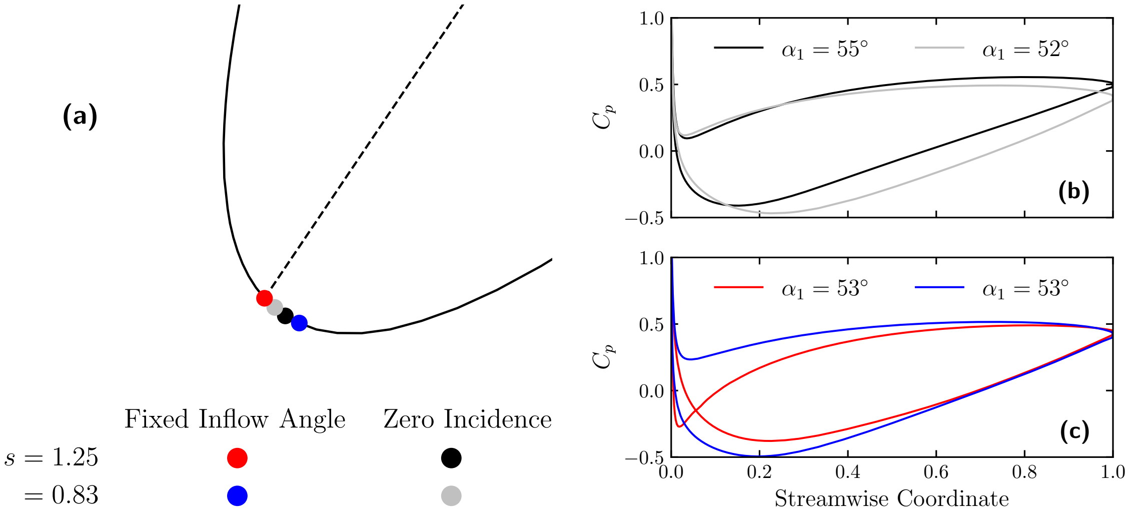

Figure 5.4 *Location of stagnation points around leading edge* ***(a)*** *and associated pressure distribution* ***(b)***, ***(c)*** *on an airfoil for different solidity and inflow angles, with a fixed inlet Mach number* $M_1 = 0.7$.. *The dashed line* (- - -) *is the chord line, starting at the leading edge of the blade.*

As an example, Fig. (5.4) shows the effect of change in solidity on the location of the stagnation point and consequent pressure distribution along the blade, with constant inlet Mach number. Fig. (5.4a) depicts the leading edge area of a blade: the four coloured dots are the stagnation points for two cascades, with solidity $s = 1.25$ and $s = 0.83$, at two flow conditions, namely fixed inlet flow angle $\alpha_1 = 53°$ and zero incidence. The dashed line represent the chord line, starting at the leading edge of the blade. Fig. (5.4b) and Fig. (5.4c) show the steady pressure coefficient around the blade for each of the cases. At fixed inlet flow angle $\alpha_1 = 53°$, an increase in solidity, i.e. a reduction in pitch, moves the stagnation point towards the suction side (see blue and red dot), enough that a suction peak develops on the pressure side (see blue and red lines). This situation is equivalent to a reduction in inlet flow angle at constant Mach number, thus an increase in mass flow rate which results in moving the operating point towards choke.

As this work focuses on stall flutter, we want to avoid choked flow, therefore, as the solidity is increased, the design or zero incidence inflow angle increases as well. In this case, the inflow angle necessary to attain zero incidence increases from $\alpha_1 = 52°$ ($s = 0.83$, gray line) to $\alpha_1 = 55°$ ($s = 1.25$, black line). A similar behaviour takes place with changes in camber, thickness and stagger angle.

5.6.2 Change in solidity

The solidity is defined as the ratio of chord over pitch $s = c/P$ and it is a highly influential parameter for both performance and aeroelastic stability of a compressor. Fig. (5.5) shows the trend of relevant steady quantities with change in solidity at different inlet Mach numbers and fixed incidence.

The increase in delivered pressure ratio, Π, at constant Mach number is due to the reduction of the bladed passage width, which in turn increases the flow deflection and reduces the mass flow rate. Ultimately, the limiting case would be characterised by the flow following the blade profile perfectly, but with mass flow rate approaching zero.

The vanishing mass flow rate also explains the reduction in lift and drag as the forces are the result of conservation of momentum.

The total pressure loss exhibits a strong positive correlation with inlet Mach number and incidence, and decreases ever so slightly with solidity.

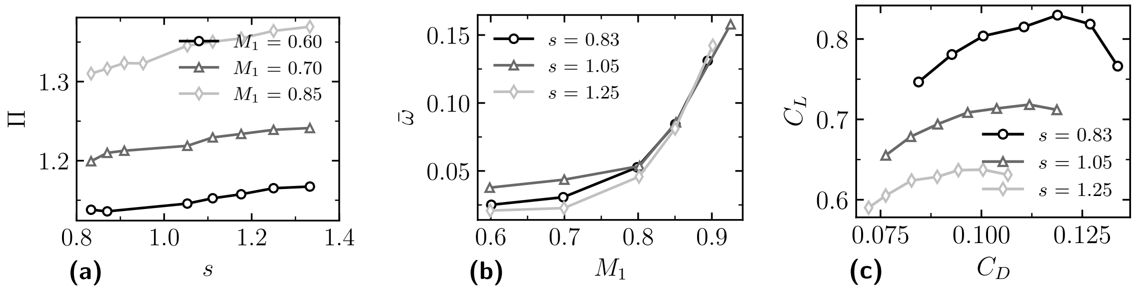

Figure 5.5 *Change in steady performance with solidity:* ***(a)*** *Pressure ratio against solidity at different inlet Mach number at constant incidence* $\beta_1 = 5°$ *;* ***(b)*** *Total pressure loss coefficient against inlet Mach number at different solidity, constant incidence* $\beta_1 = 5°$ *;* ***(c)*** *Lift against drag coefficients at different solidity and fixed* $M_1 = 0.85$*.*

Fig (5.6) shows the imaginary components of the matrix $\boldsymbol{C}$ against interblade phase angle at two different solidity values.

The magnitude of the unsteady moment and lift induced by either mode is comparable at low σ, but the latter grows much larger as σ increases for both values of s. The change in solidity exerts moderate influence on the coefficients at low σ, while its effect is significant as the interblade phase angle grows large. This behaviour is displayed more clearly in Fig. (5.7a) and Fig. (5.7b), which show the unsteady coefficients against solidity, at a fixed steady flow condition and reduced frequency, with $\sigma = 20°$ and $\sigma = 150°$ respectively.

This large change is due to the fact that as the solidity increases, at high σ, for the examined flow condition, the unsteady pressure fields upstream and downstream of the cascade change from cut-on to cut-off. There are two ways in which changing solidity affects cut-off frequencies. First, as we vary solidity by changing the pitch of the cascade, we see from Eq. (2.69) that the transverse wavenumber changes, thus altering the cut-off frequency. Moreover, the downstream flow angles and Mach number will be different with different solidity due to a change in flow deflection. The crossing of a cut-off frequency is usually associated with a sudden change in unsteady loads, which also explains the non-monotonic behaviour of the coefficients. Therefore, the value of IBPA itself is not the main driver, but rather the fact that, at this particular condition, the pressure perturbation caused by the acoustic waves near the cut-off frequency is of comparable order to the perturbation associated to vorticity waves (Vega and Corral, 2013). As a matter of fact, after $s \geq 1.2$, we can see that the coefficients' modulus decreases monotonically with solidity. Being influenced by the cut-off frequencies, this trend is obviously dependent on flow angles, freestream Mach numbers and frequency, as well as interblade phase angle.

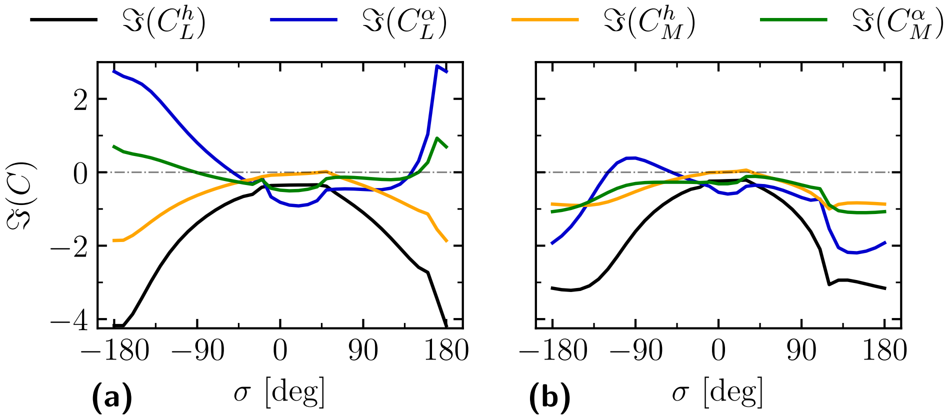

Figure 5.6 *Imaginary component of unsteady force coefficients against interblade phase angle, with fixed inlet Mach number* $M_1 = 0.85$*, incidence* $\beta_1 = 3°$ *and reduced frequency* $k = 0.5$*, at different solidity:* ***(a)*** $s = 0.833$ *;* ***(b)*** $s = 1.25$

As the values of the matrix $\boldsymbol{C}$ cannot be directly read as an indication of stability, Fig. (5.8) portrays the aerodynamic damping contributions obtained with Eq. (5.2), with increasing incidence, for a pitching axis one chord downstream of trailing edge, representative of a flap mode, at two different solidity values, with transonic flow. It is shown that an increase in inflow angle at constant Mach number reduces the total damping, irrespective of solidity, but that the magnitude of the decrease is more severe at lower solidity. This behaviour is readily explained by Fig. (5.5c), which shows that cascades with lower solidity tend to stall more easily as the incidence onto the blades is increased, thus producing a larger separation that in turn produces more destabilising work. The pitch induced lift contributes negatively at all flow conditions, while the opposite is true for the plunge induced lift. The contributions attributable to the induced moments are small and mostly cancel each other out, a behaviour already presented by Vahdati and Cumpsty (2015).

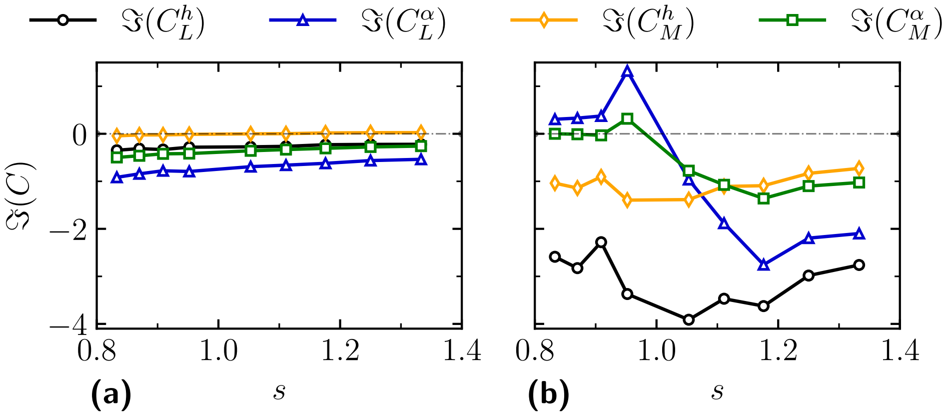

Figure 5.7 *Imaginary component of unsteady force coefficients against solidity, with fixed inlet Mach number* $M_1 = 0.85$*, incidence* $\beta_1 = 3°$ *and reduced frequency* $k = 0.5$*, at different interblade phase angle:* ***(a)*** $\sigma = 20°$ *;* ***(b)*** $\sigma = 150°$

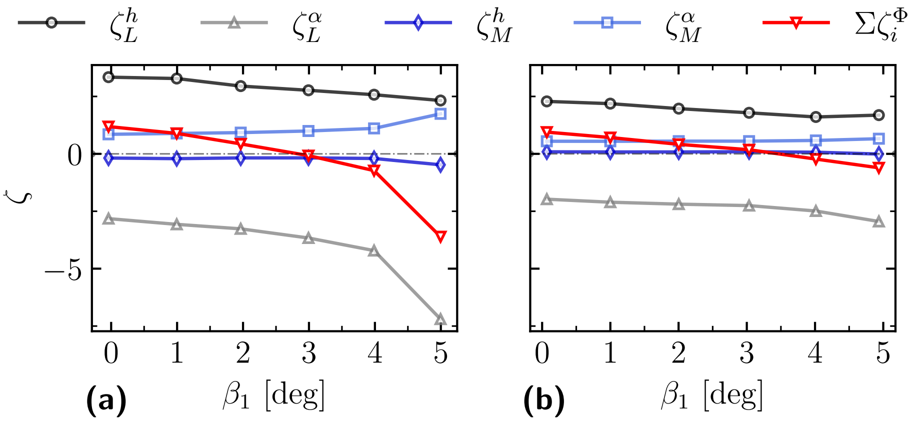

Figure 5.8 *Aerodynamic damping contributions for a flap mode at* $x = 2$ *as a function of incidence, with fixed inlet Mach number* $M_1 = 0.85$*, interblade phase angle* $\sigma = 20°$*, and reduced frequency* $k = 0.5$*, at different solidity:* ***(a)*** $s = 0.833$ *;* ***(b)*** $s = 1.25$

Finally, Fig. (5.9) shows aerodynamic damping against solidity for a flap mode in transonic flow and high incidence, at low frequency and interblade phase angle. All cascades exhibit flutter for this condition, even though the change in solidity is quite large.

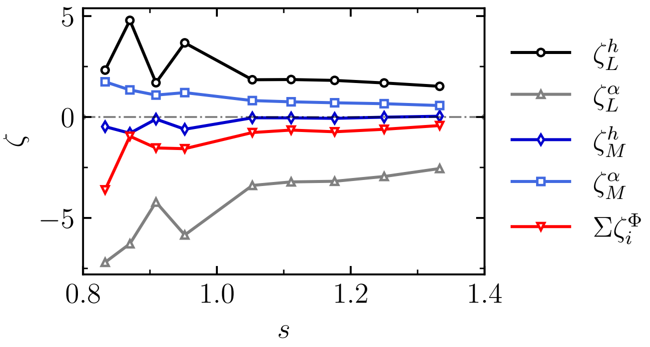

Figure 5.9 *Aerodynamic damping contributions for a flap mode at* $x = 2$*, with fixed inlet Mach number* $M_1 = 0.85$*, incidence* $\beta_1 = 5°$*, interblade phase angle* $\sigma = 20°$*, and reduced frequency* $k = 0.5$*, against solidity*

5.6.3 Change in stagger

Similarly to solidity, the stagger angle ξ is also a highly relevant parameter for cascade design, both in terms of steady and unsteady flow.

Fig. (5.10) shows that the delivered static pressure ratio increases with stagger angle. As the stagger angle is increased, the throat area of the nozzle formed by the bladed passage becomes smaller (Fig. 5.11), thus, to keep a constant inlet Mach number for a stator, the pressure drop must be lower, which in turn gives a higher back pressure while keeping a constant inlet total pressure and ultimately results into a higher pressure ratio.

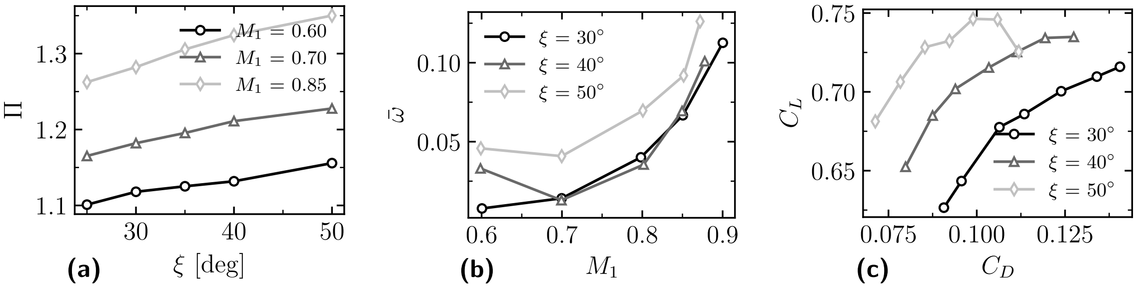

(a) **(b)** **(c)**

Figure 5.10 *Change in steady performance with stagger angle at constant incidence* $\beta_1 = 5°$ *:* ***(a)*** *Pressure ratio against stagger angle at different inlet Mach number;* ***(b)*** *Total pressure loss coefficient against inlet Mach number at different stagger angles;* ***(c)*** *Lift against drag coefficients at different stagger angles and fixed* $M_1 = 0.85$*.*

As the stagger angle increases for a constant inlet Mach number, the mass flow decreases, and so does the axial velocity component, meaning that the lift coefficient

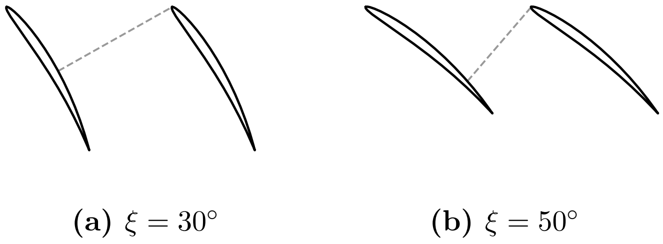

Figure 5.11 *Change in throat area with stagger angle*

must increase. At the same time, the flow deflection reduces as the covered passage length decreases, thus reducing the drag coefficient. The limiting case of zero covered passage results in near zero flow deflection which, at constant incidence, produces a larger separation on the suction side and less recovery of total pressure.

This fact is confirmed by the total pressure loss which is more severe for higher stagger angles.

The change in stagger angle produces a similar behaviour to the one observed previously due to changes in solidity. Fig. (5.12) displays the coefficients of $\boldsymbol{C}$ against interblade phase angle at two different stagger angles, which, again, shows that the magnitude of unsteady lift induced by both modes grows larger than the moment components at high σ. Fig. (5.13) shows the effect of stagger angle at two different values of interblade phase angle. Same as for solidity, the change in coefficients at low σ is much smaller than at high σ, where the variation is large enough for the pitch induced coefficients to change sign as the stagger angle is increased.

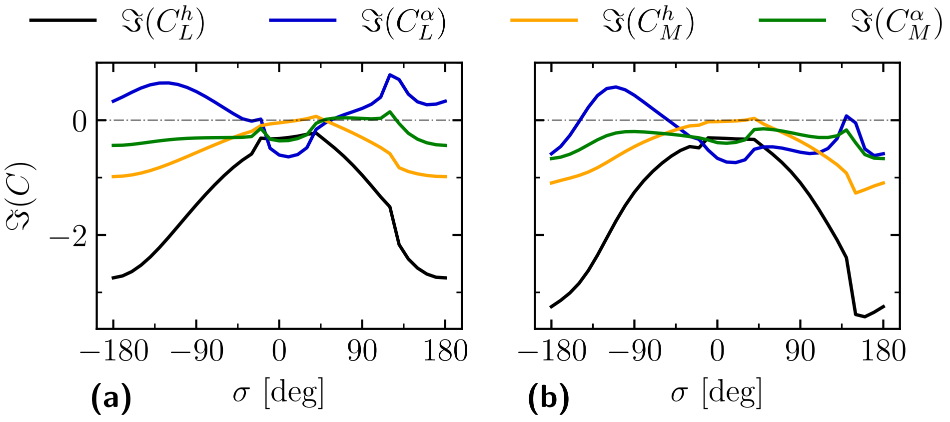

Figure 5.12 *Imaginary component of unsteady force coefficients against interblade phase angle, with fixed inlet Mach number $M_1 = 0.85$, incidence $\beta_1 = 3°$ and reduced frequency $k = 0.5$, at different stagger angles: (a) $\xi = 30°$; (b) $\xi = 50°$*

Fig. (5.14) shows aerodynamic damping against incidence, at two different stagger angles. The larger angle of attack exerts the same effect on both geometries, and, as cascades with larger stagger angle tend to stall earlier, the drop in aerodynamic damping is steeper for the case with $\xi = 50°$. The same considerations as the previous case can be drawn regarding the individual damping contributions.

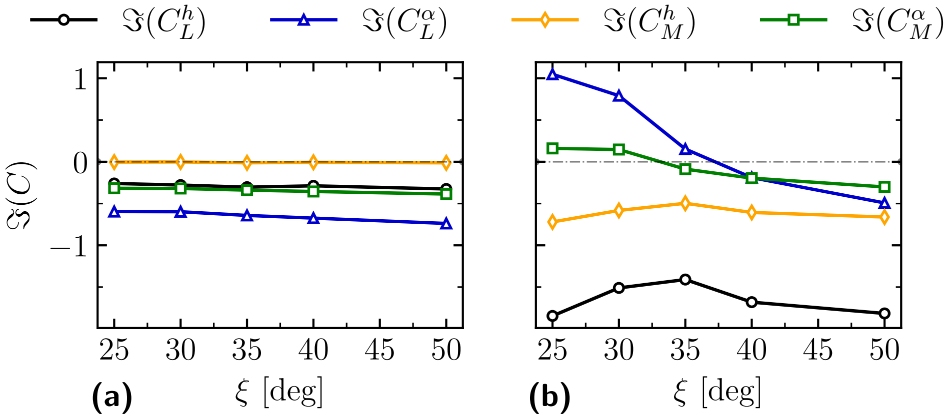

Figure 5.13 *Imaginary component of unsteady force coefficients against stagger angle, with fixed inlet Mach number $M_1 = 0.85$, incidence $\beta_1 = 3°$ and reduced frequency $k = 0.5$, at different interblade phase angle:* ***(a)*** $\sigma = 20°$ *;* ***(b)*** $\sigma = 120°$

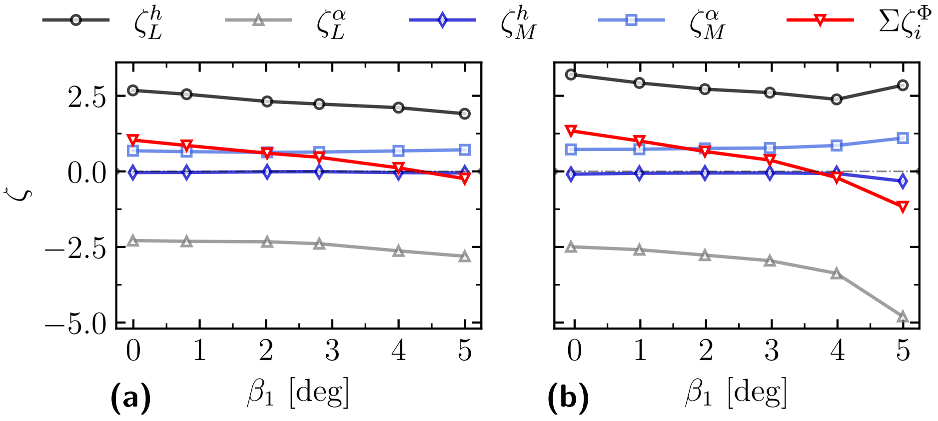

Figure 5.14 *Aerodynamic damping contributions for a flap mode at $x = 2$ as a function of incidence, with fixed inlet Mach number $M_1 = 0.85$, interblade phase angle $\sigma = 20°$, and reduced frequency $k = 0.5$, at different stagger angles:* ***(a)*** $\xi = 30°$ *;* ***(b)*** $\xi = 50°$

The plot in Fig. (5.15) shows flutter for all investigated cases at the given flow condition, with aerodynamic damping decreasing with stagger angle. This behaviour is, again, attributable to the reduction in stall margin of the cascade due to the higher stagger.

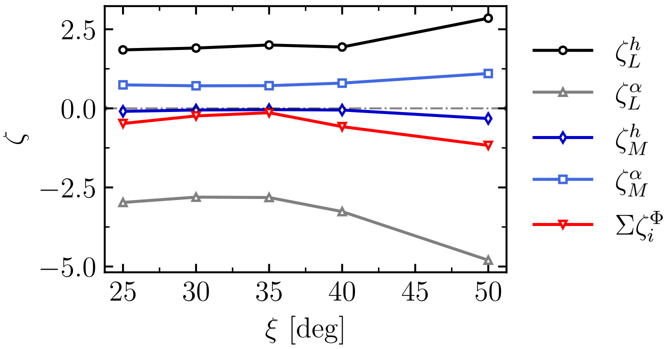

Figure 5.15 *Aerodynamic damping contributions for a flap mode at* $x = 2$*, with fixed inlet Mach number* $M_1 = 0.85$*, incidence* $\beta_1 = 5°$*, interblade phase angle* $\sigma = 20°$*, and reduced frequency* $k = 0.5$*, against stagger angle*

5.6.4 Change in camber

The blade camber is particularly important for performance design as it is closely related to the stall margin of the cascade, which, clearly, will also have an impact on aeroelastic stability.

As camber increases, the delivered pressure ratio is higher while the stall margin is reduced. The forces on the airfoil as well as the flow deflection increase as, intuitively, a more arched profile provides a larger re-direction of momentum. The total pressure losses also increase as, at given inlet Mach number and incidence, the flow separates more easily and therefore induces more losses. The results are gathered in Fig. (5.16).

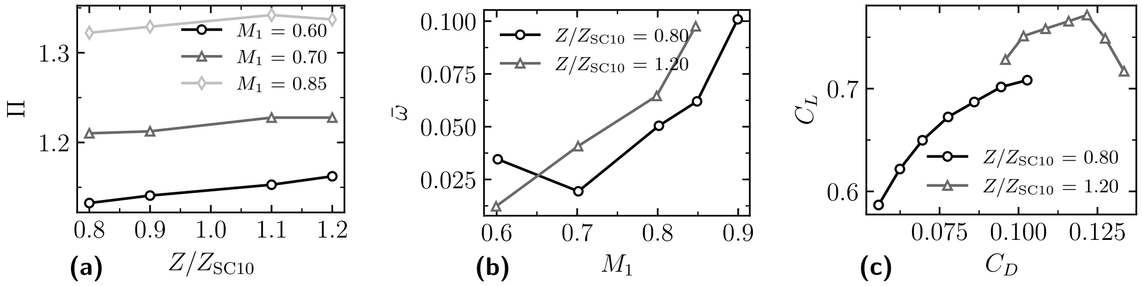

Figure 5.16 *Change in steady performance with camber at constant incidence* $\beta_1 = 5°$ *: **(a)** Pressure ratio against camber at different inlet Mach number; **(b)** Total pressure loss coefficient against inlet Mach number at different camber; **(c)** Lift against drag coefficients at different camber and fixed* $M_1 = 0.85$*.*

The behaviour of the unsteady coefficients, at low and high interblade phase angle, for different camber values is analogous to the one presented previously and it is omitted for brevity.

A more interesting trend can be seen in Fig. (5.17) and Fig. (5.18). Unlike the cascade parameters, solidity and stagger angles, changing the airfoil camber exerts a considerable influence on aerodynamic damping for the mode of interest, in particular, one can see that a reduction in camber has a beneficial effect across all inflow angles investigated. This is, again, related to the fact that a less cambered airfoil has more margin between choked flow and stall and is thus able to operate at a higher incidence without flow separation.

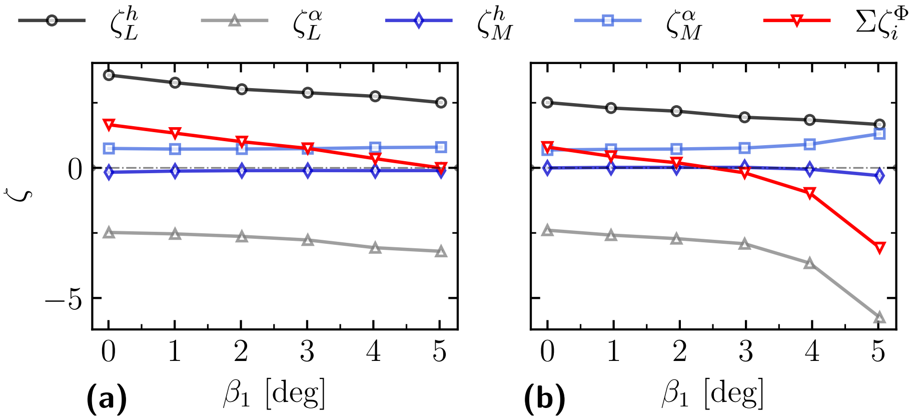

Figure 5.17 *Aerodynamic damping contributions for a flap mode at* $x = 2$ *as a function of incidence, with fixed inlet Mach number* $M_1 = 0.85$*, interblade phase angle* $\sigma = 20°$*, and reduced frequency* $k = 0.5$*, at different camber :* ***(a)*** $Z/Z_{SC10} = 0.8$ *;* ***(b)*** $Z/Z_{SC10} = 1.2$

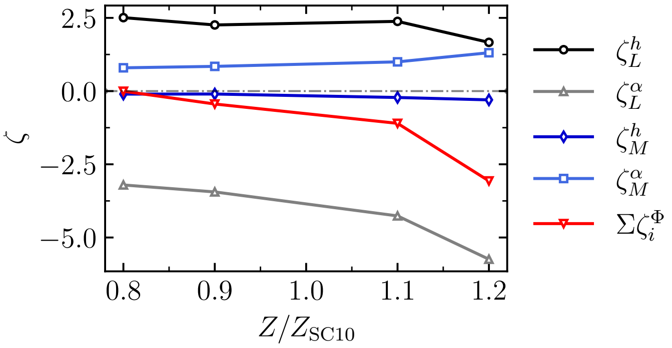

Figure 5.18 *Aerodynamic damping contributions for a flap mode at* $x = 2$*, with fixed inlet Mach number* $M_1 = 0.85$*, incidence* $\beta_1 = 5°$*, interblade phase angle* $\sigma = 20°$*, and reduced frequency* $k = 0.5$*, against camber*

A word of caution: this conclusion is not universal. If the airfoil were to be made completely uncambered or if the thickness were not fixed, then the topology of the flow at high angle of attack might change in favour of a leading edge separation, which is a case complicated enough to require a separate investigation.

5.6.5 Change in thickness

The results in Fig. (5.19) show a slight drop in pressure ratio and lift coefficient, while the drag coefficient increases as thicker airfoils tend to be more prone to flow separation. The total pressure loss increases as well.

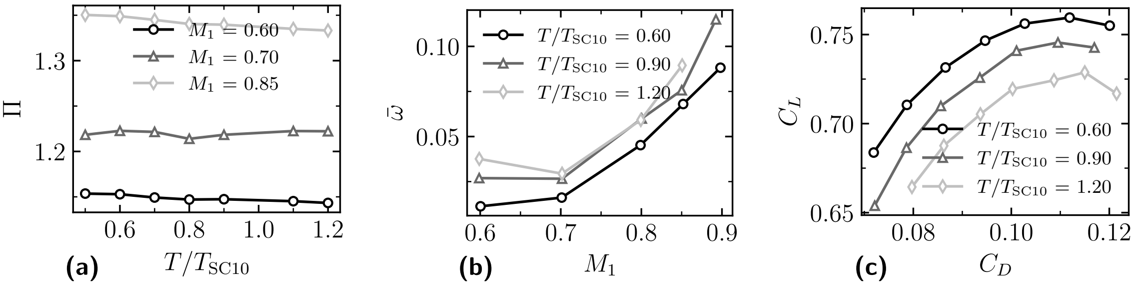

Figure 5.19 *Change in steady performance with thickness at constant incidence* $\beta_1 = 5°$ *:* ***(a)*** *Pressure ratio against thickness at different inlet Mach number;* ***(b)*** *Total pressure loss coefficient against inlet Mach number at different thickness;* ***(c)*** *Lift against drag coefficients at different thickness and fixed* $M_1 = 0.85$.

Fig. (5.20) shows a slowly decreasing trend of aerodynamic damping with thickness; three of the four contributions are largely constant across the investigated range, with the exception of that due to pitch induced lift. There is a small drop at $T/T_{SC10} = 1.1$, due to a slight departure from the desired inlet conditions, i.e. M_1 and β_1 are not exactly the same values as for the rest of the curve.

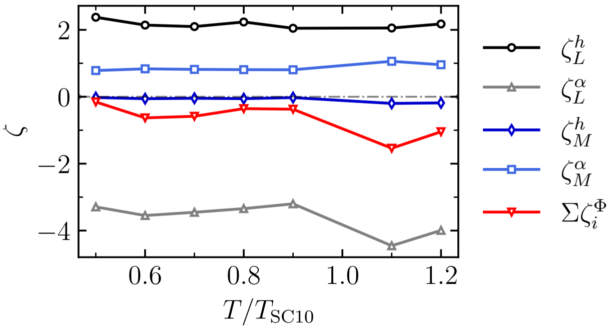

Figure 5.20 *Aerodynamic damping contributions for a flap mode at* $x = 2$*, with fixed inlet Mach number* $M_1 = 0.85$*, incidence* $\beta_1 = 5°$*, interblade phase angle* $\sigma = 20°$*, and reduced frequency* $k = 0.5$*, against thickness*

A number of conclusions can be drawn from the results presented in this Section. The magnitude of the matrix $\boldsymbol{C}$ exhibits a wide variation with interblade phase angle σ, with the lift components being usually larger than the induced moments. The investigated flow conditions are characterised by acoustic resonance at large IBPA, therefore all modifications to the geometry exert a considerable influence on the coefficients, whereas near zero interblade phase angle, where the acoustic waves are always cut-on, variation in solidity and stagger angle can only be appreciated (when compared to the order of magnitude across all IBPAs) if a significant change in steady loading and stall margin occurs. A change in camber heavily affects both quantities and is thus comparable to a change in incidence or inlet mach number. The thickness of the airfoil does not seem to produce a distinguishable trend in aerodynamic damping if the inlet conditions are kept constant.

The contribution to aerodynamic damping for a representative flap mode, due to the moments induced by both plunge and pitch, is negligible and the two appear to mostly cancel each other out and an increase in incidence, i.e. reduction of mass flow, consistently worsens stability irrespective of the cascade and airfoil geometry.

5.7 Model Selection

The surrogate model employed in the PGML framework is an FCNN. As mentioned in Section (5.2), to create a model that is capable of predicting the QoIs, a number of hyperparameters need to be tuned. The process of selecting the best setting is composed of several stages.

First, the goal of this process is to have four PGML networks, each predicting one of the quantities of interest, i.e. the components of the unsteady force matrix $\boldsymbol{C}$. This is to alleviate the burden of each machine learnt model and produce better results. Also, this is justified as mathematically these four coefficient values are decoupled.

Second, the learning dataset is composed only of the five SC10 databases introduced in Chapter (3), while the large dataset of geometry variations is held out as a validation set (more details regarding the number of computations are given in Appendix C). This means that no knowledge of change in geometry is introduced in the learning process, neither explicitly, i.e. using the data for training, nor implicitly, i.e. by finding the hyperparameters that best fit the validation set. The choice of such an approach is the true test of our hypothesis and of the quality of the input features.

Third, as per standard machine learning practice, a cross validation procedure is needed to find the hyperparameters. In this work, the common K-fold cross validation is used: the learning dataset is randomly partitioned in to K groups called folds, the PGML is trained on $K-1$ folds and the left out fold is used as test data. The number of folds is fixed at $K=5$, and as the gradient descent algorithm can fall into local optima depending on weights initialisation and data partition, the computations are repeated 16 times for each network. The output is averaged to generate a prediction, and the parameter setting yielding the best error metric is used to train the final

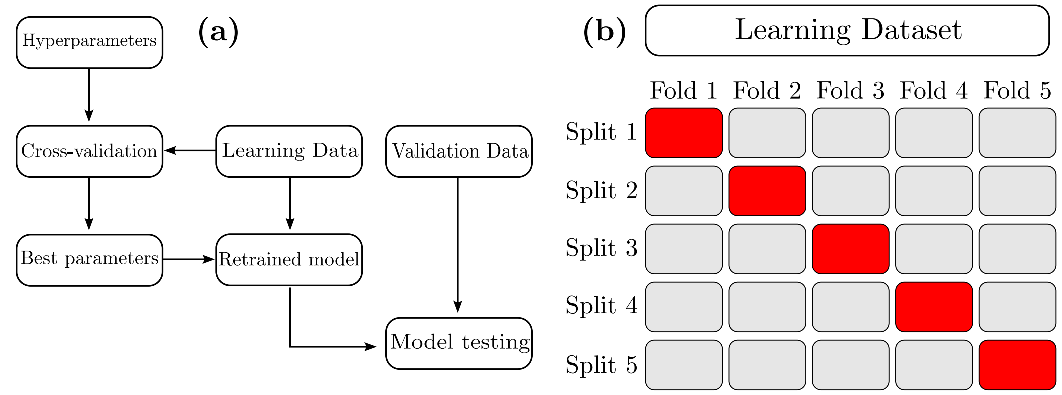

Figure 5.21 *Illustration of the PGML model selection and evaluation.* ***(a)*** *Flowchart of the full process.* ***(b)*** *Illustration of the 5-fold cross validation approach for finding the model hyperparameters, with training (* ▬ *) and test (* 🟥 *) data.*

PGML model, using all of the learning dataset. The error, or rather, the performance metric used here is the coefficient of determination R^2

$$R^2(q, \widehat{q}) = 1 - \frac{\sum_{i=0}^{m-1}(q_i - \widehat{q}_i)^2}{\sum_{i=0}^{m-1}(q_i - \bar{q})^2} \tag{5.6}$$

where q, $\bar{q}$, $\widehat{q}$ are the QoI, its mean across samples and surrogate model prediction respectively, and m is the number of samples. In this case, "best" means the greatest R^2 value. The maximum attainable value of the coefficient is $R^2 = 1$, which corresponds to a perfect model and null prediction error over all samples. Other error or performance metrics can be utilised with no change to the outcome.

Finally, as the space of possible settings is too large to be explored with a full factorial, the cross validation is run using a sample of 1024 hyperparameter combinations generated at random, by drawing from uniform distributions within the ranges specified in Appendix (A). The flowchart of the model selection process is illustrated in Fig. (5.21). The cross-validation R^2 for the four QoIs are given in Table (5.2), while the corresponding hyperparemeter settings are listed in Appendix (A).

Table 5.2 *Cross validation* R^2 *values*

	C_L^h	C_M^h	C_L^α	C_M^α
R^2	0.952	0.95	0.945	0.947

The training history of two of the PGML models are presented in Fig. (5.22), where the mean value of the cost function J across folds is plotted against the training epochs for both training and test sets. In the training process, the loss value drops over two orders of magnitude, converging near 5000 epochs. Fig. (5.23a) shows the R^2 values for the four QoIs. The performance on the training set exhibits negligible variation

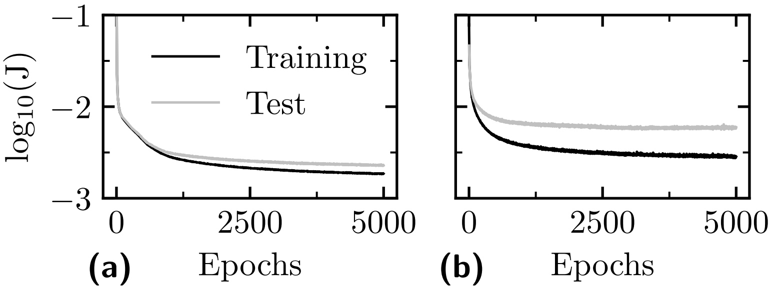

Figure 5.22 *Training history of PGML for:* ***(a)*** *Plunge induced lift coefficient* C_L^h *;* ***(b)*** *Pitch induced moment coefficient* C_M^α

across the QoIs, while the PGML framework improves the prediction capabilities of the simple FCNN ever so slightly; on the other hand, the PGML performance on the validation set varies noticeably, ranging from a maximum of $R^2 \approx 0.92$ when predicting the plunge lift coefficient, to a minimum of $R^2 \approx 0.75$ associated to the predictions of pitch moment coefficient. Furthermore, PGML performs consistently better than the FCNN, while LINSUB predicts poorly across all samples. The error distribution of

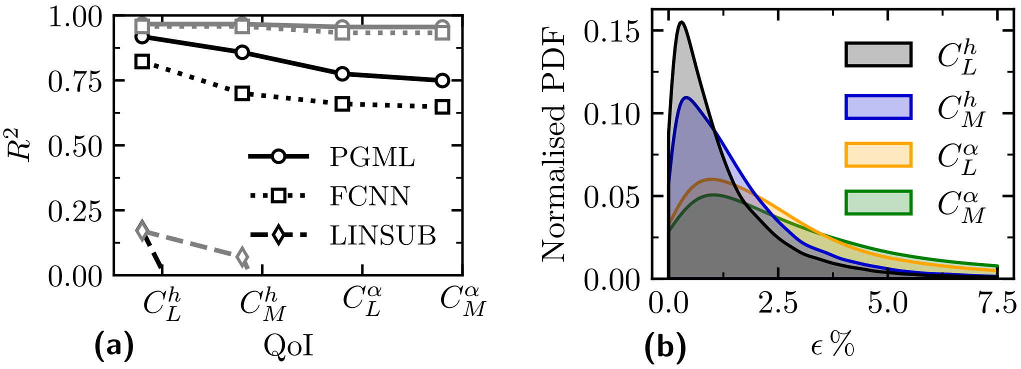

Figure 5.23 *Performance of PGML, FCNN and LINSUB:* ***(a)*** R^2 *values on training (—) and validation (—) sets;* ***(b)*** *normalised distribution of PGML relative error on validation set*

PGML on the validation set can be visualised as a probability density function (PDF). The relative error ϵ is defined as

$$\epsilon(q, \widehat{q}) = \frac{|q - \widehat{q}|}{\bar{q}} \tag{5.7}$$

Fig. (5.23b) reports the relative error distribution for each quantity of interest. For most of the validation samples, the relative errors are within 7.5%. Comparing across the QoIs, the PGML shows a generally higher accuracy in predicting plunge induced coefficients over their pitch induced counterparts, and also PGML is able to better predict unsteady lift over unsteady moments. This result is reassuring for our purposes because, as mentioned earlier, Eq. (5.2) shows that for flap modes, i.e. $x \geq 1$, the contribution of plunge induced lift to stability is dominant. These observations are in agreement with the presented R^2 values. The loss in prediction accuracy for pitch induced coefficients was anticipated in Section (5.5.2), and it is attributable to the absence of input features pertaining to the change in passage shape. As this effect is particularly relevant in pitch dominated modes, the predictions of the PGML model, although enhanced by LINSUB, result in greater errors, especially at high σ. The interblade phase angle argument is easily confirmed by plotting the QoI values from CFD against the prediction from PGML. Fig. (5.24) illustrates such a plot for all QoIs. The contour is coloured according to the absolute value of interblade phase angle and it clearly shows that, while the model performs really well at low interblade phase angles, as $|\sigma|$ is increased, the agreement between CFD and PGML degrades. The absence of a relevant feature for the prediction of pitch induced coefficient is shown in panels **(b)** and **(c)**. For several samples, the PGML model predicts nearly the same value although the coefficient computed by CFD varies considerably.

Although imperfect, the presented model fits its intended purpose: stall flutter occurs largely in the regimes where PGML performs well, i.e. flap modes, which are mostly plunge dominated, and at low interblade phase angles.

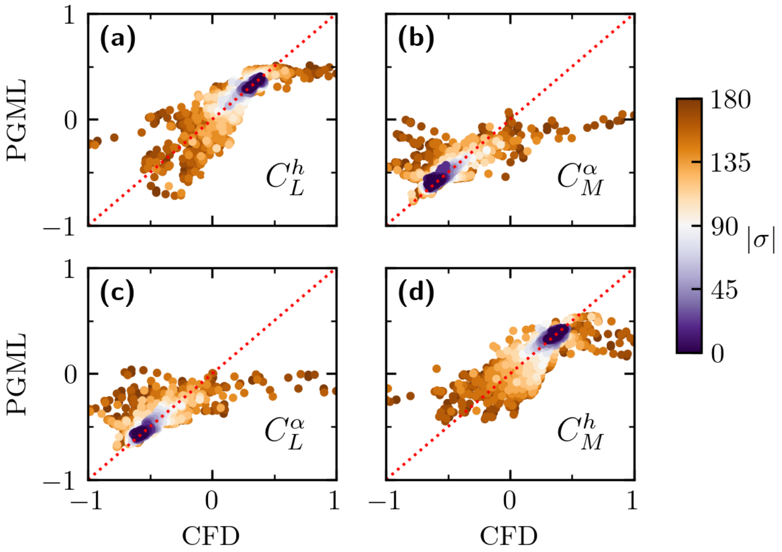

Figure 5.24 *Scatter plot of normalised QoI form validation set. The CFD and PGML predictions are on horizontal and vertical axis respectively. QoIs reported on each panel.*

5.7.1 Comparison against CFD and explanation of results

In this section, the selected machine learnt models will be examined more in depth and compared against the validation set results obtained with CFD. The validation set is composed of all the computations performed on the cascades obtained by varying the SC10 parameters one at a time. It is reiterated that, on the other hand, the training set is constituted of only SC10 computations, therefore all of the following results constitute an extrapolation in terms of geometry.

The plots in Fig. (5.25) show the behaviour of plunge induced lift and pitch induced moment with increasing solidity. The steady state conditions, $M_1 = 0.85$, $\beta_1 = 3°$, are the same for all panels. The interblade phase angle is also kept constant at $\sigma = 20°$. From left to right, the reduced frequency is respectively $k = 0.5$, $k = 0.7$, $k = 1.0$. At low interblade phase angle, as the reduced frequency is increased, the CFD and LINSUB results shift towards more negative coefficient values, corresponding to an increasingly stable configuration. This behaviour is replicated by both PGML and FCNN.

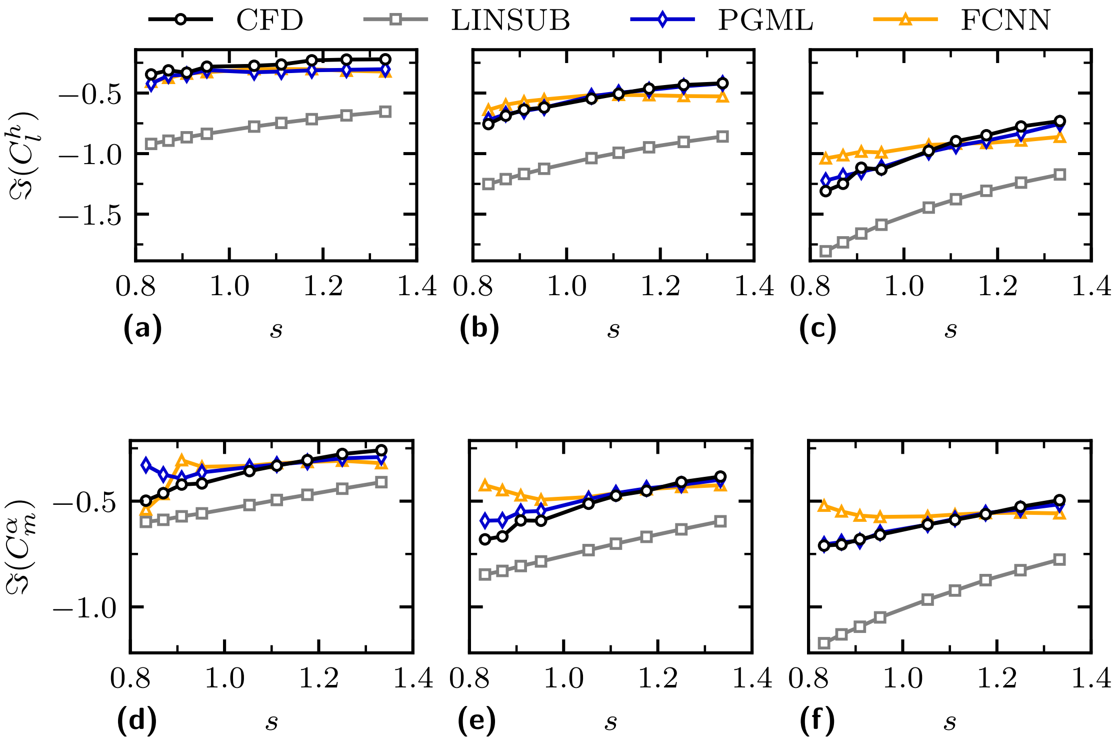

Figure 5.25 *Predictions of plunge lift and pitch moment coefficients from CFD, PGML, FCNN and LINSUB against solidity. The steady state conditions are constant at* $M_1 = 0.85$ *and* $\beta_1 = 3°$. *The panels, from left to right, are run with reduced frequency* $k = 0.5$, $k = 0.7$, $k = 1.0$, *respectively, while the interblade phase angle is constant at* $\sigma = 20°$.

The FCNN produces results that are generally close to CFD and it is able to reproduce the behaviour with increasing solidity at low frequencies, although the agreement seems to degrade both as the frequency is increased and as the cascade operates at a solidity increasingly further from $s = 1.0$. This is a foreseeable consequence of extrapolating further from the training set, i.e. a cascade with solidity $s = 1.0$.

On the other hand, the PGML model follows closely the FCNN at lower frequencies, but its predictions are visibly rectified by LINSUB at higher k, to the point that, in panels **(c)** and **(f)**, the PGML predictions become parallel to those by LINSUB and overlap with the CFD almost perfectly, while the FCNN predicts a nearly constant behaviour. Furthermore, the slope of CFD and LINSUB predictions are nearly identical throughout the frequency range and are only offset by a value.

The explanation to the similar behaviour of the computational models can be sought by investigating the unsteady loading along the blade profiles at different solidity values. As an example, the investigated conditions are those of panel **(f)** in Fig. (5.25). The loading on the flat plate, modelled in LINSUB, due to pitching motion is presented in Fig. (5.26): panel **(a)** shows the pressure jump across the flat plate, while panel **(b)** portrays the local aerodynamic work (negative means stable). Both the real and imaginary component of unsteady pressure are shown, though, as explained in Chapter (2), only the latter contributes to the aerodynamic work for these simple modeshapes. Therefore, we will refer to the imaginary component of unsteady pressure jump calculated by LINSUB as loading. The case with greater solidity is characterised by an increased loading in the fore section of the airfoil and a reduced loading in the aft section. The latter part of the airfoil contributes to the majority of the work done, due to the pitching motion taking place at the leading edge. As the phase of unsteady forcing is largely unchanged, a reduced loading results in less stabilising work done,

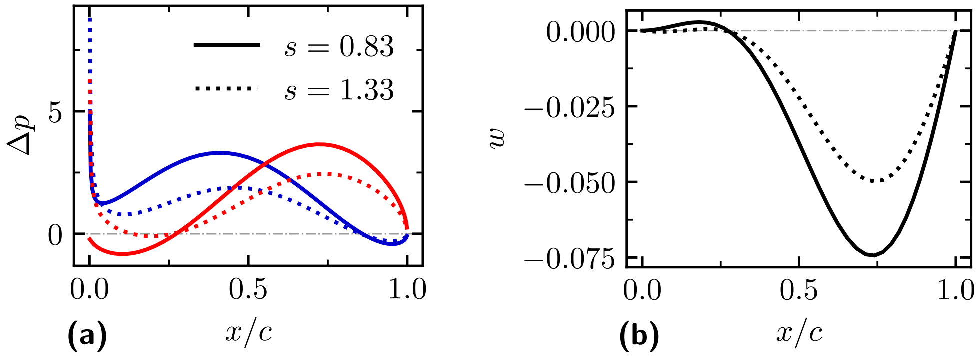

Figure 5.26 *Blade profiles due to pitching motion calculated from LINSUB:* ***(a)*** *Unsteady pressure jump, real (—) and imaginary (—) components;* ***(b)*** *Local aerodynamic work.*

therefore yielding a more unstable configuration, i.e. moment coefficient moves towards positive values.

Analogous results are extracted from CFD computations and presented in Fig. (5.27). The pressure and suction side of the blade correspond to the negative and positive abscissa, respectively, with zero being the location of the leading edge. The steady state loading is illustrated in panel **(a)** in terms on isentropic Mach number: the pressure side is unchanged, while the suction peak, and the consequent shock wave, on the suction side moves closer to the leading edge in the higher solidity case, which is a direct consequence of a reduction in the blade passage area.

The unsteady pressure coefficient and local aerodynamic work are shown in panels **(b)** and **(c)**: again, the pressure side profile shows no noticeable change and all of the difference comes from the contribution of the suction side.

The presence of a shock wave usually grabs most of the attention due to the strong spike in pressure amplitude and aerodynamic work at the suction peak; although this flow feature clearly contributes to the overall stability, we notice that after the shock the cascade with greater solidity is characterised by lower unsteady pressure and generates less stabilising aerodynamic work.

This behaviour mimics that predicted by LINSUB, which explains why the two methods show similar moment coefficient results. This is true for the investigated range, at low interblade phase angles; it would be unwise and quite possibly wrong to assume this relationship holds for solidity values far greater than the ones shown here.

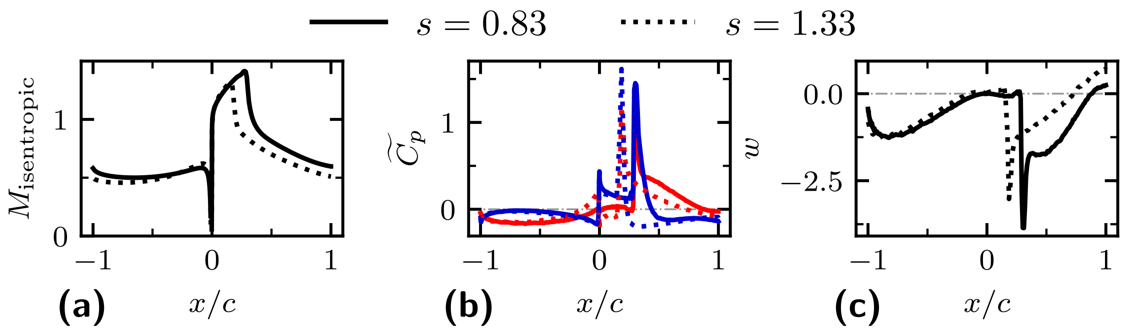

Figure 5.27 *Blade profiles due to pitching motion calculated from CFD: **(a)** Steady isentropic Mach number; **(b)** Unsteady pressure coefficient, real (—) and imaginary (—) components; **(c)** Local aerodynamic work.*

Having explained the results from the computational models, we now move onto investigating the behaviour of the machine learnt models, by calculating the importance of each feature for predictions on a specific subset of the data. The subsets in question are panels **(d)** and **(f)** of Fig. (5.25), which share the same steady state solution, but are characterised by different frequencies. The feature importance measure is the mean SHAP value

$$I_i = \frac{1}{n}\sum_{j=1}^{n} |\phi_i^{(j)}| \tag{5.8}$$

where the index i refers to a specific feature and n is the number of samples in the subset. To have a fairer comparison across different conditions, the feature importance I_i will be normalised by the magnitude of the vector of all features, so that it can only take values between 0 and 1. A value of $I_i = 1$ means that, for the set of data under examination, only feature i contributes to the prediction of the machine learnt model, while the rest of the features are unimportant. The opposite is true when $I_i = 0$. The normalised feature importance values are visualised in Fig. (5.28). The number of features shown in the plot does not include the full features set listed in Table (5.1) as inlet Mach number, frequency and interblade phase angle are kept constant.

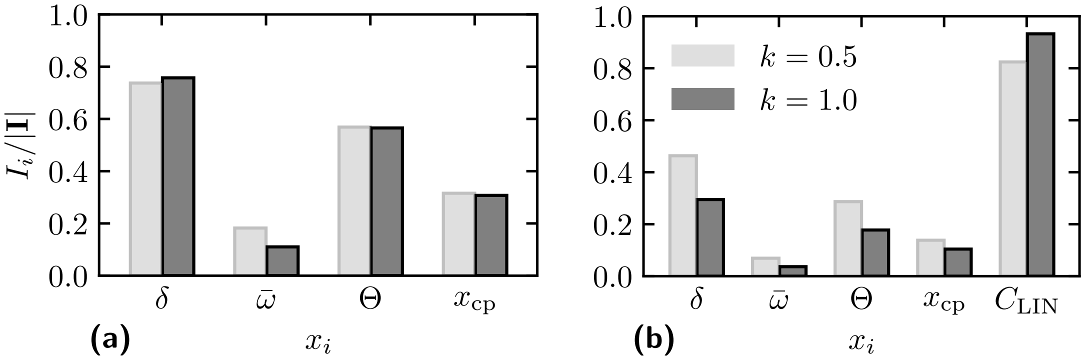

Figure 5.28 *Normalised feature importance for a dataset with changing solidity, $\sigma = 20°$: (a) FCNN; (b) PGML.*

The results for FCNN show that the model relies mostly on blockage size δ (contributions of pressure and suction side have been summed) and wake thickness Θ to generate a prediction; the location of centre of pressure x_{cp} follows while the stagnation pressure loss $\bar{\omega}$ exerts negligible influence. The change in shock location and strength is inversely correlated to the solidity, i.e. lower solidity causes the shock to move forward on the blade and creates a larger pressure drop (see Fig. (5.27a)), which in turn causes the boundary layer to separate more severely and ultimately increases blockage and wake thickness. The change in blade loading is then accompanied by the movement of the centre of pressure and by only a slight drop in $\bar{\omega}$ at this flow speed as shown in Fig. (5.5b).

The PGML results clearly show the role of LINSUB as the leading feature the model relies on to perform a prediction. The ranking of the steady state features remains the same as for the FCNN, but they become less relevant, especially with increasing frequency.

We now investigate a case with larger interblade phase angle. The plots in Fig. (5.29) show the behaviour of plunge induced lift and pitch induced moment with increasing solidity. The steady state conditions, $M_1 = 0.85$, $\beta_1 = 3°$, are the same for all panels. The interblade phase angle is kept constant at $\sigma = 150°$. From left to right, the reduced frequency is respectively $k = 0.5$, $k = 0.7$, $k = 1.0$. Unlike the low interblade phase angle case, the results from CFD and LINSUB are not simply offset by a factor, but behave rather differently with solidity.

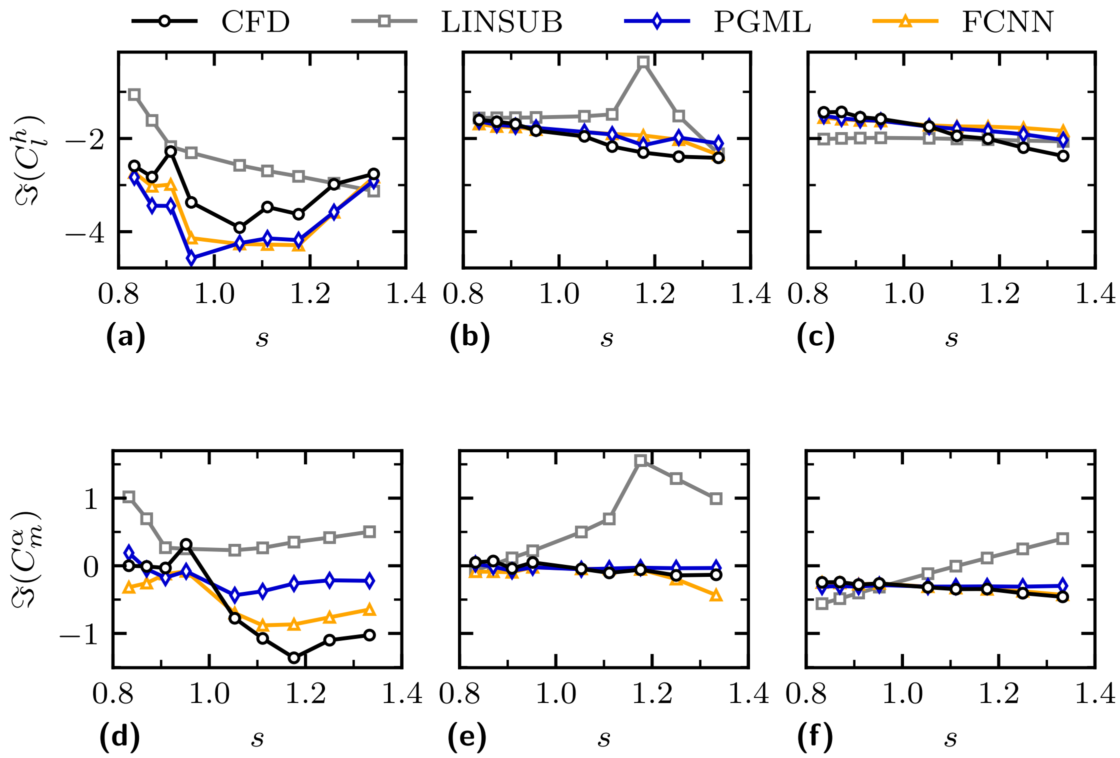

Figure 5.29 *Predictions of plunge lift and pitch moment coefficients from CFD, PGML, FCNN and LINSUB against solidity. The steady state conditions are constant at* $M_1 = 0.85$ *and* $\beta_1 = 3°$. *The panels, from left to right, are run with reduced frequency* $k = 0.5$, $k = 0.7$, $k = 1.0$, *respectively, while the interblade phase angle is constant at* $\sigma = 150°$.

With $k = 0.5$ (panels **(a)**, **(d)**), the upstream pressure field changes from cut-on to cut-off at $s \approx 0.95$, causing a spike in aerodynamic forcing, followed by a dip. After reaching a minimum, the trend is inverted and the coefficient value moves closer to zero. This non-monotonic trend is not well predicted by LINSUB, because it does not take into account the inflow angle and flow turning, hence predicting cut-off frequency at a different solidity value. PGML and FCNN approximate the shape of the CFD curve, though with some discrepancy on the predicted value.

As the frequency increases, PGML and FCNN predictions improve and nearly overlap with CFD. LINSUB produces results that move closer to CFD, but ultimately predicts a different trend with solidity. Again, we can investigate the unsteady loading and feature importance to explain the predictions of the computational and machine learnt models, respectively. The investigated conditions are those of panel **(f)** in Fig. (5.29).

The unsteady loading on the flat plate due to the pitching motion is portrayed in Fig. (5.30). The distribution of pressure jump along the chord (panel **(a)**) changes visibly with solidity. First, moving from lower to higher solidity, causes the flat plate to be more loaded from quarter chord onward; second, while the real unsteady pressure component remains positive along the chord length, the imaginary part is greater than zero for $s = 0.83$ and $x/c \geq 0.25$, whilst it stays negative for $s = 1.33$ and $x/c \leq 0.85$.

The larger amplitude translates in a larger peak of work done, while the change in imaginary pressure sign indicates a change in pressure phase with respect to blade motion and thus a different sign of aerodynamic work. Fig. (5.30b) shows the aerodynamic work: the cascade with $s = 0.83$ produces mostly stabilising work, while the opposite is true of the case with $s = 1.33$, ultimately explaining why LINSUB predicts an unstable configuration at higher solidity.

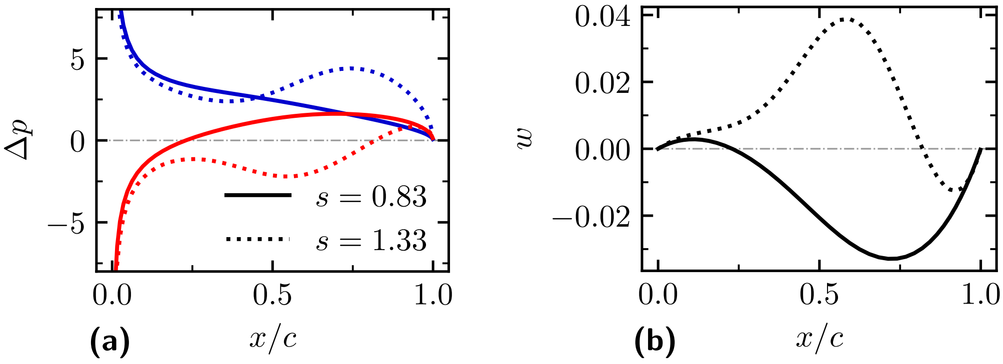

Figure 5.30 *Blade profiles due to pitching motion calculated from LINSUB:* ***(a)*** *Unsteady pressure jump, real (—) and imaginary (—) components;* ***(b)*** *Local aerodynamic work.*

The unsteady loading extracted from CFD is shown in Fig. (5.31). The steady state loading is shown in Fig. (5.27a) and is thus omitted here. Again, the difference between the two cascades comes from the unsteady pressure on the suction side: the increase in solidity produces a much larger unsteady pressure amplitude at the shock, which in turn yields a larger peak in destabilising aerodynamic work. This destabilising effect is counteracted by the work done after the shock, which has a stabilising effect. All considered, the cascade becomes more stable as the solidity increases. Unlike the low interblade phase angle case, here the blade loading does not simply offsets the predictions from LINSUB and CFD, but produces a different behaviour altogether.

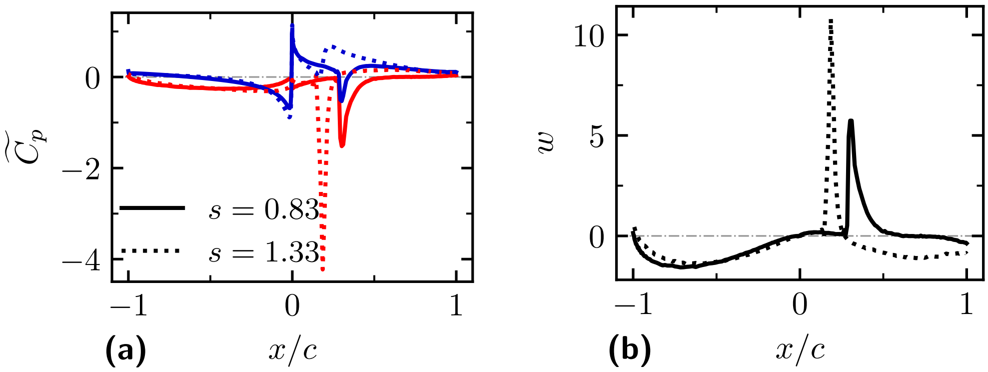

Figure 5.31 *Blade profiles due to pitching motion calculated from CFD: **(a)** Unsteady pressure coefficient, real (—) and imaginary (—) components; **(b)** Local aerodynamic work.*

The normalised feature importance is calculated on subsets composed of the data in panels **(d)** and **(f)** of Fig. (5.29), which share the same steady state solution, but are characterised by different frequencies. The results are shown in Fig. (5.32).

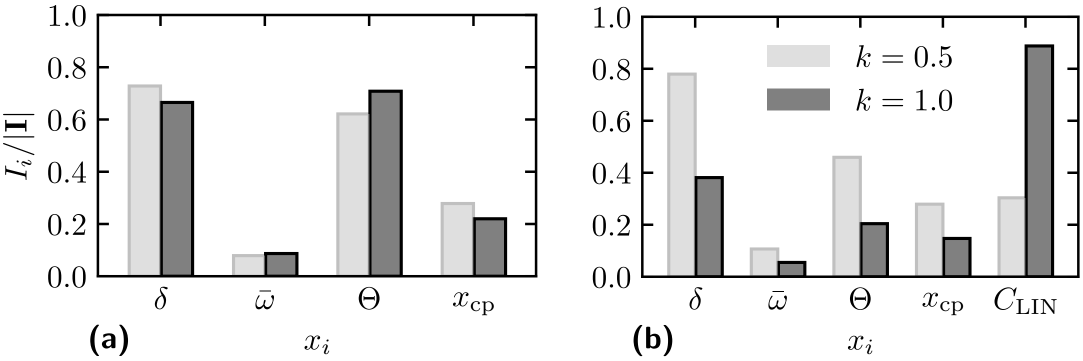

Figure 5.32 *Normalised feature importance for a dataset with changing solidity, $\sigma = 150°$: **(a)** FCNN; **(b)** PGML.*

The feature importance calculated by the FCNN is similar to that of the low interblade phase angle and does not offer any particularly new insight.

The feature importance of the PGML shows again that, at high reduced frequency, the results from LINSUB constitute the most significant feature. In contrast, the PGML seems to rely much less on LINSUB to produce predictions at $k = 0.5$ this is due to the large discrepancy in predictions between CFD and LINSUB for cases with high σ and low k, where loading and blade shape can have a large effect on the resulting aerodynamic coefficients. This behaviour displayed by the PGML is not limited to solidity variations and it does not seem influenced by the crossing of a cut-off condition: the feature importance is similar when varying the stagger angle, far from the cut-off condition (see Appendix B).

Finally, a comparison of results obtained with a sweep in camber is shown in Fig. (5.33). The steady and unsteady conditions are the same as the ones shown previously. Once again, the PGML is able to correctly predict the QoIs value across a range of conditions. We can appreciate only a small difference between the results from FCNN and PGML, and that is because the latter has learnt that LINSUB does not provide any significant guidance as the camber, and thus the loading, changes.

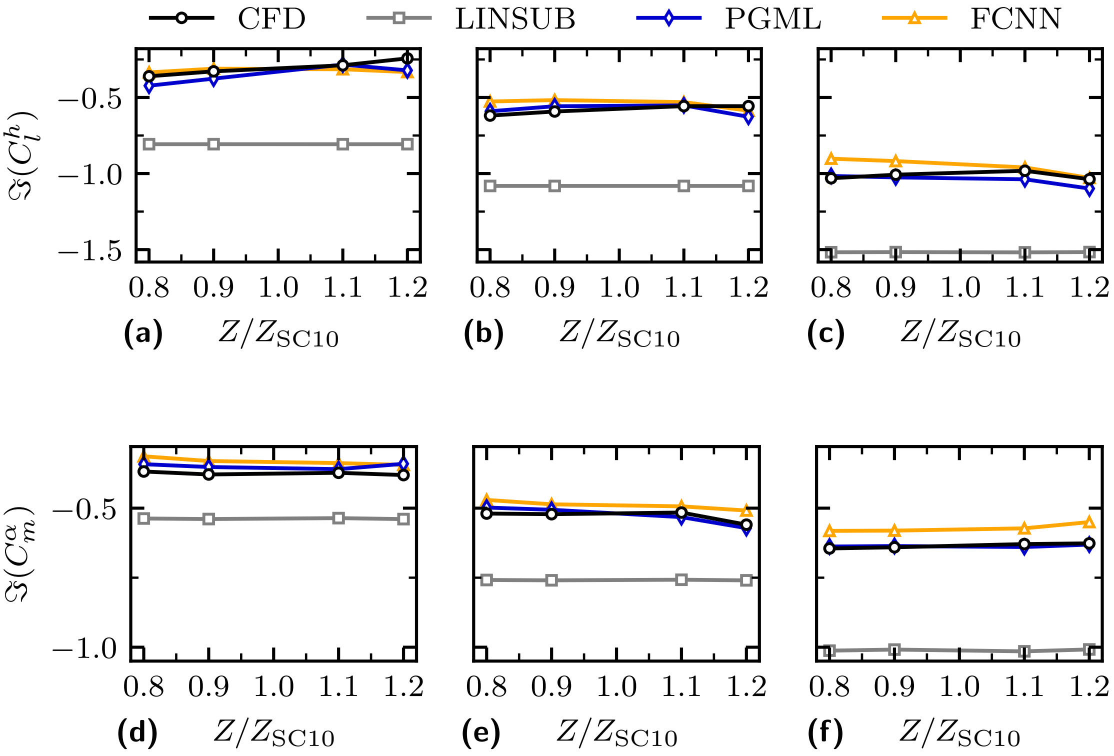

Figure 5.33 *Predictions of plunge lift and pitch moment coefficients from CFD, PGML, FCNN and LINSUB against camber. The steady state conditions are constant at* $M_1 = 0.85$ *and* $\beta_1 = 3°$. *The panels, from left to right, are run with reduced frequency* $k = 0.5$, $k = 0.7$, $k = 1.0$, *respectively, while the interblade phase angle is constant at* $\sigma = 20°$.

The feature importance in Fig. (5.34) shows this. Once again the features pertaining to blockage and flow separation are deemed the most important to make a prediction. Both models also rely on the stagnation pressure loss: as the camber increases, the cascade delivers a greater pressure ratio, but does so less efficiently and therefore the stagnation pressure loss increases. The investigated range of camber is not large enough to significantly move the centre of pressure, thus it is deemed unimportant to perform predictions on this subset. The input from LINSUB does not help capturing the change in camber, this makes intuitive sense as LINSUB is a flat plate model, though we can see that its effect is constant throughout the range, "pulling" the PGML predictions towards more negative values compared to the FCNN.

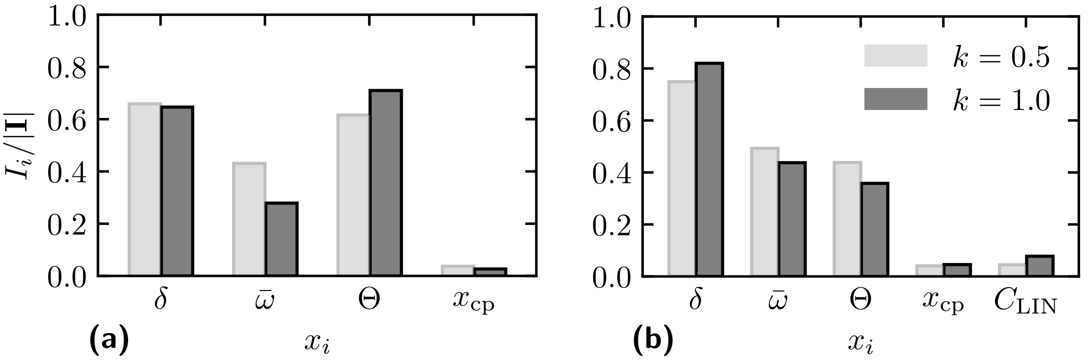

Figure 5.34 *Normalised feature importance for a dataset with changing camber: (a) FCNN; (b) PGML.*

It is important to point out that the presented local feature importance values are calculated relative to a background subset of data. For all the examples shown, we have purposefully swept one geometric variable, while keeping all the other parameters constant so that we could explain how the machine learnt model "understood" that a change in geometry was taking place. The following conclusions can be drawn:

- the PGML relies largely on the physics guidance to produce predictions when a change of solidity or stagger angle is taking place, as their effect is modelled in LINSUB; on the other hand, the FCNN has to capture these effects solely through the steady state features provided, hence producing poorer results;
- the extent to which PGML relies on LINSUB depends on the combination of interblade phase angle and reduced frequency;
- the physics input has little contribution when a change in airfoil shape is taking place, as this effect is not modelled in LINSUB; nevertheless, it still provides useful guidance by rectifying the predictions, e.g. in Fig. (5.33f) we can see the PGML output being "corrected" towards more negative values.

5.8 Increasing training database size

The results shown so far are promising, confirming the claim that the PGML framework, through the combination of carefully selected input features and a reduced order model, can improve the generalisation capabilities of a flutter machine learnt model. The method so far has relied on a single cascade geometry for training while the large database of parametric variations has only been employed as a validation set. This approach underlined the power of the proposed methodology, however it does seem unlikely that such a course of action would take place in a real design setting. In other words, we can use a small subset of the validation database to improve the PGML model. Four new geometries are added to the training database, one per parameter:

- a case with solidity $s = 0.8$
- a case with stagger $\xi = 40°$
- a case with camber $Z/Z_{SC10} = 0.8$
- a case with thickness $T/T_{SC10} = 1.1$

Only cases with $|\sigma| \leq 45°$ are added to the training. Also, rather than simply adding all of the data points from the selected geometries at once, we retrain the model several times by adding a fraction of the data each time. The hyperparameters are kept constant from the previous study. The coefficient of determination as a function of the increment in the training database size is shown in Fig. (5.35). We can see that adding more data exerts only a slight effect on the PGML model, while the FCNN performance is visibly improved, especially concerning plunge lift and moment. The results concerning the PGML model are a further confirmation of its generalisation capabilities. On the other hand, the fact that the coefficient of determination for the pitch induced forces settles around $R^2 \approx 0.75$, even though more data points are added to the training, confirms that an input feature regarding the change in passage shape is indeed required to model this mode at high interblade phase angle.

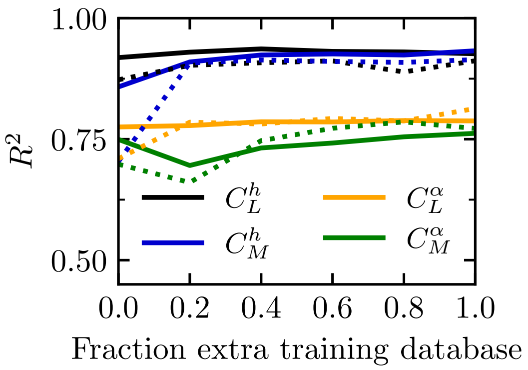

Figure 5.35 *R^2 values for PGML (——) and FCNN (······) as a function of the increment in the training database size.*

5.9 Fan Blade test case

The PGML model has so far been tested on cascades obtained as departure from the training geometry, by changing one parameter at a time. Now, one would like to test the model on a new geometry, characterised by a completely different airfoil profile which is more representative of a section of a real compressor blade.

The compressor profile is a fictitious airfoil, representative of an 80% span section of a fan blade, with chord $c = 0.1$ m, solidity $s = 1.25$ and stagger angle $\xi = 35°$. The airfoil geometry is pictured in Fig. (5.36).

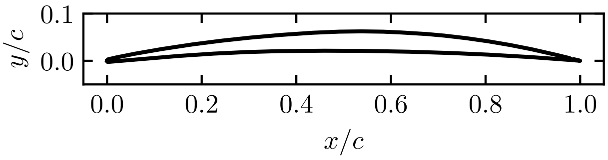

Figure 5.36 *Blade profile of a fictitious fan blade section*

5.9.1 Steady State

This section describes the main features of the steady state flow around the new test geometry. Three operating conditions are briefly examined: a subsonic, zero incidence, reference state; a transonic, positive incidence off-design condition; a transonic, negative incidence off-design condition.

Reference State

The cascade is assumed to have a subsonic design point. This reference state is characterised by an inlet Mach number $M_1 = 0.7$ and an inflow angle $\alpha_1 = 43°$, corresponding to the zero incidence condition, $\beta_1 = 0°$, defined in Section (5.6.1). The steady state solution is shown in Fig. (5.37). The contour plot shows that the flow is attached along the full length of the profile with a very thin wake. The isentropic Mach number profile, panel **(b)**, shows a large peak near the leading edge, but is otherwise smooth. The peak in isentropic Mach number is due to the small radius and thickness in the leading edge area, which leads to a strong suction even at near zero incidence.

Transonic flow, positive incidence

The transonic, off-design, operating condition described in this section is characterised by an inlet Mach number $M_1 = 0.9$ and inflow angle $\alpha_1 = 51°$, corresponding to an incidence $\beta_1 = 8°$. The steady state results, Fig. (5.38), show again the suction peak near the leading edge, followed by a strong shock wave at around quarter chord. From the contour plot, we notice only a mild flow separation despite the strong shock wave:

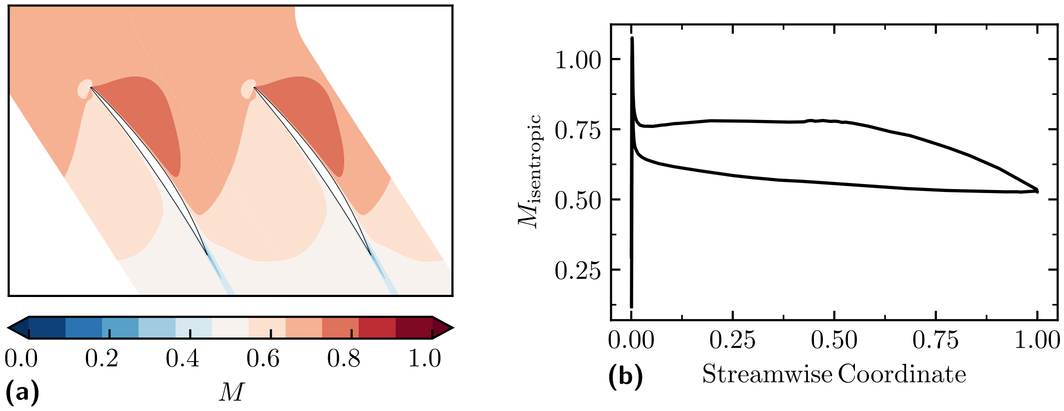

Figure 5.37 *Steady state solution at design point, $M_1 = 0.7$, $\alpha_1 = 43°$*

this is an indication of the airfoil being lightly loaded, which in turn means that the adverse pressure gradient is not very strong. The speedline of such an airfoil on a compressor map will appear rather flat.

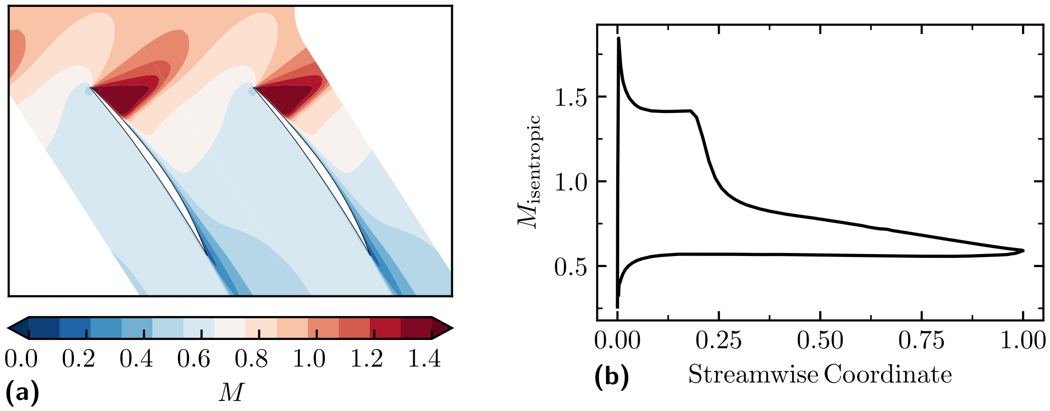

Figure 5.38 *Steady state solution near stall, $M_1 = 0.9$, $\alpha_1 = 51°$.*

Transonic flow, negative incidence

The transonic, off-design, operating condition described in this section is characterised by an inlet Mach number $M_1 = 0.9$ and inflow angle $\alpha_1 = 41°$, corresponding to an incidence $\beta_1 = -2°$. The mass flow rate is higher than nominal and the flow Mach number is greater than unity after the throat section. A shock wave covering the whole blade passage appears and impinges on suction and pressure side at three quarters chord and quarter chord respectively. The flow on the suction side consequently separates, while it stays attached on the pressure side. Again, the flow Mach number contour and isentropic Mach number around the blade are shown in Fig. (5.39)

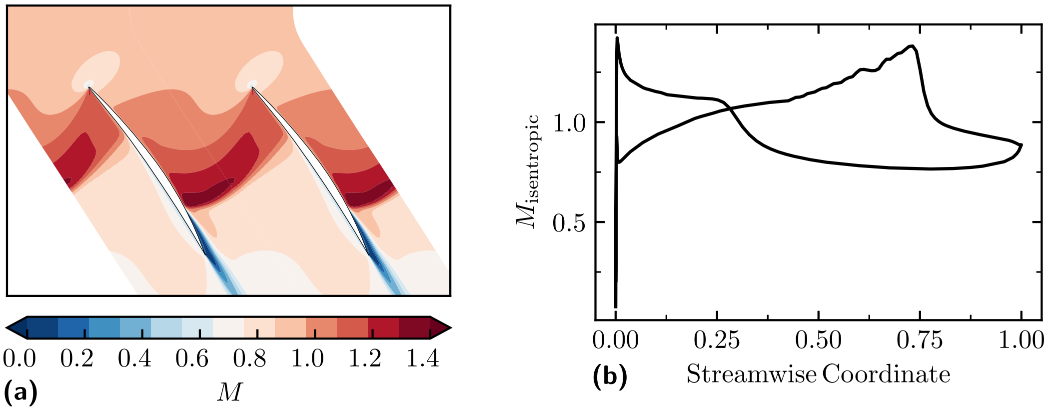

Figure 5.39 *Steady state solution near choke,* $M_1 = 0.9$*,* $\alpha_1 = 41°$*.*

5.9.2 Unsteady results and comparison with PGML

This section focuses on comparing the aerodynamic damping obtained from computation with the predictions of the PGML model. The results concern a number of operating conditions, frequencies and two relevant modeshapes from an engineering standpoint: a torsion about the center of the blade, and a flap mode about an axis one chord away from the trailing edge. These modeshapes correspond to a non-dimensional pitching axis distance $x = 0.5$ and $x = 2$, as defined in Section (4.2). We will refer to these modes simply as torsion and flap, show in Fig. (5.40). The contributions of each fundamental mode to the total aerodynamic damping are expressed in Eq. (5.2).

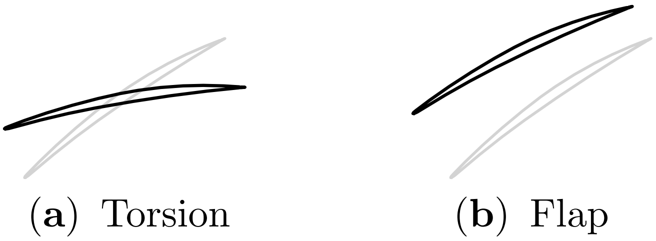

Figure 5.40 *Illustration of the torsion and flap modes used in this study.*

Design Point

The aerodynamic damping results against interblade phase angle from CFD and PGML are shown in Fig. (5.43). First and second column show plunge and pitch contributions, third column plots the total damping. The PGML prediction is the mean of 16 different networks with different initialisation, therefore a standard deviation can also be calculated. This is shown as the shaded area around the total damping. First and second row are torsion mode results with $k = 0.5$ and $k = 1.0$, while third and fourth row are flap mode results. The PGML shows excellent agreement with CFD across the full IBPA range and for both investigated frequencies, particularly for the flap mode. The plunge and pitch damping components to the torsion mode are well approximated and have comparable contributions to the total. The flap mode is dominated by the plunge lift contribution, while the pitch components are nearly zero and opposite in sign, thus cancelling each other out. These are also well captured by the machine learnt model. The PGML standard deviation grows slightly larger towards high σ, though the CFD line is always contained within the shaded area. Fig. (5.41) plots the steady blade loading, for the same inlet conditions, on the training geometry (SC10) and the current fan blade, showing a very different distribution and underlining the discrepancy between the two geometries.

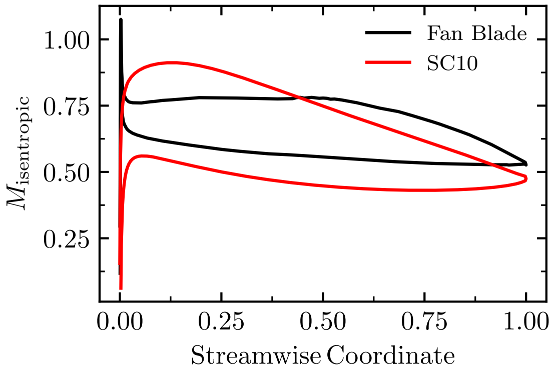

Figure 5.41 *Isentropic Mach Number profile with $M_1 = 0.7$, $\beta_1 = 0°$ of training (—) and current test (—) geometry*

Transonic flow, positive incidence

The aerodynamic damping results against interblade phase angle from CFD and PGML are shown in Fig. (5.44). This condition is more complicated than the design point: the incidence is high and the inlet Mach number is out of the training range. Nevertheless, the PGML shows, overall, very good agreement with CFD. The torsion mode is well captured at low frequency throughout most of the interblade phase angle range, with the exception of $\sigma > 135°$, while at high frequency the PGML captures the minimum damping, but predicts flutter for a larger σ range than CFD. The flap mode aerodynamic damping is also well approximated, with excellent agreement in the region of interest for stall flutter, i.e. low frequency, low σ. Similarly to above, Fig. (5.42) plots the steady blade loading, for the same inlet conditions, on the training geometry (SC10) and the current fan blade.

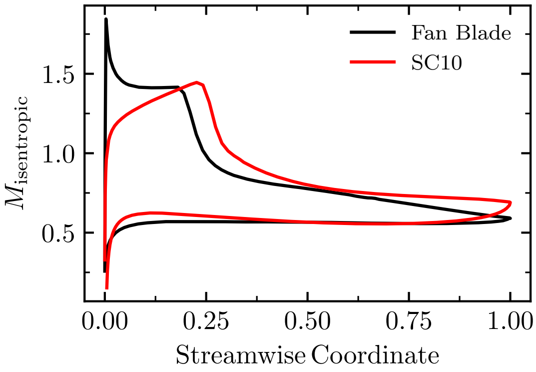

Figure 5.42 *Isentropic Mach Number profile with* $M_1 = 0.9$*,* $\beta_1 = 8°$ *of training (—) and current test (—) geometry*

Transonic flow, negative incidence

The results from CFD and PGML are shown in Fig. (5.45). The PGML fails to predict aerodynamic damping at this operating condition. This is to be expected, because the nature of energy exchange between fluid and structure in choked flow is fundamentally different from that of either classical or stalled flutter (Atassi et al., 1995; Rendu, 2016). The PGML has not been trained to predict such a flow configuration and the results clearly show it, though potential improvement, if needed, could be attained by introducing new samples to the training.

Low interblade phase angle, low frequency

So far, we have assessed the capability of the PGML model to predict the behaviour of aerodynamic damping with geometry, interblade phase angle and frequency change with fixed steady conditions. It is also important to verify that the model is able of providing reliable predictions at different steady state conditions. The results from CFD and PGML are shown in Fig. (5.46). First and second row are torsion and flap mode results with fixed inlet Mach number $M_1 = 0.9$, and show a sweep in inlet flow angle, i.e. incidence. Third and fourth row are torsion and flap mode results with a fixed inlet flow angle $\alpha_1 = 51°$, and portray a sweep in inlet Mach number. The results shown are for $\sigma = 20°$ and $k = 0.5$, a very familiar condition at this point.

The downward trend with increasing incidence is well predicted for both modes, even at high incidence, well beyond the training range set for SC10, which is $0° \leq \beta_1 \leq 6°$. The flap mode damping is under-predicted by a small amount, though the true CFD value is contained in the uncertainty band; the torsion mode damping is captured almost perfectly. In both cases, the agreement degrades at low incidence: this is due to the fact that, for this case, the null incidence value is defined using the inlet angle of the design condition, which in turn means that, for the inlet Mach number examined here, at values of $\beta_1 \leq 1°$ the cascade is in fact operating near choke. In other words the true "zero incidence" point here would be $\beta_1 = 2°$.

Similarly to above, the overall behaviour with Mach number is well approximated by the PGML with only small differences that are contained within the one standard deviation range.

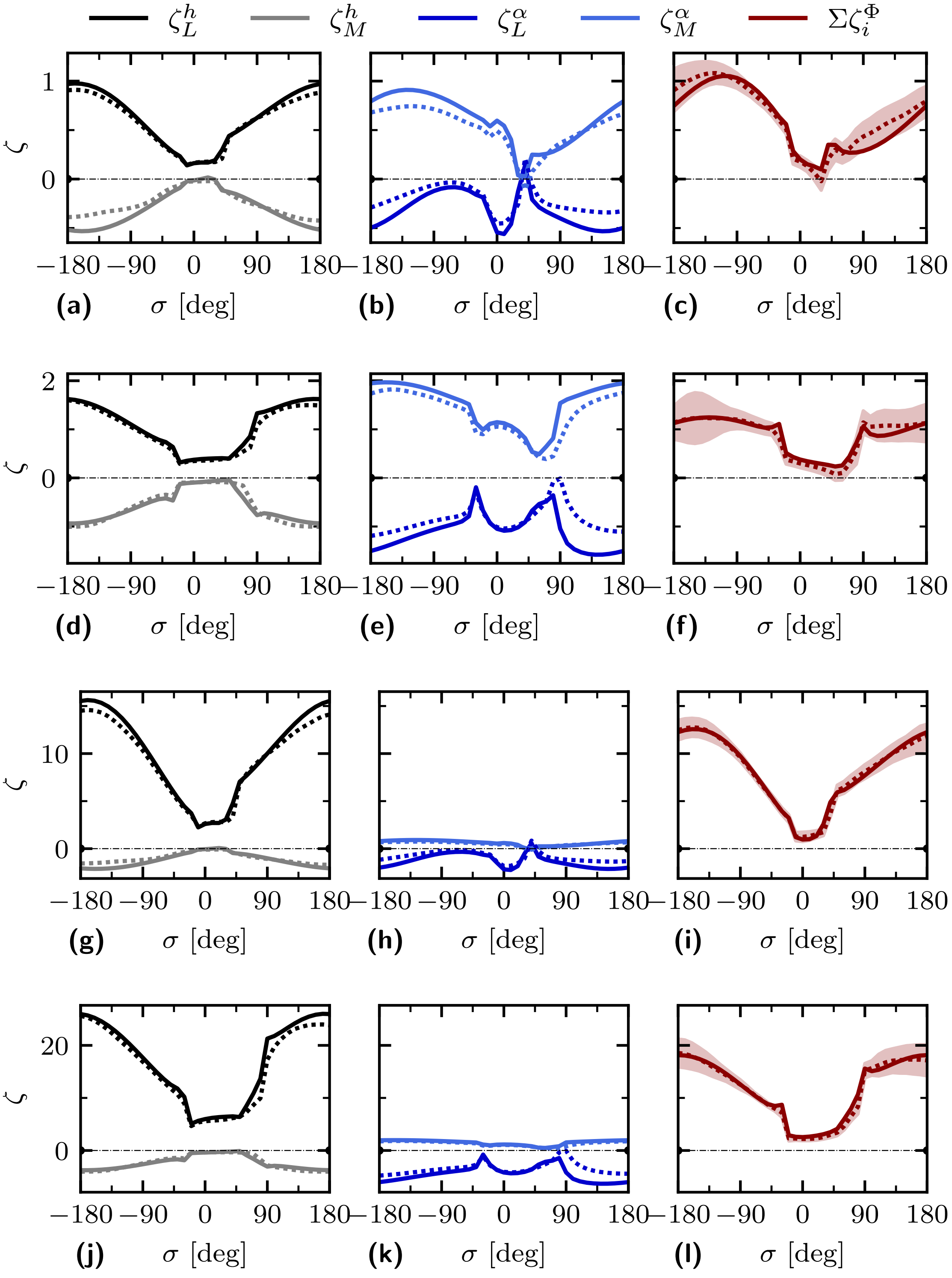

Figure 5.43 *Aerodynamic damping predictions from CFD (—) and PGML (······) at design point, $M_1 = 0.7$, $\alpha_1 = 43°$. First and second column show plunge and pitch contributions, third column plots the total damping. The shaded area is one standard deviation obtained from the different PGML predictions. First and second row are torsion mode results with $k = 0.5$ and $k = 1.0$. Third and fourth row are flap mode results.*

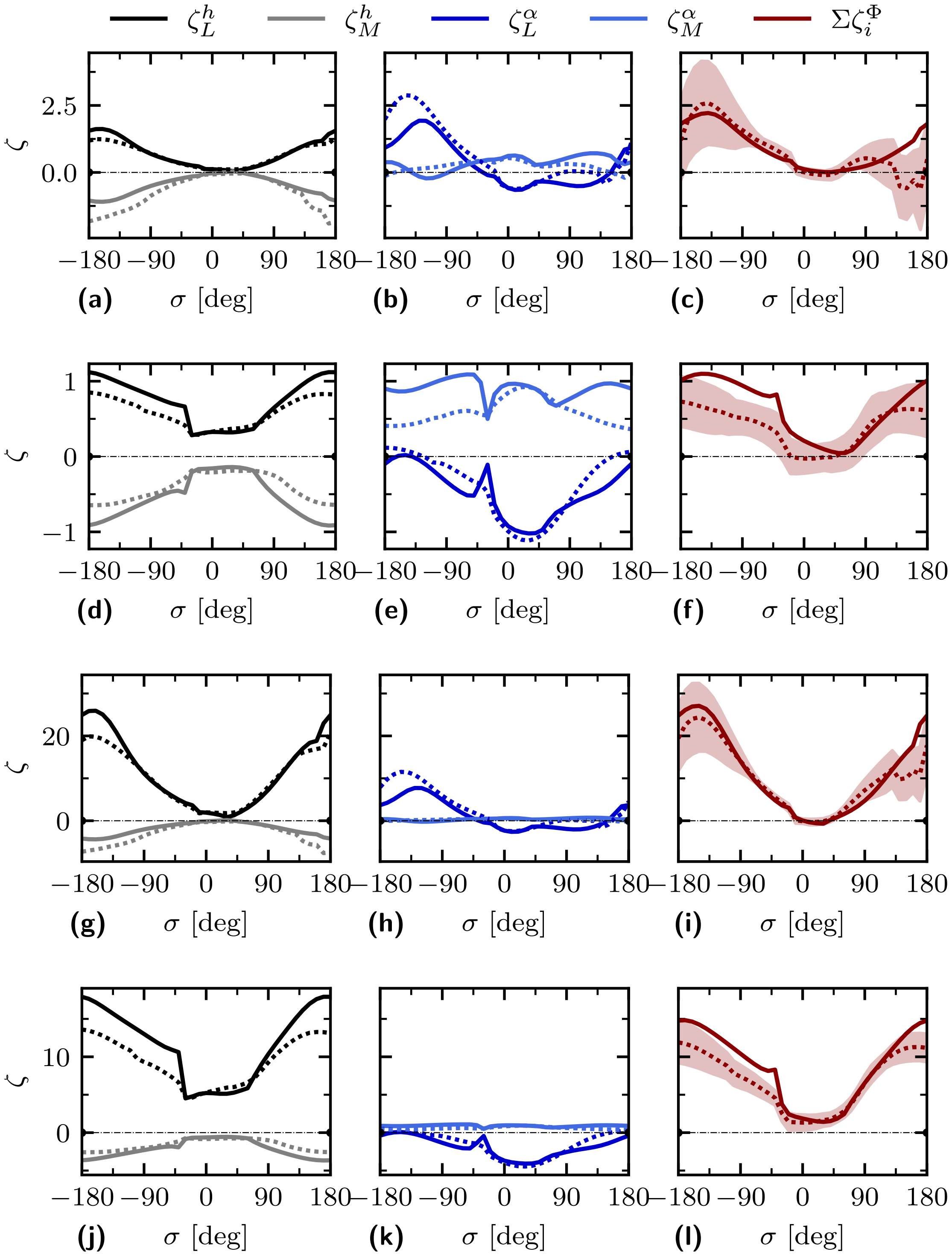

Figure 5.44 *Aerodynamic damping predictions from CFD (—) and PGML (······) with* $M_1 = 0.9$*,* $\alpha_1 = 51°$*. First and second column show plunge and pitch contributions, third column plots the total damping. The shaded area is one standard deviation obtained from the different PGML predictions. First and second row are torsion mode results with* $k = 0.5$ *and* $k = 1.0$*. Third and fourth row are flap mode results.*

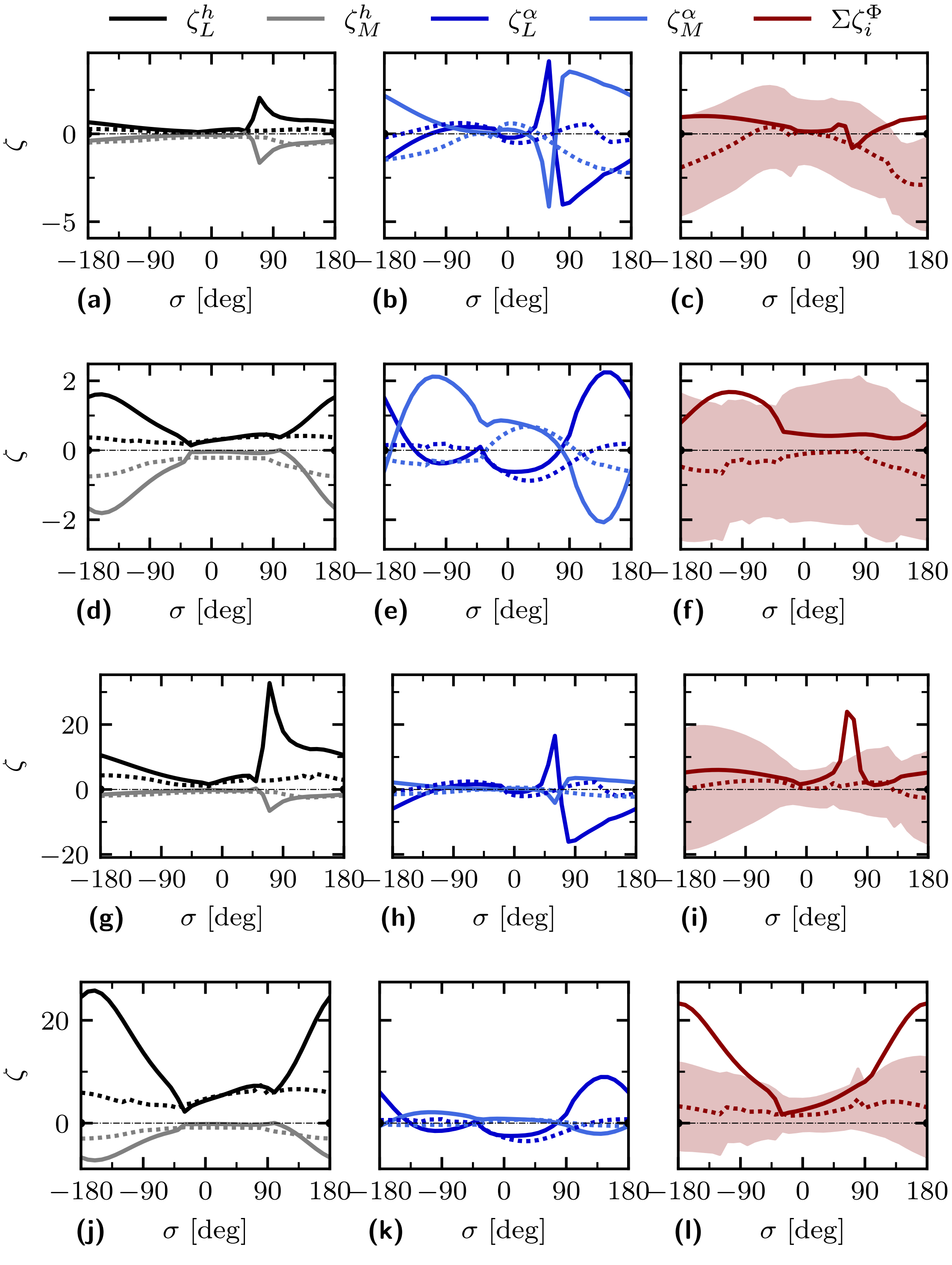

Figure 5.45 *Aerodynamic damping predictions from CFD (—) and PGML (······) with $M_1 = 0.9$, $\alpha_1 = 41°$. First and second column show plunge and pitch contributions, third column plots the total damping. The shaded area is one standard deviation obtained from the different PGML predictions. First and second row are torsion mode results with $k = 0.5$ and $k = 1.0$. Third and fourth row are flap mode results.*

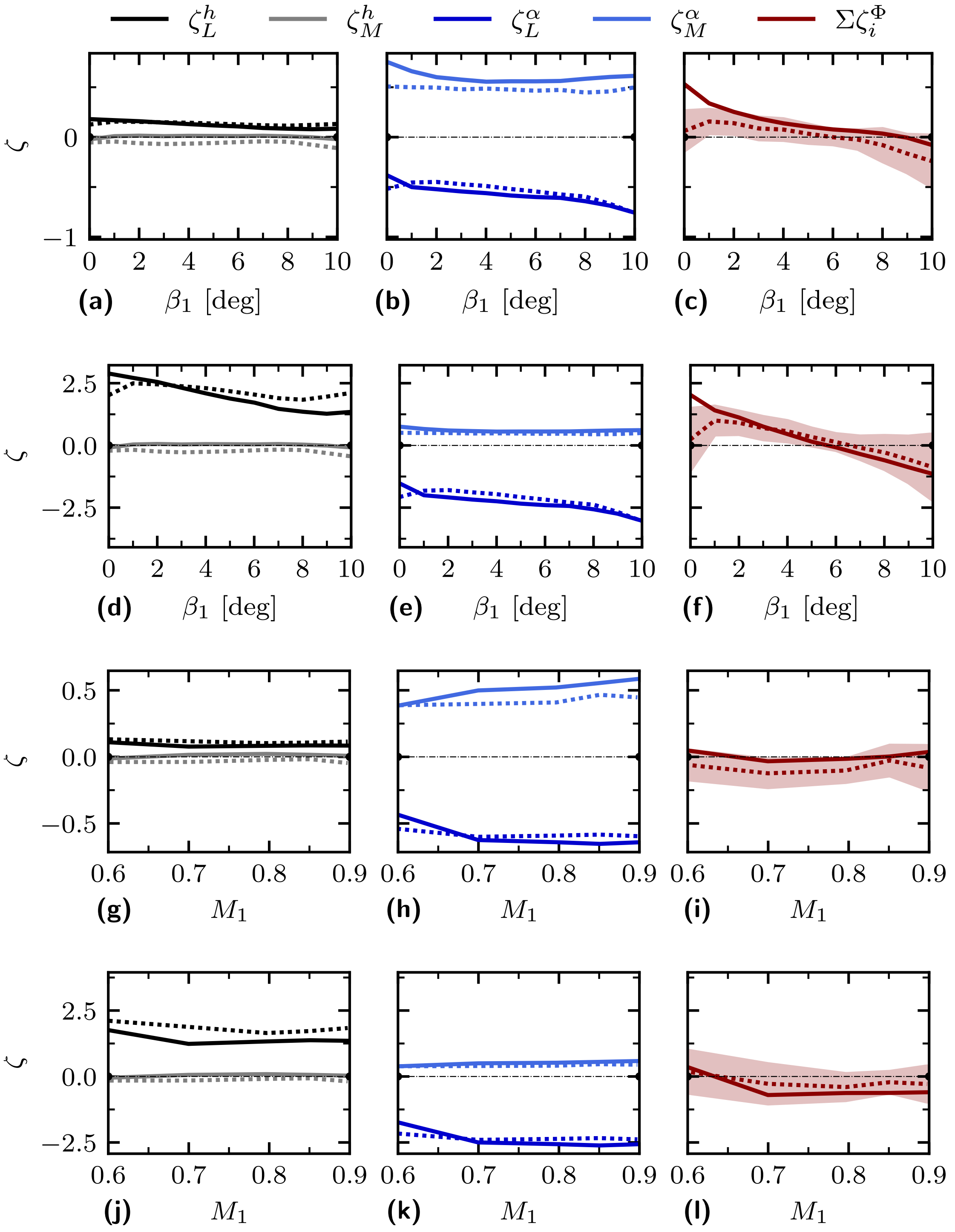

Figure 5.46 *Aerodynamic damping predictions from CFD (—) and PGML (······) with $\sigma = 20°$, $k = 0.5$. First and second column show plunge and pitch contributions, third column plots the total damping. The shaded area is one standard deviation obtained from the different PGML predictions. First and second row are torsion and flap mode results with $M_1 = 0.9$. Third and fourth row are torsion and flap mode results with $\alpha_1 = 51°$.*

Stability maps with design parameters : modeshape and reduced frequency

Two important design parameters for compressor blades are obviously reduced frequency and modeshape. Once the aerodynamic flow has been calculated, the PGML can quickly evaluate aerodynamic damping for a large number of frequency-mode pairs, in order to provide stability maps to designers.

An example of such stability maps is shown in Fig. (5.47). Each row of the figure corresponds to a different inlet Mach number, respectively $M_1 = 0.6, 0.7, 0.8, 0.9$, with a fixed inlet angle of $\alpha = 51°$ to ensure that each condition exhibits flutter and an interblade phase angle $\sigma = 0°$. The choice of zero σ is due to the fact that, in a design environment, this condition would be the simplest and the first assembly mode to be simulated and examined. The columns of the figure show results from CFD, PGML and also from the simple FCNN. The horizontal axis of each panel is the non-dimensional axis distance x, where $x = 0$ corresponds to a torsion about the leading edge, $x = 1$ about the trailing edge. The vertical axis is the reduced frequency. The black solid line is the zero damping line, while the dashed line represents the zero damping line obtained with ± 1 standard deviation from the mean PGML predictions.

First of all, we can see that the trend of aerodynamic damping with x is consistent for all Mach numbers shown. A pure pitching about the leading edge is highly stable throughout the reduced frequency range; at $x = 0.5$, that is a torsion mode, the aerodynamic damping starts to quickly decrease and reaches a minimum at $x \approx 1$. As the pitching axis moves away from the blade, the aerodynamic damping increases again and the cascade regains stability at $x \approx 2$. This behaviour had already been shown in Chapter (3) and in the literature provided. It is interesting to see that, at subsonic conditions (first and second rows of Fig. (5.47)), the zero damping line, or stability boundary, engulfs a large area, even at high reduced frequency. On the other hand, the transonic cases exhibit a much smaller region of instability.

Moving onto the comparison with the machine learnt models, we notice that the FCNN is able to approximate the CFD trends, but largely overpredicts the aerodynamic damping value, hence is not able to provide a flutter boundary for most of the flow conditions. The PGML follows the CFD trends closely, especially at lower Mach numbers, while it undepredicts aerodynamic damping at $M_1 = 0.9$. From panel **(k)**, we can see that the PGML predicts flutter for a larger range of reduced frequencies than CFD, thus reducing the available design space. Nevertheless, the values predicted by both CFD and PGML are quite close to zero and the region of largest discrepancy, i.e. $0.5 \leq x \leq 1$ and $0.75 \leq k \leq 1$, is hardly of interest since flap modes are characterised by a pitching axis that is normally downstream of the trailing edge.

We can further investigate stability as a function of frequency and modeshape by "slicing" the maps. Fig. (5.48) shows results at constant steady conditions $M_1 = 0.9$, $\alpha_1 = 51°$, and interblade phase angle $\sigma = 0°$. First and second row are sweeps of frequency for torsion and flap mode respectively, third and fourth row show a sweep of pitching axis for $k = 0.5$ and $k = 1.0$. The PGML predicts the trend with frequency correctly, while the aerodynamic damping is offset by a small value, which is roughly constant throughout the investigated range. It is interesting to notice that, as the frequency increases, the damping contribution of the cross terms, plunge induced moment and pitch induced lift, become more negative, while the higher damping is attributable to the increase of, mainly, the plunge induced lift component. Regarding the modeshape sweep, again the trend is well captured with CFD and PGML predictions nearly overlapping.

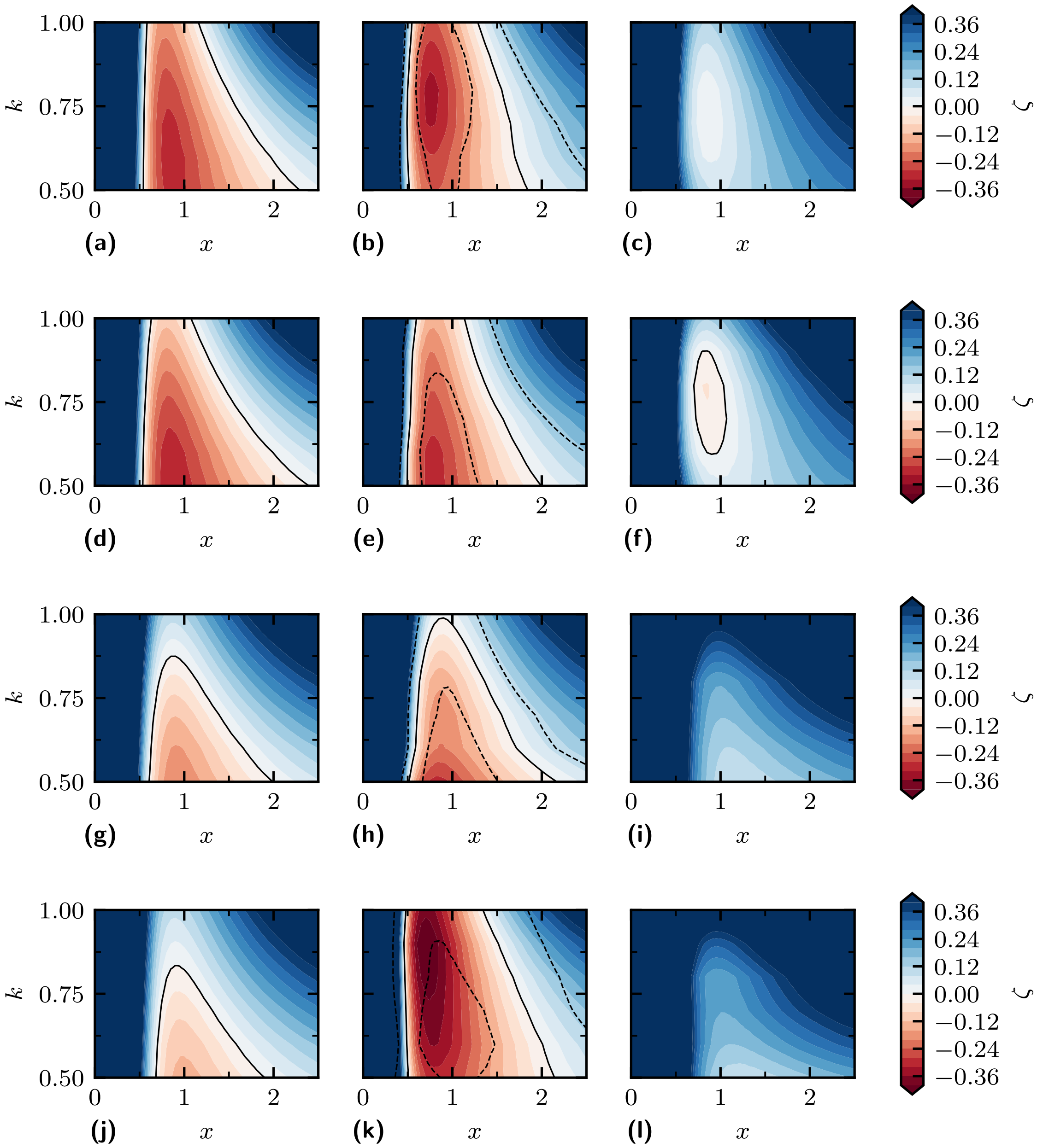

Figure 5.47 *Aerodynamic damping maps with modeshape and reduced frequency. Rows one to four show results for inlet Mach numbers* $M_1 = 0.6, 0.7, 0.8, 0.9$*, respectively. The three colums are results from CFD, PGML and FCNN. The inlet flow angle and interblade phase angle are fixed at* $\alpha = 51^\circ$ *and* $\sigma = 0^\circ$*. The solid line (—) shows the zero damping line, while the dashed line (- - -) marks the zero damping line obtained with* ± 1 *standard deviation from the mean PGML predictions.*

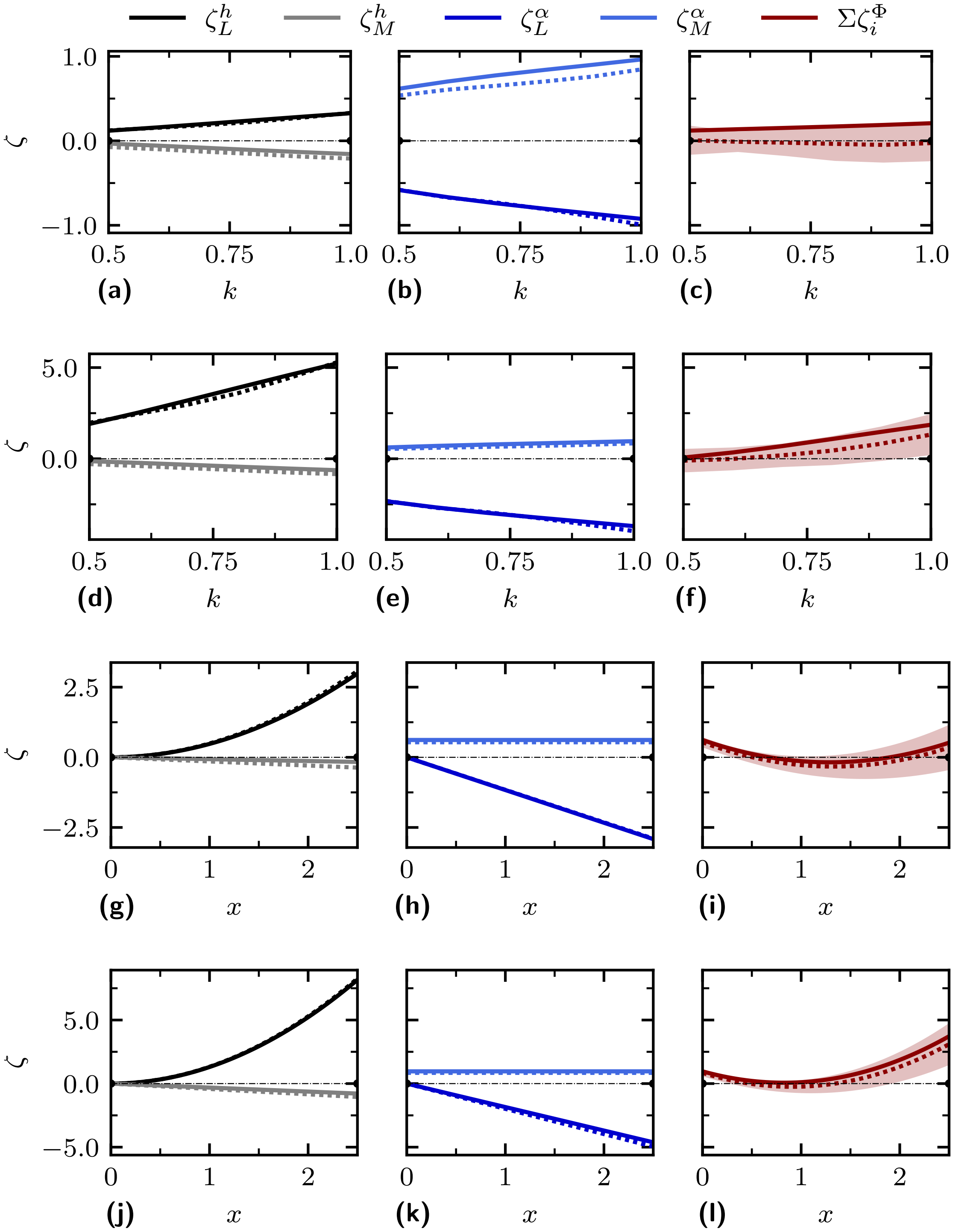

Figure 5.48 *Aerodynamic damping predictions from CFD (—) and PGML (······) with* $\sigma = 0°$, $M_1 = 0.9$, $\alpha_1 = 51°$. *First and second column show plunge and pitch contributions, third column plots the total damping. The shaded area is one standard deviation obtained from the different PGML predictions. First and second row are torsion and flap mode results as a function of reduced frequency* k. *Third and fourth row are results as a function of pitching axis* x *for* $k = 0.5$ *and* $k = 1.0$, *respectively.*

Flutter boundary on a compressor map

Although the test cascade is stationary, a compressor map equivalent to that of a rotor can be found. The constant wheel speed lines are substituted by lines of constant inlet mach number M_1 which are obtained iteratively: a value of back pressure is first imposed as outlet boundary condition, the steady-state flow is calculated and, after extracting the inlet thermodynamic quantities, the outlet pressure is adjusted and the process is repeated until convergence to a target M_1 is obtained. Each point on a fictitious speed line represents a 1° increment in flow incidence. As the blades do not impart any work on the fluid, the mass flow is plotted against static pressure ratio rather than total pressure ratio. Fig. (5.49) shows such a compressor map; the axes are normalised by the reference mass flow and pressure ratio values calculated at nominal conditions, i.e. $M_1 = 0.7$, $\alpha_1 = 43°$. The flutter boundary for a flap mode with $x = 2$ is obtained with the following approach: for each point on a speed line, unsteady computations are run at a fixed interblade phase angle and frequency; if aerodynamic damping changes sign from one point to the next, the flutter boundary is placed there. The process is repeated for all interblade phase angle and frequencies and the boundary is placed at the minimum pressure ratio where the crossing occurs. In this case, the interblade phase angle at the flutter boundary is in the range $0° \leq \sigma \leq 20°$, while the frequency is $k = 0.5$. This task is performed independently for CFD and PGML. We can see that there is good agreement and, although the PGML overpredicts the location of the flutter boundary, the true CFD value is contained within 1 standard deviation of the PGML prediction. We reiterate that the standard deviation in question comes from the fact that the PGML predictions are the mean of the output from 16 networks trained independently; therefore the shaded area in Fig. (5.49) gives an indication of the uncertainty of the PGML predicted value.

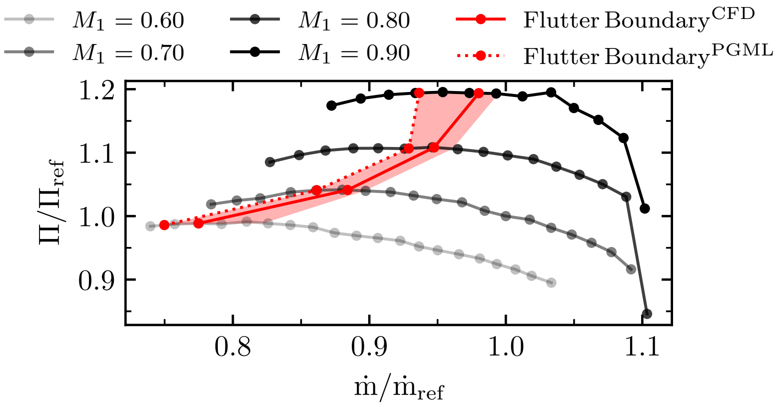

Figure 5.49 *Compressor map with flutter boundary calculated from CFD and PGML. The shaded area corresponds to the flutter boundary within* 1 *standard deviation from the mean PGML prediction.*

5.10 Summary

In this Chapter, a physics guided neural network model has been presented.

The model leverages the PGML framework which is comprised of a fully connected neural network in which predictions of the QoIs from a reduced order model (ROM) are injected at some hidden layer. The ROM employed in this work is LINSUB, a semi-analytical method which models the aeroelastic response of a cascade of unloaded blades, accounting for important parameters such as cascade geometry and flow compressibility. The required data for model training was generated using CFD. The input features to the PGML are steady state quantities that are relevant for stall flutter and carry information regarding the cascade and blade geometry as well as blade loading. The unsteady input features are interblade phase angle and reduced frequency. The QoIs are four unsteady quantities, two lift and two moment coefficients, induced by two basic modeshapes: a plunge orthogonal to the chord line, and a pitch about the leading edge. In this way, the QoIs can be combined to predict aerodynamic damping for any flapwise bending modeshape. The current implementation of the PGML thus requires a steady CFD computation at prediction time to obtain the input features. Such an approach allows us to train the model on a reduced number of training samples as there is no need to pass the geometry directly as an input feature, which would require an unfeasible number of computations to build the training database.

The PGML is first trained with SC10 data only. The hyperpameters are tuned with a random search approach and the best model is selected with a 5-fold cross validation which, again, only employs SC10 data. Consequently, the model is tested on a large database of cascades and it is found that the PGML can predict the QoIs with good degree of accuracy, especially in the low interblade phase angle region, which is of most interest for stall flutter. It is also found that the prediction accuracy for plunge induced coefficients is higher than the pitch induced ones, due to the lack of an input feature pertaining to change in passage shape.

The model is enhanced by adding a small number of samples from four different cascades and it is then tested on a geometry resembling a fan blade section. The results show very good agreement in both subsonic and transonic flow. The PGML is also able to closely resemble the flutter boundary of the test blade computed with CFD.

Chapter 6

Uncertainty of Aerodynamic Damping Predictions

The contents of this chapter have been in part published in Rauseo et al. (2022).

6.1 Introduction

The model presented in Chapter (5) proved that a combination of theory based reduced order models and meaningful inputs is a possible solution to obtain a machine learning model with generalisation capabilities. The model was able to reproduce the results from CFD with good degree of accuracy across a range of unseen geometries and operating conditions. The PGML model is built on the assumption that the computational data used for training is fully deterministic, however, although the calculations are in fact deterministic in nature, CFD can be affected by several sources of error and uncertainty. The study of uncertainty in CFD and its quantification is an active field of research. There can be several sources of uncertainty in CFD and the short summary presented here is based on a small section of the volume by Montomoli (2019).

Uncertainties in initial and boundary conditions can lead to significant errors in the predicted flow behaviour. For instance, imposing inaccurate velocity and pressure profiles at the boundaries can impact the simulation results. Unsteady aeroelastic computations in non-linear, time-accurate solvers are prone to reflection of pressure waves from the boundaries that can significantly alter the flow field (Zhao et al., 2016). The solution to this problem needs a strict oversight, and requires an extension of the computational domain with the mesh being progressively coarsened in order to numerically dissipate the waves before they reach the boundaries. This procedure is costly and, in itself, prone to errors due to discretisation of the domain. It may also cause unintentional spurious reflections from within the domain. The numerical modelling used in CFD is also a source of uncertainty. The accuracy of the numerical method, spatial and temporal discretisations, solver convergence, and, notably, turbulence modelling are all sources that contribute to the uncertainty of computational results.

The simplifications and assumptions of a computational model can introduce errors in the model, which can propagate and also increase uncertainty. Finally, manufacturing tolerances and in-service degradation to components can alter a blade profile enough to render its behaviour considerably different from that predicted with CFD, which normally only accounts for predictions on the nominal shape.

In the context of flutter, all these sources of uncertainty produce differences in mean flow aerodynamics, which can lead to significant discrepancies in aerodynamic damping in the presence of shocks and separation, due to the large unsteady pressures these flow features induce. Several examples of such sensitivity to the mean flow field can be found in literature.

Shibata and Kaji (1998) performed a linearised Euler analysis to study the influence of shock structures on the flutter boundary of a transonic rotor tip section. The authors increased the pressure ratio across the rotor, following a constant wheel speed line, and found that, as the shock is expelled from the covered passage, the cascade reaches a peak in instability at a certain pressure ratio and that aerodynamic work is extremely sensitive to the level of back pressure. Shibata and Kaji (1998) also argue that this sensitivity to pressure ratio contributes to the steep flutter boundary observed experimentally on the same rotor in a study by Adamczyk et al. (1982).

Isomura and Giles (1998) performed a viscous unsteady CFD analysis on a transonic fan and found the same effect of back pressure on the global aerodynamic work per cycle, i.e. the work does not change monotonically with pressure ratio. They found that, near the stall boundary, a change of less than 2% in computed pressure ratio can cause the rotor to become unstable. They found that the difference in aeroelastic stability with pressure ratio is caused by large oscillations of unsteady pressure at the shock foot. All the previous observations have been confirmed, according to the authors, by an experimental study.

Jutur and Govardhan (2019) carried out an experimental campaign to measure aeroelastic stability in a started and unstarted linear cascade. Their results show that as the cascade approaches the unstarted regime, i.e. the shock is expelled from the covered passage, the blades experience a sudden drop in lift and the unsteady aerodynamic work increases sharply.

Finally, an example of discrepancies between different solvers was shown by the European project FUTURE (Flutter-Free Turbomachinery Blades, Fransson (2013)), in which tests and numerical computations were carried out on a 1.5-stage compressor by several partners, both from industry and academia. Fransson (2013) (Fig. 26) reports the experimental aerodynamic damping ratio against nodal diameter and compares it to numerical predictions at the same operating condition: it can be seen that the order of magnitude and trends of damping are similar, but that the difference between numerical predictions is considerable.

It thus seems clear that, due to complexity of the task, methods for computing aerodynamic damping should not only make predictions, but also provide an estimate of the uncertainty associated with the predictions. In this Chapter, we begin investigating the uncertainty present in our database of aerodynamic damping computations. The sensitivity to small changes in mean flow field is discussed with an example similar to the literature provided; a simple machine learning technique is employed to estimate the uncertainty of a prediction, which is consequently validated with a Monte Carlo simulation; finally, a possible application is provided.

6.2 Test Case

The test case is once again the Standard Configuration 10, shown in Section (2.5). A compressor map, similar to that shown in Fig. (5.49), is reported in Fig. (6.1). The axes are normalised by the reference mass flow and pressure ratio values calculated at nominal conditions, i.e. $M_1 = 0.7$, $\beta_1 = 0°$. We reiterate that, for SC10, the incidence is defined as $\beta_1 = \alpha_1 - 55°$, with α_1 being the inflow angle. Stall line and flutter boundary are also visible; the latter was calculated with reduced frequency $k = 0.5$, and a rigid body rotation about an axis 1 chord downstream of the trailing edge as mode shape, representative of a flapwise bending mode as discussed in previous chapters. Moreover, this combination of modeshape and frequency has been chosen so that the cascade flutters before stall, enabling us to study aerodynamic damping uncertainty in both stable and unstable conditions. The stall line indicates mass flow and pressure ratio at which the cascade can no longer deliver the intended M_1. For this case, the flutter boundary occurs in the range $\sigma \in (5°, 10°)$, typical for this mode. As will be shown in the later sections, aerodynamic damping predictions come with uncertainty and, consequently, the CFD computed flutter boundary should be treated carefully in practice.

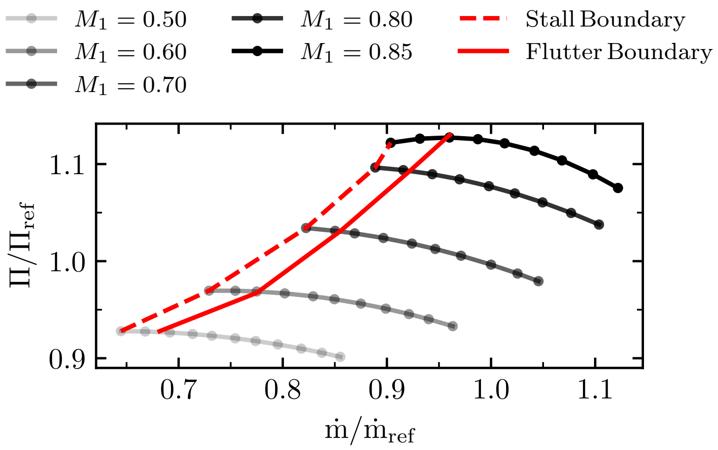

Figure 6.1 *Standard Configuration 10 compressor map with stall and flutter boundaries*

6.3 Sensitivity of Aerodynamic Damping in Transonic Flow

The literature provided in Section (6.1) shows how small uncertainties in the computed or measured pressure ratio can propagate and result in large differences in aerodynamic damping. This phenomenon is investigated in this section by performing a numerical study similar to the experimental work of Jutur and Govardhan (2019). The static pressure ratio across the cascade is increased at a constant mass flow rate of $\dot{m}/\dot{m}_{\mathrm{ref}} = 0.9$ until the stall boundary is reached. For every steady operating condition, the aerodynamic damping is computed using the familiar combination of low interblade phase angle and frequency $\sigma = 20°$, $k = 0.5$, with a flap modeshape.

The results from the computations are shown in terms of steady lift coefficient $\mathrm{C_L}$ and aerodynamic damping ζ in Fig. (6.2), which illustrates the CFD operating points that are closest to the target mass flow as black dots, while the solid line is a spline fit through those points; moreover four operating conditions are highlighted for further comparison later. From the results we can see that, as the static pressure ratio increases, the lift and aerodynamic damping coefficient vary almost linearly with it, respectively increasing and decreasing, until $\Pi/\Pi_{\mathrm{ref}} \approx 1.10$ where the lift coefficient plateaus and subsequently drops, corresponding to the blades approaching stall, and the consequent aerodynamic damping experiences a very sharp drop.

It is interesting to notice that, although Jutur and Govardhan (2019) treat the problem of supersonic cascade unstart, the resulting trends are very similar to the ones presented here, where the cascade is always unstarted, and approaches stall with subsonic inlet Mach number. This indicates that the simultaneous increase in pressure ratio and reduction of lift force corresponds to a sudden, large increase in aerodynamic work, and that this mechanism is driven by the stalling of the cascade, irrespective of whether stall is due to supersonic unstart or an increase in angle of attack in transonic flow.

For a more in-depth discussion, we now investigate some of the flow features that cause this behaviour. On Fig. (6.2a), four points are selected, each corresponding to an increasingly higher pressure ratio: points A and B are located just before the peak in lift coefficient, whereas points C and D are located right after. From Fig. (6.2b) one can see that the first pair, (A,B), is in the pressure ratio range where the slope of aerodynamic damping is shallow, whereas the latter pair (C,D) is found in the region of steep decrease. Fig. (6.3) shows the blade loading for the four selected operating conditions. Steady blade loading is expressed in terms of isentropic Mach number, unsteady loading is given by both real and imaginary components of pressure coefficient (though only the latter contributes to aerodynamic work), and the local aerodynamic work on the blade w is also shown, with $w > 0$ being unstable. In Fig. (6.3a), the isentropic Mach number distribution for these points is shown. The blade

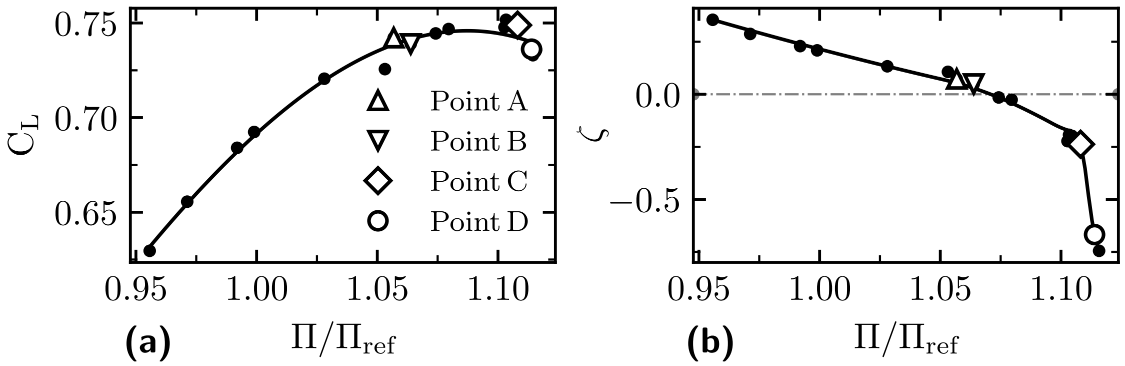

Figure 6.2 *(a) Lift and (b) aerodynamic damping coefficients computed with constant* $\dot{m}/\dot{m}_{\text{ref}} = 0.9$*,* $\sigma = 20°$*. The solid line (—) is a spline fit of the CFD points (black dots)*

loading profiles are extremely similar within each pair: (A,B) show a small region of sonic flow (see $M > 1.0$) near the leading edge on the suction side, which causes a weak shock, that is readily diffused by the mean flow; (C,D) are well into transonic regime and show a strong normal shock at about 20% chord on the suction side. The shock induces flow separation, which is visible in the contour plot of Mach number shown in Fig. (6.4).

The imaginary unsteady pressure coefficients are compared in Fig. (6.3b). Again (A,B) show a similar behaviour with high unsteady pressure localised near the leading edge; on the other hand, (C,D) almost perfectly overlap before the shock, while the unsteady pressure induced at the shock foot nearly doubles going from C to D. Also, after the shock, where the flow separates, the unsteady pressures of points C and D do not coincide. Finally, Fig. (6.3d) depicts the local aerodynamic work around the blade, which shows that the shock wave and consequent flow separation, occurring for operating points C and D, have a destabilising effect. The magnitude of aerodynamic work exchanged at operating point D is much larger than point C, explaining the sharp drop in global damping.

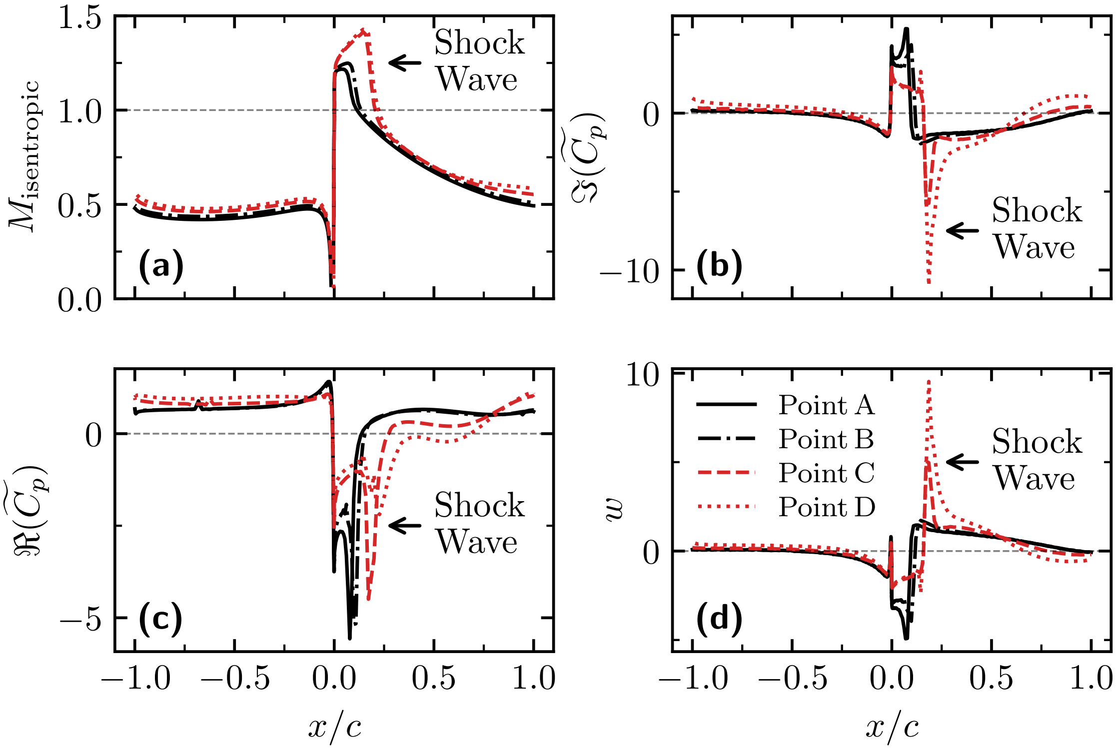

Figure 6.3 *Blade profiles at selected points:* ***(a)*** *Steady isentropic Mach number;* ***(b)*** *Imaginary component of unsteady pressure coefficient;* ***(c)*** *Real component of unsteady pressure coefficient;* ***(d)*** *Local aerodynamic work*

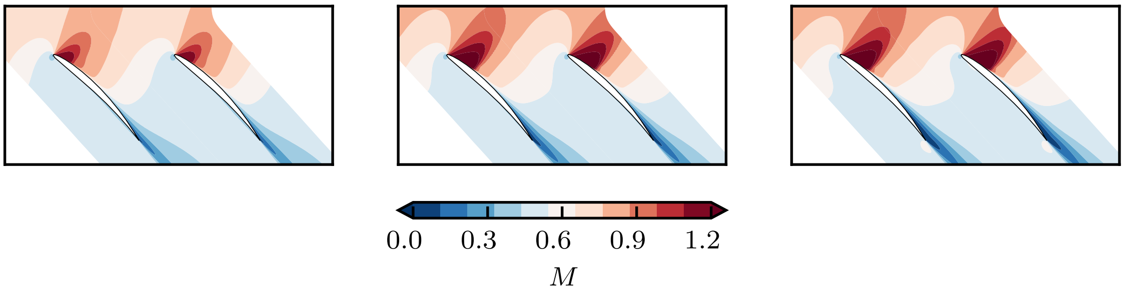

Figure 6.4 *Steady Mach Number contours computed at points* ***B,C,D****, from left to right*

The steady state loading did not shed any light on the cause of the sharp change in aerodynamic damping with pressure ratio. The matter is further investigated by examining the blockage size, δ, on the suction side of the blade, since this is where both shock wave and flow separation occur. In Fig. (6.5a), which shows blockage size near trailing edge as a function of pressure ratio, one can see that, going from C to

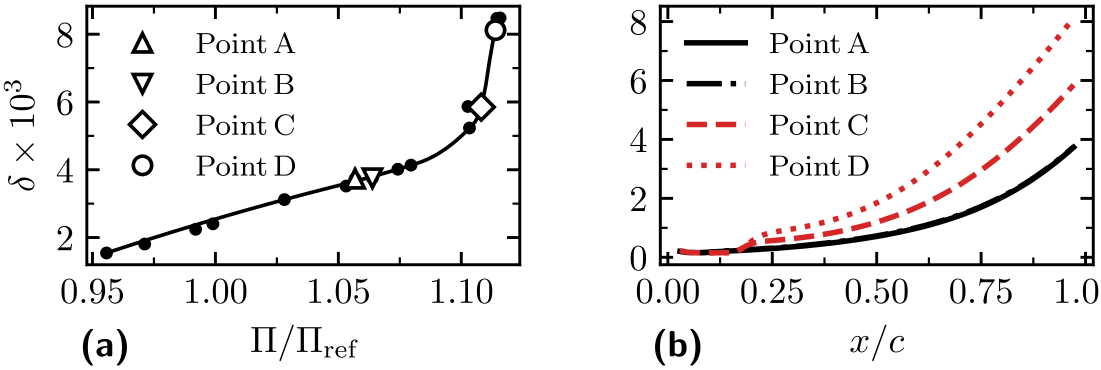

Figure 6.5 *(a) blockage size near trailing edge on suction side as a function of pressure ratio with constant* $\dot{m}/\dot{m}_{\mathrm{ref}} = 0.9$*; (b) blockage size on suction side as a function of streamwise coordinate.*

D, there is a steep increase in endwall blockage, indicating rapid growth of the shock induced separation size. The slope of the curve is nearly vertical at point D, suggesting that separation is very sensitive at this flow condition. Fig. (6.5b) shows the blockage size as a function of the streamwise coordinate for the four operating conditions. The profiles for the pair (A,B) overlap; the same is true for (C,D) until the shock (located at $x/c \approx 0.2$) is reached. After the shock wave, the separation occurring at operating point D is more severe than point C and the endwall blockage grows larger.

These results have shown that, when shock induced separation is present, computations at marginally different operating conditions can produce significantly different aerodynamic damping predictions. In practice, one can see that changes in numerical methods, turbulence modelling, grid spacing, boundary condition types or small perturbations to target mass flow and pressure ratio can all produce such mean flow differences. This implies that there is a need to account for uncertainty in flutter predictions.

6.4 Uncertainty Quantification Method

In line with the theme of this thesis, we once again seek a solely data-driven solution to find a measure of uncertainty for the aerodynamic damping predictions in our dataset. As for Chapter (3), we tackle the simpler problem of interpolation, i.e. modelling of the training geometry only, and emphasise that the main objective in this Chapter is not to build a general prediction model, but to investigate, show and quantify uncertainty of computed aerodynamic damping.

Among the plethora of methods available, random forests (Breiman, 2001) are a very popular supervised algorithm due to their ability of achieving high accuracy with limited hyper-parameters tuning. Random forests (RF) are an ensemble of decision trees. A decision tree creates a mapping between input and output through a series of “if-then” statements: starting from a root, the algorithm builds a hierarchy of nodes at which data is split in a binary fashion, until a final, leaf node is reached. In regression problems, decision trees perform optimal splits by minimising the mean squared error and, for a given test data point, a prediction is output by walking through the tree to identify the corresponding leaf and taking the weighted mean of the values in that node. To overcome the problem of overfitting the data, a random forest employs a large number of trees, each trained on a random subset of the input variables, and its prediction on a new data point is the averaged response of all trees. The uncertainty quantification method employed in this study is the Quantile Regression Forest (QRF) introduced by Meinshausen (2006). It builds on the original random forest concept and it allows to enhance predictions with prediction intervals.

Let $\{(X_i, Y_i) : i = 1, .., n\}$ be n independent observations; the random forest algorithm grows a number of trees to infer a relationship between the variable X and the response Y. Let $T(\theta)$ be a tree corresponding to the random vector θ which determines the subset of features used by the tree. Every leaf node $\ell = 1, ..., L$ in $T(\theta)$ may contain some of the observations (X_i, Y_i). As mentioned above, when a new data point x is dropped down a tree it will end up in a leaf node; suppose the leaf which contains x is denoted by $\ell(x, T)$, then, the weight $w_i(x, T)$ of each observation will be a constant if X_i belongs to the node and zero otherwise. The weights sum up to one so the expression is given by

$$w_i(x, T) = \frac{1_{\{X_i \in \ell(x,T)\}}}{\#\{j : X_j \in \ell(x, T)\}} \tag{6.1}$$

Assuming the random forest is composed of B trees, the weight of each observation will be the average over the trees

$$w_i(x) = \frac{1}{B} \sum_{b=1}^{B} w_i(x, T_b) \tag{6.2}$$

Finally, the conditional mean $\mathbb{E}(Y|X = x)$ of the response Y given x is given by

$$\widehat{\mu}(x) = \sum_{i=1}^{n} w_i(x) Y_i \tag{6.3}$$

Meinshausen (2006) argues that the weighted observations can provide not only a good approximation of the expected value of Y, but also of its full conditional distribution $F(y|X = x)$. As F is unknown, we can approximate it with an empirical distribution function

$$F_n(x) = \frac{1}{n} \sum_{i=1}^{n} \mathbf{1}_{\{X_i \leq x\}} \tag{6.4}$$

where $\mathbf{1}_{\{X_i \leq x\}}$ is an *indicator* random variable, taking value 1 when the condition is true and 0 otherwise. So, as $\mathbb{E}(Y|X = x)$ is approximated by the weighted mean over observations of Y, $\mathbb{E}(\mathbf{1}_{\{Y \leq y\}}|X = x)$ is estimated by the weighted mean over the observations of the empirical distribution function

$$\widehat{F}(y|X = x) = \sum_{i=1}^{n} w_i(x)\mathbf{1}_{\{Y_i \leq y\}} \tag{6.5}$$

From $\widehat{F}(y|X = x)$ in Eq. (6.5), one can obtain estimates of conditional quantiles for a given significance level α and form a prediction interval (PI)

$$I(x) = \left[Q_{\{\frac{\alpha}{2}\}}(x), Q_{\{1-\frac{\alpha}{2}\}}(x)\right] \tag{6.6}$$

The current definition of prediction interval is closely related to that of confidence interval (CI): for a given significance level $\alpha \in (0, 1)$, a $(1 - \alpha)$-confidence interval is an interval (a, b) such that, if we were to draw infinitely many samples and compute new CIs, then the true value of a statistic, e.g. the mean, would be contained in $100 \cdot (1 - \alpha)\%$ of the intervals. This means that CIs are defined for distributions of statistics.

On the other hand, the prediction interval is computed directly from the distribution of samples and it is thus unrelated to any particular statistic. As such, in this context $(1 - \alpha)$-prediction intervals for aerodynamic damping predictions are intervals (a, b) around multiple predictions which contain the true value of damping, i.e. the value computed from CFD, $100 \cdot (1 - \alpha)\%$ of prediction instances. This difference is important and will be pointed out again in the following sections.

Regardless, a larger prediction interval will indicate more uncertainty around a given prediction. The figure of merit in this study will be the commonly used 95% prediction interval, i.e. $\alpha = 0.05$, which in normal theory correspond to a range of $\sim \pm 2$ standard deviations around the mean.

The prediction intervals are constructed by calculating the weighted quantiles from the conditional empirical cumulative distribution function $\widehat{F}(y|X = x)$ (CDF). The procedure works as follows and it is clarified with a simple example. Suppose a test data point x is dropped down the random forest and is stored in a leaf node ℓ for each tree; the leaf nodes will each contain a subset of the observations (X_i, Y_i) with a weight w_i. The subset of dimension m can be ordered to form a strictly increasing sample $Y_1 < Y_2 \cdots < Y_m$ with weights $w_1, w_2, \ldots, w_m$. Let $s_j = \sum_{i=1}^{j} w_i$, be the sum of the first j weights and $s_m = \sum_{i=1}^{m} w_i = 1$, be the sum of all weights, then, for a quantile q, one can find j such that $s_j < q < s_{j+1}$ and find an estimate Q by linear interpolation

$$Q = Y_j + (Y_{j+1} - Y_j)\frac{q - s_j}{s_{j+1} - s_j} \tag{6.7}$$

Fig. (6.6) shows a schematic empirical distribution function with horizontal lines denoting the values $q = 0.975$ and $q = 0.025$. The estimate for the values of Q will be the interpolation of the two values directly above and below the horizontal line.

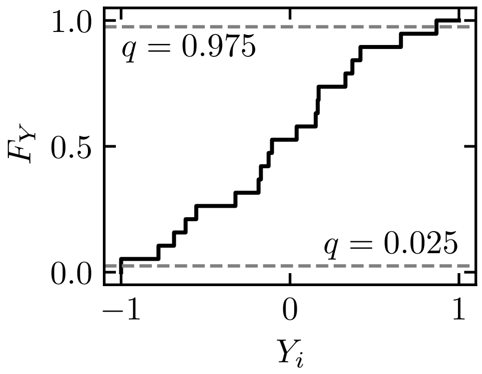

Figure 6.6 *An illustrative empirical distribution function with quantiles* $q = 0.975$ *and* $q = 0.025$

6.4.1 Training Data

The five databases of aerodynamic damping of SC10 (Chapter 3) will constitute the training data, though we limit the scope of this work to a range of interblade phase angle $\sigma \in (0°, 45°)$, a single reduced frequency $k = 0.5$ and one modeshape, the familiar rigid body rotation about an axis 1 chord length downstream of the trailing edge of the blade, which mimics a typical 1F mode. The response variable Y the model will predict is aerodynamic damping.

Random forests can provide a measure of feature importance without resorting to any other method. Therefore we provide the algorithm with three independent features and eight derived quantities based on steady flow, listed in Table (6.1), with the intention of letting the algorithm itself select the most appropriate ones.

6.4.2 Hyperparameter tuning and feature selection

The choice of hyperparameters is a fundamental step in nearly every machine learning algorithm. These parameters are not trainable and need to be selected by the user. The predictive performance of the random forest is measured with the coefficient of determination R^2 defined in Eq. (5.6), where $R^2 = 1$ indicates a perfect fit to the data. The K-fold cross validation procedure outlined in Section (5.7) is employed to provide a fair performance measure. We fix $K = 5$, and the trees in the random forest are allowed to grow indefinitely as long as a minimum of 10 data points is used to perform a node split; this leaves us with only one hyperparameter to be investigated, i.e. the number of trees B.

Table 6.1 *Set of input features*

Feature		Type
M_1	Inlet Mach Number	Independent
β_1	Incidence Angle	Independent
σ	Interblade Phase Angle	Independent
C_L	Lift Coefficient	Derived
C_D	Drag Coefficient	Derived
Π	Static Pressure Ratio	Derived
$\dot{m}$	Mass Flow Rate	Derived
δ_{SS}	Blockage at trailing edge on suction surface	Derived
δ_{PS}	Blockage at trailing edge on pressure surface	Derived
σ_U^*	Upstream Cut-off Ratio†	Derived
σ_D^*	Downstream Cut-off Ratio†	Derived

†To avoid division by zero at $\sigma = 0°$, the reciprocal is used

Furthermore, as mentioned above, some features in the dataset are redundant, i.e. they do not necessarily add new information as, for example, an operating condition for a fixed geometry can be defined by either mass flow rate and pressure ratio or lift and drag coefficient. This redundancy increases the computational cost and it is not guaranteed to improve the performance of the algorithm, therefore, a backward elimination is performed. Backward elimination is an iterative process where the least important features are dropped one at a time: starting from the full set, the random forest is trained, tested and the feature deemed least important is dropped. The process is repeated until only one feature is left in the dataset. Feature importance is measured by permutation importance (Breiman, 2001).

Fig. (6.7) shows the results of backward elimination for six random forests with $B = 2, 5, 10, 50, 100, 200$, starting from a maximum of $P = 11$ features. First, one notices that the markers overlap almost perfectly, with $B = 2, 5$ ever so slightly lower than the rest; this robustness of predictive performance to the number of trees has been observed in previous studies (Heyse et al., 2021; Scillitoe et al., 2021). By robustness, we mean that performance do not change significantly with number of trees. Second, many of the features can be removed without affecting the predictive accuracy, which settles at a value of $R^2 \approx 0.95$; significant loss in performance occurs when $P < 3$. This result is reassuring: only 3 features are needed to completely define a point in our sampling space, decreasing the value of P to less than 3 removes relevant information.

The most interesting result of the backward elimination is not the number of features, but rather which ones the algorithm selects: throughout all tests, the independent variables (see Table 6.1) are discarded first, while C_D, C_L, blockage on suction side and the cut-off ratios are deemed to be the most relevant. The choice of cut-off ratios over

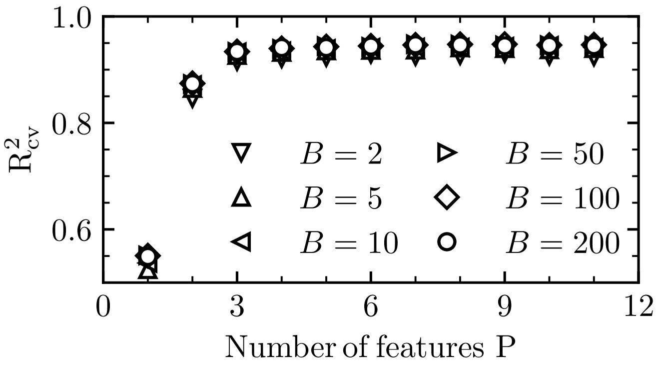

Figure 6.7 *Cross validation R^2 as a function of number of features.*

interblade phase angle is easily explainable: they are a combination of steady mean flow quantities, frequency and phase angle and, unlike σ alone, carry information regarding flow velocity, angles and thermodynamic quantities, both upstream and downstream of the blade. The suction side blockage near trailing edge, δ_{SS}, was shown to be relevant in the previous sections, especially near the stall boundary. Regarding the choice of C_L and C_D as most significant steady state features, a small discussion is in order.

Fig. (6.8a) and Fig. (6.8b) are kernel density estimate (KDE) plots that visualise the distribution of aerodynamic damping observations in the dataset, against pairs of steady state features: $\{C_L, C_D\}$ and $\{\dot{m}, \Pi\}$, respectively. The data points in the plots are categorised in two groups, corresponding to in positive and negative aerodynamic damping. As previously explained, a random forest performs a series of splits on the dataset in order to maximise the information gain at each step. One can see that, in Fig. (6.8a), there is little overlap between positive and negative samples with $C_D \geq 0.11$, therefore we expect the RF algorithm to leverage this clear separation when splitting the data. On the other hand, in Fig. (6.8b) we can see that, throughout the whole mass flow range, there is not such a simple binary split, therefore the random forest has to perform several operations to fit a line that divides the data and obtain a similar information gain. It is reiterated that, physically, both pairs of features convey the same information regarding the flow field, but, for this case, lift and drag constitute a more meaningful set of coordinates to work with.

The following feature set is employed for the remainder of the study:

$$\boldsymbol{x} = [C_L, C_D, \sigma^*_U, \sigma^*_D, \delta_{\mathrm{SS}}] \tag{6.8}$$

Lastly, we verify that the prediction intervals produced by the QRF are well calibrated. By well calibrated we mean that they abide by their definition, i.e. $(1-\alpha)$-prediction intervals are well calibrated if $100 \cdot (1-\alpha)\%$ of them contain the true value of aerodynamic damping as computed by CFD.

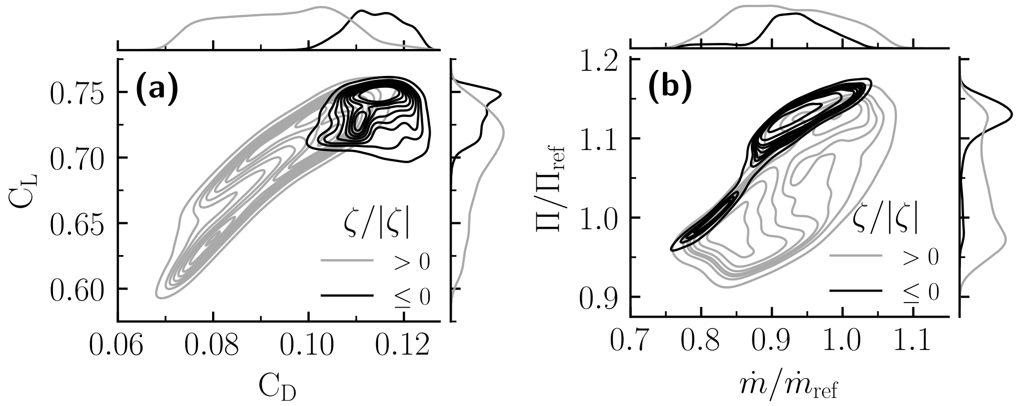

Figure 6.8 *Kernel density estimation plots of aerodynamic damping coefficient databases as a function of:* ***(a)*** C_L *and* C_D*;* ***(b)*** $\dot{m}$ *and* Π

The coverage fraction CF, i.e. the percentage of true values contained in the 95% prediction intervals, as a function of number of trees B is shown in Fig. (6.9a). The target CF = 0.95 is labelled in the plot. If prediction intervals obtain a CF larger than the target, they are said to be under-confident, i.e. they are too large; if the obtained CF is lower than the target, they are said to be over-confident. Fig. (6.9a) shows that for low values of B the intervals are over-confident. The coverage fraction converges to CF $\approx$ 97% with $B > 50$. This value of CF $\approx$ 97% indicates that the PIs are nearly perfectly calibrated, but are slightly under-confident, i.e. their size could be smaller. For the remainder of the Chapter, the number of trees is set to $B = 100$.

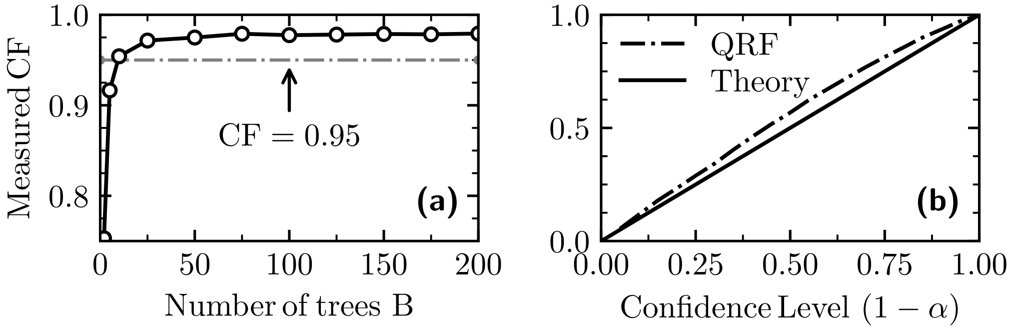

Figure 6.9 ***(a)*** *Coverage fraction convergence with number of trees;* ***(b)*** *QRF calibration curve showing the coverage fraction as a function of confidence level*

For completeness, we verify that the confidence intervals are well calibrated for all significance levels. In Fig. (6.9b) the coverage fraction of the current method (QRF) is compared to theory. The PIs from the current method are well calibrated, although slightly under-confident, throughout the range of significance levels.

6.5 Comparison of QRF with CFD

The following results show a comparison between CFD and QRF. The results from QRF will consist of a point value, which is the expected value of aerodynamic damping and will be referred to as prediction, and a 95% prediction interval, presented in the form of an error bar.

The results in Fig. (6.10) show good agreement between CFD and machine learning model, and this is to be expected since we are not trying to extrapolate outside of the input parameters range. Furthermore, we see that the prediction intervals tend to get larger as the pressure ratio increases and, finally, become very large as the cascade approaches the stall boundary. This implies that the QRF predicts high uncertainty in this region and that, according to the ML model, a CFD computation with slightly different pressure ratio could predict an aerodynamic damping value anywhere within the PI.

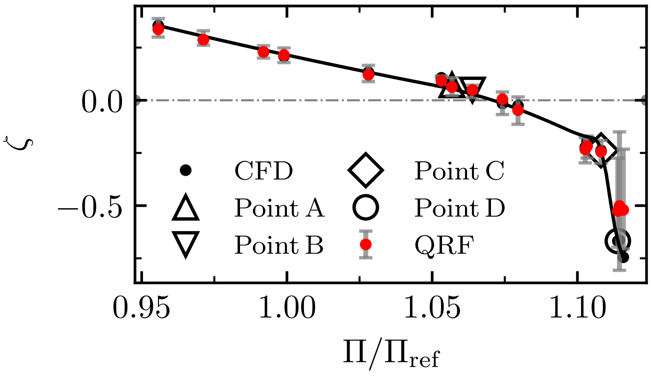

Figure 6.10 *Aerodynamic damping coefficient from CFD (markers with spline fit —) and QRF (red dots with error bars) as a function of pressure ratio with constant* $\dot{m}/\dot{m}_{\mathrm{ref}} = 0.9$*,* $\sigma = 20°$

A further comparison between QRF and CFD is shown in Fig. (6.11): a line of constant inlet Mach number $M_1 = 0.825$, at $\sigma = 20°$, is pbtained by increasing the incidence onto the blades and varying the pressure ratio. Following this line, the flow separates from the blade and, as the mass flow decreases, so does aerodynamic damping except for the last point on the curve at $\dot{m}/\dot{m}_{\mathrm{ref}} \approx 0.9$, where the monotonic trend is interrupted (see Vahdati et al. (2001) for a similar observation on a fan blade). The machine learning model almost perfectly overlaps with the CFD results, and predicts, similar to the previous test, larger prediction intervals as the mass flow decreases.

For completeness, an interblade phase angle sweep at constant $M_1 = 0.6$ and $\beta_1 = 6°$ is shown in Fig. (6.12). This condition has been chosen so that both upstream and downstream cut-off frequencies are clearly visible; these are shown as vertical

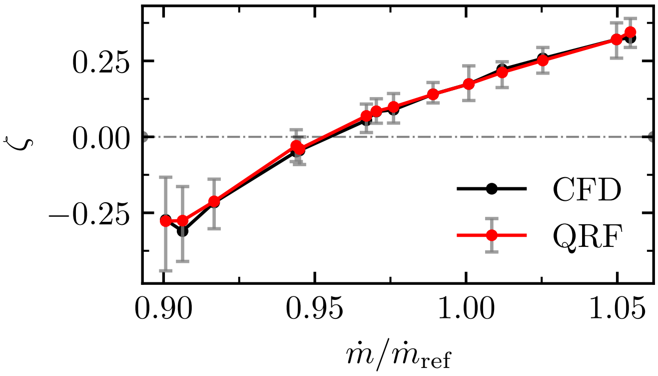

Figure 6.11 *Aerodynamic damping coefficient from CFD (—) and QRF (— with error bars) as a function of mass flow rate with constant* $M_1 = 0.825$*,* $\sigma = 20°$

lines on the plot. Again, there is very good agreement between QRF and CFD, but it is interesting to see how the prediction intervals become larger in size as the cut-off frequencies are approached. This trend is also driven by a form of sensitivity, but, whereas the previous tests have shown the influence of shock induced separation, in this case the strong response to changes in flow field is acoustic in nature. It has been shown, in this thesis and in the literature provided so far, that the unsteady pressures inside a blade passage change drastically as the pressure fields, upstream and downstream of the blade, change from cut-on to cut-off, and, in turn, this behaviour leads to large oscillations in the value of aerodynamic damping. The size of the prediction intervals in Fig. (6.12) reflects this responsiveness of the unsteady flow field, which, in our framework, is considered a type of uncertainty.

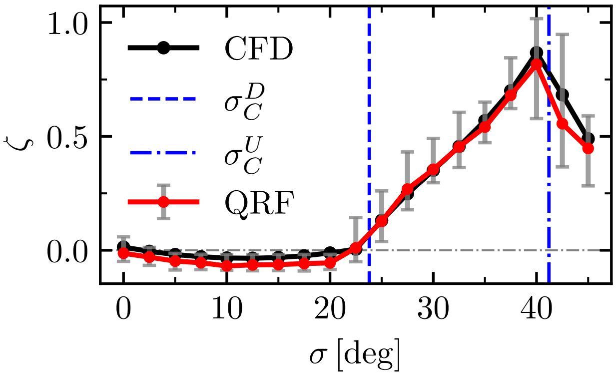

Figure 6.12 *Aerodynamic damping coefficient from CFD (—) and QRF (— with error bars) as a function of interblade phase angle with constant* $M_1 = 0.6$*,* $\beta_1 = 6°$*. The vertical lines represent downstream (- - -) and upstream (-·-·) cut-off values, respectively.*

The uncertainties shown by prediction intervals directly influence the aerodynamic damping prediction accuracy, where a small perturbation in running conditions may lead to very different outcome, i.e., false positive or false negative in stability judgment. In this context, small perturbations can be deviation from the target mass flow and pressure ratio, uncertainties in boundary conditions (e.g. changes in temperature can affect the cut-off frequencies), numerical model assumptions and turbulence modelling. Therefore, for both experimentalist and computational analyst, it can be very dangerous to rely on a singular deterministic value assumed to have 100% confidence.

6.6 Validation of Prediction Intervals

The comparison between CFD and QRF in Fig. (6.10) shows a steep decrease in aerodynamic damping that is well approximated by the surrogate model. Near the stall boundary, at high pressure ratio, the uncertainty predicted by QRF is high and it is portrayed by the large prediction intervals. Now, one would like to verify that the prediction bounds calculated by the surrogate model are actually representative of the real uncertainty. In order to complete this task though, it is important to first explore why the model outputs such intervals.

To gain understanding, three operating points are examined from Fig. (6.10), with respectively increasing pressure ratio: P8 is a high subsonic flow condition with $\Pi/\Pi_{\text{ref}} = 1.07$, low uncertainty and sits just above the zero damping line; P10 is in transonic regime with $\Pi/\Pi_{\text{ref}} = 1.103$, it is located right before the change in aerodynamic damping slope and also exhibits small uncertainty; P14 is located near the stall boundary, in the region of large QRF uncertainty at $\Pi/\Pi_{\text{ref}} = 1.114$. The sample constituted by the three points can be dropped down the random forest to identify the leaf nodes they belong to; once a leaf node is found, we can extract the observations (X_i, Y_i) and the relative weights w_i that form the empirical distribution, as explained in the previous sections. In other words, we can find the training data that the algorithm groups around the test point in order to make a prediction. The subsets obtained by dropping down the sample points can now be visualised.

Fig. (6.13) shows scatter and KDE plots of the subsets built around the three sample points; the index j refers to the test data point, while i refers to any observation in the subset belonging to the point indexed by j. Fig. (6.13a) portrays the percentage difference between the mass flow rate of the test data and the observations against the percentage difference of the pressure ratios; it shows that to make a prediction in subsonic flow (P8), the QRF model groups together points that exhibit a large difference in both delivered pressure ratio and mass flow rate, but, at the same time, Fig. (6.13b) shows the difference between the subset of observations ζ_i and the resulting aerodynamic damping prediction ζ_j is nearly zero throughout the whole range. This result shows that the variation of aerodynamic damping value at these low speed conditions is minimal, even though the change in steady characteristics might be significant. The trend is inverted as the investigated conditions go from subsonic to low (P10) and high (P14) transonic regime: the neighbourhood of observations becomes tighter around the data point in terms of steady state variables, but the deviation in terms of aerodynamic damping grows larger. At P14 for example, the subset of observations is contained within a 2% change in pressure ratio, but the damping varies widely from highly unstable to highly stable.

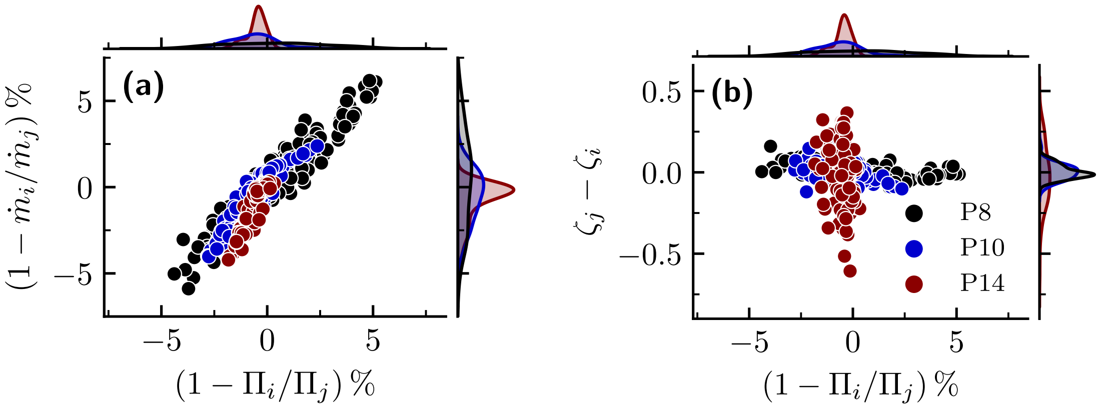

Figure 6.13 *Scatter plot and kernel density estimation of the training data subsets formed by QRF around the three test points of interest.* ***(a)*** *Percentage difference in mass flow rate against percentage difference in pressure ratio;* ***(b)*** *Difference in aerodynamic damping against percentage difference in pressure ratio.*

Fig. (6.14) clearly reinforces the observation just put forth. The empirical cumulative distribution functions (CDF), $\widehat{F}_\zeta$, obtained for P8 and P10 are mostly centered around zero, and intersect the horizontal lines representing the quantiles very close to zero, which translates into small prediction intervals. On the other hand, the CDF for P14 spans a large range of aerodynamic damping which, finally, explains why the QRF predicts such high uncertainty for this test point.

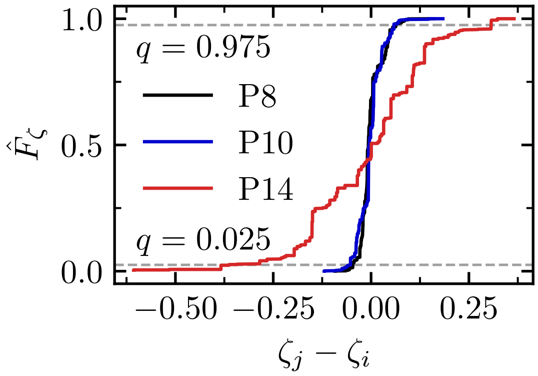

Figure 6.14 *Empirical cumulative distribution function of the difference between subset of observations* ζ_i *and the resulting aerodynamic damping prediction* ζ_j *at test point* j*. The quantiles* $q = 0.975$ *and* $q = 0.025$ *form the* 95% *prediction intervals.*

After illustrating the process followed by the QRF to predict aerodynamic damping and associated prediction intervals, a Monte Carlo (MC) analysis is performed to verify the accuracy of the predicted uncertainty. The samples are obtained by varying the back pressure, p_2; they are drawn from a normal distribution centered about the original value for each data point, p_{2j}, and with a standard deviation of 0.33%, i.e. $p_2 \sim \mathcal{N}\left(p_{2j}, \sigma_{\mathcal{N}}^2\right)$, where $\sigma_{\mathcal{N}} = p_{2j} \cdot 3.33 \times 10^{-3}$. The choice of standard deviation is so that circa 99% of the samples are within 1% of the original back pressure value, a difference small enough to be often overlooked in academic and engineering practices using CFD. The resulting mass flow rate and pressure ratio distributions for the three points of interest, again expressed as percentage difference from the original value indexed by j, are shown in Fig. (6.15). It can be seen that both distributions are well within the bounds of the subsets built by the random forest, e.g. at P14 the MC pressure ratio sample is contained within less than 1% change from the mean, as opposed to the 2% show in Fig. (6.13a).

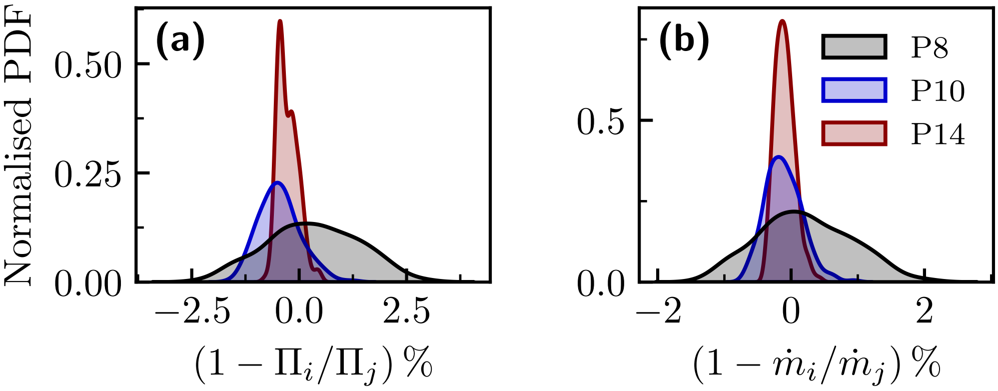

Figure 6.15 *Kernel density estimation of Monte Carlo analysis samples.* ***(a)*** *Distribution of samples against percentage difference in pressure ratio;* ***(b)*** *Distribution of samples against percentage difference in mass flow rate.*

The aerodynamic damping distributions obtained through the MC analysis can now be used to compute prediction intervals, which are compared to the ones calculated by the QRF. Fig. (6.16a) shows how the Monte Carlo PIs grow in size as the cascade approaches high pressure ratio values, and that the uncertainty portrayed by the QRF is indeed representative of the loss of robustness affecting the unsteady CFD. The size of the prediction intervals is, of course, dependent on the a priori sample distribution chosen to perform the MC computations, but, as discussed previously, the variance of the distribution was set to be very small so that every sample would fall extremely close to the mean, well within an error range that is usually accepted in CFD computations. In other words, if a CFD computation is set up to match a specific pressure ratio and mass flow rate, the results show that even a small deviation from target values can result into widely different predictions of aerodynamic damping. The mean value obtained from the Monte Carlo analysis agrees better with the QRF than the CFD; this is to be expected as the mean prediction from the surrogate model comes from a weighted mean of a subset of values that resembles the MC sample itself, whereas the CFD point is obtained from a single computation. The confidence intervals for the value of the calculated mean can be constructed through bootstrapping (Efron, 1979), a sampling with replacement technique used to estimate the variation of statistics that are themselves computed from a set of data. Fig. (6.16b) shows that the value obtained for the mean of aerodynamic damping is extremely confident, as the CIs are barely visible.

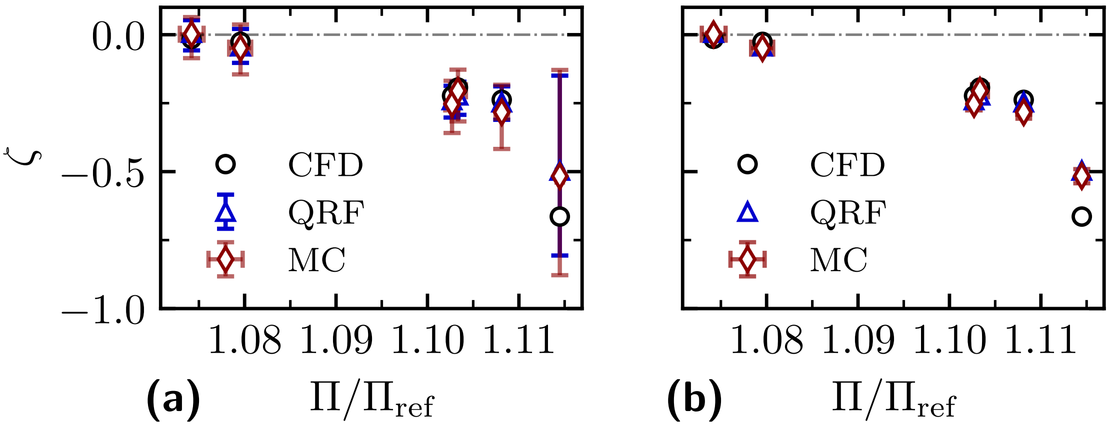

Figure 6.16 *Aerodynamic damping predictions from CFD, QRF and Monte Carlo analysis against delivered pressure ratio, with confidence intervals.* ***(a)*** *The prediction intervals from QRF (—) and MC (—) are obtained as quantiles of the distribution around a point;* ***(b)*** *The confidence intervals from MC (—) refer to the mean of the distribution and are obtained by bootstrapping.*

We can thus conclude that the prediction intervals portrayed by the QRF are not due to machine learning errors, but are representative of the real uncertainty of CFD.

6.7 Conservative Flutter Margin

Having demonstrated the effectiveness of prediction intervals in evaluating aerodynamic damping uncertainties, the proposed method is applied to determine the flutter stability of the cascade.

In Fig. (6.17), a compressor map is shown with the flutter boundary computed from CFD. The method employed to obtain this boundary has been discussed in the previous sections and it is the conventional flutter boundary that engine designers use. The equivalent flutter boundary obtained from the QRF prediction is also presented for comparison, and it shows good agreement with CFD. Based on the calculated

PIs, a more conservative flutter boundary can be drawn using the lower bound of the prediction interval around the prediction. The corresponding flutter boundary for 95% PI is also shown in Fig. (6.17); only the lower bound is used as we are after a conservative estimate, which would increase our safety margin. It can be clearly seen that the boundary moves to higher mass flows when uncertainty is taken into consideration.

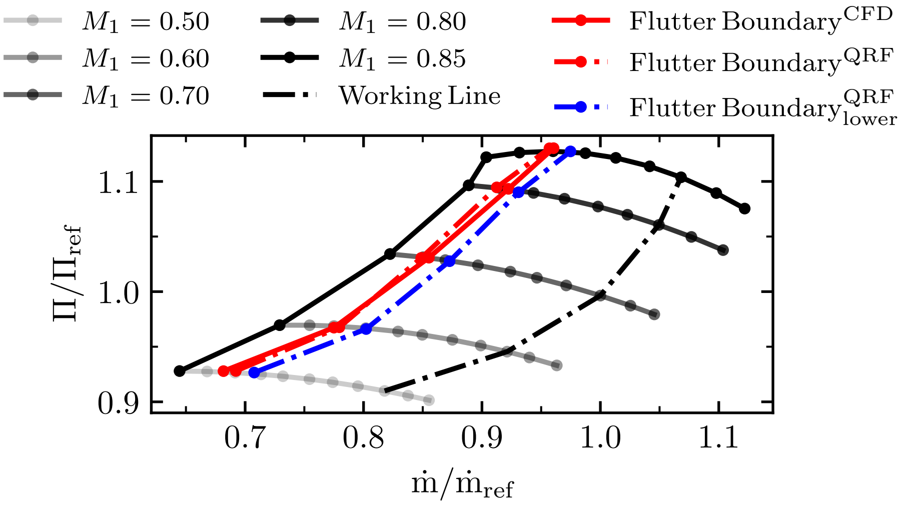

Figure 6.17 *Standard Configuration 10 compressor map with flutter boundaries computed from CFD and QRF*

To quantify the shift of flutter boundary, a flutter margin is estimated based on an artificial working line corresponding to nominal incidence $\beta_1 = 0$. For each line of constant M_1, it is possible to calculate a flutter margin FM, borrowing the surge margin expression in Cumpsty (2004) (Chapter 9)

$$\text{FM} = 1 - \frac{\Pi_{\text{wl}}}{\Pi_{\text{f}}} \cdot \frac{\dot{m}_{\text{f}}}{\dot{m}_{\text{wl}}}\bigg|_{M_1} \tag{6.9}$$

where the subscripts f and wl stand for flutter and working line respectively.

Table (6.2) shows the comparison of flutter margin obtained from CFD and the lower bound of 95% prediction interval around the QRF prediction. On average a 10 $\sim$ 20% difference is seen between the two estimates, which is non-negligible for compressor design. Moreover, the current study focuses on a specific geometry and confined range of flow and vibration parameters; the difference in flutter margin estimates can be much larger for realistic fan and compressor with complex flows. The difference in flutter margin represents inherent aerodynamic damping uncertainties which is conventionally neglected in practice. Conventional engineering approach addresses this issue by taking the deterministic value with unknown confidence and apply empirical safety factor to achieve a desired safety margin. It is envisaged that the proposed prediction interval can be used as guidance for the decision of safety factor and hence aid more efficient and reliable blade design.

Table 6.2 *Flutter margin loss accounting for uncertainty*

M_1	$\mathrm{FM}_{\mathrm{CFD}}$	$\mathrm{FM}_{\mathrm{lower}}$	$\Delta\mathrm{FM}$
0.50	0.18254	0.15027	17.68%
0.60	0.17769	0.14776	16.85%
0.70	0.17338	0.15387	11.25%
0.80	0.14741	0.13708	7.01%
0.85	0.12179	0.10643	12.61%

6.8 Summary

In this Chapter, the uncertainty of aerodynamic damping predictions on a compressor cascade has been shown.

The uncertainty is a direct consequence of the sensitivity of unsteady flow solutions to the mean flow. It has been shown that aerodynamic damping predictions, in the presence of shock waves and flow separation, are not robust near the stall boundary, and can vary significantly even with negligible changes to the steady state solution. In practice, this means that if a target operating point (i.e. mass flow rate and pressure ratio pair) is to be matched for analysis, discrepancies that are often deemed acceptable can produce a considerable difference in unsteady flow field. To overcome such issues, aerodynamic damping models should be able to accompany their predictions with a measure of uncertainty.

A machine learning based method to quantify uncertainty (QRF) in a database of aerodynamic damping computations has been presented. The model has been trained on predictions from a linearised aeroelastic solver, and it has been validated by comparing its predictions to CFD for different flow regimes. The model has been cross validated to find the best hyperparameters and it was shown to be able to accurately interpolate within the range of parameters it has been trained on. The uncertainty of aerodynamic damping has been quantified by enhancing the model predictions with 95% prediction intervals. It was found that the model is capable of portraying the uncertainty due sensitivity of unsteady flow due to both shock induced separation, in a high working line regime, and to changes in the acoustic nature of upstream and downstream pressure fields. The confidence intervals produced by the QRF have been validated against a Monte Carlo analysis, which confirmed the results from the ML model.

To underline the engineering usefulness of such an approach in determining aerodynamic damping, the ML model was then used to produce a conservative flutter boundary on a compressor map, using the lower bound of prediction intervals, rather than the single prediction from CFD only.

Chapter 7

Conclusions and Future Work

7.1 Conclusions

In this thesis we have applied data-driven techniques for the computations of aerodynamic damping of turbomachinery. The efforts were specifically devoted towards stall flutter of compressor blades and, being a first application of such approaches to this topic, the analyses were limited to two-dimensional cascades.

After presenting the computational and machine learning methods, in Chapter (2) the discrepancies between predictions of time-linearised and time-accurate solvers were assessed for the main test case of this work. It is found that the main differences come from the inaccuracies of non-reflecting boundary conditions in the time-accurate solver, and from the limited number of blades modelled in the influence coefficient computations. Adding blade passages increases the compliance between the two and, in particular, there is excellent agreement in the minimum damping computed by both codes.

Chapter (3) lays the groundwork for the data-driven model, offering a possible application.

The work of Chapter (3) and a semi-analytical model reviewed in Chapter (4) are combined through the PGML framework to build a physics guided neural network model. It is found that the model is able to generalise to unseen geometries thanks to the combination of: 1) meaningful input features based on integrated steady state quantities which allow the model to detect a change in geometry and flow conditions; 2) manipulating hidden layers of the neural network by injecting results from the semi-analytical model. It is also found that aerodynamic damping for plunge dominated modes, such as the flapwise bending modes of interest for stall flutter, is computed to a high degree of accuracy; on the other hand, pitch dominated modes predictions are less accurate due to non negligible passage effects for which no input feature is devised. A particularly important result is that even training on a single geometry yields very promising results, thus increasing the applicability of this approach in a *small data regime*. The work of this Chapter fulfills the objective put forth at the beginning of this manuscript, constituting the main contribution of this thesis.

Finally, Chapter (6) underlines the need of accounting for uncertainty in the steady state flow computations when performing analyses aimed at computing aeroelastic stability. It is found that the value of aerodynamic damping is extremely sensitive to such uncertainty, especially near stall.

As with any other machine learning based solution, an inquiry about this work is unmistakably led with a fair question: *where do you find enough data?* One might argue that, unlike the turbulence modelling community which is gifted with large databases originating from scale resolving computations and experiments, the turbomachinery aeroelastician has to work in a data scarce environment. At the same time though, the current practice of compressor aeroelastic design leverages an extensive and ubiquitous application of CFD. Such an approach generates large volumes of data that often provide no added value, beyond the intended purpose of assessing stability. Moreover, even if a design is deemed unfit, the data obtained from computations can still be useful. It is therefore argued here that the proposed approach of combining steady state data and reduced order models through machine learning can be feasible in an industrial setting, and it is worth pursuing further.

7.2 Comments on the role of the reduced order model

The results of Chapter (5) have amply shown that the PGML framework is able to better predict aerodynamic damping when compared to a conventional FCNN. This is true for a range of geometries and flow conditions, even though both the FCNN and PGML have been trained on the same data. This set of data is of higher fidelity than the one coming from LINSUB, which lacks the effects of loading and viscosity, and should thus provide no added value. This leads us to a fundamental question that has not been addressed so far: how can a low order model improve the predictions of an ML model trained on high order data? What information is LINSUB providing that our dataset is lacking?

The quantity of interest of PGML and FCNN models is the matrix of aerodynamic coefficients $\boldsymbol{C}$, defined in Eq. (5.1). A linear combination of these coefficients can yield a measure of stability for any modeshape, i.e. plunge, pitch and flap, which ultimately expresses a normalised aerodynamic work per cycle, as shown in Eq. (2.48). The current choice of scaling makes sense for low reduced frequencies, $k \ll 1$, because, citing Corral and Vega (2016), it assumes that the characteristic unsteady pressure is due solely to a quasi-steady motion, i.e. the characteristic unsteady pressure is proportional to the dynamic head $\widetilde{p}_{c1} \sim \rho v^2 \cdot \bar{q}/c$, thus ignoring the dependency of phasing between unsteady pressure and airfoil displacement with the frequency. Corral and Vega (2016) also show that, for $k \sim 1$, one must take into consideration the fact that unsteady pressure is due to the velocity induced by the vibration, thus the characteristic pressure scales as $\widetilde{p}_{c2} \sim \rho v \cdot \omega \bar{q}$; therefore $\widetilde{p}_{c2} = k \cdot \widetilde{p}_{c1}$. This consideration leads to a more appropriate scaling of the work per cycle

$$\zeta = -\frac{\mathcal{W}}{\pi\, b\, \bar{q}^2\, (p_0 - p_1)\, k} \tag{7.1}$$

note the explicit dependency from reduced frequency k as opposed to the definition of Eq. (2.48). This dependency from frequency is, ultimately, what LINSUB provides and the reason why it can correct an ML model trained on high order data. The choice of quantity of interest for this work, although quite common, was based on the assumption that the work per cycle could be normalised by steady quantities only. This assumption is incorrect in the frequency regime investigated here, therefore, while the FCNN has no way of being corrected to make predictions outside of the training range, the PGML model is corrected because LINSUB takes into account the unsteadiness and provides information that was lost due to the incorrect normalisation of the work per cycle.

7.3 Future Work

Improved Quantity of Interest

The first and foremost improvement to the quantity of interest has been discussed in the previous Section. A further improvement could be dividing the aerodynamic work per cycle, and thus damping, into two components: a mean value which depends on the frequency and a first harmonic which depends on the steady flow field. An expression for such a model is, again, given by Corral and Vega (2016)

$$\zeta = \bar{\zeta}\, k + \widetilde{\zeta}\, \sin(\sigma + \phi(k)) \tag{7.2}$$

where $\bar{\zeta}$ is the mean value, $\widetilde{\zeta}$ is the first harmonic coefficient and ϕ is a phase. In this form, each quantity can be predicted by a separate ML model, which can be combined with Eq. (7.2) yielding predictions for the whole IBPA range, rather than single point values. This definition ignores higher order harmonics and acoustic resonances, which, although important, can be overlooked in first approximation.

Improved Reduced Order Model

The PGML in this work is based on a semi-analytical model for unloaded blades in a cascade. A simple improvement to the PGML can be attained by leveraging a more accurate ROM which models the effects of blade loading. Possible candidates are the models from Atassi and Akai (1980), Barbarossa et al. (2016), Corral and Vega (2017) or fast computations such as linearised Euler. Also, as the PGML performs better than the ROM, the output of one PGML model could be used as ROM to train a better model.

Introducing a measure of uncertainty

The considerations made about uncertainty in Chapter (6) are valid for the PGML model as well. Therefore, rather than building the ML model with a deterministic neural network, we can use probabilistic counterparts that can capture uncertainty by training distributions of weights and activations, rather than single values (Blundell et al., 2015; Chang, 2021).

Extension to three-dimensional flows

A simple solution to extending the PGML to three-dimensional flows is to compute the overall aerodynamic damping as a sum of spanwise 2D sections. This process though can be ill-conditioned as the final result is obtained as the algebraic sum of large numbers whose accuracy is highly dependent on the number of sections (Casoni and Benini, 2021). Moreover, the interaction between spanwise sections has been shown to be important by Rendu et al. (2019), therefore the applicability of such an approach would be limited. Two possible solutions are outlined below:

1. compute the overall aerodynamic damping as a sum of spanwise 2D sections and apply a correction to account for the interaction between the different panels. This solution would require a rigorous characterisation of the spanwise interaction and quantification of discrepancies between the simple 2D stacking and a full 3D solution. For instance, the radial migration of flow plays an important role in inducing destabilising work in fan blades, thus, as 2D sections do not allow any out-of-plane velocity component, the effect of this flow feature must be accounted for in the interaction model. It is difficult to say whether this solution is viable without further investigation, however, at first glance it does appear to be cumbersome

2. train the machine learnt model directly with results from 3D URANS computations. The input and output features will be radial profiles, rather than point values, while simpler computational methods such as linearised Euler could be used as reduced order model.

References

Abadi, M., Agarwal, A., Barham, P., Brevdo, E., Chen, Z., Citro, C., Corrado, G. S., Davis, A., Dean, J., Devin, M., Ghemawat, S., Goodfellow, I., Harp, A., Irving, G., Isard, M., Jia, Y., Jozefowicz, R., Kaiser, L., Kudlur, M., Levenberg, J., Mané, D., Monga, R., Moore, S., Murray, D., Olah, C., Schuster, M., Shlens, J., Steiner, B., Sutskever, I., Talwar, K., Tucker, P., Vanhoucke, V., Vasudevan, V., Viégas, F., Vinyals, O., Warden, P., Wattenberg, M., Wicke, M., Yu, Y., and Zheng, X. (2015). TensorFlow: Large-scale machine learning on heterogeneous systems. Software available from tensorflow.org. [Cited on pages 15 and 79.]

Adamczyk, J. J. (1978). Analysis of Supersonic Stall Bending Flutter in Axial-Flow Compressor by Actuator Disk Theory. Technical Report TP-1345, NASA. [Cited on page 13.]

Adamczyk, J. J., Stevans, W., and Jutras, R. (1982). Supersonic Stall Flutter of High-Speed Fans. *Journal of Engineering for Power*, 104(3):675–682. [Cited on page 128.]

Akai, T. J. and Atassi, H. (1980). Aerodynamic and Aeroelastic Characteristics of Oscillating Loaded Cascades at Low Mach Number - Part II: Stability and Flutter Boundaries. *Journal of Engineering for Power*, 102(2):352–356. [Cited on page 13.]

ANSYS, Inc. (2021). ANSYS CFX-Solver Theory Guide, Release 20.1. [Cited on page 39.]

Aotsuka, M. and Murooka, T. (2014). Numerical Analysis of Fan Transonic Stall Flutter. volume Volume 7B: Structures and Dynamics of *Turbo Expo: Power for Land, Sea, and Air*. V07BT35A020. [Cited on page 12.]

Atassi, H. and Akai, T. J. (1980). Aerodynamic and Aeroelastic Characteristics of Oscillating Loaded Cascades at Low Mach Number - Part 1: Pressure Distribution, Forces, and Moments. *Journal of Engineering for Power*, 102(2):344–351. [Cited on pages 13, 67, and 151.]

Atassi, H., Fang, J., and Ferrand, P. (1995). Acoustic blockage effects in unsteady transonic nozzle and cascade flows. *33rd Aerospace Sciences Meeting and Exhibit*. [Cited on pages 9, 10, and 115.]

Ayer, T. C. and Verdon, J. M. (1996). Validation of a Nonlinear Unsteady Aerodynamic Simulator for Vibrating Blade Rows. volume Volume 5: Manufacturing Materials and Metallurgy; Ceramics; Structures and Dynamics; Controls, Diagnostics and Instrumentation; Education; General of *Turbo Expo: Power for Land, Sea, and Air*. V005T14A035. [Cited on page 37.]

Barbarossa, F., Parry, A. B., Green, J. S., and di Mare, L. (2016). An Aerodynamic Parameter for Low-Pressure Turbine Flutter. *Journal of Turbomachinery*, 138(5):051001. [Cited on pages 13 and 151.]

Barth, T. and Jespersen, D. (1989). The design and application of upwind schemes on unstructured meshes. AIAA 27th Aerospace Sciences Meeting. [Cited on page 39.]

Belkin, M., Hsu, D., Ma, S., and Mandal, S. (2019). Reconciling modern machine-learning practice and the classical bias–variance trade-off. *Proceedings of the National Academy of Sciences*, 116(32):15849–15854. [Cited on page 58.]

Bendiksen, O. (1991). A new approach to computational aeroelasticity. 32nd Structures, Structural Dynamics, and Materials Conference, pages 1712–1727. [Cited on page 14.]

Blundell, C., Cornebise, J., Kavukcuoglu, K., and Wierstra, D. (2015). Weight Uncertainty in Neural Networks. In *Proceedings of the 32nd International Conference on International Conference on Machine Learning - Volume 37*, ICML'15, page 1613–1622. JMLR.org. [Cited on page 152.]

Bontemps, T. (2020). *Flottement fan et couplage acoustique : analyse et modélisation*. PhD thesis, École Centrale de Lyon. Thèse de doctorat dirigée par Aubert, Stéphane Mécanique des fluides Lyon 2020. [Cited on pages xv, xxv, 2, 10, and 12.]

Breiman, L. (2001). Random Forests. *Machine Learning*, 45(1):5–32. [Cited on pages 48, 133, and 137.]

Brunton, S. L., Noack, B. R., and Koumoutsakos, P. (2020). Machine learning for fluid mechanics. *Annual Review of Fluid Mechanics*, 52(1):477–508. [Cited on page 15.]

Campbell, W. (1924). The Protection of Steam-Turbine Disk Wheels From Axial Vibration - Part II - Exposition of the Nature and Theory of Vibration in Turbine Wheels. *Gen. Electr. Rev.*, 27(7):459–484. [Cited on page 5.]

Carta, F. O. (1967). Coupled Blade-Disk-Shroud Flutter Instabilities in Turbojet Engine Rotors. *Journal of Engineering for Power*, 89(3):419–426. [Cited on page 50.]

Casoni, M. and Benini, E. (2021). A Review of Computational Methods and Reduced Order Models for Flutter Prediction in Turbomachinery. *Aerospace*, 8(9). [Cited on pages 12 and 152.]

Chang, D. T. (2021). Probabilistic deep learning with probabilistic neural networks and deep probabilistic models. [Cited on page 152.]

Chen, J. (2022). *Convolutional neural networks for steady flow prediction around 2D obstacles*. Theses, Université Paris sciences et lettres. [Cited on pages xvi and 46.]

Clark, S. T., Kielb, R. E., and Hall, K. C. (2012). Developing a Reduced-Order Model to Understand Non-Synchronous Vibration (NSV) in Turbomachinery. volume Volume 7: Structures and Dynamics, Parts A and B of *Turbo Expo: Power for Land, Sea, and Air*, pages 1373–1382. [Cited on page 6.]

Clark, W. S. and Hall, K. C. (1999). A Time-Linearized Navier–Stokes Analysis of Stall Flutter . *Journal of Turbomachinery*, 122(3):467–476. [Cited on page 14.]

Collar, A. R. (1946). The Expanding Domain of Aeroelasticity. *The Journal of the Royal Aeronautical Society*, 50(428):613–636. [Cited on pages xv, 3, and 4.]

Corral, R., Crespo, J., and Gisbert, F. (2004). Parallel multigrid unstructured method for the solution of the navier-stokes equations. 42nd AIAA Aerospace Sciences Meeting and Exhibit. [Cited on page 14.]

Corral, R. and Gallardo, J. M. (2014). Nonlinear dynamics of bladed disks with multiple unstable modes. *AIAA Journal*, 52(6):1124–1132. [Cited on page 13.]

Corral, R., Gallardo, J. M., and Martel, C. (2009). A Conceptual Flutter Analysis of a Packet of Vanes Using a Mass-Spring Model. *Journal of Turbomachinery*, 131(2). 021016. [Cited on page 6.]

Corral, R. and Vega, A. (2016). Physics of Vibrating Turbine Airfoils at Low Reduced Frequency. *Journal of Propulsion and Power*, 32(2):325–336. [Cited on pages 59, 150, and 151.]

Corral, R. and Vega, A. (2017). Quantification of the Influence of Unsteady Aerodynamic Loading on the Damping Characteristics of Airfoils Oscillating at Low-Reduced Frequency—Part I: Theoretical Support. *Journal of Turbomachinery*, 139(3):031009. [Cited on pages 13 and 151.]

Crawley, E. (1987). Aeroelastic Formulations for Turbomachines and Propellers. In Platzer, M. F. and Carta, F. O., editors, *AGARD Manual on Aeroelasticity in Axial-Flow Turbomachines*, volume 2, pages 19.1–19.24. [Cited on pages 27 and 28.]

Cumpsty, N. (2004). *Compressor Aerodynamics*. Number v. 10 in Compressor aerodynamics. Krieger Publishing Company. [Cited on pages 86 and 146.]

Daw, A., Thomas, R. Q., Carey, C., J.S., R., Appling, A. P., and Karpatne, A. (2020). Physics-guided architecture (pga) of neural networks for quantifying uncertainty in lake temperature modeling. In *Proceedings of the 2020 SIAM International Conference on Data Mining (SDM)*, pages 532–540. [Cited on page 77.]

Debrabandere, F., Tartinville, B., Hirsch, C., and Coussement, G. (2012). Fluid–Structure Interaction Using a Modal Approach. *Journal of Turbomachinery*, 134(5). 051043. [Cited on page 14.]

Dixon, S. and Hall, C. (2013). *Fluid Mechanics and Thermodynamics of Turbomachinery*. Elsevier Science. [Cited on pages 84 and 86.]

Donini, N. (2012). Aeroelasticity of Turbomachines Linearized Flutter Analysis. Master's thesis, Politecnico di Milano. Available at http://hdl.handle.net/10589/71845. [Cited on pages xvii, 72, and 73.]

Dow, E. and Wang, Q. (2012). Quantification of structural uncertainties in the k -w turbulence model. 52nd AIAA/ASME/ASCE/AHS/ASC Structures, Structural Dynamics and Materials Conference. [Cited on page 15.]

Dowell, E. H., editor (2015). *A Modern Course in Aeroelasticity*, pages 428–429. Springer, 5th edition. [Cited on page 10.]

Ducharme, E. H. (1987). *Velocity scaled aeroelastic testing of an unducted fan*. PhD thesis, Massachusetts Institute of Technology. [Cited on page 6.]

Duraisamy, K., Iaccarino, G., and Xiao, H. (2019). Turbulence modeling in the age of data. *Annual Review of Fluid Mechanics*, 51(1):357–377. [Cited on page 15.]

Efron, B. (1979). Bootstrap Methods: Another Look at the Jackknife. *The Annals of Statistics*, 7(1):1 – 26. [Cited on page 145.]

Emery, J. C., Herrig, J. L., and Erwin, J. R. (1958). Systematic Two-Dimensional Cascade Tests of NACA 65-Series Compressor Blades at Low Speeds. Technical Report 1368, NACA. [Cited on page 87.]

Fletcher, R. (1987). *Practical Methods of Optimization*. Number v. 2 in A Wiley-Interscience publication. Wiley. [Cited on page 55.]

Florea, R., Hall, K. C., and Cizmas, P. G. (1998). Reduced-order modeling of unsteady viscous flow in a compressor cascade. *AIAA journal*, 36(6):1039–1048. [Cited on page 16.]

Frannson, T. and Verdon, J. (1991). Update Report on Standard Configurations for Unsteady Flow through Vibrating Axial-flow Turbomachine Cascades. Progress report. [Cited on pages 37, 72, and 73.]

Fransson, T. (2013). Flutter-free turbomachinery blades (FUTURE). Technical report, European Commission. [Cited on page 128.]

Frey Marioni, Y., Adami, P., Vazquez Diaz, R., Cassinelli, A., Sherwin, S., and Montomoli, F. (2022). Development of Machine-Learnt Turbulence Closures for Wake Mixing Predictions in Low-Pressure Turbines. volume Volume 10C: Turbomachinery — Design Methods and CFD Modeling for Turbomachinery; Ducts, Noise, and Component Interactions of *Turbo Expo: Power for Land, Sea, and Air*. V10CT32A032. [Cited on page 78.]

Frey Marioni, Y., de Toledo Ortiz, E. A., Cassinelli, A., Montomoli, F., Adami, P., and Vazquez, R. (2021). A machine learning approach to improve turbulence modelling from dns data using neural networks. *International Journal of Turbomachinery, Propulsion and Power*, 6(2). [Cited on page 77.]

Försching, H. (1994). Aeroelastic Stability of Cascades in Turbomachinery. *Progress in Aerospace Sciences*, 30(3):213–266. [Cited on page 27.]

Gambitta, M., Beirow, B., and Schrape, S. (2022). A Digital Twin of Compressor Blisk Manufacturing Geometrical Variability for the Aeroelastic Uncertainty Quantification of the Aerodynamic Damping. volume Volume 8A: Structures and Dynamics of *Turbo Expo: Power for Land, Sea, and Air*. V08AT21A021. [Cited on pages 16 and 81.]

Giles, M. (1992). An Approach for Multi-Stage Calculations Incorporating Unsteadiness. volume Volume 1: Turbomachinery of *Turbo Expo: Power for Land, Sea, and Air*. V001T01A092. [Cited on page 14.]

Giles, M. B. (1990). Non-Reflecting Boundary Conditions for Euler Equation Calculations. *AIAA Journal*, 28(12):2050–2058. [Cited on pages 26, 32, and 34.]

Glorot, X. and Bengio, Y. (2010). Understanding the difficulty of training deep feedforward neural networks. In Teh, Y. W. and Titterington, M., editors, *Proceedings of the Thirteenth International Conference on Artificial Intelligence and Statistics*, volume 9 of *Proceedings of Machine Learning Research*, pages 249–256, Chia Laguna Resort, Sardinia, Italy. PMLR. [Cited on page 167.]

Hall, K. C. and Crawley, E. F. (1989). Calculation of unsteady flows in turbomachinery using the linearizedeuler equations. *AIAA Journal*, 27(6):777–787. [Cited on page 37.]

Hall, K. C. and Lorence, C. B. (1993). Calculation of Three-Dimensional Unsteady Flows in Turbomachinery Using the Linearized Harmonic Euler Equations. *Journal of Turbomachinery*, 115(4):800–809. [Cited on page 14.]

Hall, K. C., Thomas, J. P., and Clark, W. S. (2002). Computation of Unsteady Nonlinear Flows in Cascades Using a Harmonic Balance Technique. *AIAA Journal*, 40(5):879–886. [Cited on page 14.]

Hammond, J., Pepper, N., Montomoli, F., and Michelassi, V. (2022). Machine learning methods in cfd for turbomachinery: A review. *International Journal of Turbomachinery, Propulsion and Power*, 7(2). [Cited on page 15.]

He, K., Zhang, X., Ren, S., and Sun, J. (2015). Delving deep into rectifiers: Surpassing human-level performance on imagenet classification. [Cited on page 167.]

He, X., Tan, J., Rigas, G., and Vahdati, M. (2022). On the explainability of machine-learning-assisted turbulence modeling for transonic flows. *International Journal of Heat and Fluid Flow*, 97:109038. [Cited on page 78.]

He, X., Zhao, F., and Vahdati, M. (2020). Uncertainty Quantification of Spalart-Allmaras Turbulence Model Coefficients for Simplified Compressor Flow Features. *Journal of Fluids Engineering*, 142(9). [Cited on pages xvi and 47.]

Heyse, J. F., Mishra, A. A., and Iaccarino, G. (2021). Estimating rans model uncertainty using machine learning. *Journal of the Global Power and Propulsion Society*, (May):1–14. [Cited on page 137.]

Höhn, W. (2000). *Numerical investigation of blade flutter at or near stall in axial turbomachines.* PhD thesis, KTH. [Cited on page 37.]

Isomura, K. and Giles, M. B. (1998). A Numerical Study of Flutter in a Transonic Fan. *Journal of Turbomachinery*, 120(3):500–507. [Cited on pages 11, 12, and 128.]

Jia, X., Huang, H., and Wang, D. (2021). Effect of Fan Blade Vibration Mode on Flutter Stability. volume GPPS Xian 21 of *Proceedings of Global Power and Propulsion Society*. [Cited on page 12.]

Jin, X., Cai, S., Li, H., and Karniadakis, G. (2021). Nsfnets (navier-stokes flow nets): Physics-informed neural networks for the incompressible navier-stokes equations. *Journal of Computational Physics*, 426:109951. [Cited on page 77.]

Jutur, P. and Govardhan, R. N. (2019). Flutter in Started and Unstarted Transonic Linear Cascades: Simultaneous Measurements of Unsteady Loads and Shock Dynamics. *Journal of Turbomachinery*, 141(12). 121004. [Cited on pages 128 and 130.]

Kedward, L., Allen, C., and Rendall, T. (2017). Efficient and exact mesh deformation using multiscale rbf interpolation. *Journal of Computational Physics*, 345:732–751. [Cited on pages 74 and 86.]

Khalid, S. A., Khalsa, A. S., Waitz, I. A., Tan, C. S., Greitzer, E. M., Cumpsty, N. A., Adamczyk, J. J., and Marble, F. E. (1999). Endwall Blockage in Axial Compressors. *Journal of Turbomachinery*, 121(3):499–509. [Cited on page 83.]

Kingma, D. P. and Ba, J. (2014). Adam: A method for stochastic optimization. [Cited on page 79.]

Kiss, A. L. A. (2021). *Forced Response System Identification of Gas Turbine Fan Flutter*. PhD thesis, Massachusetts Institute of Technology. [Cited on page 83.]

Lecun, Y. (1989). *Generalization and network design strategies*. Elsevier. [Cited on page 55.]

Lieblein, S. and Roudebush, W. H. (1956). Theoretical Loss Relation for Low-Speed 2D Cascade. Technical Report 3662, NACA. [Cited on page 84.]

Ling, J., Kurzawski, A., and Templeton, J. (2016). Reynolds averaged turbulence modelling using deep neural networks with embedded invariance. *Journal of Fluid Mechanics*, 807:155–166. [Cited on page 15.]

Ling, J. and Templeton, J. (2015). Evaluation of machine learning algorithms for prediction of regions of high reynolds averaged navier stokes uncertainty. *Physics of Fluids*, 27(8):085103. [Cited on pages 15, 78, and 81.]

Lundberg, S. M. and Lee, S.-I. (2017). A unified approach to interpreting model predictions. In *Proceedings of the 31st International Conference on Neural Information Processing Systems*, NIPS'17, page 4768–4777, Red Hook, NY, USA. Curran Associates Inc. [Cited on page 49.]

Manepalli, A., Albert, A., Rhoades, A., and Feldman, D. (2019). Emulating numeric hydroclimate models with physics-informed cgans. In *NeurIPS 2019 Workshop on Tackling Climate Change with Machine Learning*. [Cited on page 77.]

Marshall, J. and Imregun, M. (1996). A Review of Aeroelasticity Methods with Emphasis on Turbomachinery Applications. *Journal of Fluids and Structures*, 10(3):237–267. [Cited on page 12.]

McKay, M. D., Beckman, R. J., and Conover, W. J. (1979). A comparison of three methods for selecting values of input variables in the analysis of output from a computer code. *Technometrics*, 21(2):239–245. [Cited on page 54.]

Meinshausen, N. (2006). Quantile regression forests. *Journal of Machine Learning Research*, 7(35):983–999. [Cited on page 134.]

Meirovitch, L. (2001). *Fundamentals of Vibrations*. McGraw-Hill higher education. McGraw-Hill. [Cited on page 30.]

Menter, F. R., Kuntz, M., Langtry, R., Hanjalic, K., Nagano, Y., and Tummers, M. J. (2003). Ten years of industrial experience with the sst turbulence model, 4th:; internal symposium, turbulence, heat and mass transfer. In *4th Internal Symposium on Turbulence, heat and mass transfer*, volume 4, pages 625–632, New York. Begell House. [Cited on page 39.]

Michelassi, V. and Ling, J. (2021). Challenges and opportunities for artificial intelligence and high-fidelity simulations in turbomachinery applications: A perspective. *Journal of the Global Power and Propulsion Society*, (May):1–14. [Cited on page 15.]

Molnar, C. (2022). *Interpretable Machine Learning*. 2 edition. [Cited on page 48.]

Montgomery, M. and Verdon, J. (1997). A Three-Dimensional Linearized Unsteady Euler Analysis for Turbomachinery Blade Rows. Technical Report CR-4770, NASA. [Cited on page 37.]

Montomoli, F. (2019). *Uncertainty Quantification in Computational Fluid Dynamics and Aircraft Engines*. Springer International Publishing. [Cited on page 127.]

Motta, V., Guardone, A., and Quaranta, G. (2015). Influence of airfoil thickness on unsteady aerodynamic loads on pitching airfoils. *Journal of Fluid Mechanics*, 774:460–487. [Cited on page 16.]

Ning, W. and He, L. (1998). Computation of Unsteady Flows Around Oscillating Blades Using Linear and Nonlinear Harmonic Euler Methods. *Journal of Turbomachinery*, 120(3):508–514. [Cited on page 14.]

Nipkau, J. (2011). *Analysis of mistuned blisk vibrations using a surrogate lumped mass model with aerodynamic influences*. PhD thesis, BTU Cottbus. [Cited on page 41.]

Oldenburg, J., Borowski, F., Öner, A., Schmitz, K., and Stiehm, M. (2022). Geometry aware physics informed neural network surrogate for solving navier–stokes equation (gapinn). *Advanced Modeling and Simulation in Engineering Sciences*, 9. [Cited on page 77.]

Opgenoord, M. M. J., Drela, M., and Willcox, K. E. (2018). Physics-based low-order model for transonic flutter prediction. *AIAA Journal*, 56(4):1519–1531. [Cited on page 16.]

Panovsky, J. and Kielb, R. E. (1999). A Design Method to Prevent Low Pressure Turbine Blade Flutter . *Journal of Engineering for Gas Turbines and Power*, 122(1):89–98. [Cited on page 11.]

Pawar, S., San, O., Aksoylu, B., Rasheed, A., and Kvamsdal, T. (2021). Physics guided machine learning using simplified theories. *Physics of Fluids*, 33(1):011701. [Cited on pages 16 and 78.]

Petrie-Repar, P. (2006). Development of an Efficient and Robust Linearised Navier-Stokes Flow Solver. In Hall, K. C., Kielb, R. E., and Thomas, J. P., editors, *Unsteady Aerodynamics, Aeroacoustics and Aeroelasticity of Turbomachines*, pages 437–448, Dordrecht. Springer Netherlands. [Cited on pages 14 and 21.]

Raissi, M., Perdikaris, P., and Karniadakis, G. (2019). Physics-informed neural networks: A deep learning framework for solving forward and inverse problems involving nonlinear partial differential equations. *Journal of Computational Physics*, 378:686–707. [Cited on pages 15 and 77.]

Rauseo, M., Vahdati, M., and Zhao, F. (2021). Machine Learning Based Sensitivity Analysis of Aeroelastic Stability Parameters in a Compressor Cascade. *International Journal of Turbomachinery, Propulsion and Power*, 6(3). [Cited on page 51.]

Rauseo, M., Zhao, F., Vahdati, M., and Rendu, Q. (2022). Uncertainty Quantification of Computational Flutter Estimates of a Compressor Cascade. volume Volume 8A: Structures and Dynamics of *Turbo Expo: Power for Land, Sea, and Air*. V08AT21A010. [Cited on page 127.]

Rendu, Q. (2016). *Modélisation des écoulements transsoniques décollés pour l'étude des interactions fluide-structure*. PhD thesis, École Centrale de Lyon. Thèse de doctorat dirigée par Jacob, Marc C. et Aubert, Stéphane Mécanique des fluides Lyon 2016. [Cited on pages xv, 3, 6, 53, and 115.]

Rendu, Q., Aubert, S., and Ferrand, P. (2020). Numerical identification of mechanisms triggering 2d choke flutter in transonic fan. *Journal of Fluids and Structures*, 97:102879. [Cited on page 10.]

Rendu, Q., Vahdati, M., and Salles, L. (2019). Radial Decomposition of Blade Vibration to Identify a Stall Flutter Source in a Transonic Fan. *Journal of Turbomachinery*, 141(10). [Cited on pages 11, 12, and 152.]

Robinson, H., Pawar, S., Rasheed, A., and San, O. (2022). Physics guided neural networks for modelling of non-linear dynamics. *Neural Networks*, 154:333–345. [Cited on page 78.]

Rolls-Royce (2015). *The Jet Engine*. Wiley, 5th edition. [Cited on page 1.]

Sanders, A. J., Hassan, K. K., and Rabe, D. C. (2004). Experimental and Numerical Study of Stall Flutter in a Transonic Low-Aspect Ratio Fan Blisk . *Journal of Turbomachinery*, 126(1):166–174. [Cited on page 12.]

Sayma, A., Vahdati, M., and Imregun, M. (2000). An Integrated Nonlinear Approach for Turbomachinery Forced Response Prediction. Part I: Formulation. *Journal of Fluids and Structures*, 14(1):87–101. [Cited on page 14.]

Scillitoe, A., Seshadri, P., and Girolami, M. (2021). Uncertainty quantification for data-driven turbulence modelling with mondrian forests. *Journal of Computational Physics*, 430:110116. [Cited on page 137.]

Shapley, L. S. (1953). A value for n-person games. In Kuhn, H. W. and Tucker, A. W., editors, *Contributions to the Theory of Games II*, pages 307–317. Princeton University Press, Princeton. [Cited on page 49.]

Shibata, T. and Kaji, S. (1998). Role of shock structures in transonic fan rotor flutter. In *Proceedings of the 8th International Symposium on Unsteady Aerodynamics and Aeroelasticity of Turbomachines, Stockholm, Sweden, Sept. 14–18, 1997*, pages 733–747. Springer. [Cited on page 128.]

Singh, A. P., Medida, S., and Duraisamy, K. (2017). Machine-learning-augmented predictive modeling of turbulent separated flows over airfoils. *AIAA Journal*, 55(7):2215–2227. [Cited on page 15.]

Smith, S. N. (1972). Discrete Frequency Sound Generation in Axial Flow Turbomachines. *British A.R.C.* R. & M. No. 3709. [Cited on pages 13 and 70.]

Spalart, P. and Allmaras, S. (1994). A one-equation turbulence model for aerodynamic flows. *Recherche Aerospatiale*, 1:5–21. [Cited on page 22.]

Srinivasan, A. V. (1997). Flutter and Resonant Vibration Characteristics of Engine Blades. *Journal of Engineering for Gas Turbines and Power*, 119(4):742–775. [Cited on pages 6, 7, and 11.]

Srivastava, R., Bakhle, M. A., and Keith, T. G. (2003). Numerical simulation of aerodynamic damping for flutter analysis of turbomachinery blade rows. *Journal of Propulsion and Power*, 19(2):260–267. [Cited on page 12.]

Srivastava, R., Sankar, L. N., Reddy, T. S. R., and Huff, D. L. (1991). Application of an efficient hybrid scheme for aeroelastic analysis of advanced propellers. *Journal of Propulsion and Power*, 7(5):767–775. [Cited on page 13.]

Stapelfeldt, S. and Brandstetter, C. (2020). Non-synchronous vibration in axial compressors: Lock-in mechanism and semi-analytical model. *Journal of Sound and Vibration*, 488:115649. [Cited on page 5.]

Stapelfeldt, S. and Vahdati, M. (2018). On the Importance of Engine-Representative Models for Fan Flutter Predictions. *Journal of Turbomachinery*, 140(8). 081005. [Cited on pages 12 and 53.]

Stapelfeldt, S. and Vahdati, M. (2019). Improving the Flutter Margin of an Unstable Fan Blade. *Journal of Turbomachinery*, 141(7). 071006. [Cited on page 11.]

Tracey, B., Duraisamy, K., and Alonso, J. (2013). Application of supervised learning to quantify uncertainties in turbulence and combustion modeling. 51st AIAA Aerospace Sciences Meeting including the New Horizons Forum and Aerospace Exposition. [Cited on page 15.]

Tyler, J. M. and Sofrin, T. G. (1962). Axial flow compressor noise studies. In *SAE Technical Paper*. SAE International. [Cited on page 8.]

Vahdati, M. and Cumpsty, N. (2015). Aeroelastic Instability in Transonic Fans. *Journal of Engineering for Gas Turbines and Power*, 138(2). 022604. [Cited on pages xvi, 9, 11, 12, 52, 53, 59, and 90.]

Vahdati, M., Sayma, A. I., Marshall, J. G., and Imregun, M. (2001). Mechanisms and prediction methods for fan blade stall flutter. *Journal of Propulsion and Power*, 17(5):1100–1108. [Cited on pages 11 and 140.]

Vahdati, M., Simpson, G., and Imregun, M. (2011). Mechanisms for Wide-Chord Fan Blade Flutter. *Journal of Turbomachinery*, 133(4). 041029. [Cited on pages 11 and 12.]

van Albada, G. D., van Leer, B., and Roberts, W. W., J. (1982). A comparative study of computational methods in cosmic gas dynamics. *Astronomy and Astrophysics*, 108(1):76–84. [Cited on page 23.]

Vega, A. (2016). *Impact of the Unsteady Aerodynamics of Oscillating Airfoils on the Flutter Characteristics of Turbomachines*. PhD thesis, Universidad Politecnica de Madrid. [Cited on page 31.]

Vega, A. and Corral, R. (2013). Physics of Vibrating Airfoils at Low Reduced Frequency. volume Volume 7B: Structures and Dynamics of *Turbo Expo: Power for Land, Sea, and Air*. V07BT33A008. [Cited on page 89.]

Wada, Y. and Liou, M.-S. (1997). An accurate and robust flux splitting scheme for shock and contact discontinuities. *SIAM Journal on Scientific Computing*, 18(3):633–657. [Cited on page 23.]

Wang, J.-X., Wu, J.-L., and Xiao, H. (2017). Physics-informed machine learning approach for reconstructing reynolds stress modeling discrepancies based on dns data. *Phys. Rev. Fluids*, 2:034603. [Cited on page 78.]

Whitehead, D. S. (1960). Force and Moment Coefficients for Vibrating Aerofoils in Cascade. *British A.R.C.* R. & M. No. 3254. [Cited on pages 13 and 70.]

Whitehead, D. S. (1962). Bending Flutter of Unstalled Cascade Blades at Finite Deflection. *British A.R.C.* R. & M. No. 3386. [Cited on pages 13 and 73.]

Whitehead, D. S. (1972). Vibration and Sound Generation in a Cascade of Flat Plates in Subsonic Flow. *British A.R.C.* R. & M. No. 3685. [Cited on pages 13 and 68.]

Whitehead, D. S. (1987). Classical Two-Dimensional Methods. In Platzer, M. F. and Carta, F. O., editors, *AGARD Manual on Aeroelasticity in Axial-Flow Turbomachines*, volume 1, pages 3.1–3.30. [Cited on pages 68 and 73.]

Whitehead, D. S. (1990). A finite element solution of unsteady two-dimensional flow in cascades. *International Journal for Numerical Methods in Fluids*, 10(1):13–34. [Cited on page 14.]

Willard, J., Jia, X., Xu, S., Steinbach, M., and Kumar, V. (2022). Integrating scientific knowledge with machine learning for engineering and environmental systems. *ACM Comput. Surv.*, 55(4). [Cited on page 15.]

Willcox, K. E. (1999). *Reduced-Order Aerodynamic Models for Aeroelastic Control of Turbomachines*. PhD thesis, Massachusetts Institute of Technology. [Cited on page 16.]

Wong, M. T. M. (1997). System Modeling and Control Studies of Flutter in Turbomachinery. Master's thesis, Massachusetts Institute of Technology. [Cited on page 83.]

Wu, J.-L., Wang, J.-X., and Xiao, H. (2016). A bayesian calibration–prediction method for reducing model-form uncertainties with application in RANS simulations. *Flow, Turbulence and Combustion*, 97(3):761–786. [Cited on page 15.]

Xiao, H. and Cinnella, P. (2019). Quantification of model uncertainty in rans simulations: A review. *Progress in Aerospace Sciences*, 108:1–31. [Cited on page 15.]

Yamamoto, O. and August, R. (1992). Structural and aerodynamic analysis of a large-scale advanced propeller blade. *Journal of Propulsion and Power*, 8(2):367–373. [Cited on page 13.]

Yao, W. and Marques, S. (2017). Application of a high-order CFD harmonic balance method to nonlinear aeroelasticity. *Journal of Fluids and Structures*, 74:427–444. [Cited on page 14.]

Yonekura, K., Wada, K., and Suzuki, K. (2022). Generating various airfoils with required lift coefficients by combining naca and joukowski airfoils using conditional variational autoencoders. *Engineering Applications of Artificial Intelligence*, 108:104560. [Cited on page 81.]

Zahn, R. and Breitsamter, C. (2022). Airfoil buffet aerodynamics at plunge and pitch excitation based on long short-term memory neural network prediction. *CEAS Aeronaut J*, (13):43–55. [Cited on page 16.]

Zhang, W., Kou, J., and Wang, Z. (2016). Nonlinear aerodynamic reduced-order model for limit-cycle oscillation and flutter. *AIAA Journal*, 54(10):3304–3311. [Cited on page 16.]

Zhang, W., Wang, B., Ye, Z., and Quan, J. (2012). Efficient method for limit cycle flutter analysis based on nonlinear aerodynamic reduced-order models. *AIAA Journal*, 50(5):1019–1028. [Cited on page 16.]

Zhao, F., Nipkau, J., and Vahdati, M. (2016). Influence of acoustic reflections on flutter stability of an embedded blade row. *Proceedings of the Institution of Mechanical Engineers, Part A: Journal of Power and Energy*, 230(1):29–43. [Cited on pages 53 and 127.]

Zhao, F., Smith, N., and Vahdati, M. (2017). A Simple Model for Identifying the Flutter Bite of Fan Blades. *Journal of Turbomachinery*, 139(7). 071003. [Cited on page 9.]

Appendix A

PGML hyperparameters

Definitions

The batch size $|B|$ is the number of samples employed to perform one training step.

The symbols $\mathcal{N}$ and $\mathcal{U}$ indicate normal and uniform distributions, respectively.

The Xavier initialisation (Glorot and Bengio, 2010) draws samples from either:

- a truncated normal distribution centered on zero with standard deviation $\sigma_{\mathcal{N}} = \sqrt{2/(N_{\text{in}} + N_{\text{out}})}$ where N_{in} is the number of input units in the weight tensor and N_{out} is the number of output units in the weight tensor.
- a uniform distribution within $[-a, a]$, where $a = \sqrt{6/(N_{\text{in}} + N_{\text{out}})}$

The He initialisation (He et al., 2015) draws samples from either:

- a truncated normal distribution centered on zero with standard deviation $\sigma_{\mathcal{N}} = \sqrt{2/N_{\text{in}}}$
- a uniform distribution within $[-a, a]$, where $a = \sqrt{6/N_{\text{in}}}$

The Standard scaler rescales the features to have zero mean and unit variance.

The He scaler rescales the features to have zero mean and standard deviation $\sigma_{\mathcal{N}} = \sqrt{2/N_{\text{features}}}$.

Table A.1 *Hyperparameters optimisation range for PGML networks*

Hyperparameter		Choice
Activation	$g(z)$	Sigmoid, tanh, ReLU, Swish
Batch Size	$\lvert B\rvert$	2^x, $x \sim \mathcal{U}(5, 10)$
Epochs		$\sim \mathcal{U}(500, 10000)$
Initialisation		He, Xavier, Random
Hidden Layers	L	$\sim \mathcal{U}(2, 15)$
Learning Rate	η	$\sim \mathcal{U}(\text{1e-5}, \text{1e-2})$
Neurons per layer	N_L	$\sim \mathcal{U}(2, 15)$
Physics Layer		$\sim \mathcal{U}(1, L-1)$
Regularisation	$\log_{10}(\lambda)$	$\sim \mathcal{U}(-5, 0)$
Scaler		Standard, Min-Max, He

Table A.2 *Hyperparameters of PGML networks*

Hyperparameter		C_L^h	C_M^h	C_L^α	C_M^α
Activation	$g(z)$	ReLU	ReLU	Swish	Swish
Batch Size	$\lvert B\rvert$	512	256	256	96
Epochs		5000	4000	4000	5000
Initialisation		He-$\mathcal{N}$	Xavier-$\mathcal{U}$	He-$\mathcal{N}$	Xavier-$\mathcal{U}$
Hidden Layers	L	5	5	6	5
Learning Rate	η	0.003	0.006	0.002	0.004
Neurons per layer	N_L	9	6	8	8
Physics Layer		4	1	5	4
Regularisation	$\log_{10}(\lambda)$	-4	-4	-5	-5
Scaler		Standard	Standard	Min-Max	Standard

Appendix B

Further PGML results

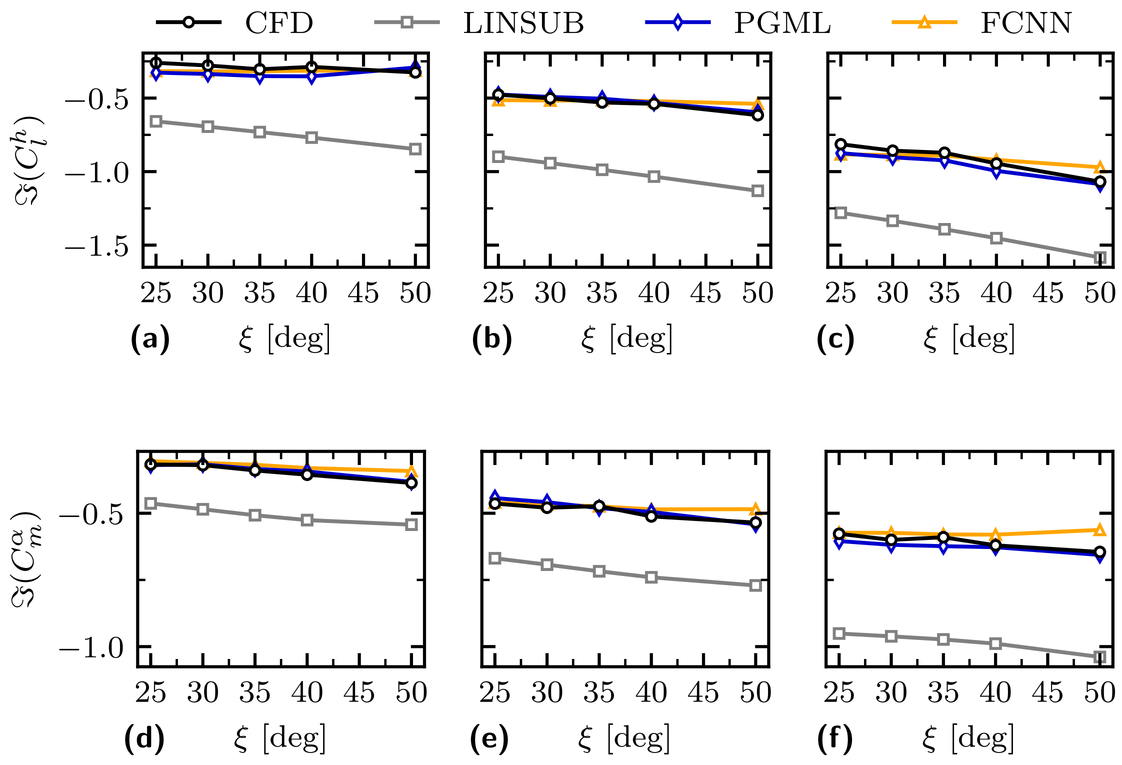

Figure B.1 *Predictions of plunge lift and pitch moment coefficients from CFD, PGML, FCNN and LINSUB against stagger angle. The steady state conditions are constant at* $M_1 = 0.85$ *and* $\beta_1 = 3°$*. The panels, from left to right, are run with reduced frequency* $k = 0.5$*,* $k = 0.7$*,* $k = 1.0$*, respectively, while the interblade phase angle is constant at* $\sigma = 20°$*.*

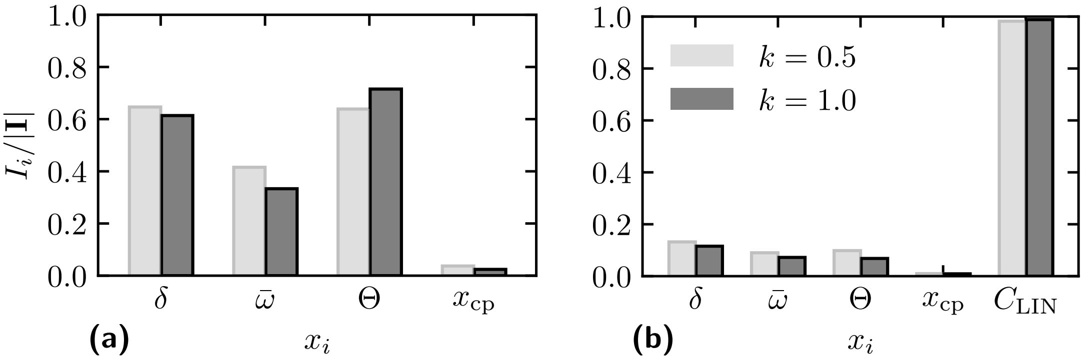

Figure B.2 *Normalised feature importance for a dataset with varying stagger angle, $\sigma = 20°$: (a) FCNN; (b) PGML.*

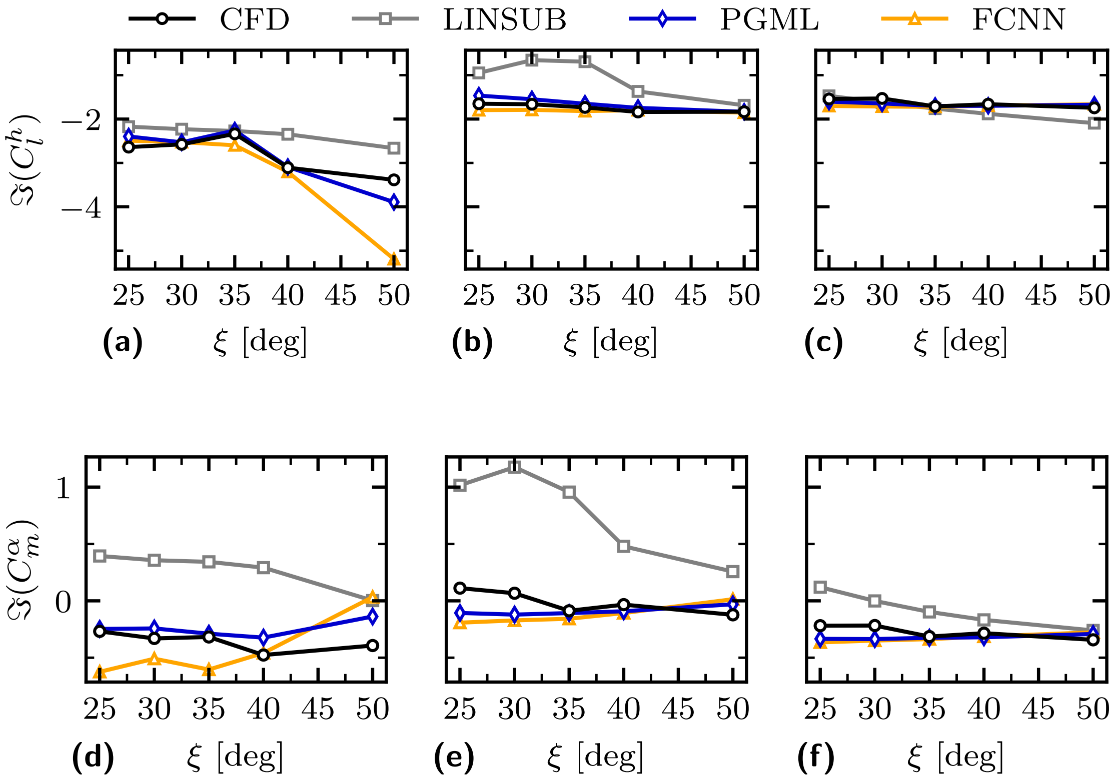

Figure B.3 *Predictions of plunge lift and pitch moment coefficients from CFD, PGML, FCNN and LINSUB against stagger angle. The steady state conditions are constant at $M_1 = 0.85$ and $\beta_1 = 3°$. The panels, from left to right, are run with reduced frequency $k = 0.5$, $k = 0.7$, $k = 1.0$, respectively, while the interblade phase angle is constant at $\sigma = 150°$.*

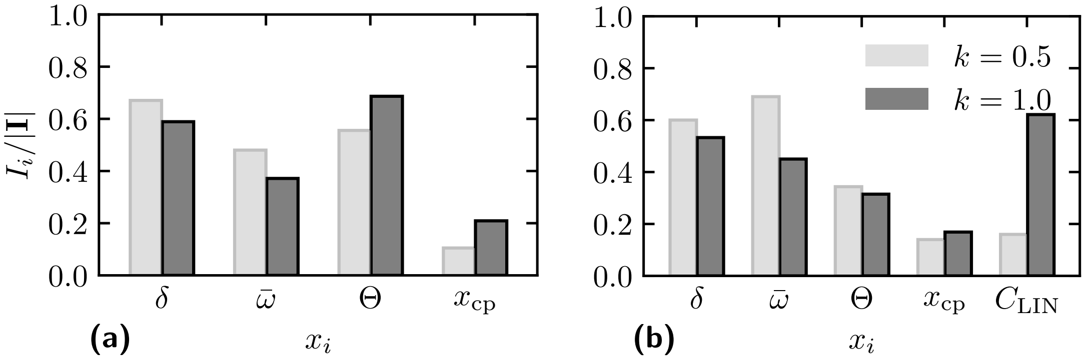

Figure B.4 *Normalised feature importance for a dataset with varying stagger angle,* $\sigma = 150°$*: (a) FCNN; (b) PGML.*

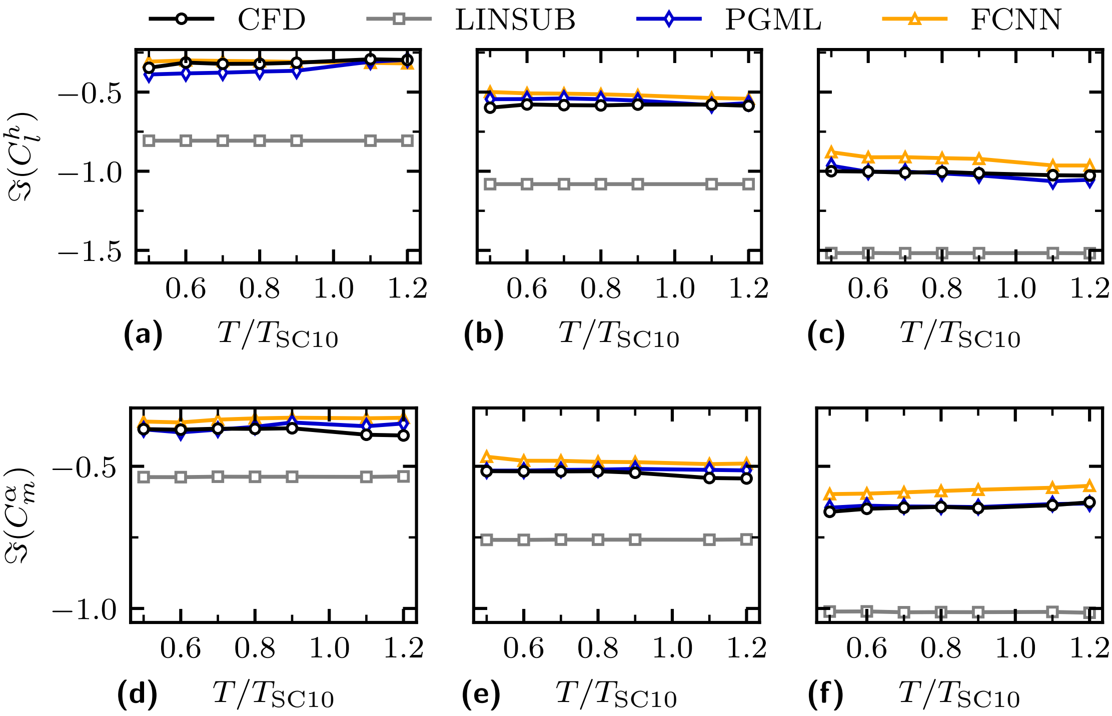

Figure B.5 *Predictions of plunge lift and pitch moment coefficients from CFD, PGML, FCNN and LINSUB against airfoil thickness. The steady state conditions are constant at* $M_1 = 0.85$ *and* $\beta_1 = 3°$*. The panels, from left to right, are run with reduced frequency* $k = 0.5$*,* $k = 0.7$*,* $k = 1.0$*, respectively, while the interblade phase angle is constant at* $\sigma = 20°$*.*

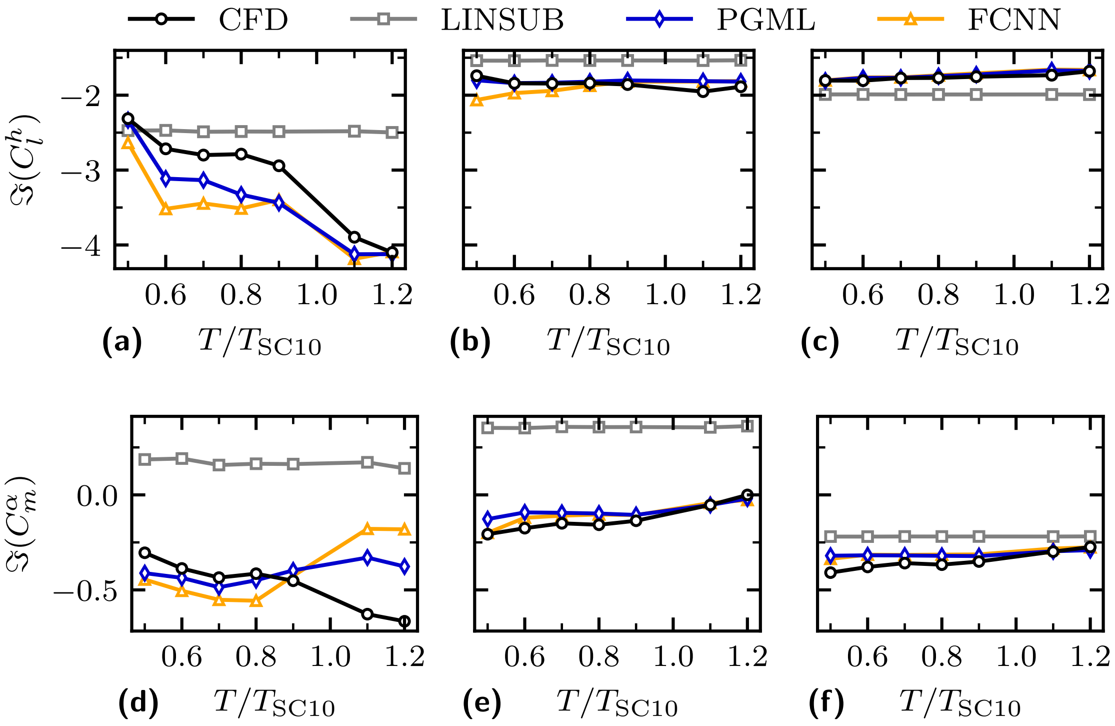

Figure B.6 *Predictions of plunge lift and pitch moment coefficients from CFD, PGML, FCNN and LINSUB against airfoil thickness. The steady state conditions are constant at* $M_1 = 0.85$ *and* $\beta_1 = 3°$*. The panels, from left to right, are run with reduced frequency* $k = 0.5$, $k = 0.7$, $k = 1.0$*, respectively, while the interblade phase angle is constant at* $\sigma = 150°$.

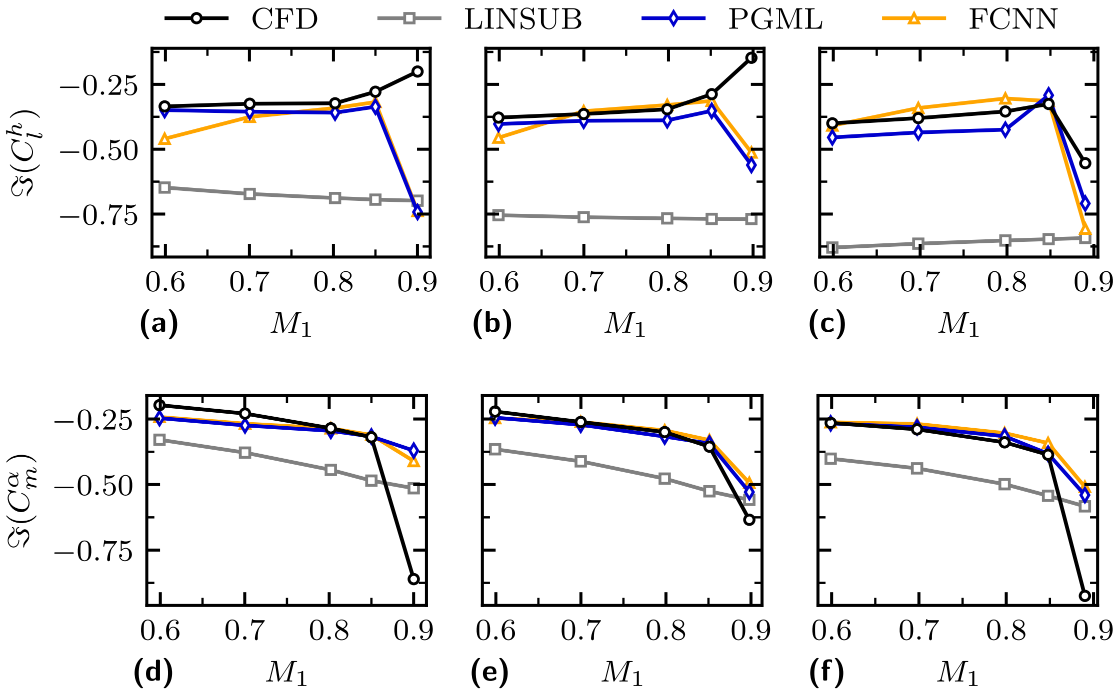

Figure B.7 *Predictions of plunge lift and pitch moment coefficients from CFD, PGML, FCNN and LINSUB against inlet Mach number. The incidence is constant at* $\beta_1 = 3°$ *and reduced frequency* $k = 0.5$. *The panels, from left to right, are run with stagger angle* $\xi = 30°$, $\xi = 40°$, $\xi = 50°$, *respectively, while the interblade phase angle is constant at* $\sigma = 20°$.

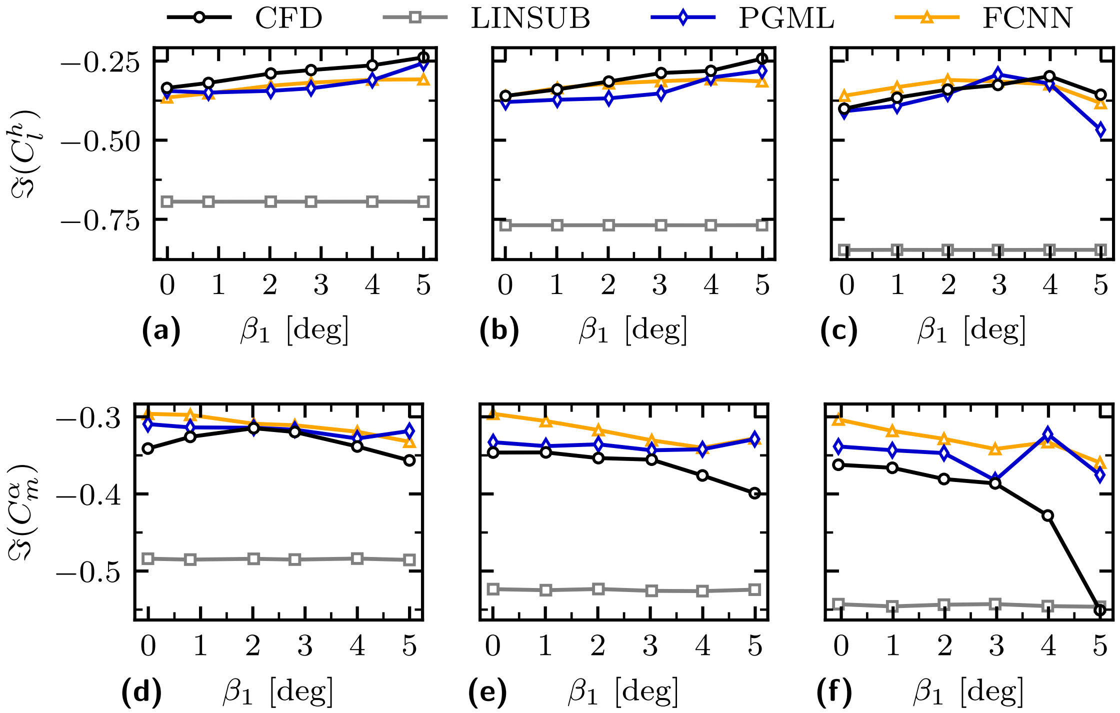

Figure B.8 *Predictions of plunge lift and pitch moment coefficients from CFD, PGML, FCNN and LINSUB against incidence. The inlet Mach number is constant at* $\beta_1 = 0.85$ *and reduced frequency* $k = 0.5$. *The panels, from left to right, are run with stagger angle* $\xi = 30°$, $\xi = 40°$, $\xi = 50°$, *respectively, while the interblade phase angle is constant at* $\sigma = 20°$.

Appendix C

Computational Cost

The machine used for all computations employs an Intel(R) Xeon(R) W-2145 CPU with a 3.70GHz clock frequency, 8 cores and 16GB RAM.

The steady state solver uses a pseudo-time stepping technique to march the solution to convergence. In this study, a steady CFD solution is considered converged if every point in the domain has a density residual of order 10^{-9}. On average, the equivalent CPU time elapsed to obtain a converged solution for the cases in this thesis is $10,000$ seconds. The unsteady solver uses a preconditioned GMRES scheme to find the solution to the system arising from the linearisation of the URANS equations. In this study, an unsteady CFD solution is considered converged if the residual is of order 10^{-9}. On average, the equivalent CPU time elapsed to obtain a converged solution is 60 seconds. Two unsteady simulations are necessary to compute the four unsteady coefficients.

LINSUB calculates all four coefficients with a single computation. On average, the equivalent CPU time elapsed is 0.6 seconds.

The computational cost associated with post-processing routines is ignored as: 1) it is negligible compared to computations, 2) the routines have not been optimised.

The training set is composed of 5 databases of Standard Configuration 10 sets of computations, for a total of 3968 data points. The time elapsed to compute the databases amounts to approximately 11100 equivalent CPU hours, including one steady state, two time-linearised and one LINSUB computations.

The validation set employed in Chapter (5) is composed of 25 different cascades, each obtained by varying one parameter of the original Standard Configuration 10:

- 7 cases with different airfoil thickness
- 4 cases with different airfoil camber
- 5 cases with different stagger angle

- 9 cases with different cascade solidity

For each cascade, a total of 35 steady state computations is run:

- 7 inlet flow angles
- 5 inlet Mach numbers

For each steady state flow, a total of 444 time-linearised computations is run:

- 2 modeshapes
- 6 reduced frequency values
- 37 interblade phase angles

Therefore, 388500 time-linearised computations are needed to compute the validation set. The estimated CPU time for the CFD computations amounts to 8900 hours, while for the PGML it amounts to 2460 hours. The reduction in computational time from CFD to PGML is approximately 70%. If we account for the time elapsed for the generation of the training data, the PGML requires an additional 50% in computational time when compared to CFD. This is assuming that no data are available, which is untrue for a real industrial setting.